Polymerisation Catalysts enabling Carbon Dioxide Utilization



University of Oxford

Department of Chemistry

St. Catherine's College

February 2023

A thesis submitted in partial fulfilment of the requirements for the degree of Doctor of Philosophy in Chemistry

For my family and friends

Declaration

All work presented in this thesis was carried out at the University of Oxford, by the author, unless otherwise stated.

The copyright of this thesis rests with the author and is made available under a Creative Commons Attribution Non-Commercial No Derivatives licence. Researchers are free to copy, distribute or transmit the thesis on the condition that they attribute it, that they do not use it for commercial purposes and that they do not alter, transform or build-upon it. For any reuse or distribution, researchers must make clear to others the licence terms of this work.

Abstract

This thesis describes the development of homogeneous catalysts for epoxide/carbon dioxide (CO_2) ring-opening copolymerisation (ROCOP). The objective is to increase understanding of the polymerisation mechanism and factors controlling catalyst performance. It ends with an application of the best catalyst to polymerisation of epoxide, carbon dioxide and lactide using 'switch' catalysis.

Chapter 1 provides an introduction to the ROCOP of epoxides and CO_2, with a particular focus on catalyst development and mechanism. It also introduces the concept of 'switchable' catalysis.

Chapter 2 details the mechanistic exploration of a high performance heterodinuclear Co(III)K(I) catalyst for propylene oxide/carbon dioxide (CO_2) ring-opening copolymerisation (ROCOP). A detailed computational investigation of the full catalytic cycle is performed and barriers match with experimental ones. The proposed mechanism occurs with a rate determining step involving epoxide activation at Co(III) and nucleophilic attack by a carbonate bound to the K(I). Further examination, both experimentally and computationally, of the cyclic carbonate formation is undertaken and showed that it occurs *via* both a random chain scission and chain 'unzipping' mechanism.

Chapter 3 details a structure-activity study of the Co(III)K(I) catalyst system underpinned by the findings in Chapter 2. The investigation explores the effect of ligand structure on the Co(III/II) redox potential, activity and selectivity in propene oxide (PO)/carbon dioxide (CO_2) ring-opening copolymerisation (ROCOP). It rationalises the effects of these changes using the polymerisation mechanism. The key finding is that a lower redox potential, corresponding to higher electron density at Co(III), leads to higher activity and selectivity in propylene oxide (PO)/carbon dioxide (CO_2) ring-opening copolymerisation (ROCOP).

Chapter 4 details the application of a high activity and selectivity Co(III)K(I) catalyst to the 'switchable' catalysis of ally glycidyl ether (AGE)/CO_2 and *L*-lactide (*L*-LA), producing a block polymer (PLLA-*b*-PAGEC-*b*-PLLA). The experimental method, involving a new gas line, is developed and the characterisation proofs of 'switch' are presented.

Chapter 5 outlines the key developments of this thesis and suggests potential future directions for the research.

Chapter 6 provides experimental details for Chapter 2-4.

Chapter 7 is an appendix that provides supplementary information, figures and data that support the work and discussion through Chapter 2-4.

Acknowledgements

Firstly, I would like to thank Prof. Charlotte Williams for giving me the opportunity to work in her group, and for her supervision over the course of my DPhil and masters. Your guidance, support, and encouragement have always been greatly appreciated.

I would also like to thank the Williams group as a whole, past and present, for creating a great and friendly working environment. Special thanks goes to George for putting up with all my questions throughout my time here, also to Arron for helping me. To Thom for the help with depolymerisations as well as reading through my whole thesis in great detail. Thank you to my dugout, Holly, Sandy, Lukas and Rachel for entertainment and to Fran, Kam and Kat for all the good chat. Holly, thank you so much for supporting me and making everything fun and light-hearted even in the tough times.

I would also like to thank my family for all their support over the years. Most of all, I would like to thank Alex for keeping me sane and for supporting me throughout everything, I would not have made it here without you.

List of Publications

Lindeboom, W., Fraser, D. A. X., Durr, C. B. & Williams, C. K. Heterodinuclear Zn(II), Mg(II) or Co(III) with Na(I) Catalysts for Carbon Dioxide and Cyclohexene Oxide Ring Opening Copolymerizations. *Chem. Eur. J.* **27**, 12224, (2021).

Diment, W. T., Lindeboom, W., Fiorentini, F., Deacy, A. C. & Williams, C. K. Synergic Heterodinuclear Catalysts for the Ring-Opening Copolymerization (ROCOP) of Epoxides, Carbon Dioxide, and Anhydrides. Acc. Chem. Res. **55**, 1997-2010, (2022).

Deacy, A. C., Phanopoulos, A., Lindeboom, W., Buchard, A. & Williams, C. K. Insights into the Mechanism of Carbon Dioxide and Propylene Oxide Ring-Opening Copolymerization Using a Co(III)/K(I) Heterodinuclear Catalyst. *J. Am. Chem. Soc.* **144**, 17929-17938, (2022).

Lindeboom, W., Deacy, A. C., Phanopoulos, A., Buchard, A. & Williams, C. K. Predicting Co(III)K(I) Catalyst Performances Using Reduction Potentials in Carbon Dioxide and Propene Oxide Ring Opening Copolymerizations.. ***(Submitted)***

Abbreviations

Å	Angstrom
AGE	Allyl Glycidyl Ether
Ar	Aryl
ATR-IR	Attenuated Total Reflectance Infrared
A. U.	Arbitrary Units
b	Block
BDM	Benzenedimethanol
BDI	β-diimine
BO	Butylene Oxide
Bz	Benzoate
C	Celsius
Cat.	Catalyst
CHD	Cyclohexene-1,2-diol
CHO	Cyclohexene Oxide
COSY	Correlated Spectroscopy
Conv.	Conversion
Cp	Cyclopentadienyl
CTA	Chain Transfer Agent
D	Diffusion Coefficient
Đ	Dispersity
DBU	1,8-Diazabicyclo[5.4.0]undec-7-ene
DCM	Dichloromethane
ΔG	Change in Gibbs Free Energy
DGA	Diglycolic Anhydride
DFT	Density Functional Theory

DOSY	Diffusion Ordered NMR Spectroscopy
DSC	Differential Scanning Calorimetry
equiv.	Equivalents
Et	Ethyl
FT	Fourier Transform
g	gram
GPC	Gel Permeation Chromatography
h	hour
HMBC	Heteronuclear Multiple Bond Correlation
HSQC	Heteronuclear Single Quantum Coherence
IR	Infrared
k	Rate Constant
kcal	Kilogram
k_{obs}	Observed Rate Constant
L	Ligand
LA	Lactide
m	Minute
M	Metal
Me	Methyl
mg	milligram
mol	mole
M_n	Number Average Molecular Mass
NMR	Nuclear Magnetic Resonance
OAc	Acetate
P	Polymer chain
PAGEC	Poly(allyl glycidyl ether carbonate)

PCHC	Poly(cyclohexene carbonate)
PLA	Poly(lactic acid)
PLLA	Poly(*L*-lactic acid)
PPC	Poly(propylene carbonate)
ppm	Parts Per Million
PPN	Bis(triphenylphosphine)imine
R	Generic Substituent
RDS	Rate Determining Step
ROCOP	Ring-Opening Copolymerisation
ROP	Ring-Opening Polymerisation
s	Second
SEC	Size Exclusion Chromatography
t	Time
T	Temperature
T_d	Decomposition Temperature
^{t}Bu	*tert*-butyl
T_g	Glass Transition Temperature
TGA	Thermogravimetric Analysis
THF	Tetrahydrofuran
TOF	Turnover Frequency
TON	Turnover Number
vs.	versus
X	Generic coligand
XRD	X-ray Diffraction

List of Figures, Schemes and Tables

Figure 1.1 Polycarbonate derived polyurethane synthesis. 19

Scheme 1.1 Illustration of reaction mechanism of the ROCOP of carbon dioxide with propylene oxide along with potential side-reactions (cyclic carbonate and polyether formation). 21

Scheme 1.2 Polycyclohexene Carbonate (PCHC) and Polypropylene Carbonate (PPC) synthesis with CO_2. 22

Scheme 1.3 Mononuclear mechanism for mononuclear complex. 23

Scheme 1.4 Bicomponent mechanism for monometallic catalyst with ionic co-catalyst**.** 24

Scheme 1.5 'Chain Shuttling' Mechanism. 25

Figure 1.2 Porphyrin catalysts for CO_2/Epoxide ROCOP. 26

Figure 1.3 Bimetallic porphyrin catalyst for CO_2/Epoxide ROCOP. 27

Figure 1.4 Salen catalyst for CO_2/Epoxide ROCOP. 28

Figure 1.5 Tethered metal salen catalysts. 29

Figure 1.6 Dinuclear Zinc catalysts. 30

Figure 1.7 Tethered dinuclear salen catalysts. 31

Figure 1.8 Dinuclear catalysts. 32

Figure 1.9 Illustration of the potential energy surface for the rate limiting step of alternating copolymerization of cyclohexene oxide and carbon dioxide. 32

Figure 1.10 A Comparison between homo- and heterobimetallic zinc and magnesium complexes reported by the Williams' group. **B** crystal structure of Zn Mg catalyst with THF. 33

Figure 1.11 Dinuclear Zinc catalyst. 34

Figure 1.12 Multinuclear Catalysts. 35

Figure 1.13 Tertiary and Quaternary phosphonium borane catalyst. 35

Table 1.1 Selected catalysts for the of PO/CO_2 ROCOP. 36

Figure 1.14 Macrocyclic ligand studied in this thesis. 37

Figure 1.15 Macrocyclic ligand derivatives and variations. 38

Figure 1.16 Hexa-coordinate Co(II) complex. 39

Figure 1.17 Co(III)M(I) heterodinuclear catalyst for CO_2/epoxide ROCOP. 40

Figure 2.1 a) Illustration of the Co(III)K(I) heterodinuclear catalyst **1**. b) illustration of the 'bowl'-shape conformation of the ligand resulting in 'concave' and 'convex' faces. c) ORTEP representation of the molecular structure of catalyst 1 obtained through single crystal X-ray diffraction. d) Illustration of the 'Z'-shape conformation of the ligand resulting in complexes with 'top' (κ_2-acetate) and 'bottom' (κ_1-acetate) faces. 48

Figure 2.2 Illustrations of the potential energy surfaces for the initiation of propylene oxide and carbon dioxide copolymerisation using catalyst **1**, where propylene oxide coordination occurs at Co(III). 49

Figure 2.3 Illustrations of the potential energy surfaces for the alternating copolymerisation of propylene oxide and carbon dioxide using catalyst **1**, where propylene oxide coordination occurs at Co(III). 51

Figure 2.4 Illustrations of the potential energy surfaces for the alternating copolymerisation of propylene oxide and carbon dioxide using catalyst **1**, where propylene oxide coordination occurs at K(I). 52

Figure 2.5 a) Eyring analysis for the transition state barrier to ring opening of propylene oxide during propagation using catalyst **1**.[1] b) Key intermediates of ring-opening of PO. 54

Scheme 2.1 'Chain-Shuttling' mechanism proposed by Williams and co-workers for Zn(II)Zn(II) catalysts for CHO/CO_2 ROCOP. 55

Figure 2.6 Bound (**TS1$_{Co}$**) *versus* associated (**TS1$_{Co}$'**) carbonate to the K(I) centre in the transition state of the ring-opening of PO. 55

Scheme 2.2 Simple mechanism of PO/CO_2 ROCOP and side reactions. 56

Figure 2.7 Illustration of the potential energy surface for the backbiting reaction of CO_2 with Propylene oxide using 1 starting from a) the cobalt-carbonate intermediate **VI$_{Co}$** and b) the cobalt-alkoxide intermediate **II$_{Co}$**. 57

Figure 2.8 Plot showing the change in concentration of carbonate linkages (−OC(O)O−) in both PPC and PC against time using catalyst **1**, at 45 °C, obtained by a) *in situ* IR spectroscopy and b) NMR spectroscopy with an exponential fit to the data allowing for the determination of the pseudo first-order rate coefficient. 59

Figure 2.9 a) Catalysed depolymerisation of PPC to PC using catalyst **1**. b) Eyring analysis, i.e., a plot of ln(k_b/T) vs 1/T, for the decomposition of PPC into PC using catalyst **1**. Where $k_b = k_{obs}$/[**1**] and k_{obs} is the gradient of the plot of ln[PPC]$_t$/[PPC]$_0$ vs time (s) (Table S2.1). 60

Figure 2.10 a) Molar mass and dispersity against time using catalyst **1**, at 45 °C. b) GPC traces of time points. c) Molar mass and dispersity against conversion using catalyst **1**, at 45 °C. 61

Scheme 2.3 Representation of chain-end 'unzipping' mechanism and random chain scission mechanism. 62

Figure 2.11 ^{1}H NMR spectrum ($CDCl_3$) of PPC-OH and end-capped PPC. *marks residual THF and Et_2O and # marks residual DCM. 62

Figure 2.12 GPC traces of PPC-OH and PPC-OAc. 63

Figure 2.13 $^{31}P\{^1H\}$ NMR spectrum ($CDCl_3$) of PPC-OH and PPC-OAc using an end group titration. 63

Figure 2.14 TGA data for PPC-OH and PPC-OAc. 64

Figure 2.15 Plot showing the change in concentration of carbonate linkages (−OC(O)O−) in both PPC and PC against time using catalyst **1** and PPC-OAc, at 45 °C, obtained by *in situ* IR spectroscopy. 65

Scheme 2.4 Illustration of the reaction equilibria of reversible CO_2 insertion between intermediates **II$_{Co}$** and **VI$_{Co}$**. 65

Table 2.1 Pressure Dependence of the Polymer Selectivity for CO_2/PO Reaction using Catalyst **1**. 66

Figure 3.1 Structures of selected literature catalysts. 72

Scheme 3.1 Synthesis of complexes **1-3$_R$** from **LH$_2$**. (i) KOAc, $Co(OAc)_2$, MeCN, 25 °C, 30 min, N_2 (ii) Diamine, MeCN, 25 °C, 16 h, N_2 (iii) AcOH, air, MeCN, 48 h. **3$_{OMe}$**: (i) $Ba(ClO_4)_2$, MeCN, 25 °C then diamine, 24 h (ii) Guanidinium Sulfate, H_2O/$CHCl_3$, 25 °C, 16 h (iii) KOAc, $Co(OAc)_2$, MeCN, 25 °C, 16 h, N_2 (iv) AcOH, air, MeCN, 48 h. 74

Scheme 3.2 Synthesis of complexes **3$_{OMe}$** from **LH$_2$**. (i) $Ba(ClO_4)_2$, MeCN, 25 °C then diamine, 24 h (ii) Guanidinium Sulfate, H_2O/$CHCl_3$, 25 °C, 16 h (iii) KOAc, $Co(OAc)_2$, MeCN, 25 °C, 16 h, N_2 (iv) AcOH, air, MeCN, 48 h. 75

Figure 3.2 ^{1}H NMR spectra ($CDCl_3$, 298 K) spectra of **2-3$_R$** (integrated individual spectra in appendix: Fig. S3.1–S3.31). 76

Figure 3.3 Molecular structures (determined by X-ray diffraction, H-atoms omitted for clarity, thermal ellipsoids at 50% probability) of complexes **1** and **3$_H$**. Selected bond lengths are shown 77

with complete bond lengths and angles, with crystallographic refinement data, presented in Tables S3.1.

Figure 3.4 Stacked IR spectra of complexes **2-3$_R$** (Fig. S3.32). 78

Figure 3.5 Cyclic voltammogram of **3$_H$**. 79

Table 3.1 Summary of Electrochemical Data for Complexes **1-3$_R$**. 80

Scheme 3.3 PO/CO_2 ROCOP to synthesise poly(propylene carbonate) (PPC) polyols and propylene carbonate (PC). The catalyst is applied using a chain transfer agent to ensure high selectivity for α,ω-hydroxyl telechelic polymer chains (catalyst: CTA, 1:20). 81

Table 3.2 ROCOP of CO_2/PO of Complexes **1-3**. 81

Scheme 3.4 Cobaltate Dinuclear Mechanism for the PO/CO_2 Ring Opening Copolymerisation. 82

Figure 3.6 Exemplar Catalyst Activity Data for Catalyst **3$_H$**. a) Plot showing changes to the absorbance at 1750 cm^{-1} (carbonyl stretch) versus time plot for PPC formation. b) Semi-logarithmic concentration vs. time plot used to determine k_{obs}. 83

Figure 3.7 a) Eyring analysis of backbiting of PPC using **3$_{Cl}$**. These experiments were conducted from 45 to 60 °C, using [**3$_{Cl}$**] 3 mM and [PPC] 300 mM in neat PO (14 M) and were analysed to full conversion, where [PPC] is defined as the monomeric unit concentration. b) Reaction scheme showing consumption of PPC to PC. 84

Figure 3.8 a) $E_{1/2}$(III/II) vs. k_p plot of complexes **3$_R$**. b) $E_{1/2}$(III/II) vs. PPC selectivity plot of complexes **3$_R$**. c) Summary of relationship between rate and selectivity and accuracy of the predicting method. 85

Figure 3.9 a) E_{Red}(II/I) vs. k_p plot of complexes **1** and **3$_R$**. b) E_{Red}(II/I) vs. PPC selectivity plot of complexes **1** and **3$_R$**. 86

Fig. 3.10 a) Imine Chemical Shift versus log $k_{p,\ 3R}$. b) Imine Chemical Shift versus PPC selectivity. 86

Figure 3.11 a) Activity Hammett plot of complexes **3$_R$**. b) Selectivity Hammett plot of complexes **3$_R$**. 87

Figure 3.12 Summary of relationship between rate and selectivity and accuracy of the predicting method. 88

Figure 3.13 Rate determining step of **1-3$_R$**. 89

Figure 3.14 Schematic illutrating the selectivity limiting reactions of the Co(III)-alkoxide intermediate which can undergo either 1) Propagation by carbon dioxide insertion or 2) PC formation by intramolecular reactions. stability. 90

Figure 3.15 Literature PO/CO_2 salen catalysts. 93

Table 3.3 Literature PO/CO_2 salen catalysts. 94

Fig. 3.16 Neodynium-zinc catalyst for CHO/CO_2 ROCOP. 95

Figure 4.1 Polymer Structures. 100

Scheme 4.1 Allyl Glycidyl Ether (AGE) and Carbon Dioxide ROCOP (20 bar CO_2 pressure, neat AGE). 101

Table 4.1 Data for AGE/CO_2 ROCOP using **1**. 101

Figure 4.2 ^{1}H NMR spectrum ($CDCl_3$, 298K) of the crude product AGE/CO_2 polymerisation (Table 4.2, Entry 3). 102

Table 4.2 Catalyst loading and solvent assessment for AGE/CO_2 ROCOP using **1**. 103

Figure 4.3 SEC traces of AGE/CO_2 ROCOP corresponding to entries 1, 3 and 5 from Table 4.2. 104

Figure 4.4 ^{1}H NMR spectrum ($CDCl_3$) of pure PAGEC. $CHCl_3$ marked by *. 105

Figure 4.5 DSC performed on PAGEC (3rd heating cycle), showing its T_g = -19 °C (M_n = 27.8 kg mol^{-1}, $Đ$ = 1.17). 106

Figure 4.6 TGA data for PAGEC (M_n = 27.8 kg mol^{-1}, $Đ$ = 1.17). 106

Scheme 4.2 Ring-opening polymerisation of *L*-lactide. 107

Table 4.3 ROP of *L*-lactide with alternating solvents and temperature using cat. **1**. 107

Table 4.4 *L*-Lactide polymerisations with **1** with different *L*-Lactide loadings. 108

Figure 4.7 ^{1}H NMR spectrum ($CDCl_3$, 298K) of pure PLLA. $CHCl_3$ marked by *. 109

Figure 4.8 DSC of PLLA (3rd heating cycle), showing T_g = 52 °C and T_m = 140 °C (M_n = 6.8 kg mol^{-1}, $Đ$ = 1.12). 110

Figure 4.9 TGA of PLLA (M_n = 6.8 kg mol^{-1}, $Đ$ = 1.12). 110

Scheme 4.3 Synthesis of block copolymers of AGE, CO_2 and *L*-Lactide, by 'switch' catalysis. 111

Figure 4.10 Diagram of triple-manifold steel Schlenk line for high pressure CO_2 reactions. 112

Figure 4.11 Picture of triple-manifold steel Schlenk line for high pressure CO_2 reactions. 113

Figure 4.12 SEC traces of PAGEC and PLLA-*b*-PAGEC-*b*-PLLA of initial switch attempt. 114

Table 4.5 Data for the PAGEC initiated block polymer formation. 114

Scheme 4.4 Detailed synthesis of block copolymers of AGE, CO_2 and *L*-Lactide, by 'switch' catalysis, 1:20:1,000:10,000 Cat:CHD:*L*-LA:AGE, 7.5 mL (initial) AGE (neat), 50 °C, 20 bar CO_2. Split into **A** ROCOP of AGE/CO_2, **B** addition of *L*-LA and **C** vacuum/nitrogen cycles and *L*-LA ROP. 115

Figure 4.13 ^{1}H NMR spectra ($CDCl_3$) showing PAGEC and then PLLA-PAGEC-PLLA formation. 115

Figure 4.14 ^{1}H NMR spectrum of pure PLLA-*b*-PAGEC-*b*-PLLA with peak assignments. 116

Figure 4.15 SEC traces of 'switch' before and after addition of *L*-lactide. 117

Fig. 4.16 ^{31}P NMR spectrum ($CDCl_3$, 298K) of phosphorous end-group titration of PAGEC, PLLA and the block-copolymer. 117

Fig. 4.17 ^{1}H DOSY NMR spectrum ($CDCl_3$, 298K) the PLLA-PAGEC-PLLA. 118

Figure 4.18 DSC traces for PAGEC, PLLA-*b*-PAGEC-*b*-PLLA triblock-copolymer and PLLA (third cycles). 119

Figure 4.19 TGA of PLLA-*b*-PAGEC-*b*-PLLA triblock-copolymer. 120

Figure 4.20 Alternative epoxides/polycarbonates and the T_gs. 123

Figure 5.1 Structure of catalyst **1** and proposed RDS (by DFT). 126

Figure 5.2 Proposed Future Catalyst Design Targets. 128

Figure 5.3 Proposed Future 'Switch' Catalysis and Polymers. 129

Table of Contents

Declaration 3
Abstract 4
Acknowledgements 6
List of Publications 7
Abbreviations 8
List of Figures, Schemes and Tables 11
Chapter 1 – Introduction 18
1.1 Plastics and Polycarbonates 19
1.2 Epoxide/CO2 ROCOP 20
1.3 Mechanism: Monometallic, Dinuclear and Bicomponent 22
1.4 Brief Summary of CO2/epoxide ROCOP Catalysts 25
1.4.1 Heterogeneous Catalysts 25
1.4.2 Porphyrin Catalysts 26
1.4.3 Monometallic Salen Complexes and Bifunctional Catalysts 28
1.4.4 Bifunctional Tethered Catalysts 29
1.4.5 Dinuclear Catalysts 30
1.4.6 Multinuclear Catalysts 34
1.4.7 Organocatalysts 35
1.5 Summary of PO/CO2 ROCOP Catalysts 36
1.6 History of Salen/Crown-ether Ligand 37
1.7 Aims and Objectives 40
1.8 References 42
Chapter 2 – Theoretical and Experimental Mechanistic Investigation into Co(III)K(I) Complexes 44
2.1 Introduction and Aims 45
2.2 Experimental and DFT Mechanistic Insight into PO/CO2 ROCOP of Co(III)K(I) Heterobimetallic Catalysts 48
2.2.1 Initiation 49
2.2.2 Propagation 49
2.2.2.1 Cobalt-activated PO Mechanism 50
2.2.2.2 Potassium-activated PO Mechanism 53
2.2.2.3 Cobalt versus Potassium Activated PO Mechanism 53
2.2.3 Investigation of Side Reactions 56
2.2.4 Limits of selectivity 65
2.2.5 Discussion 67

2.3 Conclusion and Outlook 68
2.4 References 69
Chapter 3 – Effect of Catalyst Ligand Backbone in Heterodinuclear Catalyst for PO/CO_2 Catalysis 70
3.1 Introduction and Aims 71
3.2 Synthesis and Characterisation of Heterobimetallic Co(III)K(I) Complexes 74
3.2.1 NMR Spectroscopy 76
3.2.2 X-ray Crystallography 77
3.2.3 Infrared Spectroscopy 78
3.2.4 Cyclic Voltammetry 79
3.3 ROCOP of PO and CO_2, with Complexes **1-3$_R$** 80
3.4 Discussion 88
3.4.1 Rate Limiting Step 88
3.4.2 Selectivity Limiting Step 89
3.4.3 Polymerisation Catalysis Implications 91
3.4.4 Comparison with Wider Field 93
3.5 Conclusions and Outlook 96
3.6 References 97
Chapter 4 – Heterobimetallic Co(III)K(I) Catalyst for the Switchable Copolymerisation of Epoxide, CO_2 and Lactide 98
4.1 Introduction and Aims 99
4.2 Allyl Glycidyl Ether (AGE) and Carbon Dioxide Copolymerisation 101
4.2.1 AGE/CO2 ROCOP Optimisation 101
4.2.2 PAGEC Characterisation 105
4.3 *L*-Lactide Ring-Opening Polymerisation 107
4.3.1 Polymerisation Catalysis 107
4.3.2 PLLA Characterisation 109
4.4 'Switchable' Catalysis using of AGE, CO_2 and *L*-Lactide 111
4.4.1 Building triple-manifold steel Schlenk line for high pressure CO_2 reactions 111
4.4.2 Use of PAGEC chain transfer agent for *L*-lactide ROP 114
4.4.3 Switch Catalysis 115
4.5 Discussion 120
4.6 Conclusion and Outlook 122
4.7 References 124
Chapter 5 – Thesis Conclusion and Outlook 125
5.1 Thesis Summary 126

5.2 Outlook 127
5.2.1 Future Catalyst Design 127
5.2.2 Future for 'Switch' Catalysis with **1** 129
5.3 References 131
Chapter 6 – Experimental Details 132
6.1 General Considerations 133
6.2 General PO/CO_2 Copolymerisation Procedure 133
6.3 General PPC to PC Procedure 134
6.4 General AGE/CO_2 Copolymerisation Procedure 134
6.5 General *L*-Lactide Polymerisation Procedure 134
6.6 General Switch Polymerisation of AGE, CO2 and *L*-Lactide 135
6.7 End Group Titration and Analysis by $^{31}P\{^{1}H\}$ NMR Spectroscopy 135
6.8 Methods 135
6.9 Characterisation Data for Chapter 2 137
6.10 Characterisation Data for Chapter 3 139
6.11 Characterisation Data for Chapter 4 142
6.12 References 144
Chapter 7 – Appendix 145
Publication: Insights into the Mechanism of Carbon Dioxide and Propylene Oxide Ring-Opening Copolymerization Using a Co(III)/K(I) Heterodinuclear Catalyst 180
Publication: Predicting Co(III)K(I) Catalyst Performances Using Reduction Potentials in Carbon Dioxide and Propene Oxide Ring Opening Copolymerizations. 190

Chapter 1

Introduction

1.1 Plastics and Polycarbonates

Plastics have become a key part of our daily lives with the first synthetic plastic developed in the early 20th century. The application of polymeric materials rapidly expanded and within decades could be found in clothing, cutlery, cars, electronics, medical industry and our homes.[1-4] The wide scope of applicability comes from the wide range of mechanical and chemical properties obtained at relatively low synthetic cost.[1] Through the years, production of plastic has increased drastically and, as of 2018, it has reached almost 360 million tonnes globally with the largest proportion going to packaging followed by construction and automotive sector.[4]

Polyurethanes are a class of polymer used in an array of commercial applications such as rigid foams, solid elastomers, flexible slab and flexible moulded foams.[5-6] Polyurethanes make up approximately 8% of today's polymer market.[4] The major starting materials used in polyurethane production are petrochemical-derived, with a only minor proportion of the polymers being synthesised from natural products, such as sugars, castor oil and bio-based glycerols.[7]

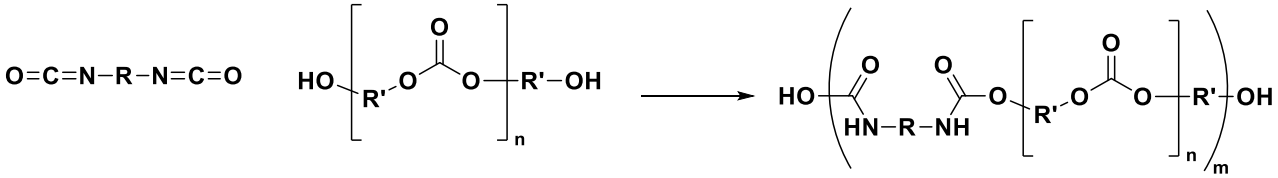


Figure 1.1 Polycarbonate derived polyurethane synthesis.

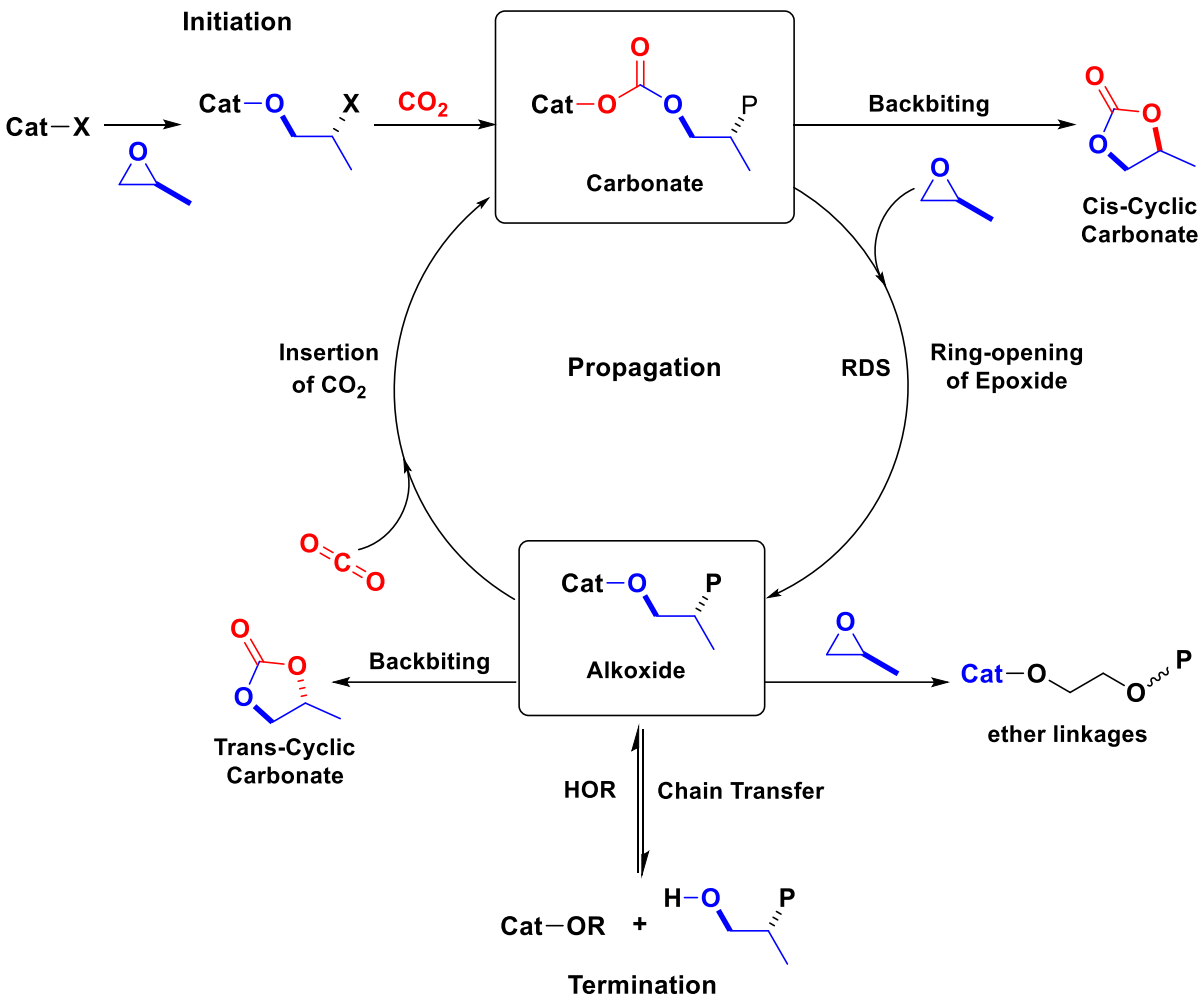
Polyurethanes are synthesised *via* polycondensation reactions between a diol (generally a polyol) and diisocyanate (Figure 1.1). Polyols are polyfunctional alcohols (containing at least one hydroxyl group), such as polycarbonate, polycaprolactone, poly(ethylene adipate) and poly(propylene oxide) glycol. Polyols can be divided into four main classes: polyethers, amine-terminated polyethers, polyesters and polycarbonates, with the polyethers making up the greatest proportion of the market due to their low cost.[5] For polyester-based urethanes, to increase the hydrolytic resistance, polycaprolactone or hexamethylene polycarbonate-based polyols are used, which are generally more expensive monomers. Polycarbonate polyols, however, generally show the best physical properties, but also represent the class which is most expensive to produce.

A current alternative method, which has shown economic viability, to produce polycarbonate is by the copolymerisation of CO_2 and epoxides, such as propylene oxide (PO) and cyclohexene oxide (CHO).[8] The use of CO_2 is attractive due to the possibility to obtain high-value products derived from a low-cost, renewable and non-toxic source.[9] Furthermore, when polycarbonate polyols with only 20 wt% CO_2 uptake are compared to conventional polyether polyols a reduction of 11–20% in greenhouse gas emission and a saving 13–16% of fossil resources.[10-11] Currently polymers obtained from this process are already commercialized, specifically as polypropylene carbonate (PPC) obtained from the copolymerisation of CO_2/PO, however, rate and selectivity improvements remain necessary.[8, 10]

1.2 Epoxide/CO_2 ROCOP

The coupling of epoxides and CO_2 to form polycarbonate was first reported by Inoue in 1969.[12] The ring-opening copolymerisation (ROCOP) of carbon dioxide and epoxides is driven thermodynamically by the release of ring strain of the epoxide, as it is ring-opened.[13] This pathway is less thermally intensive than polycondensation reactions (the primary method of polycarbonates synthesis) and so also allows for the synthesis of thermally-sensitive polymers. Furthermore, there are a wide scope of epoxides, many manufactured at scale, providing highly tuneable polymer properties.[14-17] The 100% atom economy of CO_2/epoxide ROCOP also decreases process waste.

The utilisation of carbon dioxide for polycarbonate synthesis adds value to waste CO_2.[18] The use of carbon dioxide as a C_1 feedstock provides a safer and more sustainable route to carbonate functionalised polymers.[8, 11, 16, 19] CO_2 containing polycarbonates have been applied in polycarbonate polyols for polyurethane synthesis and show potential as scratch resistant materials, elastomers and rigid plastics.[10, 18, 20-25]



Scheme 1.1 Illustration of the reaction mechanism of the ROCOP of carbon dioxide with propylene oxide along with potential side-reactions (cyclic carbonate and polyether formation).

The PO/CO_2 ROCOP catalysis can be split into four elementary steps (Scheme 1.1):

1. **Initiation** involves the activation of an epoxide by coordination to a Lewis acid centre followed by ring-opening from an initiating group provided by the co-ligand. The initiator is commonly an alkoxide, halide or carboxylate. This is followed by rapid insertion of CO_2 to enter the propagation cycle.

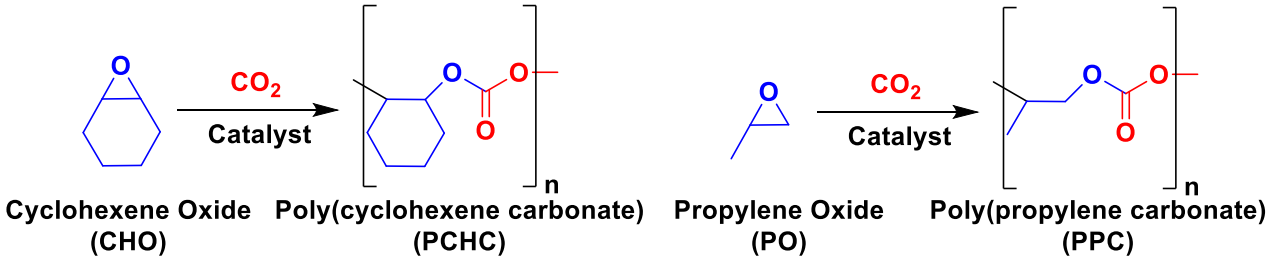
2. **Ring-opening of epoxide** involves its pre-activation via coordination to a Lewis centre and its subsequent nucleophilic attack and ring-opening by a labile carbonate group. This is one half of the propagation cycle.

3. **Carbon dioxide insertion** occurs with reaction of CO_2 into an activated catalyst-alkoxide bond. In the cases where kinetic analyses are conducted, this step is usually not rate determining, although there are some exceptions.

4. **Termination** occurs after addition of protic reagents, including water, and result in formation of a hydroxyl end-capped polymer chain.

Selectivity for polycarbonate can be commonly diminished by the consecutive ring opening of epoxide monomers introducing ether linkages. Alternatively, the thermodynamically favoured *trans*-cyclic carbonate product can form by backbiting of the alkoxide intermediate.[25] *Cis*-cyclic carbonate is less commonly observed and forms from the carbonate intermediate backbiting.[25-26]

The polymerisation is often carried out in presence of alcohol as a chain transfer agent (CTA), these reactions reversibly and rapidly exchange the growing polymer chain between the catalyst and protic species.[27] It is worth noting that bimodal molecular weight distribution can result when there are two different initiation species, leading to two sets of growing polymer chains. This multimodality can have a dramatic impact on the resultant polymer properties (both positive and negative), including changes in melting point, glass transition temperature, tensile strength and elongation at break.[28]



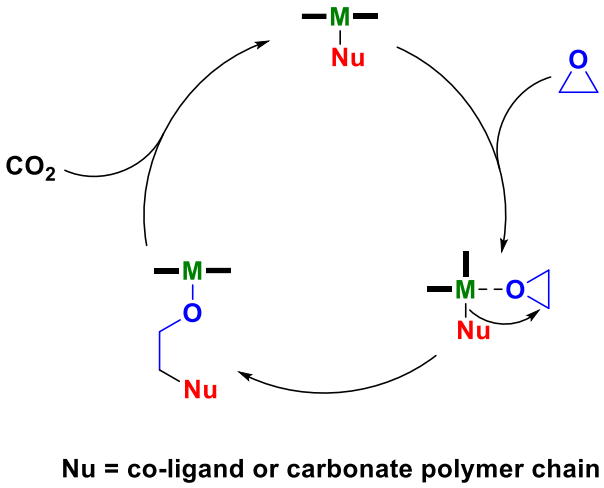
Scheme 1.2 Polycyclohexene Carbonate (PCHC) and Polypropylene Carbonate (PPC) synthesis with CO_2.

The polycarbonate studied and targeted in this thesis is polypropylene carbonate (PPC) but there is also some investigation of polycyclohexene carbonate (PCHC) (Scheme 1.2). PPC is the focus due to its industrial potential and the large-scale, low cost routes to the monomer.

1.3 Mechanism: Monometallic, Dinuclear and Bicomponent

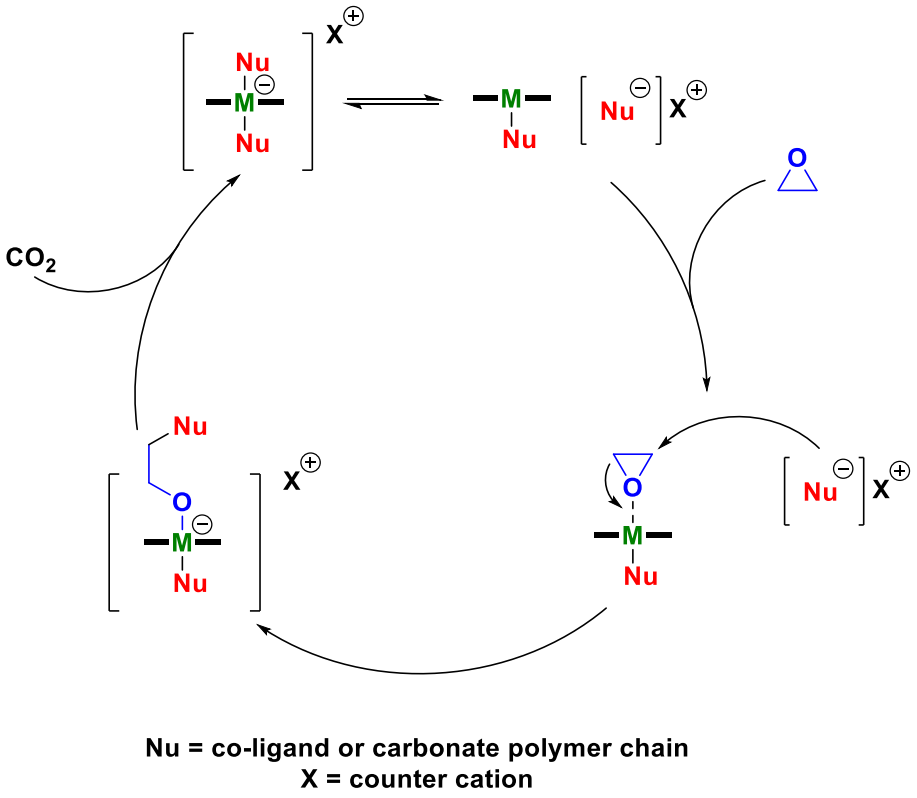
There are three main mechanisms proposed for epoxide/CO_2 ROCOP: monometallic, dinuclear and bicomponent. Mononuclear mechanism proceeds with the coordination of an epoxide and nucleophile at a single site, followed by nucleophilic ring-opening of the epoxide and subsequent carbon dioxide insertion (Scheme 1.3).[9, 29] If observed, it generally corresponds to

a first order dependence on catalyst concentration and commonly first order in epoxide and zeroth in CO_2 due to the ring-opening of the epoxide generally being the rate determining step.



Scheme 1.3 Mononuclear mechanism for mononuclear complex.

In contrast, bicomponent initiation involves a discrete nucleophilic species ring-opening an activated epoxide and is the most prevalent pathway catalysts operating with a co-catalyst (Scheme 1.4).[9] The co-catalyst can coordinate to the metal centre and increase its nucleophilicity leading to an increase in the rate of ring-opening of the epoxide. Additionally, the cation binds electrostatically to any 'free' alkoxide and carbonate anionic intermediates, helping reduce the extent of cyclic carbonate formation (Scheme 1.4).[9, 30] These catalysts sometimes operate without a co-catalyst but in these cases a dinuclear mechanism generally dominants.[31]

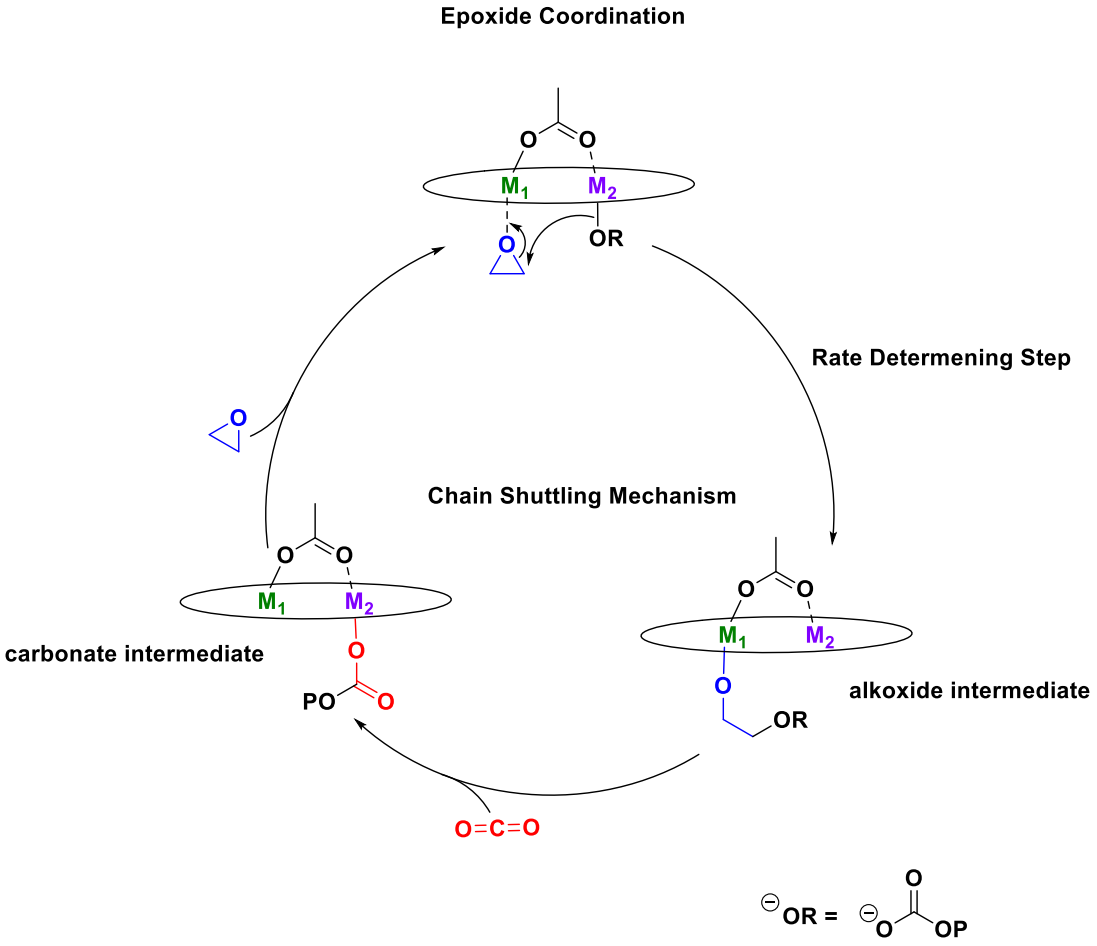


Scheme 1.4 Bicomponent mechanism for monometallic catalyst with ionic co-catalyst**.**

The Dinuclear mechanism does occur quite commonly and involves 2 metals in the active site (Scheme 1.5).[9, 19, 29] It involves a second order dependence on catalyst concentration where dimer formation is required. Dinuclear propagation occurs between two metal sites. Here, the epoxide and nucleophile, generally, reside on different metal centres, with the intermediate alkoxide generated intermolecularly.[9, 29] The most successful dinuclear catalysts are complexes where metal coordination allows cooperation and accelerates all steps.

For dinuclear complexes, a 'Chain Shuttling' mechanism was first proposed by Williams and co-workers to rationalize kinetic data and structure-activity data (Scheme 1.5).[13] 'Chain Shuttling' mechanism involves the segmentation of mechanistic roles of the two metals in the RDS, with one providing the nucleophilic carbonate and the other activating the epoxide. Furthermore, with two different metals, kinetics and Eyring analyses suggested that each specific metal has one of the distinct functions within the catalytic cycle. This separation of

metal roles leads to increased rate of ring-opening of the epoxide, which the rate determining step in the mechanism.[32]



Scheme 1.5 'Chain Shuttling' Mechanism.

1.4 Brief Summary of CO_2/epoxide ROCOP Catalysts

1.4.1 Heterogeneous Catalysts

The first catalysts reported for CO_2/epoxide ROCOP were solid-state heterogeneous catalysts derived from dialkyl zinc (ZnR_2).[12, 33-35] These catalyst systems showed low activity and selectivity, producing significant amount of ether linkages as well as cyclic carbonate by-products and required high carbon dioxide pressure (≥50 bar). Despite these limitations, this pioneering work has contributed significantly to the field of CO_2/epoxide ROCOP.

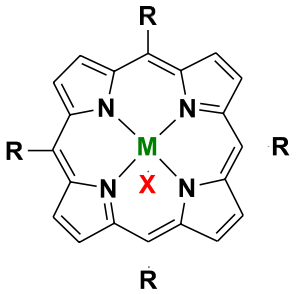
Later zinc glutarates were also shown to have greater activity for CO_2/epoxide ROCOP but high pressure conditions were necessary to observe any activity and only moderate selectivity for polycarbonate were observed.[36-38] They were also able to produce poly(carbonate-*co*-ester)s from CO_2, PO and ε-caprolactone.[39]

Double metal cyanide catalysts based on $Zn_3(Co(CN)_6)_2$ are used commercially in CO_2/PO ROCOP.[40-43] These showed significantly higher activities, but only yield low CO_2 incorporation and form cyclic carbonate.

The greatest issues with heterogenous catalysts are low selectivity for polycarbonate, as well as the necessity for high pressure. Furthermore, the mechanism by which they operate is poorly understand and difficult to study. For these reasons, there is a major drive to optimise homogenous catalysts, which allow for detailed mechanistic study and give better polymerisation control.

This thesis exclusively deals with homogenous catalysis.

1.4.2 Porphyrin Catalysts



A1: M=Al(III), R=Ph, X=OMe
A2: M=Mn(III), R=Ph, X=OAc
A3: M=Co(III), R=Ph, X=Cl
A4: M=Al(III), R=C_6F_5, X=Cl
A5: M=Co(III), R=p-C_6H_4OMe, X=Cl
A6: M=Co(III), R=p-$C_6H_4O^iPr$, X=Cl
A7: M=Co(III), R=p-$C_6H_4NO_2$, X=Cl

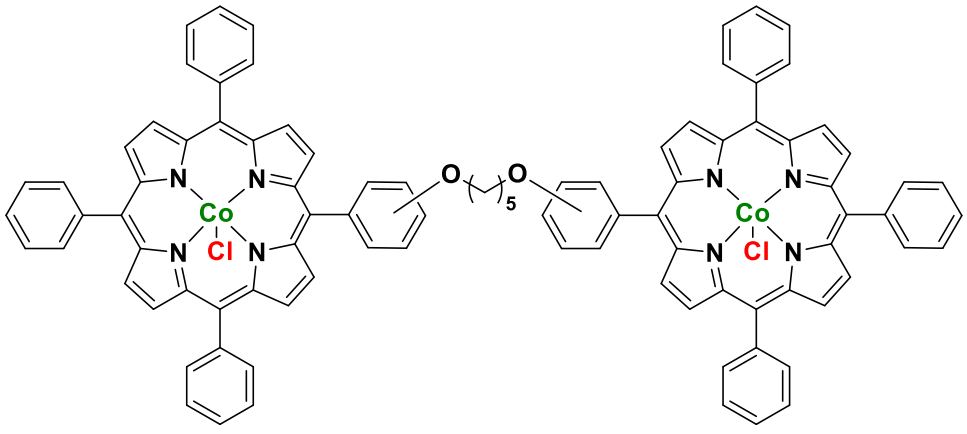
Figure 1.2 Porphyrin catalysts for CO_2/Epoxide ROCOP.

Metalloporpyhyins are an important class of homogeneous CO_2/epoxide ROCOP catalysts. These were first reported by Inoue and team in 1978, with the first being an aluminium(III) porphyrin (Fig. 1.2, **A1**).[44] However, selectivity for carbonate linkages was low (40%). In 1983, Inoue showed an improvement on this, using 1-methylimidazole as co-catalyst to give increased selectivity and rates (Fig. 1.2, **A1**).[45] Inoue and co-workers were also the first to report a catalyst active at 1 bar CO_2 for the copolymerisation of CHO with CO_2 with good selectivity for polycarbonate using a Mn(III) porphyrin (Fig. 1.2, **A2**).[46] Cobalt TPP catalysts have also been observed to be active catalysts for CHO/CO_2

copolymerisation with a DMAP co-catalyst (21 h^{-1}, 80 °C, 0.2 mol%, 50 bar, CHO, 7 M in DCM) (Fig. 1.2, **A3**).[47]

Chisholm and co-workers went on to make a series of Al(III), Cr(III) and Co(III) porphyrin catalysts active for PO/CO_2 ROCOP, showing that 5,10,15,20-tetrakis(pentafluorophenyl)porphyrin (TFPP) catalysts were the fastest in the presence of co-catalyst, specifically the TFPP Al(III)Cl (Fig. 1.2, **A4**). These gave selectivities for PPC up to 98%, but with relatively low molecular weights and requiring high CO_2 pressure (3 h^{-1}, 25 °C, 0.7 mol%, 50 bar, PO 10 M in $CDCl_3$).[48-50]

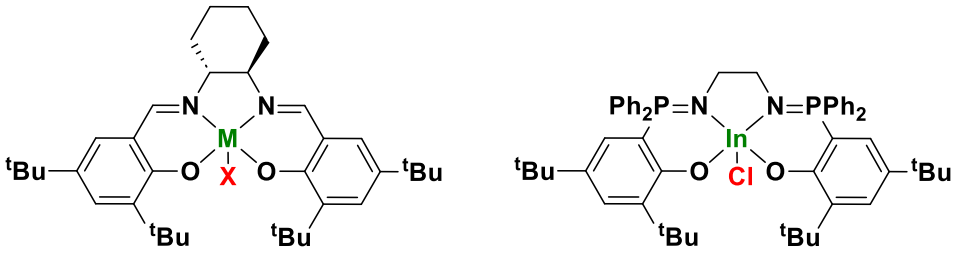
Rieger and co-workers showed that PPC selectivity could be tuned by changing the substituents on the porphyrin (Fig. 1.2).[51] PPC selectivity of 10 - 90% was feasible with a maximum TOF of 103 h^{-1} (30 °C, 0.05 mol%, 30 bar, PO neat) (Fig. 1.2, **A3** and **A5**-**A7**). The group went on to explore ligands where two porphyrins were covalently connected via an ether bridge (Fig. 1.3, **A8**). As porphyrins have been reported to follow bimetallic mechanisms in the absence of co-catalyst, and a bicomponent in the presence of co-catalyst, for CO_2/epoxide ROCOP, it was thought tethering together two individual catalysts would increase rate. However, in the study they show that the monometallic-porphyrins showed higher rates than the dinuclear metal porphyrins, perhaps due to an unfavourable steric arrangement of the linker.[52]



A8

Figure 1.3 Bimetallic porphyrin catalyst for CO_2/Epoxide ROCOP.

1.4.3 Monometallic Salen Complexes and Bifunctional Catalysts



B1: M = Cr(III), X = Cl
B2: M = Co(III), X = OAc
B3: M = Co(III), X = $OBzF_5$

B4

Figure 1.4 Salen catalyst for CO_2/Epoxide ROCOP.

Salen ligands have been studied for decades and were first reported in 1938 by Tsumaki *et al*.[53] Since then they have found many uses, one of which is as catalysts for epoxide/CO_2 ROCOP. Darensbourg was the first to report a metal salen catalyst active for CO_2/epoxide copolymerisation, in 2002, with a chiral [Cr(III)Cl salen], which showed >99% selectivity for carbonate linkages (Fig. 1.4, **B1**).[54] These catalysts were later shown to operate by a bimetallic mechanism without co-catalyst but by a bicomponent mechanism when PPNCl or co-catalyst was added. Evidence for this comes from the rate dependence on catalyst concentration being second-order without co-catalyst. When co-catalyst is added the order in catalysts is between first- and second- and there is a complex dependence on co-catalysts concentration.[9, 30-31, 54] A monometallic mechanism in inhibited by the planar ligand structure which prevents the polymer and monomer from adopting a mutually *cis*-configuration needed for chain growth.[9] The first Cr-salen catalyst had a low rate of 10 h^{-1} (80 °C, 58.5 bar, 0.040 mol%, neat CHO). This was further improved by adding up to 5 equivalence of *N*-methyl imidazole (a neutral co-catalyst), giving a TOF of 32 h^{-1}, under otherwise equivalent conditions.[54]

Significantly, metal salen catalysts also showed activity for PO/CO_2 ROCOP. In 2003, Coates and co-workers reported cobalt(III) salen catalyst for PO/CO_2 ROCOP, showing moderate TOF and very good selectivity for polycarbonate (Fig. 1.4, **B2**) (TOF 59 h^{-1}, selectivity for PPC >99%, 0.2 mol%, 55 bar, 25 °C).[55] Adding co-catalyst (PPNCl) led to an overall rate increase of two orders of magnitude (Fig. 1.4, **B3**) (TOF 1100 h^{-1}, selectivity for PPC >99%, 0.05 mol%, 14 bar, 22 °C).[56]

Nevertheless, catalyst and co-catalyst systems are sub-optimal since polymerisations stop at low catalyst loading due to the need for the two components to work together in solution. This limitation has motivated tethering of the catalyst and co-catalyst, i.e. bifunctional catalysts.

Indium(III) (phosphasalens), operating without co-catalyst, have also shown promise as catalysts for CO_2/epoxide copolymerisation (Fig. 1.4, **B4**).[57] These catalysts are unusual in displaying a mononuclear mechanism in CO_2/CHO ROCOP. The large ionic radius of In(III) was proposed to allow cis-coordination of the growing chain and epoxide, the correct conformation for mononuclear chain growth.

1.4.4 Bifunctional Tethered Catalysts

Bifunctional catalysts are those in which the co-catalyst is bound covalently to the ligand framework.[19] They show higher activity and operate at low loadings – these systems have been highly optimised and investigated.

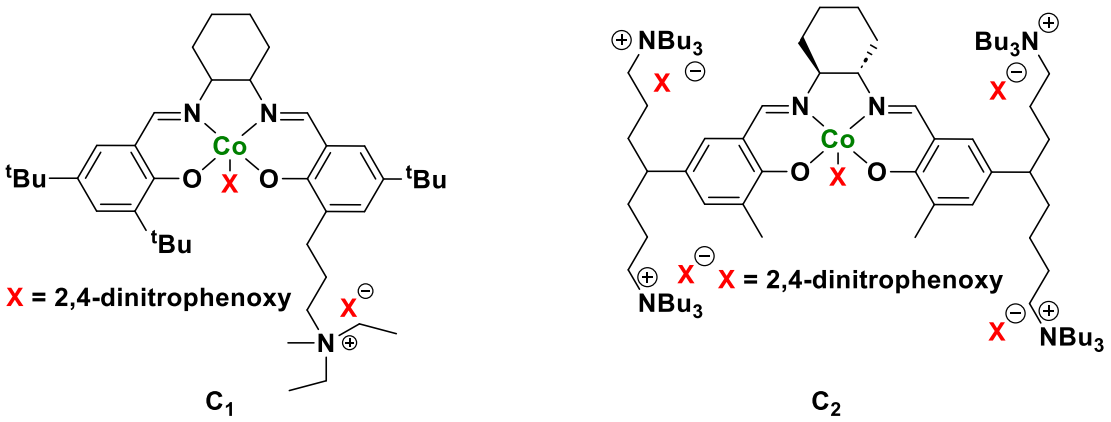


Figure 1.5 Tethered metal salen catalysts.

The bifunctional cobalt(III) catalysts showed high activity for both CHO/CO_2 and PO/CO_2 polymerisation (Fig. 1.5, **C1**). TOFs of 3020 h^{-1} and 5160 h^{-1} were achieved for CHO/PO_2 and PO/CO_2, respectively (90°C, 25 bar CO_2, selectivity for PCHC >99%, selectivity PPC >90%, 0.02 mol%).[58] The bifunctional Co(III) catalysts retain higher activities due to their stability at high temperature (generally Co(III) is thermally reduced to Co(II) resulting in inactive catalysts).[59] Furthermore, these bifunctional catalysts retain high activity even under high dilution conditions (catalyst:epoxide 1:4000 loadings, 0.025 mol% catalyst).

Lu and co-workers showed that the bifunctional catalyst had a first order dependence in catalyst concentration, while a comparative monometallic cobalt (III) catalyst with a co-catalyst showed an order of 1.61.[60] This indicates an intramolecular mechanism for the bifunctional catalyst. These catalysts also show a reduced activation barrier. Lee and co-workers optimized the structures, adding multiple tethered co-catalysts to the salen ligand (Fig. 1.5, **C2**), resulting in the fastest catalyst for PO/CO_2 ROCOP, with a TOF of 26,000 h^{-1} (selectivity for PPC >99%, 1:40,000 = 0.002 mol%, 20 bar CO_2, 80 °C).[61] However, these ligands are very hard to synthesise, requiring more than 8 steps. They also form polycarbonate with multimodal molar mass distributions and may be problematic when used with steel due to corrosion of pipes due to anions such as chloride.

1.4.5 Dinuclear Catalysts

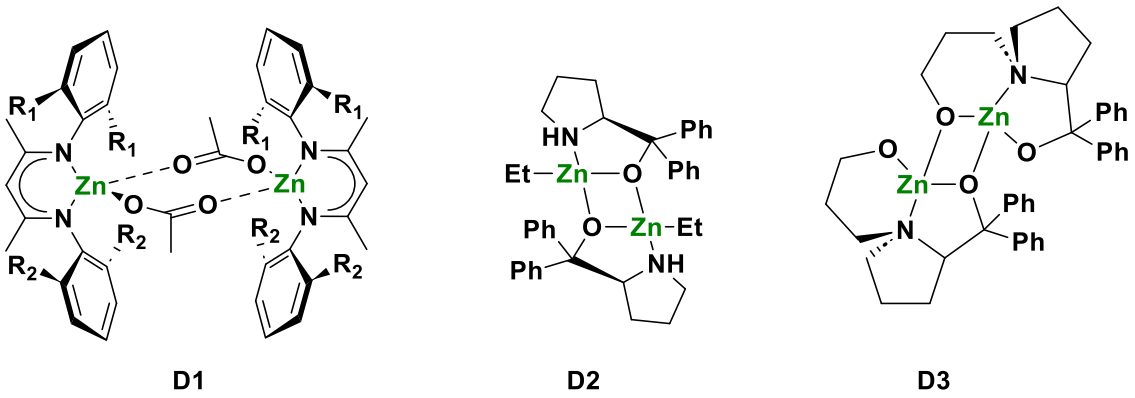


Figure 1.6 Dinuclear Zinc catalysts.

Zinc-β-diimine (Zn-BDI) catalysts show good activity and selectivity in CO_2/CHO ROCOP, they were pioneered by Coates and co-workers. In CHO/CO_2 ROCOP, the best Zn-BDI catalyst showed a TOF of 247 h^{-1} (PCHC selectivity 94%, 0.1 mol% cat, 7 bar CO_2, 50 °C) (Fig. 1.6, **D1**).[62] A mechanistic study revealed a rate law that was zero-order in CO_2 pressure, first-order in epoxide concentration and showed an order from 1.0 to 1.8 for catalyst concentration, depending on the steric bulk of the BDI substituents. The kinetic data was rationalized by invoking dimerization of the complexes. For complexes with large substituents, dimerization was disfavoured leading to a reduction in rate. This was further supported by

the isolation of x-ray crystal structures, of di-zinc carbonate and alkoxide intermediates, which all showed dimer structures. The mechanism was, therefore, proposed as bimetallic mechanism and a subtlety was that only the loosely bound dimers showed high activity strongly bound dimers, and those where sterics prevented dimerization, were inactive.[63]

In 1999, Nozaki reported chiral dizinc catalysts for epoxide/CO_2 ROCOP, which gave enantiomeric excess (ee) of up to 76% biased to (R,R)-enantiomer for CHO/CO_2 ROCOP (Fig. 1.6, **D2**).[64] The same catalyst was active for PO/CO_2, however, the resultant ee was significantly lower (34%).[65] In 2017, Meyer and co-workers reported a similar di-zinc catalyst which was active at 1 bar CO_2, showing TOFs up to 149 h^{-1} (selectivity for PCHC >98%, 80 °C, 1 bar CO_2) (Fig. 1.6, **D3**).[66]

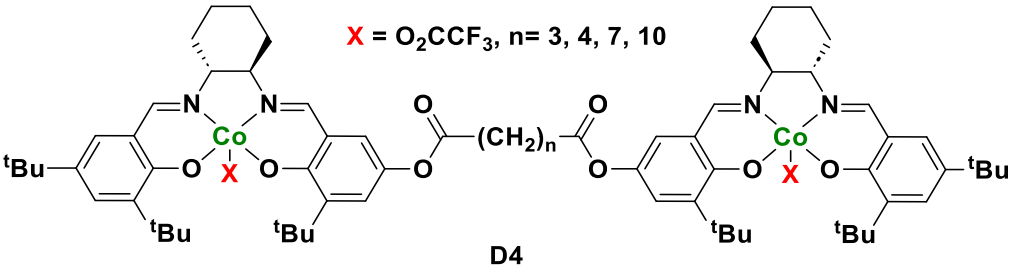
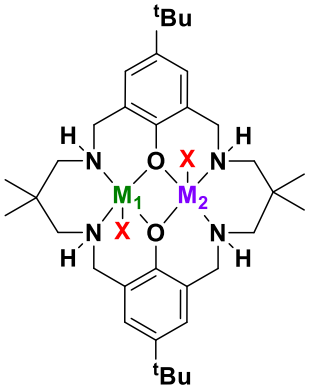


Figure 1.7 Tethered dinuclear salen catalysts.

Another method of improving rate and facilitating a bimetallic pathway is to join two metal salen complexes. In 2010, Nozaki and co-workers group reported a tethered dinuclear Co(III) catalyst, with a TOF >300 h^{-1} (87% selectivity for PPC at 40°C, 53 bar CO_2, 0.033 mol%) (Fig. 1.7, **D4**).[31] The catalyst was proposed to follow a bimetallic mechanism. However, the TOF of the catalyst was much increased with the addition of PPNCl up to 1740 h^{-1} with a selectivity for PPC of 94% (40°C, 53 bar CO_2, 0.01 mol%).[31]



	M_1	M_2	X
D5	Zn	Zn	OAc
D6	Mg	Mg	OAc
D7	Co(II)	Co(II)	OAc
D8	Co(II)	Co(III)	OAc
D9	Zn	Mg	OAc
D10	Co(II)	Mg	OAc
D11	Fe(II)	Mg	OAc

Figure 1.8 Dinuclear catalysts.

In 2009, the Williams group reported a di-zinc catalyst active for CHO/CO_2 ROCOP at 1 bar CO_2 pressure, it showed a TOF of 17, >99% PCHC selectivity, 0.1 mol% of cat. and 80 °C (Fig. 1.8, **D4**).[67] Changing the metals to Co(II) or Mg(II) increased the activity, with the di-Co(II) catalyst showing a TOF of 172 h^{-1} for CHO/CO_2 ROCOP (80 °C, 1 bar CO_2 pressure, 0.1 mol% cat.) (Fig. 1.8, **D6** and **D7**). A Co(II)Co(III) catalyst showed a significantly greater activity with a TOF of 480 h^{-1} (100 °C, 0.1 mol% cat, 1 bar CO_2 pressure, >99% selectivity) (Fig. 1.8, **D8**).[32, 68]

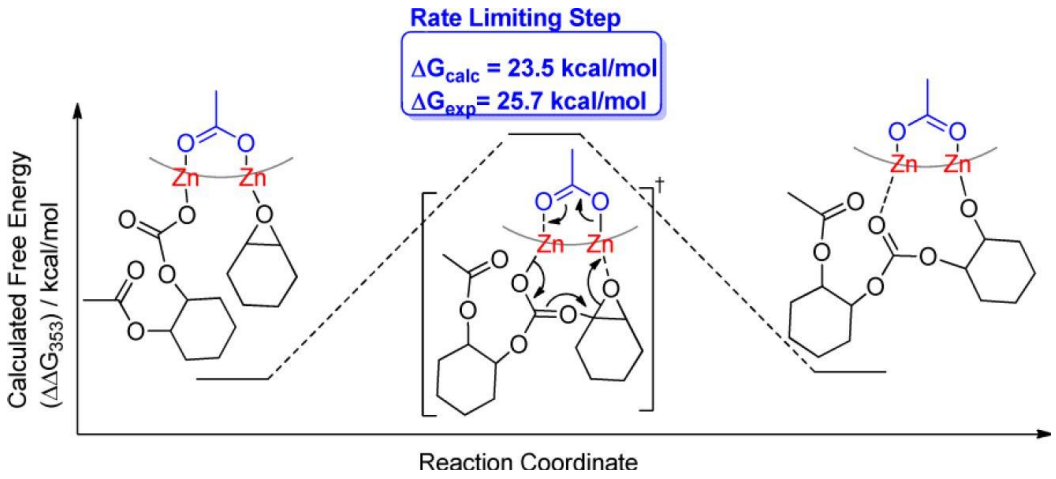


Figure 1.9 Illustration of the potential energy surface for the rate limiting step of alternating copolymerization of cyclohexene oxide and carbon dioxide.[13]

In situ ATR-IR spectroscopy studies of both catalyst and rate law showed first order dependence in both CHO and catalyst concentration. DFT investigations using the di-zinc catalyst revealed the 'Chain Shuttling' mechanism (Fig. 1.9).[13] In this mechanism, each metal plays a distinct role, with one activating the epoxide and the other providing a labile carbonate. One of the acetate ligands initiates the

polymerisation while the other remains coordinated and shuttles in an opposite direction to chain growth. All these dinuclear catalysts have metal centre separations of 3-4 Å, which further facilitates the cooperative mechanism.[68]

When two different metals are used, it was hypothesised that the more Lewis acidic metal activates the epoxide, while the other provides the labile carbonate: these heterodinuclear catalyst have shown dramatic increases in rates.[32] This motivated exploration of heterodinuclear catalysts, with the first examples being reported by our team in 2014.[67]

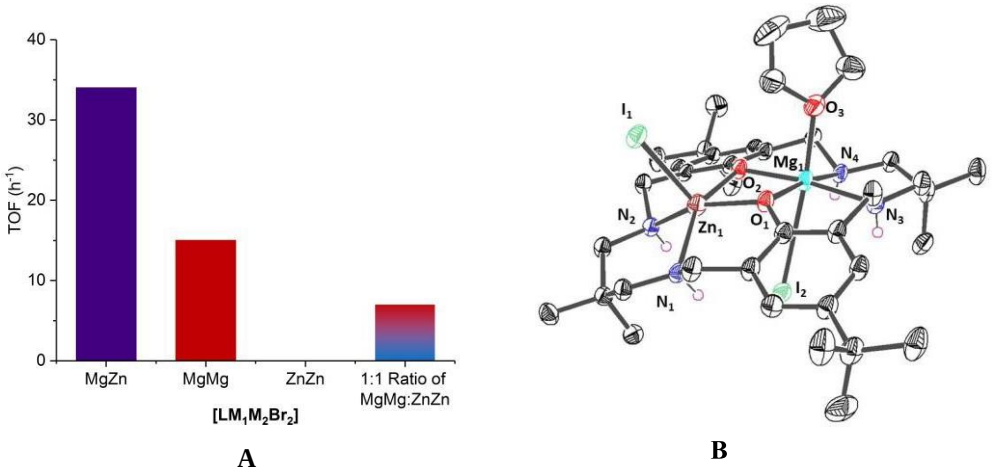
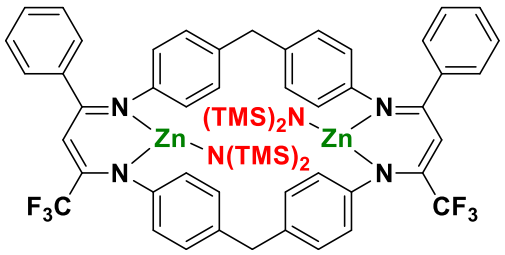


Figure 1.10 A Comparison between homo- and heterobimetallic zinc and magnesium complexes reported by the Williams' group.[15, 67, 69-70] **B** crystal structure of Zn Mg catalyst with THF.[71]

Heterodinuclear catalysts have shown great potential and work by exploiting different characteristics of the metals in order to optimize the catalytic cycle. Williams and co-workers reported a Zn(II)Mg(II) catalyst first, followed by other metal combinations (Fig. 1.8, **D9**-**D11**).[69-70] These catalysts demonstrate enhanced activity, especially under 1 bar pressure, when compared to equivalent Zn(II)Zn(II), Mg(II)Mg(II) or a 1:1 mixture of two (Fig. 1.10**A**).[15, 67, 69-70]

The increased rate is rationalised by the chain shuttling mechanism since the Mg(II) should enhance epoxide activation to attack by a Zn(II)-carbonate (Fig. 1.10**B**). The Zn(II)Mg(II) catalyst showed an overall second-order rate law, with first-order dependence on catalyst and CHO concentration, and a zero-order dependence on CO_2 pressure.[70] Williams and co-workers went on to study the effect of different transition metals; cobalt (II) was targeted due to the high activity of the homobimetallic cobalt

catalysts in CHO/CO_2 ROCOP. The hetereodinculear Mg(II)Co(II) catalyst is the fastest CHO/CO_2 ROCOP catalyst at 1 bar CO_2 (TOF 1205 h^{-1}, 120 °C, 1 bar CO_2, 0.05 mol% catalyst and 99% PCHC selectivity). At 140 °C with 20 bar CO_2 pressure a TOF of 12,462 h^{-1} was observed with >99 selectivity for PCHC and 0.05 mol% catalyst loading showing remarkable temperature stability.[72] Similar to the Zn(II)Mg(II) catalyst, metal synergy is proposed to increase the rates. Detailed kinetic analyses comparing Co(II)Co(II), Mg(II)Mg(II) and Co(II)Mg(II) catalyst established the basis for the synergy. The Co(II) centre reduces the transition state enthalpy while the Mg(II) reduces the transition state entropy.[72] Further work investigated a series of M(II)Mg(II), with M(II) being first row transition metals, and showed a wide variety of activities. The Fe(II)Mg(II) catalyst was as active as the Co(II)Mg(II) and highly selective for CHO/CO_2 ROCOP (Fig. 1.8, **D11**).[73]



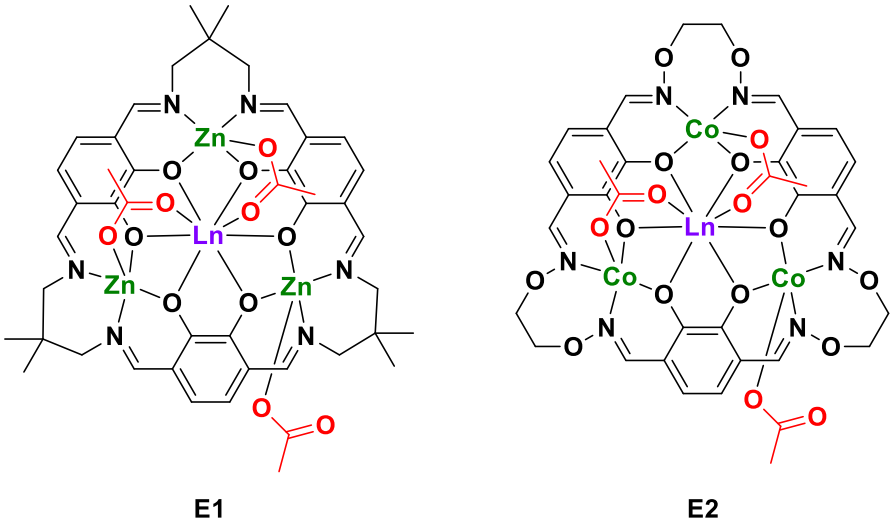
D12

Figure 1.11 Dinuclear Zinc catalyst.

Building on the work of Coates and co-workers, Rieger and co-workers reported a catalyst based on a tethered Zn BDI system (Fig. 1.11, **D12**).[74] Their catalyst showed high turn-over frequencies for CHO/CO_2 ROCOP of 5,900 h^{-1}, at 30 bar CO_2 pressure and 100 °C.[74-77]

1.4.6 Multinuclear Catalysts

In 2018, Okuda and Mashima reported a series of Zn_3Ln catalysts.[78] The most active was Zn_3Ce catalyst for CHO/CO_2 ROCOP (Fig. 1.11, **E1**). The Zn_3Ce catalyst showed activity at CO_2 pressures as low as 3 bar, but its best activity was achieved at 10 bar with a TOF of 370 h^{-1} (100 °C, 0.05 mol% catalyst loading) affording perfectly alternating PCHC. Further work by Mashima and Nozaki and co-workers, applied a similar ligand but featuring a different backbone.[79] The $Co(II)_3Nd(III)$ catalyst shows the highest TOF of 1625 h^{-1} (0.0047 mol% catalyst loading, 20 bar CO_2, 130 °C) (Fig. 1.12, **E2**).[79]

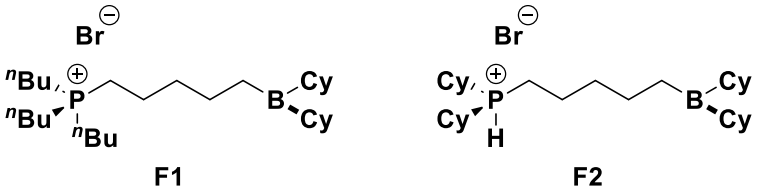


E1 E2

Figure 1.12 Multinuclear Catalysts.

1.4.7 Organocatalysts

In 2016, an organoborane catalyst system was reported for CO_2/epoxide ROCOP.[80] Triethyl boron (TEB) was applied with various co-catalysts, from ^{t}BuOM salts to PPNCl and ammonium salts and was active for PO/CO_2 and CHO/CO_2 ROCOP. The best catalysts showed a low TOF, but good PPC selectivity.[80] Using other alkylene oxides resulted in TOFs of up to 88 h^{-1} (0.15-0.6 mol% TEB loading, 10 bar, 60 °C).[81]



F1 F2

Figure 1.13 Tertiary and Quaternary phosphonium borane catalyst.

Recently, a team working at ExxonMobil reported tertiary and quaternary phosphonium borane catalysts for CO_2/CHO ROCOP (Fig. 1.13, **F1** and **F2**).[82] The best catalysts had quaternary phosphonium salts and a C5 linker (Fig. 1.12, **G1**). Observed rate coefficients (k_{obs}) of up to 2.3 x 10^{-4} s^{-1} were found with selectivities for PCHC >99% (28 bar CO_2, 80 °C).

1.5 Summary of PO/CO_2 ROCOP Catalysts

The copolymerisation of PO and CO_2 remains challenging as activities are typically significantly lower than with CHO and fewer catalysts can selectively produce PPC. This lack of selectivity for PPC arises because ether linkages and cyclic carbonate generally form readily. The progress to date will be highlighted in this section.

Table 2.1 Selected catalysts for the of PO/CO_2 ROCOP.[31, 48-51, 54-56, 58-59]

Catalyst	Co-cat.	Temp. (°C)	*p*CO2 (Bar)	Cat. Loading (mol%)	[PO] (M)	TOF (h^{-1})	PPC Selectivity
A4	[PPN]Cl	25	50	0.7	10	3	98
BEt3	[NBu_4]Cl	60	10	0.03	7.5	49	83
B2	-	25	55	0.2	Neat	71	99
A6	[PPN]Cl	30	30	0.05	Neat	103	90
B1 (X=N3)	[PPN]Cl	60	34	0.05	Neat	192	93
D1	-	40	53	0.033	Neat	300	87
B3	[PPN]Cl	22	14	0.05	Neat	1100 (s-PO)	99
D1	[PPN]Cl	40	53	0.01	Neat	1740	94
C1	-	90	25	0.02	Neat	5160	90
C2	-	80	20	0.004	Neat	26000	99

TOF is not an ideal comparison measurement for catalysts as it is limited by a single kinetic measurement and does not account for temperature, pressure or concentration effects, however, it is the main figure reported in literature and so used here for comparison.

As can be seen in Table 1.1, a large range of activities (under varying conditions) are observed for PO/CO_2 ROCOP catalysts. A range of metals are used in these catalysts, specifically Al(III), Cr(III) and Co(III), with Co(III) shown to be the most active **D1, B3, C1** and **C2**).[31, 56, 58-59] Inherently, all active PO/CO_2 ROCOP catalysts have M(III) active sites. However, the catalysts exhibiting the highest activity are also the most challenging to synthesis due to the need to install co-catalyst tethers to the ligand (**C1** and **C2**).[58-59] It is worth noting that the fastest catalysts also operate at the highest temperature. High temperature CO_2/PO ROCOP is typically challenging due to catalyst decomposition and cyclic carbonate formation.

Given the wide range of activities a 'good' catalyst for PO/CO_2 ROCOP would have high selectivity for PPC (e.g. >95%), be able to work at high temperature (e.g. 50-80 °C), be compatible with chain transfer agents (e.g. 10-100 equiv.), have a good TOF (>300 h^{-1}) and should be readily synthesized.

1.6 History of Salen/Crown-ether Ligand

Crown ethers have been used in chemistry for decades and their synthesis was first reported by Pedersen in 1967.[83]

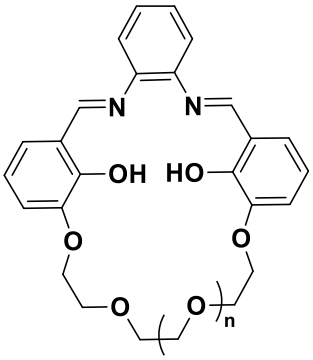


Figure 1.14 Macrocyclic ligand studied in this thesis.

The ligand used in this thesis features a 'salen' and 'crown ether' macrocycle and was first reported, in 1988, by Reinhoudt and co-workers (Fig. 1.14).[84] They focused on the complexation of UO_2 and Ni(II) ions and subsequently explored different imine linkers and modifications to the crown ether moiety by adding phenoxy species. They reported Ni(II), Cu(II) and Zn(II) coordinated complexes in the salen moiety with Ba(II), Li(I), Na(I) and K(I) complexed in the crown ether moiety.[85] They showed that the reduction potential of the transition metals depend on the complexed alkali-metal (Li^+, Na^+, and K^+) or alkaline-earth-metal (Ba^{2+}) cations in the polyether cavity.[85] The s-block metal caused an increase in the redox potential of around 100 mV, with Ba^{2+} inducing the largest shifts. The shifts of the half-wave potential were also shown to be dependent on the crown ether ring size, with a shorter ether linkers resulting in a larger shift. The rigidity of the ether units also resulted in a smaller shift.[85]

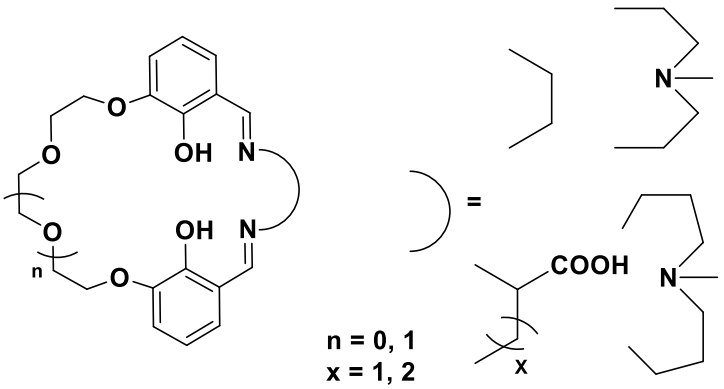


Figure 1.15 Macrocyclic ligand derivatives and variations.

Vigato and co-workers further investigated this ligand and prepared various transition metal/lanthanide heterodinuclear complexes as well as homo- and heterodinuclear lanthanide complexes.[86-90] They explored both imine and amine macrocyles, with various nitrogen linkers (Fig. 1.15). The complexes showed electronic, magnetic, and ferromagnetic coupling between the lanthanide and the transition metals.[89]

Interestingly, lanthanide and s-block metal heterodinuclear complexes were also studied.[91-92] Vigato and Casellato found that 15-crown-5 derivatives showed high equilibrium binding constants with Na^+ and Ca^{2+}, likely due to their ionic radii, while Li^+ and K^+ have very low binding constants.[91] They explored M(III)Na(I) complexes with both cyclic and acyclic variants of the ligand where shown to be highly stable in solution.[93-94]

Yang and co-workers went on to explore this ligand some years later, with Co(II)/M(I/II) (M = Na(I), K(I), Ca(II), Sr(II) and Ba(II)).[95] They studied the effect on electronic properties and increasing redox potentials depending on the second metal. These changes were attributed to inductive effects from the Lewis acid, which leads to a decrease in electron density at the metal, making them easier to reduce. The complex which resulted in the most positive Co(II) reduction potential, featured the most Lewis acidic s-block metal (Ca(II)) and resulting in an increase in redox potential of 300 mV.[95]

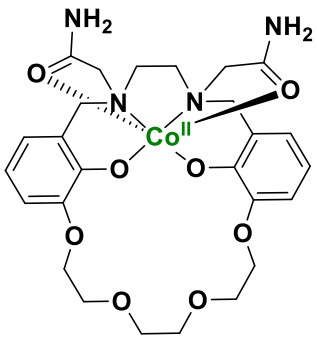


Figure 1.16 hexa-coordinate Co(II) complex.[96]

Others produced ligands featuring two amine, amide and alkoxide donors to the Co(II) making it coordinationally saturated (6 coordinated, Fig. 1.16). These complexes were studied for use as a magnetic resonance probe for Ca(II) but also shows selective binding for Na(I), K(I) and Mg(II).[96] Further experimentation allowed for the calculation of the s-block metal dissociation constants: K(I) showed a lower dissociation constant than Na(I).

Yang and co-workers then synthesised Mn(IV)/M(I/II) complexes, where M(I/II) = K(I),Na(I), Ba(II) and Sr(II) and showed that the redox potentials (Mn(III/IV) where more positive, increasing by up to 400 mV with the s-block metals with the greatest charge density (Sr(II) and Ba(II)).[97] These Mn(IV)/s-block complexes were used, by Cundari and co-workers, in methane activation. A large shift in the HOMO level was observed with higher charge metals compared with a mononuclear Mn(IV) which agreed strongly with Yang and co-workers work.[98]

Heterodinuclear Ni(II) complexes with Ca(II), Na(I), Nd(III) and Y(III) were also reported. These showed a linear increase in Metal-to-Ligand Charge-Transfer with higher oxidation state metals.[99] Yang and co-workers also explored these heterodinuclear Ni(II) complexes with Na(I) and Ba(II). The cyclic voltammetry traces of these complexes showed anodic shifts when s-block metals were coordinated, by up to 340 mV with Ba(II). Additionally, DFT of both Fe(II)/(III) and Ni(II) complexes, with K(I), suggested an induced electrostatic potential.[100]

Additionally, actinides have been shown to coordinate to the ligand's salen-like moieties. U(IV) complexes with Na(I), K(I), Ca(II), Nd(III) and Y(III) have been made showing anodic shifts with larger and more highly charged metal ions, and diminished electron transfer rates with higher charge density

metals.[101]

Fe(II) and Fe(III) were active for C-H bond activation.[102] Coordinating K(I) and Ba(II) resulted in an increase of the Fe(III/II) redox potential of 0.44 V with K(I) and 0.64 V with Ba(II). A manganese(III) chloride complex was active for alkene epoxidation.[103] Various chiral nitrogen linkers were used to assess the influences of ligand chirality on the enantioselectivity of the epoxidation.

Most recently, the Williams group has reported Co(III)M(I) catalysts, coordinated by the ligand, for CHO/CO_2 and PO/CO_2 ROCOP (Fig. 1.17).[104-105] The Co(III)Na(I) complex was shown to have the highest rate when using 1 bar for CHO/CO_2 ROCOP achieving a TOF of 1590 h^{-1} (1 bar CO_2, 0.025 mol% cat. loading, >99% PCHC selec.).[105] Both Co(III)Na(I) and Co(III)K(I) complexes are first examples of heterodinuclear catalysts for PO/CO_2 ROCOP.[104] The Co(III)K(I) was found to be the most with the high selectivity for PPC and TOF of up to 800 h^{-1} (PPC selec. 93%, 0.025% mol cat. loading, 30 bar CO2). Both catalysts showed rate laws with a first-order in epoxide, first-order in catalyst and zero-order in CO_2 concentrations.[104-105] These catalysts will be explored further in this thesis.

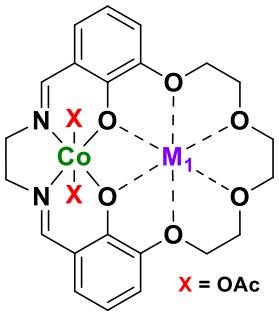


Figure 1.17 Co(III)M(I) heterodinuclear catalyst for CO_2/epoxide ROCOP.

1.7 Aims and Objectives

This thesis will focus on the development of homogenous catalysts for copolymerisations of epoxides with carbon dioxide, with a particular focus on the ROCOP of PO and CO_2. The goal is to expand the understanding of CO_2/PO catalysts, in terms of both the reaction mechanism and the factors influencing the catalysis. Chapters 2-4 start from the recent development of Co(III)K(I) catalyst (Fig. 1.16). These chapters will explore the following questions:

Chapter 2: Can the mechanism by which the Co(III)K(I) catalyst operates be determined? To address this question both experimental and computational approaches will be explored. What are the roles of

the Co(III) and the K(I) centres? What effects do side reactions have on the catalysis?

Chapter 3: What effect does substitution of the ligand, specifically the active site nitrogen linker group have on the electron density of the metals and does alternating electronics influence catalysis? Can the activity of new catalysts be predicted?

Chapter 4: Can the Co(III)K(I) catalyst be applied to make block polymers by ‘switch’ catalysis? Will commercial monomers like epoxide, CO2 and lactide enchain selectively? Can ABA block polymers be prepared featuring ‘hard’ (A), ‘soft’ (B), ‘hard’ (A) sequences?

1.8 References

1. Zhang, X.; Fevre, M.; Jones, G. O.; Waymouth, R. M., *Chem. Rev.* **2018,** *118*, 839-885.
2. Geyer, R.; Jambeck, J. R.; Law, K. L., *Sci. Adv.* **2017,** *3*, 25-29.
3. In *Science to Enable Sustainable Plastics - A white paper from the 8th Chemical Sciences and Society Summit (CS3)*, 2020; p 82.
4. PlasticsEurope; EPRO In *Plastics - the Facts 2019*, 2019; p 42.
5. Szycher, M., *Szycher's Handbook of Polyurethanes*. Second ed.; CRC Press: 2013.
6. Akindoyo, J. O.; Beg, M. D. H.; Ghazali, S.; Islam, M. R.; Jeyaratnam, N.; Yuvaraj, A. R., *RSC Adv.* **2016,** *6*, 114453-114482.
7. Avar, G.; Meier-Westhues, U. C., H.;; Achten, D., Polyurethanes. In *Polymer Science: A Comprehensive Reference*, Eds. Elsevier: 2012.
8. Darensbourg, D. J.; Wilson, S. J., *Green Chem.* **2012,** *14*, 2665-2671.
9. Klaus, S.; Lehenmeier, M. W.; Anderson, C. E.; Rieger, B., *Coord. Chem. Rev.* **2011,** *255*, 1460-1479.
10. von der Assen, N.; Bardow, A., *Green Chem.* **2014,** *16*, 3272-3280.
11. Zhu, Y.; Romain, C.; Williams, C. K., *Nature* **2016,** *540*, 354-362.
12. Inoue, S.; Koinuma, H.; Tsuruta, T., *J. Polym. Sci., Part B: Polym. Lett.* **1969,** *7*, 287-292.
13. Buchard, A.; Jutz, F.; Kember, M. R.; White, A. J. P. P.; Rzepa, H. S.; Williams, C. K., *Macromolecules* **2012,** *45*, 6781-6795.
14. Kember, M. R.; Buchard, A.; Williams, C. K., *Chem. Commun.* **2011,** *47*, 141-163.
15. Saini, P. K.; Fiorani, G.; Mathers, R. T.; Williams, C. K., *Chem. Eur. J.* **2017,** *23*, 4260-4265.
16. Paul, S.; Zhu, Y.; Romain, C.; Brooks, R.; Saini, P. K.; Williams, C. K., *Chem. Commun.* **2015,** *51*, 6459-6479.
17. Darensbourg, D. J.; Poland, R. R.; Escobedo, C., *Macromolecules* **2012,** *45*, 2242-2248.
18. Chapman, A. M.; Keyworth, C.; Kember, M. R.; Lennox, A. J. J. J.; Williams, C. K., *ACS Catal.* **2015,** *5*, 1581-1588.
19. Kozak, C. M.; Ambrose, K.; Anderson, T. S., *Coord. Chem. Rev.* **2018,** *376*, 565-587.
20. Von Der Assen, N.; Jung, J.; Bardow, A., *Energy Environ. Sci.* **2013,** *6*, 2721-2734.
21. Lee, S. H.; Cyriac, A.; Jeon, J. Y.; Lee, B. Y., *Polym. Chem.* **2012,** *3*, 1215-1220.
22. Langanke, J.; Wolf, A.; Hofmann, J.; Böhm, K.; Subhani, M. A.; Müller, T. E.; Leitner, W.; Gürtler, C., *Green Chem.* **2014,** *16*, 1865-1870.
23. Stößer, T.; Li, C.; Unruangsri, J.; Saini, P. K.; Sablong, R. J.; Meier, M. A. R. R.; Williams, C. K.; Koning, C., *Polym. Chem.* **2017,** *8*, 6099-6105.
24. Hauenstein, O.; Reiter, M.; Agarwal, S.; Rieger, B.; Greiner, A., *Green Chem.* **2016,** *18*, 760-770.
25. Buchard, A.; Kember, M. R.; Sandeman, K. G.; Williams, C. K., *Chem. Commun.* **2011,** *47*, 212-214.
26. Castro-Osma, J. A.; Lamb, K. J.; North, M., *ACS Catal.* **2016,** *6*, 5012-5025.
27. Inoue, S., **2000,** *38*, 2861-2871.
28. Ward, I. M.; Sweeney, J., *Mechanical Properties of Solid Polymers*. 3rd ed.; Wiley: United Kingdom, 2012; p 1-18.
29. Chisholm, M. H.; Zhou, Z., *J. Am. Chem. Soc.* **2004,** *126*, 11030-11039.
30. Darensbourg, D. J.; Mackiewicz, R. M., *J. Am. Chem. Soc.* **2005,** *127*, 14026-14038.
31. Nakano, K.; Hashimoto, S.; Nozaki, K., *Chem. Sci.* **2010,** *1*, 369-373.
32. Kember, M. R.; Jutz, F.; Buchard, A.; White, A. J. P.; Williams, C. K., *Chem. Sci.* **2012,** *3*, 1245-1255.
33. Hirano, T.; Inoue, S.; Tsuruta, T., *Makromol. Chem.* **1975,** *176*, 1913-1917.
34. Hirano, T.; Inoue, S.; Tsuruta, T., *Makromol. Chem.* **1976,** *177*, 3245-3253.
35. Inoue, S.; Hirano, T.; Tsuruta, T., *Polym. J.* **1977,** *9*, 101-106.
36. Eberhardt, R.; Allmendinger, M.; Zintl, M.; Troll, C.; Luinstra, G. A.; Rieger, B., *Macromol. Chem. Phys.* **2004,** *205*, 42-47.
37. Kim, J. S.; Ree, M.; Lee, S. W.; Oh, W.; Baek, S.; Lee, B.; Shin, T. J.; Kim, K. J.; Kim, B.; Lüning, J., *J. Catal.* **2003,** *218*, 386-395.
38. Ree, M.; Bae, J. Y.; Jung, J. H.; Shin, T. J., *J. Polym. Sci., Part A: Polym. Chem.* **1999,** *37*, 1863-1876.
39. Hwang, Y.; Kim, H.; Ree, M., *Macromolecular Symposia* **2005,** *224*, 227-238.
40. Robertson, N. J.; Qin, Z.; Dallinger, G. C.; Lobkovsky, E. B.; Lee, S.; Coates, G. W., *Dalton Trans.* **2006**, 5390-5395.
41. Chen, S.; Guo-Rong, Q. I.; Hua, Z. J.; Yan, H. Q., *J. Polym. Sci., Part A: Polym. Chem.* **2004,** *42*, 5284-5291.
42. Kang, K.; Park, J.; Hyoung, S.; Oh, J. Y. Process for the production of polyether carbonate polyols. 1020100095, 2014.
43. Haider, K. W.; McDaniel, K. G.; Hayes, J. E.; Shen, J. Polyether carbonate polyols made via double metal cyanide (DMC) catalysis. US8134022B2, 2011.
44. Takeda, N.; Inoue, S., *Makromol. Chem.* **1978,** *179*, 1377-1381.
45. Aida, T.; Inoue, S., *J. Am. Chem. Soc.* **1983,** *105*, 1304-1309.
46. Sugimoto, H.; Ohshima, H.; Inoue, S., *Stud. Surf. Sci. Catal.* **2004,** *153*, 247-250.
47. Sugimoto, H.; Kuroda, K., *Macromolecules* **2008,** *41*, 312-317.
48. Chatterjee, C.; Chisholm, M. H., *Inorg. Chem.* **2011,** *50*, 4481-4492.
49. Chatterjee, C.; Chisholm, M. H., *Inorg. Chem.* **2012,** *51*, 12041-12052.
50. Chatterjee, C.; Chisholm, M. H.; El-Khaldy, A.; McIntosh, R. D.; Miller, J. T.; Wu, T., *Inorg. Chem.* **2013,** *52*, 4547-4553.
51. Anderson, C. E.; Vagin, S. I.; Xia, W.; Jin, H.; Rieger, B., *Macromolecules* **2012,** *45*, 6840-6849.
52. Anderson, C. E.; Vagin, S. I.; Hammann, M.; Zimmermann, L.; Rieger, B., *ChemCatChem* **2013,** *5*, 3269-3280.
53. Tsumaki, T., *Bull. Chem. Soc. Jpn.* **1938,** *13*, 252-260.
54. Darensbourg, D. J.; Yarbrough, J. C., *J. Am. Chem. Soc.* **2002,** *124*, 6335-6342.
55. Qin, Z.; Thomas, C. M.; Lee, S.; Coates, G. W., *Angew. Chem. Int. Ed.* **2003,** *42*, 5484-5487.

56. Cohen, C. T.; Chu, T.; Coates, G. W., *J. Am. Chem. Soc.* **2005,** *127*, 10869-10878.
57. Thevenon, A.; Cyriac, A.; Myers, D.; White, A. J. P.; Durr, C. B.; Williams, C. K., *J. Am. Chem. Soc.* **2018,** *140*, 6893-6903.
58. Ren, W.-M. M.; Zhang, X.; Liu, Y.; Li, J.-F. F.; Wang, H.; Lu, X.-B. B., *Macromolecules* **2010,** *43*, 1396-1402.
59. Wendlandt, W. W.; Smith, J. P., *J. Inorg. Nucl. Chem.* **1963,** *25*, 1267-1272.
60. Liu, J.; Ren, W. M.; Liu, Y.; Lu, X. B., *Macromolecules* **2013,** *46*, 1343-1349.
61. S, S.; Min, J. K.; Seong, J. E.; Na, S. J.; Lee, B. Y., *Angew. Chem. Int. Ed.* **2008,** *47*, 7306-7309.
62. Cheng, M.; Moore, D. R.; Reczek, J. J.; Chamberlain, B. M.; Lobkovsky, E. B.; Coates, G. W., *J. Am. Chem. Soc.* **2001,** *123*, 8738-8749.
63. Moore, D. R.; Cheng, M.; Lobkovsky, E. B.; Coates, G. W., *J. Am. Chem. Soc.* **2003,** *125*, 11911-11924.
64. Nakano, K.; Nozaki, K.; Hiyama, T., *J. Am. Chem. Soc.* **2003,** *125*, 5501-5510.
65. Nozaki, K.; Nakano, K.; Hiyama, T., *J. Am. Chem. Soc.* **1999,** *121*, 11008-11009.
66. Schütze, M.; Dechert, S.; Meyer, F., *Chem. Eur. J.* **2017,** *23*, 16472-16475.
67. Saini, P. K.; Romain, C.; Williams, C. K., *Chem. Commun.* **2014,** *50*, 4164-4167.
68. Kember, M. R.; White, A. J. P.; Williams, C. K., *Macromolecules* **2010,** *43*, 2291-2298.
69. Garden, J. A.; Saini, P. K.; Williams, C. K., *J. Am. Chem. Soc.* **2015,** *137*, 15078-15081.
70. Trott, G.; Garden, J. A.; Williams, C. K., *Chem. Sci.* **2019,** *10*, 4618-4627.
71. Deacy, A. C.; Durr, C. B.; Garden, J. A.; White, A. J. P.; Williams, C. K., *Inorg. Chem.* **2018,** *57*, 15575-15583.
72. Deacy, A. C.; Kilpatrick, A. F. R.; Regoutz, A.; Williams, C. K., *Nat. Chem.* **2020,** *12*, 372-380.
73. Reis, N. V.; Deacy, A. C.; Rosetto, G.; Durr, C. B.; Williams, C. K., *Chem. Eur. J.* **2022,** *28*, e202104198.
74. Kissling, S.; Lehenmeier, M. W.; Altenbuchner, P. T.; Kronast, A.; Reiter, M.; Deglmann, P.; Seemann, U. B.; Rieger, B., *Chem. Commun.* **2015,** *51*, 4579-4582.
75. Kissling, S.; Altenbuchner, P. T.; Lehenmeier, M. W.; Herdtweck, E.; Deglmann, P.; Seemann, U. B.; Rieger, B., *Chem. Eur. J.* **2015,** *21*, 8148-8157.
76. Lehenmeier, M. W.; Kissling, S.; Altenbuchner, P. T.; Bruckmeier, C.; Deglmann, P.; Brym, A.-K. K.; Rieger, B., *Angew. Chem. Int. Ed.* **2013,** *52*, 9821-9826.
77. Reiter, M.; Vagin, S.; Kronast, A.; Jandl, C.; Rieger, B., *Chem. Sci.* **2017,** *8*, 1876-1882.
78. Nagae, H.; Aoki, R.; Akutagawa, S. N.; Kleemann, J.; Tagawa, R.; Schindler, T.; Choi, G.; Spaniol, T. P.; Tsurugi, H.; Okuda, J.; Mashima, K., *Angew. Chem. Int. Ed.* **2018,** *57*, 2492-2496.
79. Asaba, H.; Iwasaki, T.; Hatazawa, M.; Deng, J.; Nagae, H.; Mashima, K.; Nozaki, K., *Inorg. Chem.* **2020**, 0-5.
80. Zhang, D.; Boopathi, S. K.; Hadjichristidis, N.; Gnanou, Y.; Feng, X., *J. Am. Chem. Soc.* **2016,** *138*, 11117-11120.
81. Jia, M.; Zhang, D.; de Kort, G. W.; Wilsens, C.; Rastogi, S.; Hadjichristidis, N.; Gnanou, Y.; Feng, X., *Macromolecules* **2020,** *53*, 5297-5307.
82. Schaefer, J.; Zhou, H.; Lee, E.; Lambic, N. S.; Culcu, G.; Holtcamp, M. W.; Rix, F. C.; Lin, T.-P., *ACS Catal.* **2022,** *12*, 11870-11885.
83. Pedersen, C. J., *J. Am. Chem. Soc.* **1967,** *89*, 7017-7036.
84. van Staveren, C. J.; Van Eerden, J.; van Veggel, F. C. J. M.; Harkema, S.; Reinhoudt, D. N., *J. Am. Chem. Soc.* **1988,** *110*, 4994-5008.
85. Van Veggel, F. C. J.; Harkema, S.; Bos, M.; Verboom, W.; Van Staveren, C. J.; Gerritsma, G. J.; Reinhoudt, D. N., *Inorg. Chem.* **1989,** *28*, 1133-1148.
86. Casellato, U.; Tamburini, S.; Tomasin, P.; Vigato, P. A., *Inorg. Chim. Acta* **1997,** *262*, 117-121.
87. Brianese, N.; Casellato, U.; Tamburini, S.; Tomasin, P.; Vigato, P. A., *Inorg. Chim. Acta* **1999,** *293*, 178-194.
88. Casellato, U.; Tamburini, S.; Tomasin, P.; Vigato, P. A.; Aime, S.; Botta, M., *Inorg. Chem.* **1999,** *38*, 2906-2916.
89. Caneschi, A.; Sorace, L.; Casellato, U.; Tomasin, P.; Vigato, P. A., *Eur. J. Inorg. Chem.* **2004**, 3887-3900.
90. Tamburini, S.; Sitran, S.; Peruzzo, V.; Vigato, P. A., *Eur. J. Inorg. Chem.* **2009**, 155-167.
91. Barge, A.; Botta, M.; Casellato, U.; Tamburini, S.; Vigato, P. A., *Eur. J. Inorg. Chem.* **2005,** *2*, 1492-1499.
92. Tamburini, S.; Vigato, P. A.; Gatos, M.; Bertolo, L.; Casellato, U., *Inorg. Chim. Acta* **2006,** *359*, 183-196.
93. Cassol, A.; Di Bernardo, P.; Zanonato, P. L.; Tamburini, S.; Tomasin, P.; Vigato, P. A., *Supramol. Chem.* **2001,** *13*, 469-488.
94. Casellato, U.; Tamburini, S.; Tomasin, P.; Vigato, P. A., *Inorg. Chim. Acta* **2004,** *357*, 4191-4207.
95. Reath, A. H.; Ziller, J. W.; Tsay, C.; Ryan, A. J.; Yang, J. Y., *Inorg. Chem.* **2017,** *56*, 3713-3718.
96. Du, K.; Thorarinsdottir, A. E.; Harris, T. D., *J. Am. Chem. Soc.* **2019,** *141*, 7163-7172.
97. Chantarojsiri, T.; Reath, A. H.; Yang, J. Y., *Angew. Chem. Int. Ed.* **2018,** *57*, 14037-14042.
98. Najafian, A.; Cundari, T. R., *Inorg. Chem.* **2019,** *58*, 12254-12263.
99. Kumar, A.; Lionetti, D.; Day, V. W.; Blakemore, J. D., *Chem. Eur. J.* **2018,** *24*, 141-149.
100. Kang, K.; Fuller, J.; Reath, A. H.; Ziller, J. W.; Alexandrova, A. N.; Yang, J. Y., *Chem. Sci.* **2019**, 10135-10142.
101. Kumar, A.; Lionetti, D.; Day, V. W.; Blakemore, J. D., *J. Am. Chem. Soc.* **2020,** *142*, 3032-3041.
102. Chantarojsiri, T.; Ziller, J. W.; Yang, J. Y., *Chem. Sci.* **2018,** *9*, 2567-2574.
103. Martinez, A.; Hemmert, C.; Gornitzka, H.; Meunier, B., *J. Organomet. Chem.* **2005,** *690*, 2163-2171.
104. Deacy, A. C.; Moreby, E.; Phanopoulos, A.; Williams, C. K., *J. Am. Chem. Soc.* **2020,** *142*, 19150-19160.
105. Lindeboom, W.; Fraser, D. A. X.; Durr, C. B.; Williams, C. K., *Chem. Eur. J.* **2021,** *27*, 12224.

Chapter 2

Theoretical and Experimental Mechanistic Investigation into Co(III)K(I) complexes

2.1 Introduction and Aims

There is a significant need for more active ROCOP catalysts for PO/CO_2, however, the mechanistic understanding by which these catalysts operate is still poorly understood. What separates an active catalyst from an inactive one still eludes researchers and is important for future catalytic design.

Recently, we reported a heterodinuclear Co(III)K(I) complex coordinated by a macrocyclic ligand featuring both Schiff base and crown ether binding pockets. This complex showed good activity for PO/CO2 ROCOP with TOF = 800 h^{-1} (0.025 mol %, 70 °C, 30 bar).[1] Even in the first report, its activity exceeds that of many di-Co(III) catalysts, and it has the additional benefit of removing half the cobalt and replacing it with potassium, a cheaper, nontoxic, readily available alkali metal (see chapter 1). The catalyst is synthesized in three synthetic steps in good yields (74%). Further, it was stable to excess chain- transfer agent (up to 250 equiv); such additives are important to make polyols (<5 kg mol^{-1}).[1] This new catalyst meets many of the requirements for carbon dioxide/PO ROCOP. As such, a better understanding of its mechanism and how to improve activity would be very useful. In this area of catalysis, there are surprisingly few prior mechanistic investigations and thus there are many open questions including: (1) What are the roles of the different metals in the catalytic cycle? (2) What are the relative reaction barriers to polymerization? (3) How can polymer selectivity, over cyclic carbonate, be maximized? and (4) Are there design implications for future dinuclear catalysts that can be uncovered?

The aim of this work is increase the understanding of the mechanism of a recently reported Co(III)K(I) catalyst.[1] Kinetic, by-product analysis and a computed mechanism will be presented, with the DFT work performed by Dr. Antione Buchard (University of Bath) and Dr. Andraes Phanopolous (Imperial College London). Experimental work was conducted by me.

The mechanistic analysis is set in context of the wider field to show the state-of-the-art approach taken here and future areas for investigation.

DFT calculations were run using Gaussian 16 (Revision C.01).[2] The reaction free energies were calculated using the hybrid exchange-correlation ωB97X-D functional, which includes D2

dispersion corrections described by Grimme.[3-4] A functional screening was undertaken on key transition states for both pathways, with the surveyed functionals including B3LYP[5-6] with Grimme's D3 dispersion correction including Becke-Johnson damping (GD3BJ),[7-8] M06[9] with Grimme's D3 dispersion correction (GD3)[10] and PBE0[11-12] with GD3BJ.[7-8] NBO analysis was performed using NBO 6.0.[13] QTAIM analysis was conducted using the AIMAll package.[14] Data are presented from *very fine* mesh calculations. Standard cut-offs for plotting the data with AIMAll were used. Non-covalent interactions were analysed using the NCIPLOT 3.0 program.[15]

The split valence 6-31+g(d,p) basis sets were used for carbon and hydrogen. This lower basis set was chosen as these elements do not bind directly to either catalytic metal centre, but extra diffuse functions were added to capture more mid- and long-range interactions, for instance with growing polymer chains. The triple-ζ 6-311+g(d) basis set was used for potassium and all heteroatoms. Cobalt centres were described with the Stuttgart SDD ECP and associated basis sets.

Geometry optimisation calculations were performed without symmetry constraints and using an "ultrafine" grid for numerical integration. All structures are optimized using the self-consistent reaction field (SCRF) approach with conductor-like polarisable continuum model (CPCM).[16] In polymerization reactions, the propylene oxide (PO) monomer also serves as the solvent but is not implemented as a standard solvent in Gaussian16. A CPCM model for PO was therefore implemented by using the built- in non-polar parameters of tetrahydrofuran, modified with the polar parameters of propylene oxide (ε=16, n^2=1.867) ([SCRF=(cpcm,solvent=tetrahydrofuran),read] and [eps=16/epsinf=1.867)].

Free enthalpies were corrected using Goodvibes software,[17] with Grimme's quasiharmonic approximation applied with a frequency cut-off value of 100.0 wavenumbers, a frequency scale factor = 1.0. To account for experimental conditions, a temperature of 323.15 K and concentrations of 14.1156 mol L^{-1} (for neat PO), 4.787 mol L^{-1} (for CO_2 dissolved in PO at 50 bar and 313.15 K)[18] and 0.003 mol L^{-1} (for any metal complex species) were also applied.

All intermediates and transition states were characterised by normal coordinate analysis revealing

either precisely zero or one imaginary frequency, respectively. In the case of transition states, the imaginary frequency corresponds to the mode of the intended reaction step. Full coordinates for all the calculated stationary points are included as part of the supplementary information (.xyz).

Full coordinates for all structures, together with computed energies and vibrational frequency data, are available via the corresponding Gaussian 16 output files and calculation spreadsheet, stored in the open- access digital repository, DOI: 10.6084/m9.figshare.20026409.

2.2 Experimental and DFT Mechanistic Insight into PO/CO2 ROCOP of Co(III)K(I) Heterobimetallic Catalysts

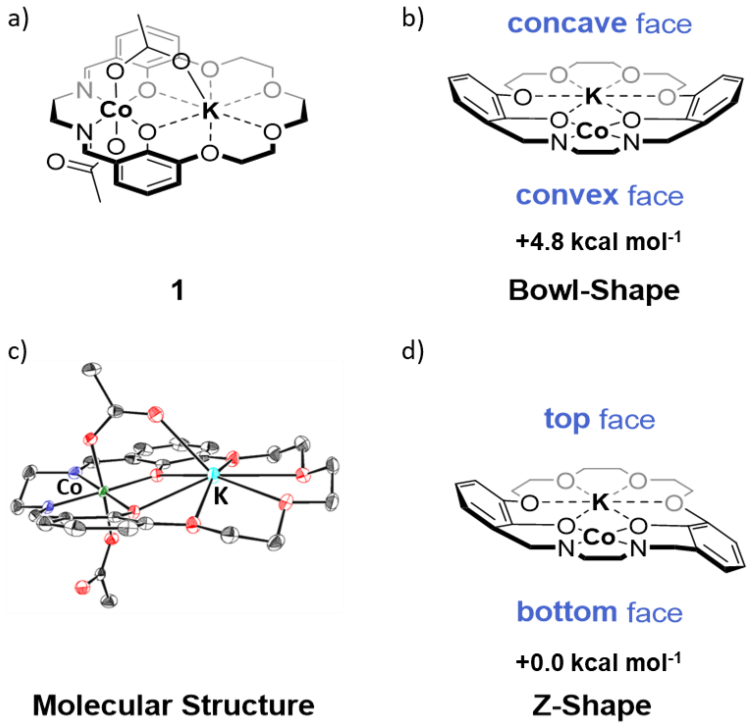


Figure 2.1 a) Illustration of the Co(III)K(I) heterodinuclear catalyst **1**. b) illustration of the 'bowl'-shape conformation of the ligand resulting in 'concave' and 'convex' faces. c) ORTEP representation of the molecular structure of catalyst 1 obtained through single crystal X-ray diffraction. d) Illustration of the 'Z'-shape conformation of the ligand resulting in complexes with 'top' (κ_2-acetate) and 'bottom' (κ_1-acetate) faces.[1]

The molecular structure of complex **1** was first elucidated via single crystal X-ray diffraction and confirms the coordination of the cobalt(III) centre in the ligand's Schiff base binding cavity and the potassium(I) in the crown ether moiety (Fig. 2.1 a and c).[1] This solid-state molecular structure was used as the basis for the DFT structure optimisation which indicated that the same structure has a low energy in PO (the reaction solvent and that used in all DFT investigation). The structure features one bridging (κ_2) and one κ_1-acetate ligand which are the initiating groups. Furthermore, in both states the complex adopts a Z-shape confirmation as the lowest energy state (Fig. 2.1 d). However, in solution DFT suggests the bowl shape should also be readily accessible, as it is only +4.8 kcal mol^{-1} higher in Gibbs free energy compared with the Z-shape (Fig. 2.1 b).

From this ground state structure, the mechanism was explored computationally, with specific focus on initiation, propagation and selectivity of the reaction.

2.2.1 Initiation

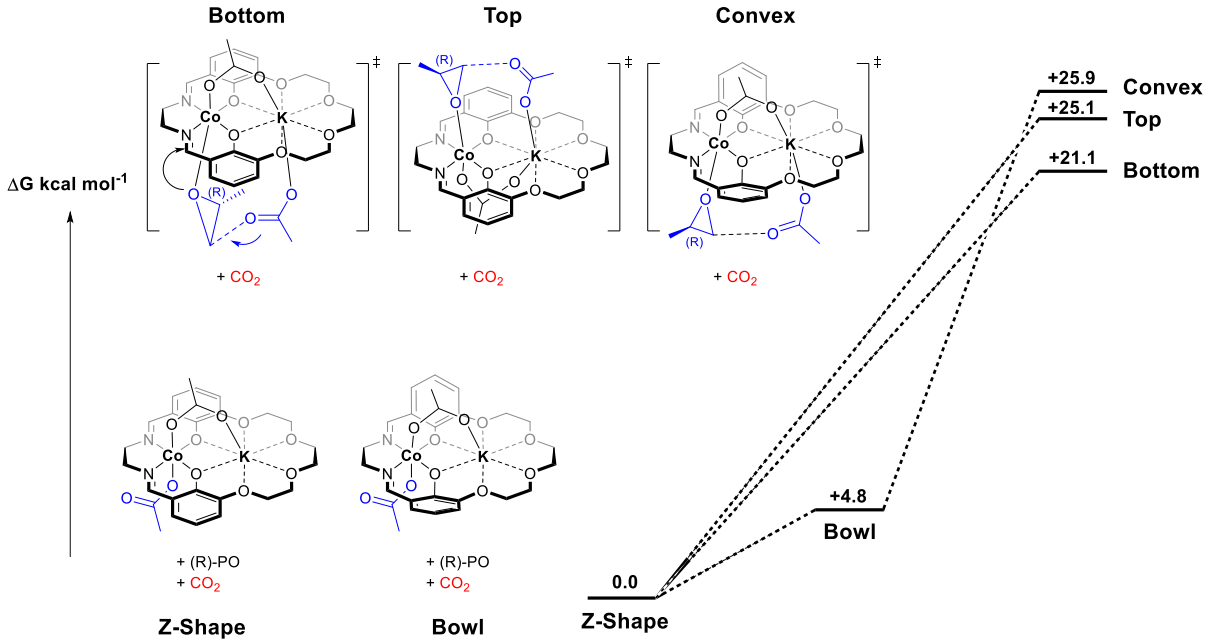


Figure 2.2 Illustrations of the potential energy surfaces for the initiation of propylene oxide and carbon dioxide copolymerisation using catalyst **1**, where propylene oxide coordination occurs at Co(III).

DFT calculations of the initiation process were conducted with propylene oxide coordination at the cobalt centre, as opposed to potassium, as this coordination geometry results in significantly lower propagation barriers (21.2 *versus* 34.6 kcal mol^{-1}). The calculations were conducted using both the 'Z'- and 'bowl'-shape ligand conformations since their energy differences in the ground state were only +4.8 kcal mol^{-1}. For the 'Z'-shape ligand conformation, propylene oxide ring-opening barriers were +21.1 and +25.1 kcal mol^{-1} for the 'bottom' and 'top' faces, respectively (Fig. 2.2). In contrast, the ring-opening of the propylene oxide on the 'convex' face of the 'bowl' shape conformation had a transition state barrier of

+25.9 kcal mol^{-1} (relative to 'Z'-shape ground state). The equivalent attack from the catalyst's 'concave' face could not be optimized due to the increased steric crowding and is much higher in energy.

2.2.2 Propagation

Here the goal was to understand the goals of the different metals in the reaction, key intermediates to the rate limiting step and the reaction energy barriers. Two different dinuclear polymerisation pathways were considered: one involving propylene oxide coordination at the Co(III) centre (Figure 2.3) and the other with propylene oxide coordination at the K(I) centre (Figure 2.4).

In order to model a growing chain, the acetate ligand was replaced with a carbonate group: the key intermediate in propagation. This structure was taken as the zero-energy point throughout the further discussion. Furthermore, for simplification of the model, all DFT data was presented with only *R*-PO, but no significant difference in energy was observed for the use of *S*-PO in the model. In all experiments *rac*-PO was used.

2.2.2.1 Cobalt-activated PO Mechanism

The first step in the Co(III)-activated mechanism is the formation of intermediate $\mathbf{I_{Co}}$, which is +5.6 kcal mol^{-1} higher in energy than the ground state catalyst structure (Fig. 2.3). The formation of this intermediate, involving the coordination of PO at the Co(III) centre, is promoted by the high concentration of PO in the reaction mixture, which forces the equilibrium towards PO-coordination. The ring-opening of PO subsequently occurs *via* nucleophilic attack from the carbonate coordinated to the potassium. This proceeds by the transition state $\mathbf{TS1_{Co}}$, with energy of +21.2 kcal mol^{-1}, to form a stabilized cobalt alkoxide intermediate ($\mathbf{II_{Co}}$), having an energy of -2.9 kcal mol^{-1}. In the calculated structure of $\mathbf{II_{Co}}$, an adjacent polymer chain carbonate (or acetate during initiation) group is observed to coordinate to the potassium centre. A pre-organization step precedes CO_2 insertion and involves breaking of the dative bond between the carbonyl on the polymer chain to potassium, yielding a Co-alkoxide intermediate ($\mathbf{III_{Co}}$, +4.4 kcal mol^{-1}) where the growing polymer chain has rotated 180 ° along the Co-O bond axis.

Subsequently, carbon dioxide coordination at potassium occurs by an end-on binding mode with a K-O_{CO2} distance of 3.13 Å ($\mathbf{IV_{Co}}$, +5.0 kcal mol^{-1}). Carbon dioxide insertion involves a moderate energy transition state ($\mathbf{TS2_{Co}}$, +13.3 kcal mol^{-1}) to form an isoenergetic zwitterionic intermediate ($\mathbf{V_{Co}}$, +13.2 kcal mol^{-1}). In the last propagation step, the zwitterionic intermediate rearranges to form a stabilized Co-carbonate intermediate ($\mathbf{VI_{Co}}$, -6.7 kcal mol^{-1}). Therefore, the Gibbs free energy to CO_2 insertion is $\Delta G^{\dagger}_{calc}$ = +16.2 kcal mol^{-1} with respect to the alkoxide intermediate $\mathbf{II_{Co}}$. The next ring-opening of PO has a transition state ($\mathbf{TS1_{Co}*}$) energy of +15.6 kcal mol and a Gibbs free energy with respect to the carbonate intermediate $\mathbf{VI_{Co}}$ of $\Delta G^{\dagger}_{calc}$ = +22.2 kcal mol^{-1}.

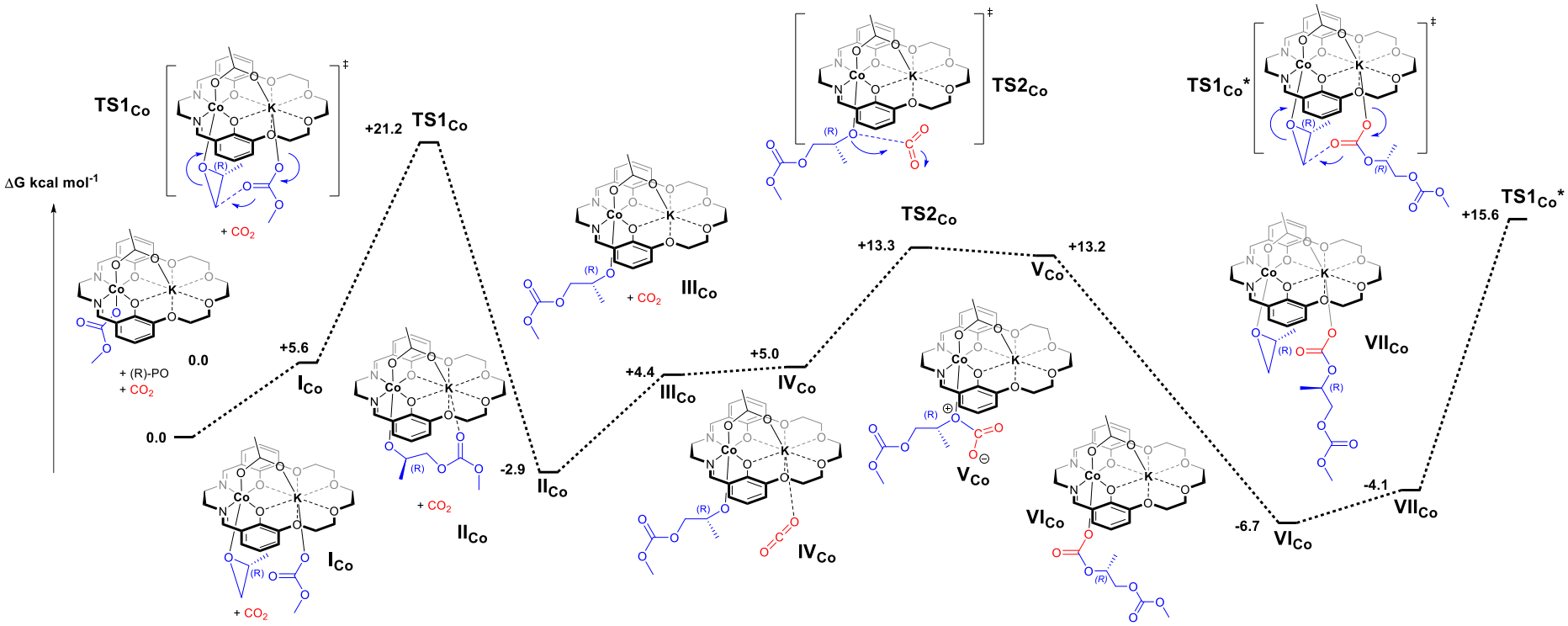


Figure 2.3 Illustrations of the potential energy surfaces for the alternating copolymerisation of propylene oxide and carbon dioxide using catalyst **1**, where propylene oxide coordination occurs at Co(III).

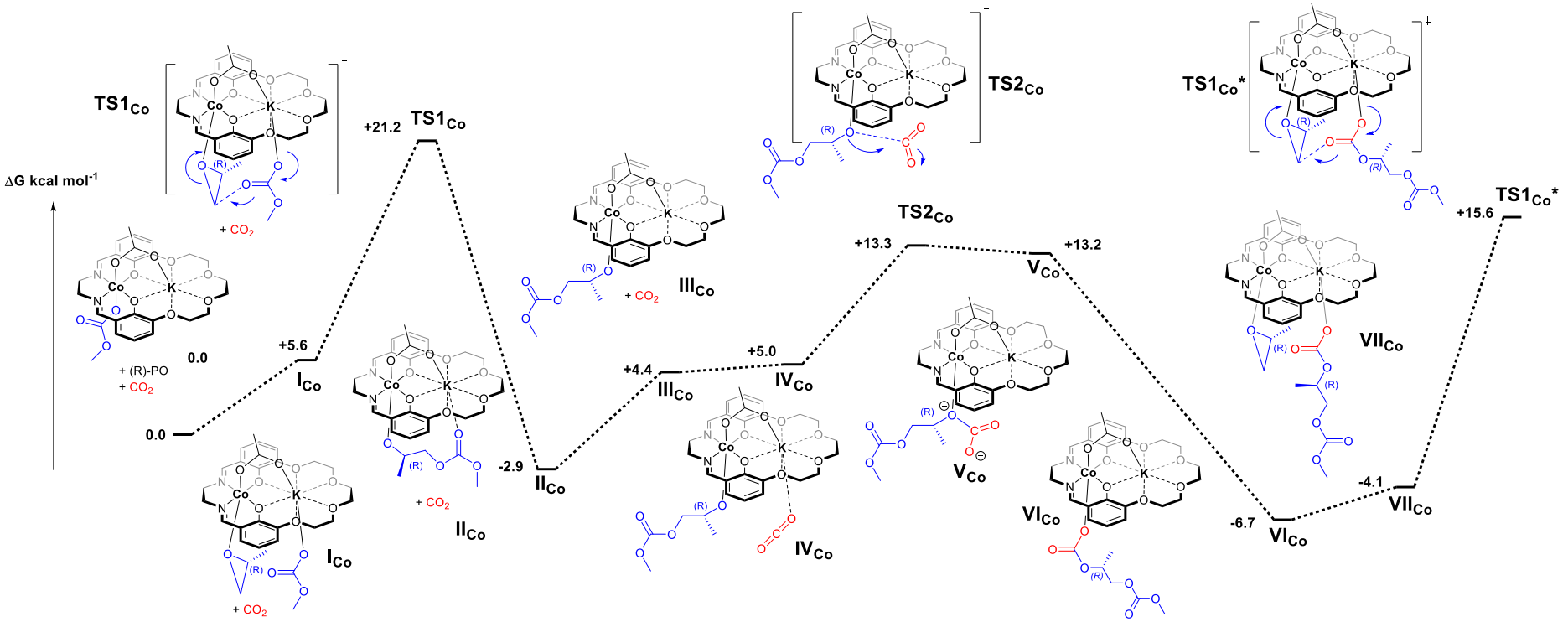


Figure 2.4 Illustrations of the potential energy surfaces for the alternating copolymerisation of propylene oxide and carbon dioxide using catalyst **1**, where propylene oxide coordination occurs at K(I).

.

2.2.2.2 Potassium-activated PO Mechanism

An alternative pathway was calculated in which initial coordination of PO takes place at the K(I) centre. Here, the formation of the PO-coordinated intermediate is slightly endothermic (**I_K**, +0.5 kcal mol^{-1}) and favoured over coordination of PO at the Co(III) centre (**I_{Co}**, +5.6 kcal mol^{-1}). The difference in energy likely arises likely due to the greater number of accessible coordination sites and lack of geometric constraints at potassium (Fig. 2.4). In the next step, the potassium-activated epoxide is ring-opened by the Co(III) coordinated carbonate nucleophile (**$TS1_K$**, +34.6 kcal mol^{-1}) forming a potassium-alkoxide intermediate. The intermediate is stabilized by chelation of the polymer-chain carbonate (or acetate) group to the adjacent cobalt centre (**II_K**, +22.0 kcal mol^{-1}). This is significantly higher in energy than the respective cobalt-alkoxide (**II_{Co}**), with a difference of +24.9 kcal mol^{-1}. The lower stability of **II_K** than **II_{Co}** is attributed to both the weaker potassium-oxygen bond and to a weaker cobalt-carbonate chelation. The insertion of carbon dioxide follows similar structural changes to those observed for the Co-activated epoxide mechanism. First a pre-organization of the polymer chain occurs to form a higher energy intermediate (**III_K**, +32.4 kcal mol^{-1}), then carbon dioxide enters the reactivity sphere but is not activated by the cobalt center with a Co-O_{CO2} distance measuring 4.35 Å, (**IV_K**, +35.6 kcal mol^{-1}). This is followed by CO_2 insertion into the potassium-alkoxide bond (**$TS2_K$**, +36.2 kcal mol^{-1}) forming a zwitterionic intermediate (**V_K**, +17.9 kcal mol^{-1}) and finally by rearrangement to form the cobalt-carbonate intermediate (**VI_K**, -6.7 kcal mol^{-1}; identical to **VI_{Co}** intermediate).

2.2.2.3 Cobalt *versus* Potassium Activated PO Mechanism

Comparing the energy barriers for PO ring-opening reveals that the cobalt-activated epoxide mechanism is an overall lower energy pathway to PO opening than the potassium activated epoxide mechanism. The critical, rate limiting, barriers are $\Delta G^{\dagger}_{calc}$ = +22.2 kcal mol^{-1} (Co-activated) and $\Delta G^{\dagger}_{calc}$ = +36.2 kcal mol^{-1} (K-activated), respectively. The difference between the barriers suggests that the potassium activated pathway is very unlikely to occur experimentally.

For the cobalt-activated epoxide pathway, the rate-determining step is the ring opening of the epoxide having an energy barrier of $\Delta G^{\dagger}_{calc}$ = +22.2 kcal mol^{-1}. This step is higher in energy compared with the insertion of CO_2 ($\Delta G^{\dagger}_{calc}$ = +16.2 kcal mol^{-1}). Further support for the Co-activated pathway comes when

the experimental transition state energy barrier is compared with the calculated value. The polymerisation kinetics analysis already indicated that the rate determining step is propylene oxide ring opening since the rate law was first order in epoxide and catalyst concentrations but zero order in CO_2 pressure. Finally, the calculated epoxide ring opening barrier is closely comparable to the experimentally determined ring-opening barrier, $\Delta G^{\dagger}_{exp}$ = +22.1 kcal mol^{-1} (92.6 kJ mol^{-1}) at 50 °C (Fig. 2.5).

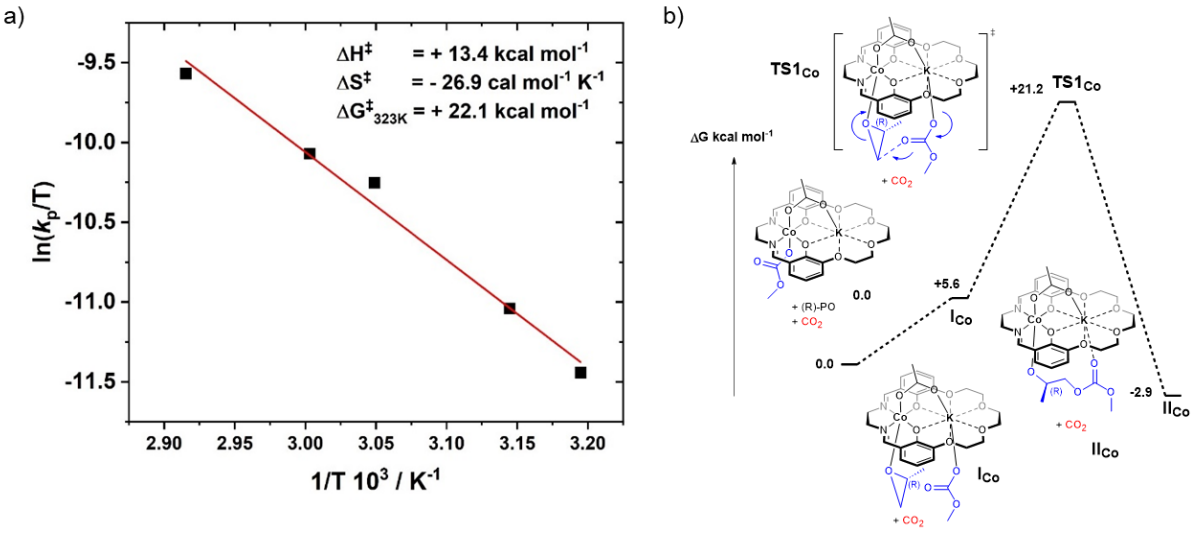
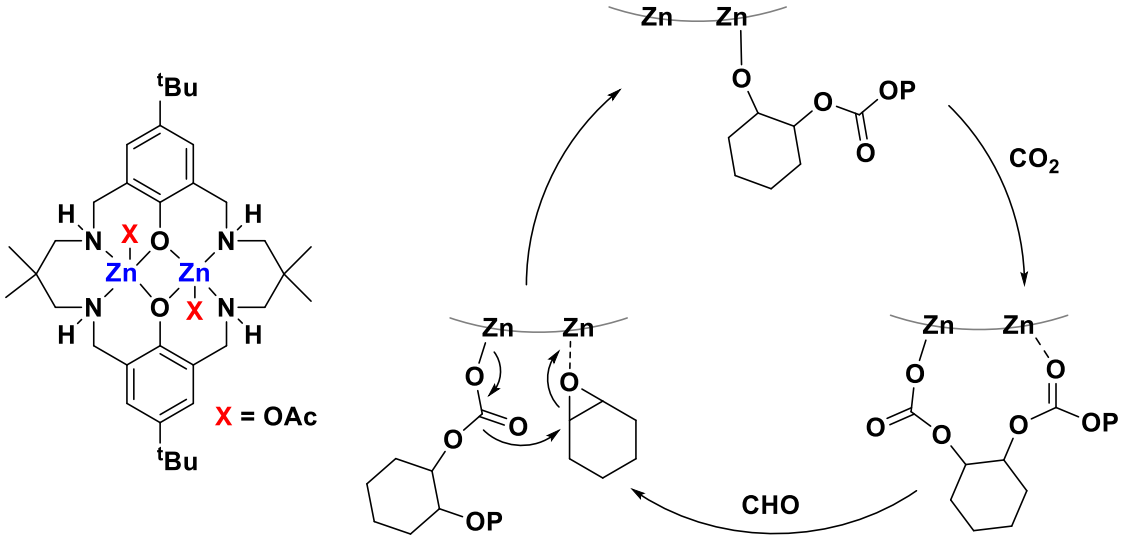


Figure 2.5 a) Eyring analysis for the transition state barrier to ring opening of propylene oxide during propagation using catalyst **1**.[1] b) Key intermediates of ring-opening of PO.

Previously, a DFT investigation into the mechanism of cyclohexene oxide/carbon dioxide ROCOP using a di-zinc macrocyclic catalyst implicated a 'chain-shuttling' mechanism was reported (Scheme 2.1).[19] In that mechanism, the polymer chain migrates between the Zn(II) centres twice during each complete propagation cycle. This means that one Zn(II) site is always coordinated to the alkoxide intermediate (after epoxide ring opening) and the other coordinates the carbonate intermediate (after carbon dioxide insertion), in other words each centre has a single distinct role in the mechanism.



Scheme 2.1 'Chain-Shuttling' mechanism proposed by Williams and co-workers for Zn(II)Zn(II) catalysts for CHO/CO_2 ROCOP.[19]

For the Co(III)K(I) PO/CO_2 ROCOP catalysis, the DFT investigation suggests that both the alkoxide and carbonate intermediates are coordinated to the cobalt centre during propagation (**II_{Co}** and **VI_{Co}**), which is different to the 'Chain-Shuttling' mechanism. The rate-determining step (**$TS1_{Co}$**) involves propylene oxide activation at the cobalt centre with the potassium centre transiently stabilizing a polymer carbonate group. The Co-activated dinuclear pathway suggests that the role of cobalt is both to activate epoxide and to provide the labile alkoxide and carbonate nucleophiles. This mechanism suggests that the Schiff base binding moiety is important since it coordinates Co(III): future structure-activity relationship studies should focus on this part of the ligand.

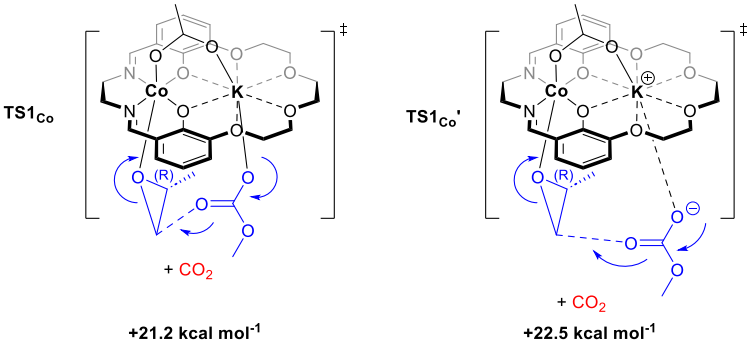
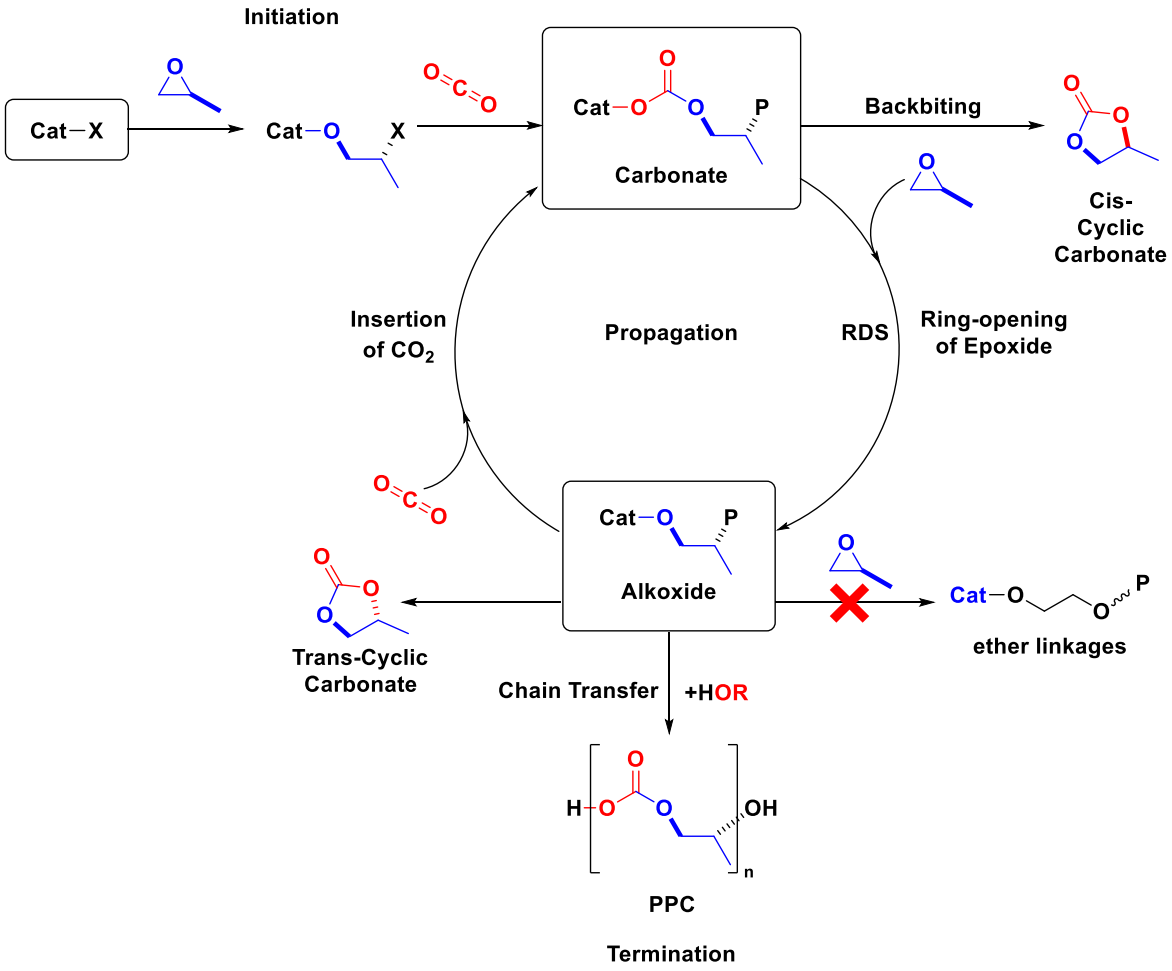


Figure 2.6 Bound (**$TS1_{Co}$**) *versus* associated (**$TS1_{Co}$'**) carbonate to the K(I) centre in the transition state of the ring-opening of PO.

In the Co-activated epoxide dinuclear mechanism, the carbonate nucleophile is modelled as covalently bonded to potassium (Fig. 2.6). Nonetheless, an alternative speciation where the carbonate anion is only associated with the cationic potassium centre resulted in a transition state barrier that was only slightly

higher (**TS1$_{Co}$'**; +22.5 kcal mol^{-1}). Given the similarity in the two barriers, it is experimentally credible that either K-coordinated or anionic carbonate nucleophiles are involved in the propagation mechanism. In the latter model, the role of potassium in the catalyst structure would be to stabilize the carbonate anion. Such an ionic coordination mode is reminiscent of the understanding of how catalyst/co-catalyst systems operate.[20-23] Nonetheless it is very important to emphasize that using potassium salts as separate additives to Co(III) salen catalysts results in nonselective polymerisation catalysis (Polymer selectivity = 41 %, 0.05 mol%, 15 bar CO_2, 25 °C).[24] Thus, even if the role of potassium is as a stabilizing cation, it must be coordinated within the macrocyclic ligand for effective catalysis. Overall, the DFT calculations do not allow for unambiguous characterization of the role of potassium in the cycle, but the Co-coordinated mechanism seems more likely.

2.2.3 Investigation of Side Reactions



Scheme 2.2 Simple mechanism of PO/CO_2 ROCOP and side reactions.

There are two main side reactions in PO/CO_2 ROCOP: (1) backbiting to form cyclic carbonate (CC), either from the alkoxide or carbonate intermediate, and (2) consecutive insertions of PO to form ether linkages (Scheme 2.2). For catalyst **1** (and any subsequent catalysts presented in this chapter) no ether linkages are observed in the polymers and so this was not further explored. However, depending on the reaction conditions, a significant proportion of CC can be observed. Experimentally, no cyclic carbonate was observed at 40 °C (20 bar), whilst 86% CC was observed at 70 °C (6 bar). Thus, CC formation should be better understood as it is key to the selectivity.

DFT calculations of the two backbiting reactions were conducted using catalyst **1** (Fig. 2.7). The Co-carbonate intermediate can react, via a transition state where a carbonate coordinates at the potassium (Fig. 2.7a). Nucleophilic attack (intramolecular-S_N2) of the cobalt-carbonate at the least hindered carbon-oxygen bond proceeds with a transition state barrier of +25.8 kcal mol^{-1} (**$TS3_{Co}$**). This results in the formation of a chain-shortened Co-carbonate intermediate (**0.0**), together with an equivalent of propylene carbonate. Propylene carbonate is thermodynamically favoured and thus has an energy of −15.7 kcal mol^{-1}. This backbiting reaction has a Gibbs free energy of $\Delta G_{calc}^{\dagger}$ = +31.9 kcal mol^{-1} (against **VI_{Co}**) and is +9.7 kcal mol^{-1} higher in energy than epoxide ring opening and, therefore, is unlikely to compete with propagation under the experimental polymerisation conditions.

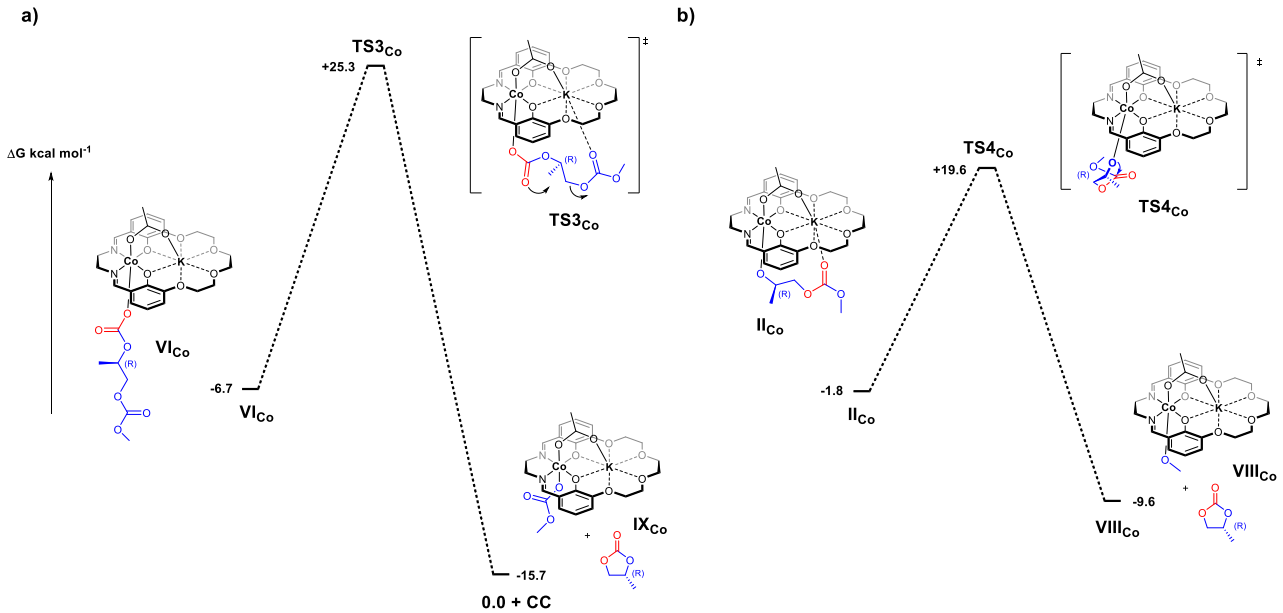


Figure 2.7 Illustration of the potential energy surface for the backbiting reaction of CO_2 with Propylene oxide using 1 starting from a) the cobalt-carbonate intermediate **VI_{Co}** and b) the cobalt-alkoxide intermediate **II_{Co}**.

In the alternative CC formation mechanism, the backbiting takes places via Co-alkoxide intermediate (**II$_{Co}$**) (Fig. 2.7b). To access the transition state, the polymer chain de-coordinates from the adjacent potassium centre, with the chain rotating 90° along the Co-O bond axis. Nucleophilic attack occurs from the Co-alkoxide at the neighbouring carbonyl carbon, via an intramolecular addition-elimination reaction, with a transition state energy of +19.6 kcal mol^{-1} (**TS4$_{Co}$**). No subsequent TS was identified, and the transformation results in the reformation of a chain-shortened cobalt-alkoxide intermediate (**VIII$_{Co}$**), along with one equivalent of propylene carbonate. The Gibbs free energy barrier of this backbiting reaction is $\Delta G_{calc}^{\dagger}$ = 22.4 kcal mol^{-1}, which is competitive with the epoxide ring-opening barrier. Thus, the calculations suggest that the cobalt-alkoxide intermediate might undergo both copolymerisation and backbiting under experimental conditions.

These DFT results highlight the need to measure the rate of propylene carbonate formation to understand the product selectivity. Usually such measurements are made during polymerisations, but this can cause problems. To consider how best to make the measurements, it is useful to consider the criteria for the determination of a reaction energy barrier:

1. The barrier being measured must be rate-determining (pre- or post-transition state barriers must be lower in energy).
2. The chemical structure of any model compound must resemble the energy minima prior to the rate-determining step.
3. Competing side reactions must be minimized or removed (high product selectivity).

In this field, the barrier to backbiting (**TS4**) is almost always determined by analysis of the by-products of CO_2/PO ROCOP. Such analyses assume that the barrier to backbiting (**TS4**) is greater than the barrier to epoxide ring opening (**TS1**). Although such an assumption may be acceptable for some copolymerisations, such as cyclohexene oxide/CO_2, since backbiting transitions through a strained bicyclic carbonate are significantly higher in energy, it is much less likely to be correct for propylene carbonate.

Indeed, the barrier to Co-alkoxide backbiting was calculated as near equivalent to epoxide ring opening (+22.4 vs +22.2 kcal mol^{-1}), suggesting it cannot be determined appropriately during polymerisation. Another detraction of using the polymerisation side reactions to determine the barriers to cyclic carbonate formation is that cyclic carbonate is often the minor product, especially at low reaction temperatures, i.e. rate and conversion measurements are significantly less accurate.

An alternative approach would be to determine the rate of propylene carbonate formation from the catalysed depolymerisation of poly(propylene carbonate) (PPC). The PPC end-groups must be hydroxyls but this is feasible using diol as a chain transfer agent. These hydroxyl chain ends should react with the catalyst to generate a Co-alkoxide intermediate, which is structurally identical to (**II_{Co}**). Since there is no epoxide ring-opening step (**TS1**) during depolymerisation, the alkoxide intermediate backbiting will unequivocally be the rate-determining step. Measuring the rate of PPC backbiting also removes any competition from CO_2 insertion (**TS2**), ensuring that all of the catalyst effects backbiting.

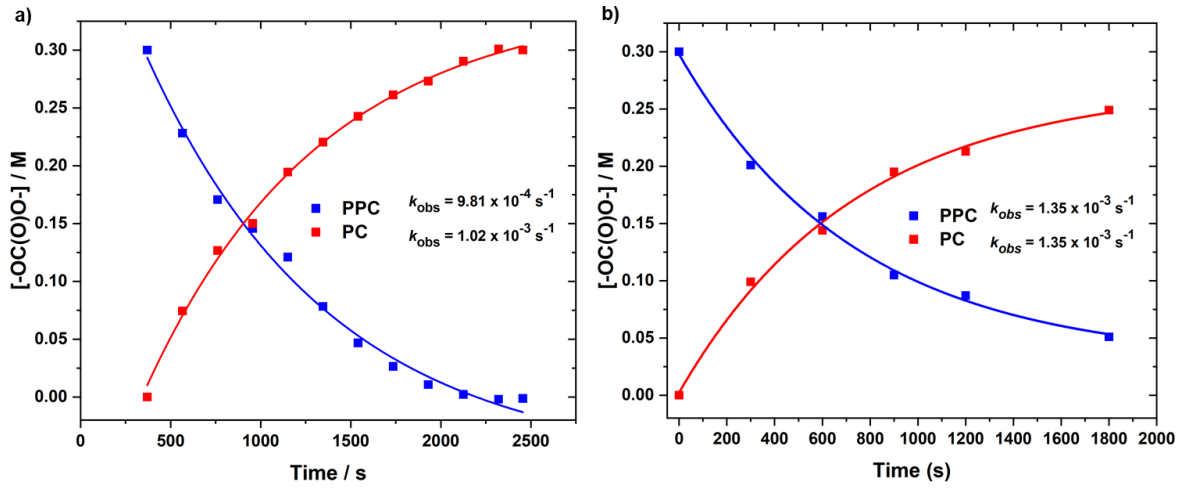


Figure 2.8 Plot showing the change in concentration of carbonate linkages (−OC(O)O−) in both PPC and PC against time using catalyst **1**, at 45 °C, obtained by a) *in situ* IR spectroscopy and b) NMR spectroscopy with an exponential fit to the data allowing for the determination of the pseudo first-order rate coefficient.

To experimentally determine the Co-alkoxide backbiting barrier, the rate of PPC depolymerisation to form propylene carbonate (PC), using catalyst **1**, was monitored over the temperature range of 40-60 °C. The reaction was conducted by adding 3 mM catalyst to a 0.3 M solution of PPC in PO (6 mL), and *in situ* IR spectroscopy was used to interrogate changes in the intensity of absorptions assigned to PPC (1750 cm^{-1}) and propylene carbonate, PC, (1810 cm^{-1}). For comparison, under equivalent

conditions, the experiment was repeated and aliquots were regularly removed and analysed by NMR spectroscopy, these results were consistent with rates determined by *in situ* IR spectroscopy (Fig. 2.8). A dilute polymer solution was used to prevent any diffusion limitations to the rate of reaction so as to ensure that the depolymerisation barrier was properly measured. An exponential decrease in PPC concentration, with a concomitant increase in PC concentration, was observed, indicating a 1st order rate dependence in carbonate concentration (Fig. 2.8 and 2.9a). Eyring analysis allowed for the determination of the free energy of backbiting, as $\Delta G_{323}^{\ddagger}$ = +19.5 kcal mol^{-1} (where $\Delta H^{\ddagger}$ = +23.2 kcal mol^{-1} $\Delta S^{\ddagger}$ = + 11.4 cal mol^{-1} K^{-1}), which is in line with the DFT calculations for propylene carbonate formation (**TS4$_{Co}$** = +22.4 kcal mol^{-1}) (Fig. 2.9b).

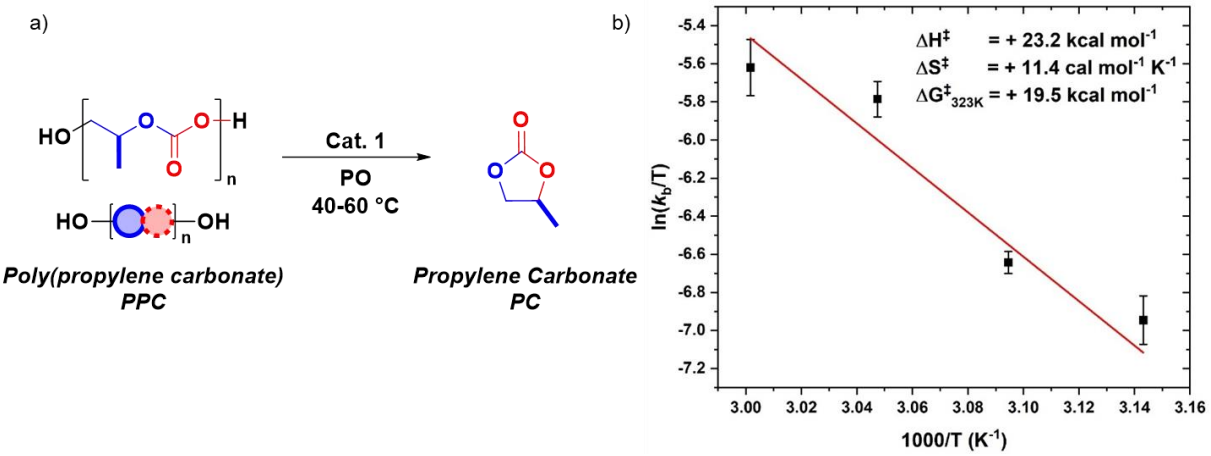


Figure 2.9 a) Catalysed depolymerisation of PPC to PC using catalyst **1**. b) Eyring analysis, i.e., a plot of ln(k_b/T) vs 1/T, for the decomposition of PPC into PC using catalyst **1**. Where k_b = k_{obs}/[**1**] and k_{obs} is the gradient of the plot of ln[PPC]$_t$/[PPC]$_0$ vs time (s) (Table S2.1).

To further investigate the depolymerisation of PPC to PC, the PPC molar mass and dispersity were also measured throughout the reaction (Fig. 2.10). The PPC molar mass decreased linearly with conversion (Fig. 2.8b and 2.10). Furthermore, a linear increase in dispersity was also observed over time corresponding to an exponential increase with respect to conversion. It should be noted that at 20 min (71% conv.) and 30 min (83% conv.) the GPC trace shows a new peak (towards 1000 g mol^{-1}) while showing little shift in the main distribution (Fig. 2.10b). At these high conversions, the concentrations the polymer were significantly reduced, which may explain reduced sample resolution.

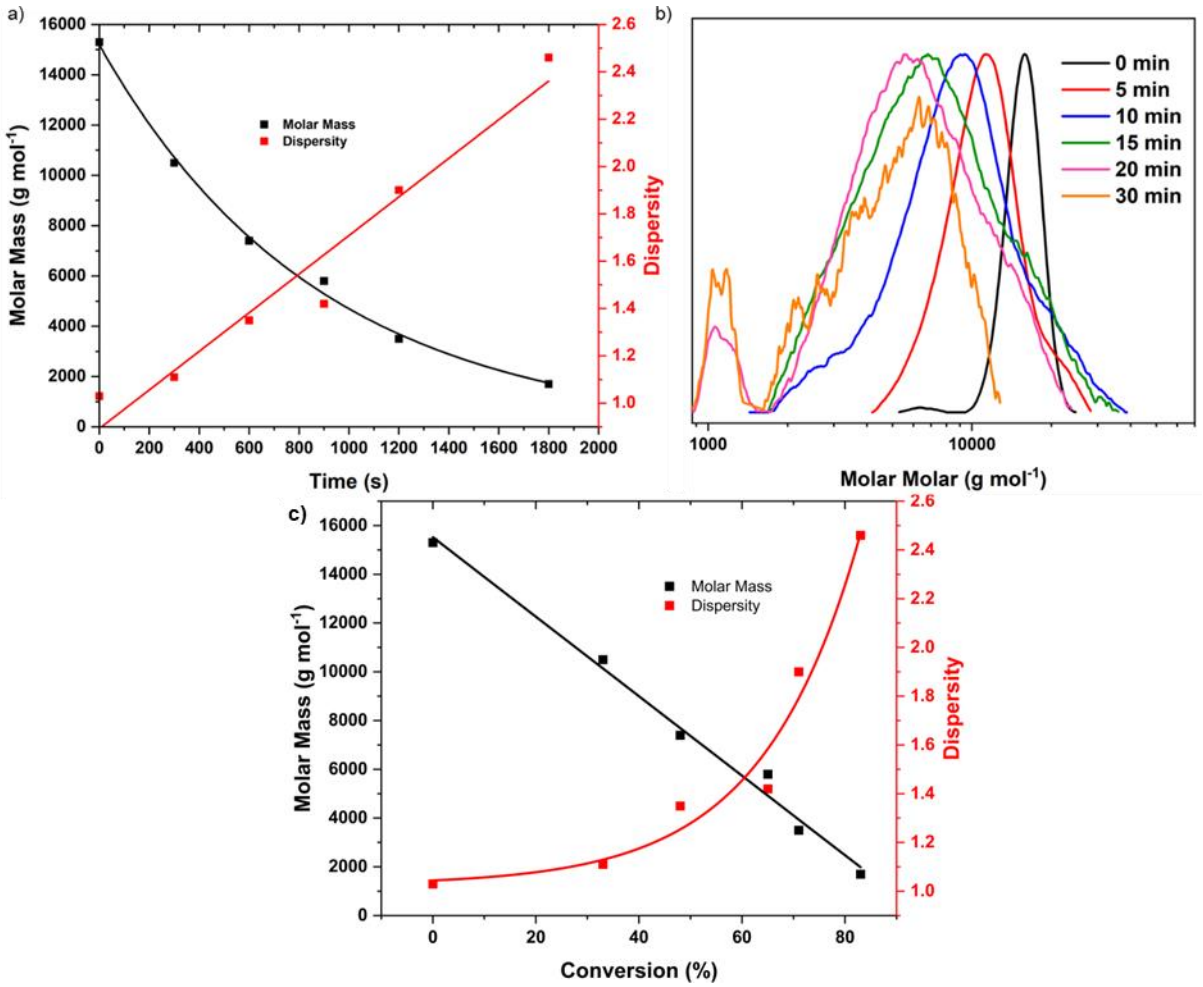
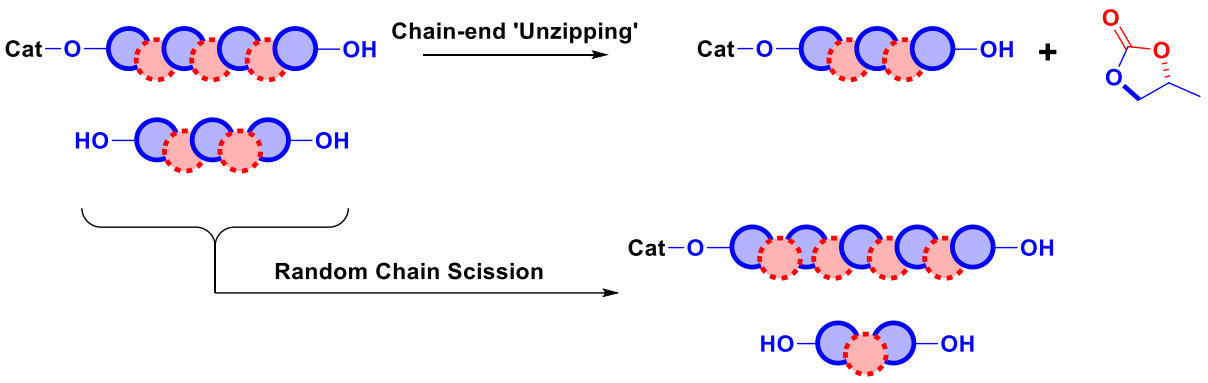


Figure 2.10 a) Molar mass and dispersity against time using catalyst **1**, at 45 °C. b) GPC traces of time points. c) Molar mass and dispersity against conversion using catalyst **1**, at 45 °C.

The increase in dispersity is an indication of random chain scission during the backbiting process and supports the kinetics which show a first order dependence on carbonate unit concentration. The random chain scission causes fragmentation of the polymer chains resulting in broadening of the dispersity over the course of the reaction (Fig. 2.10, Scheme 2.3). Conversely, a chain-end unzipping mechanism, i.e. where the catalyst attacks the carbonate unit nearest to the chain-end forming a polymer progressively one repeat unit smaller, shows a linear decrease in molar mass and narrow dispersity throughout the reaction (Scheme 2.3). Nonetheless, such a mechanism might indicate a zeroth order rate dependence on carbonate unit concentration, with rates dependent only on the chain end concentration which should remain constant throughout the reaction. However, this is not observed for catalyst **1**.



Scheme 2.3 Representation of chain-end 'unzipping' mechanism and random chain scission mechanism.

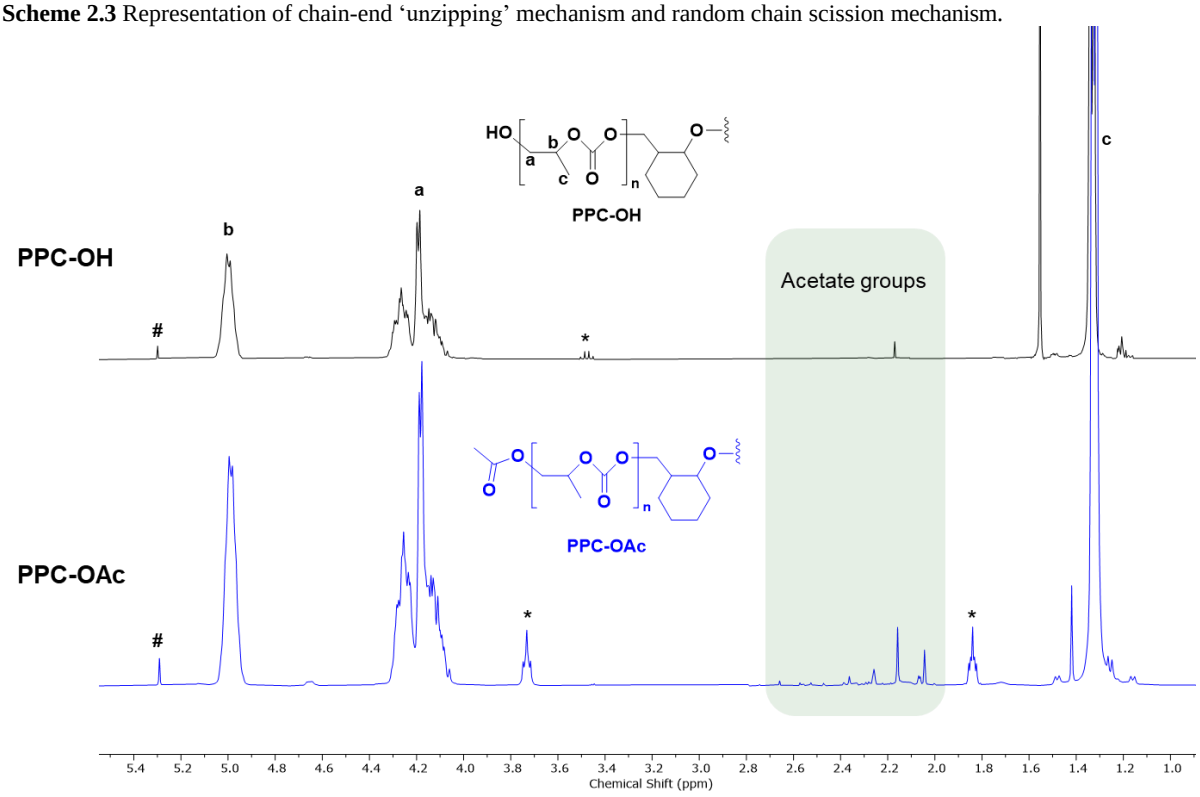


Figure 2.11 ^{1}H NMR spectrum ($CDCl_3$) of PPC-OH and end-capped PPC. *marks residual THF and Et_2O and # marks residual DCM.

To further study the random chain scission mechanism, the hydroxy-terminated PPC (PPC-OH) was end-capped with acetyl chloride to form α,ω-acetylated PPC (PPC-OAc), i.e. feature exclusively acetate end-groups (Fig. 2.11). In the ^{1}H NMR spectrum, the PPC-OH shows a small peak in the acetate region (highlighted in green) attributed to residual catalyst initiation. The PPC-OAc showed a series of acetate peaks in this region likely due to the regio-random and racemic PPC structure.

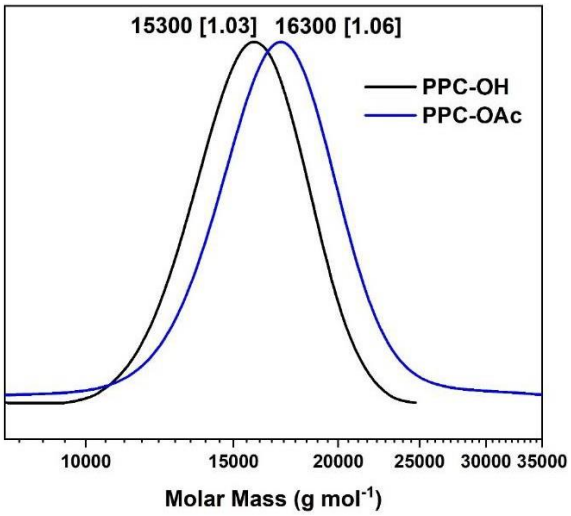


Figure 2.12 GPC traces of PPC-OH and PPC-OAc.

The PPC was not degraded by the end-capping, as shown by GPC (Fig. 2.12), where molar mass values remain very similar (small differences are expected).

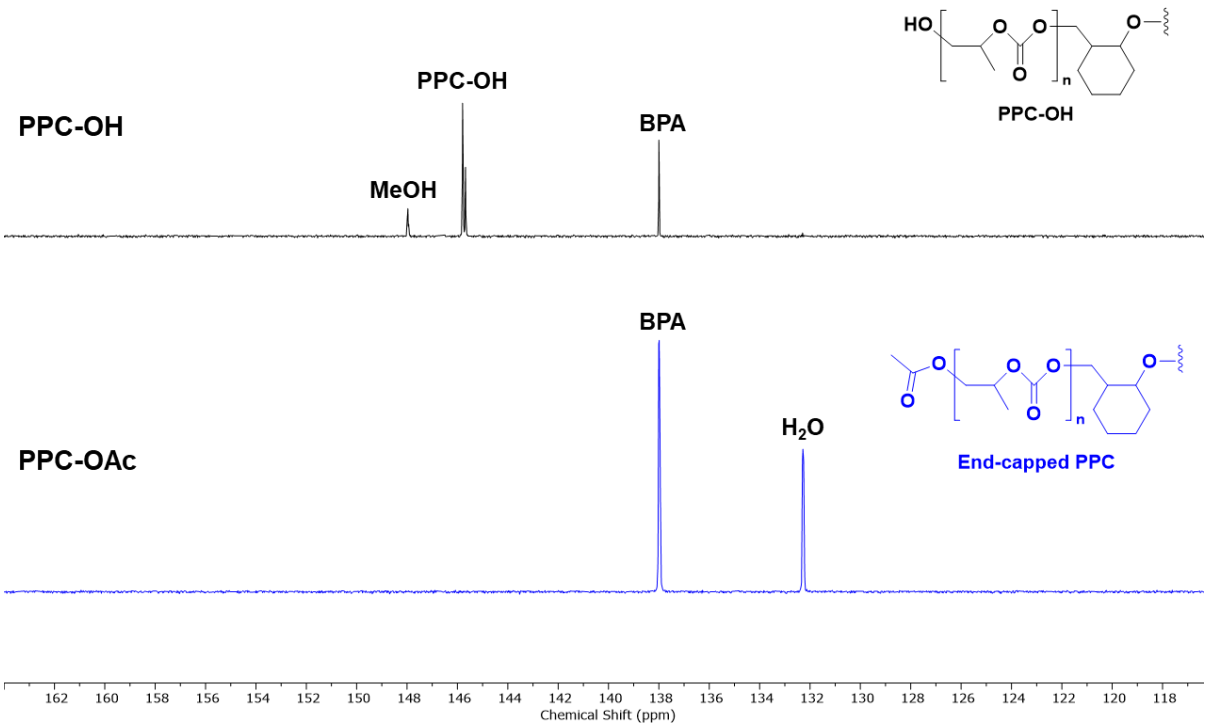


Figure 2.13 $^{31}P\{^{1}H\}$ NMR spectrum ($CDCl_3$) of PPC-OH and PPC-OAc using an end group titration.

The phosphorous end-group titration involves the reaction of the polymer end-groups with excess solution of 2-chloro-4,4,5,5-tetramethyldiozaphospholane. A solution of Bisphenol A (BPA) is added

as a calibrant to allow accurate comparison between different spectra.[25] The phosphorous end-group titration further supports the formation of PPC-OAc, it shows complete consumption of PPC-OH (Fig. 2.13).[8] Further evidence for PPC-OAc formation was provided by the thermal degradation experimental data. It is well known that end-capping polycarbonates (and other oxygenated polymers) improves the thermal stability, by preventing chain unzipping reactions.[26] For PPC-OH, the $T_{d,\,onset}$ was 217 °C, which is significantly lower than that of PPC-OAc, $T_{d,\,onset}$ of 261 °C (Fig. 2.14).

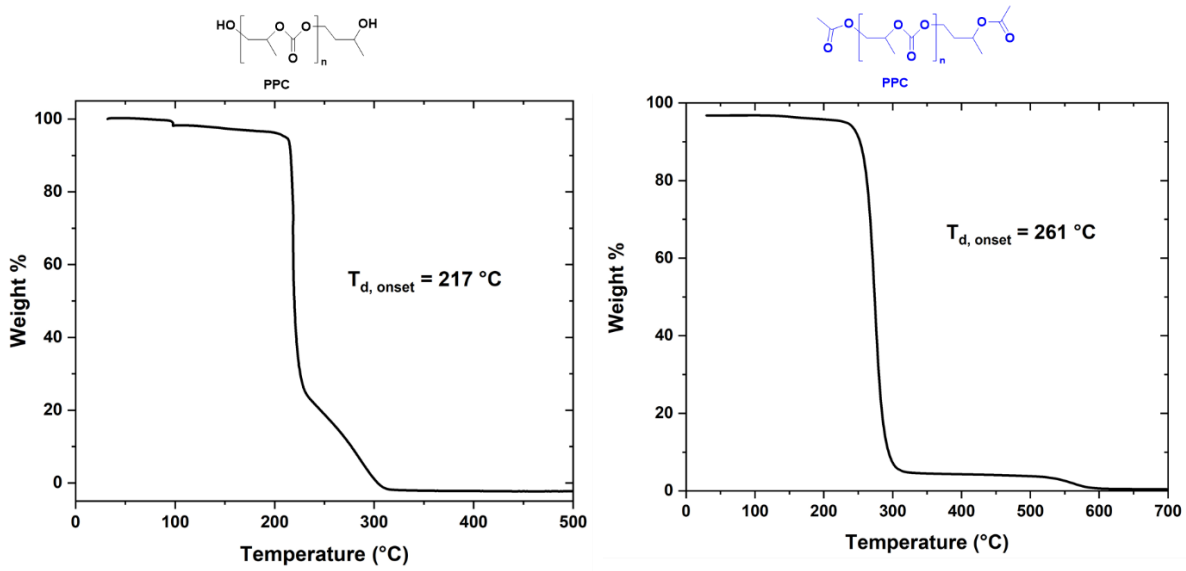


Figure 2.14 TGA data for PPC-OH and PPC-OAc.

The PPC-OAc was subjected to the catalysed backbiting reaction, under the same conditions as for PPC-OH (Fig. 2.15). The PPC-OAc showed complete degradation to PC. PPC-OAc showed slower rates of backbiting (taking over 30 times longer to fully convert). This was attributed to the lower amount of -OH chain-ends present at any given time, which are needed to actually form the alkoxide and hence cyclic carbonate. The experiment supports the random chain scission mechanism, rationalising the increase in dispersity throughout the reaction, but also confirming that both chain scission and backbiting require chain-ends with their concentration being a significant factor in determining rate.

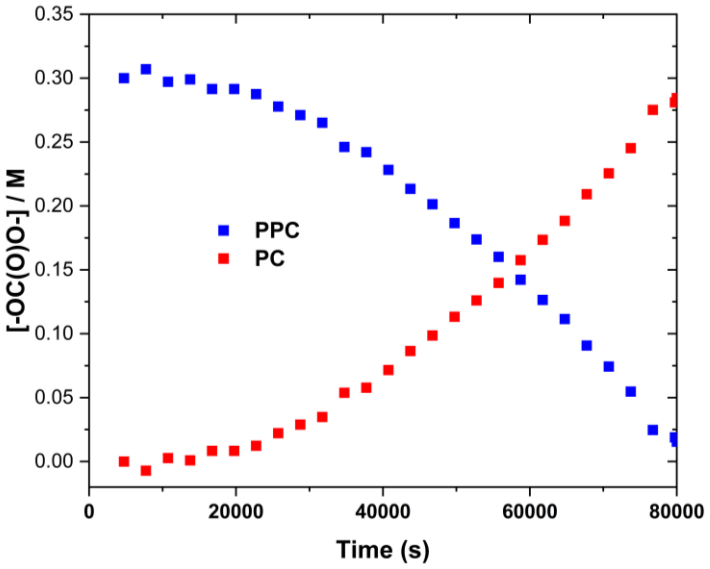
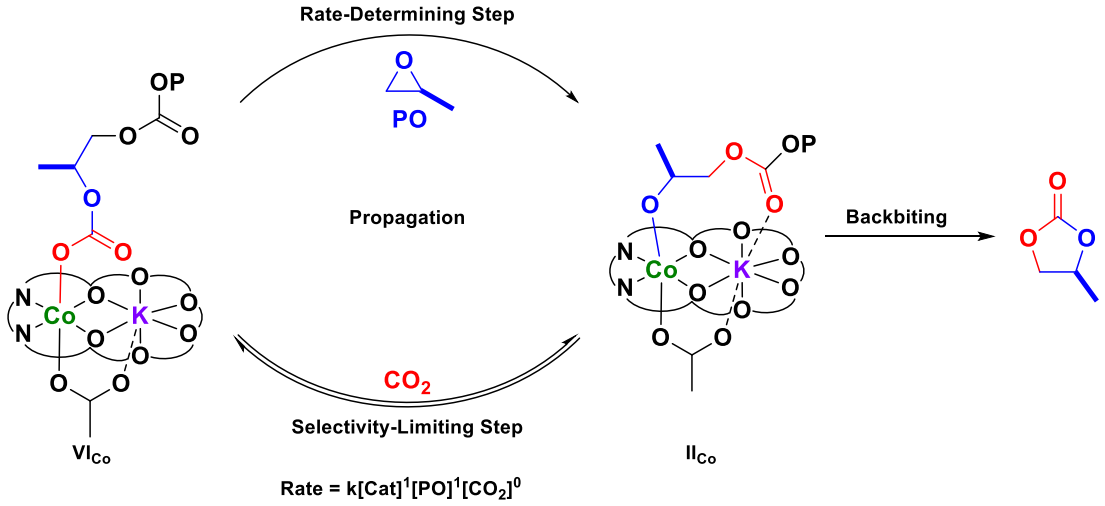


Figure 2.15 Plot showing the change in concentration of carbonate linkages (−OC(O)O−) in both PPC and PC against time using catalyst **1** and PPC-OAc, at 45 °C, obtained by *in situ* IR spectroscopy.

2.2.4 Limits of selectivity

The DFT calculations suggest that the barriers to the carbonation ($\mathbf{II_{Co}} \rightarrow \mathbf{VI_{Co}}$) and decarbonation ($\mathbf{VI_{Co}} \rightarrow \mathbf{II_{Co}}$) reactions are accessible under the conditions of polymerisation (16.2 and 20.0 kcal mol^{-1}, respectively). The difference in free energy between the alkoxide and carbonate intermediates, $\mathbf{II_{Co}}$ and $\mathbf{VI_{Co}}$, is also small ($\Delta G \sim 3.7$ kcal mol^{-1}), and the reaction system is sealed. These findings suggest the insertion of CO_2 into the cobalt-alkoxide bond is an equilibrium (Scheme 2.4).



Scheme 2.4 Illustration of the reaction equilibria of reversible CO_2 insertion between intermediates $\mathbf{II_{Co}}$ and $\mathbf{VI_{Co}}$.

To test this notion, the experimental conditions were moderated and changes to the PPC vs PC selectivity were monitored. At 30 bar CO_2 pressure and constant temperature (70 °C), the reaction

showed high polymer selectivity (>90%). As the pressure was decreased from 30 to 6 bar, at the same temperature (70 °C), the cyclic carbonate selectivity increased from 7 to 86% (Table 2.1).

Table 2.1 Pressure Dependence of the Polymer Selectivity for CO_2/PO Reaction using Catalyst **1**.[a]

Entry	CO_2 Pressure (bar)	CO_2 Concentration (M)[b]	Conversion (%)[c]	CO_2 selectivity (%)[d]	Polymer selectivity (%)[e]	Cyclic carbonate selectivity (%)	TOF (h^{-1})[f]
1	6	0.6	11	>99	14	86	277
2	10	1.3	23	>99	46	54	667
3[1]	20	2.8	30	>99	63	37	833
4[1]	30	4.3	28	>99	93	7	834

[a]Reaction conditions: 1 (3 mM), PO (6 mL), 1,2-cyclohexane diol (60 mM), 70 °C, 1.4 h. [b]Data supplied by ref 7.[27] [c]PO conversion determined from the relative integrals in the ^{1}H NMR spectrum of the resonances assigned to PPC (4.92 ppm, 1H), PC (4.77 ppm, 1H), and PPO (3.46−3.64 ppm, 3H) against mesitylene (6.70 ppm). [d]CO2 uptake (%) determined by the relative integrals in the ^{1}H NMR spectrum of the resonances assigned to (PPC + PC)/PPO. [e]Polym selectivity (%) determined by the relative integrals in the ^{1}H NMR spectrum of the resonances assigned to PPC/(PC + PPC). [f]Turn-over frequency (TOF) = TON/time (h).

These experimental observations are fully consistent with an insertion equilibrium since high pressures drive the equilibrium to the Co-carbonate intermediate, which does not undergo backbiting. Conversely, decreasing the carbon dioxide pressure, and so the concentration of CO_2 in solution, results in a lower concentration of $\mathbf{VI_{Co}}$. The lower carbonate intermediate concentration reduces the rate of polymer propagation and increases the concentration of the alkoxide intermediate, $\mathbf{II_{Co}}$. Since backbiting reactions are feasible from the alkoxide intermediate, increasing its concentration increases the selectivity for (and rate of) cyclic carbonate formation. The overall rate of propylene oxide consumption decreases with decreasing pressure and may be due to the competitive coordination of propylene carbonate vs propylene oxide.

Furthermore, a series of experiments changing the polymerisation temperature were used to test the equilibrium hypothesis. The polymerisation temperature was increased from 50 to 70 °C, at constant CO_2 pressure (20 bar). At higher temperatures, the formation of cyclic carbonate was favoured (7% at 50 °C vs 27% at 70 °C). This can also be rationalized as the insertion of CO_2 into the cobalt-alkoxide bond is exothermic ($\Delta H_{II\text{-}VI}$ = -5.4 kcal mol^{-1}), and an increase in temperature should decrease the equilibrium constant thereby increasing the concentration of $\mathbf{II_{Co}}$. In addition, the concentration of CO_2 dissolved in an epoxide, at a fixed pressure, decreases with increasing temperature, further driving the

equilibrium in favour of $\mathbf{II_{Co}}$. Finally, considering the entropic factors, as $\Delta S^{\ddagger} < 0$ for polymerisation, epoxide ring opening becomes less favoured with increasing temperature. In contrast, as $\Delta S^{\ddagger} > 0$ for the backbiting reaction, the formation of cyclic carbonate becomes more favoured with increasing temperature.

2.2.5 Discussion

The Co(III)K(I) catalyst is a rare example of a single site catalyst active for PO/CO_2 ROCOP and operating without any cocatalyst. There are very few other investigations into the PO/CO_2 ROCOP mechanism, the majority of studies apply DFT calculations to investigate individual steps, such as epoxide binding, CO_2 insertion, chain dissociation, or backbiting reactions, independent of the complete cycle.[28-33] One rationale for these "simplified" investigations is that the presence of the co-catalyst complicates the active site speciation.

There has been significantly more focus and success in CHO/CO_2 copolymerisation. This is likely because of the greater ring strain of CHO compared with PO, leading to higher rates of polymerisation.[34] Further, the formation of bicyclic carbonate (cyclohexene carbonate) has a high barrier to formation, thereby increasing selectivity in CHO/CO_2 ROCOP and enabling polymerisations at higher temperatures (>100 °C are typical).[35] Catalysts such as the Mg(II)Co(II) catalyst showed activities >12,000 h^{-1} for CO_2/CHO ROCOP (20 bar CO_2), but an activity of just 5 h^{-1} and a polymer selectivity of 2% when using propylene oxide essentially rendering it inactive for the copolymerisation.[36] Rieger and team reported a dinuclear "tethered" Zn-β-diimine catalyst showing an outstanding activity in CHO/CO_2 ROCOP (TOF = 155,000 h^{-1} , 100 °C, 30 bar), but it showed <1% selectivity for carbonate when using PO, producing mostly polyether.[37-38] Rieger and co-workers subsequently used DFT to investigate the differences in reactivity between CHO and PO using the di-Zn catalyst.[38] They suggested that the formation of a highly stable zinc alkoxide intermediate prohibited further reactivity. The insertion of carbon dioxide was proposed to become rate-determining, and both sequential propylene oxide insertion and backbiting to cyclic carbonate were proposed as competitive.

The di-Zn(II) alkoxide intermediate is proposed to be stabilized by a very close intermetallic distance of 3.58 Å, a value that is significantly lower than for the other calculated catalyst structures (5-6 Å). In

contrast, in this work the Co-alkoxide intermediate is comparatively less stable allowing for onward reactions to form PPC. The calculated metal-metal distances for intermediates $\mathbf{I_{Co}}$-$\mathbf{VI_{Co}}$ range between 3-4 Å, also supported in the solid-state structure, and thus short metal-metal distances are not in themselves a limitation to such catalysis. Rather, it appears that the K(I) plays a pivotal role in enhancing the reactivity of the alkoxide intermediate, perhaps through its weaker chelation to the polymer chain compared with metals like Zn(II) or Mg(II), which fail to catalyse PO/CO_2 ROCOP.

It is clear from this work that generally, catalyst design has perhaps been "overly focussed" on attempting to reduce the epoxide ring-opening barrier rather than also considering the intermediate stability as well as their importance to side reactions. With this system, and likely others, when using propylene oxide, it is imperative to control the relative stability of the alkoxide intermediate and the CO_2 insertion equilibrium. These aspects are likely to be controlled by both the catalyst structure and by the process conditions. In the best-case scenario, the transition state for epoxide ring opening has a low barrier, the catalyst-alkoxide intermediate is relatively destabilized compared with other intermediates, and the carbon dioxide insertion equilibrium favours the catalyst-carbonate intermediate.

2.3 Conclusion and Outlook

A full mechanistic exploration of the ring-opening copolymerisation of PO/CO_2 using a Co(III)K(I) (**1**) complex was performed, with a specific focus on cyclic carbonate formation and understanding of insertion processes. The DFT, supported by experimental results, showed that the rate determining step involves epoxide coordination at the Co(III) centre, with K(I) providing the carbonate nucleophile.

Further understanding was gained in the cyclic carbonate formation which is the only side reaction observed experimentally, with a new method of finding the backbiting barrier presented. It was found that the barrier to cyclic carbonate was similar to that for propagation, selectivity is therefore determined by the CO_2 insertion equilibrium between the alkoxide and the carbonate intermediates.

This mechanism and understanding will inform future catalyst design specifically moving focus away from propagation and towards selectivity concerns. This is applied in Chapter 3.

2.4 References

1. Deacy, A. C.; Moreby, E.; Phanopoulos, A.; Williams, C. K., *J. Am. Chem. Soc.* **2020,** *142*, 19150-19160.
2. Frisch, M. J.; Trucks, G. W.; Schlegel, H. B.; Scuseria, G. E.; Robb, M. A.; Cheeseman, J. R.; Scalmani, G.; Barone, V.; Petersson, G. A.; Nakatsuji, H.; Li, X.; Caricato, M.; Marenich, A. V.; Bloino, J.; Janesko, B. G.; Gomperts, R.; Mennucci, B.; Hratchian, H. P.; Ortiz, J. V.; Izmaylov, A. F.; Sonnenberg, J. L.; Williams; Ding, F.; Lipparini, F.; Egidi, F.; Goings, J.; Peng, B.; Petrone, A.; Henderson, T.; Ranasinghe, D.; Zakrzewski, V. G.; Gao, J.; Rega, N.; Zheng, G.; Liang, W.; Hada, M.; Ehara, M.; Toyota, K.; Fukuda, R.; Hasegawa, J.; Ishida, M.; Nakajima, T.; Honda, Y.; Kitao, O.; Nakai, H.; Vreven, T.; Throssell, K.; Montgomery Jr., J. A.; Peralta, J. E.; Ogliaro, F.; Bearpark, M. J.; Heyd, J. J.; Brothers, E. N.; Kudin, K. N.; Staroverov, V. N.; Keith, T. A.; Kobayashi, R.; Normand, J.; Raghavachari, K.; Rendell, A. P.; Burant, J. C.; Iyengar, S. S.; Tomasi, J.; Cossi, M.; Millam, J. M.; Klene, M.; Adamo, C.; Cammi, R.; Ochterski, J. W.; Martin, R. L.; Morokuma, K.; Farkas, O.; Foresman, J. B.; Fox, D. J. *Gaussian 16 Rev. C.01*, Wallingford, CT, 2016.
3. Chai, J. D.; Head-Gordon, M., *J. Chem. Phys.* **2008,** *128*, 084106.
4. Alipour, M.; Fallahzadeh, P., *Phys. Chem. Chem. Phys.* **2016,** *18*, 18431-18440.
5. Becke, A. D., *J. Chem. Phys.* **1993,** *98*, 5648-5652.
6. Lee, C.; Yang, W.; Parr, R. G., *Phys Rev B Condens Matter* **1988,** *37*, 785-789.
7. Grimme, S.; Ehrlich, S.; Goerigk, L., *J. Comput. Chem.* **2011,** *32*, 1456-1465.
8. Becke, A. D.; Johnson, E. R., *J. Chem. Phys.* **2005,** *123*, 154101.
9. Zhao, Y.; Truhlar, D., *Theor. Chem. Acc.* **2008,** *120*, 215-241.
10. Grimme, S.; Antony, J.; Ehrlich, S.; Krieg, H., *J. Chem. Phys.* **2010,** *132*, 154104.
11. Perdew, J. P.; Burke, K.; Ernzerhof, M., *Phys. Rev. Lett.* **1996,** *77*, 3865-3868.
12. Adamo, C.; Barone, V., *J. Chem. Phys.* **1999,** *110*, 6158-6170.
13. Glendening, E. D.; Landis, C. R.; Weinhold, F., *J. Comput. Chem.* **2013,** *34*, 2134-2134.
14. AIMAll (Version 13.10.19), Keith, T. A. TK Gristmill Software, Overland Park, KS, USA (2013) (aim.tkgristmill.com).
15. Johnson, E. R.; Keinan, S.; Mori-Sánchez, P.; Contreras-García, J.; Cohen, A. J.; Yang, W., *J. Am. Chem. Soc.* **2010,** *132*, 6498-6506.
16. Barone, V.; Cossi, M., *The Journal of Physical Chemistry A* **1998,** *102*, 1995-2001.
17. Luchini, G.; Alegre-Requena, J.; Funes-Ardoiz, I.; Paton, R., *F1000Research* **2020,** *9*.
18. Foltran, S.; Cloutet, E.; Cramail, H.; Tassaing, T., *J. Supercrit. Fluids* **2012,** *63*, 52–58.
19. Buchard, A.; Jutz, F.; Kember, M. R.; White, A. J. P.; Rzepa, H. S.; Williams, C. K., *Macromolecules* **2012,** *45*, 6781-6795.
20. Klaus, S.; Lehenmeier, M. W.; Anderson, C. E.; Rieger, B., *Coord. Chem. Rev.* **2011,** *255*, 1460-1479.
21. S, S.; Min, J. K.; Seong, J. E.; Na, S. J.; Lee, B. Y., *Angew. Chem. Int. Ed.* **2008,** *47*, 7306-7309.
22. Na, S. J.; S, S.; Cyriac, A.; Kim, B. E.; Yoo, J.; Kang, Y. K.; Han, S. J.; Lee, C.; Lee, B. Y., *Inorg. Chem.* **2009,** *48*, 10455-10465.
23. Darensbourg, D. J.; Rodgers, J. L.; Mackiewicz, R. M.; Phelps, A. L., *Catal. Today* **2004,** *98*, 485-492.
24. Lu, X.-B.; Shi, L.; Wang, Y.-M.; Zhang, R.; Zhang, Y.-J.; Peng, X.-J.; Zhang, Z.-C.; Li, B., *J. Am. Chem. Soc.* **2006,** *128*, 1664-1674.
25. Spyros, A.; Argyropoulos, D. S.; Marchessault, R. H., *Macromolecules* **1997,** *30*, 327-329.
26. Hauenstein, O.; Reiter, M.; Agarwal, S.; Rieger, B.; Greiner, A., *Green Chem.* **2016,** *18*, 760-770.
27. Foltran, S.; Cloutet, E.; Cramail, H.; Tassaing, T., *J. Supercrit. Fluids* **2012,** *63*, 52-58.
28. Luinstra, G. A.; Haas, G. R.; Molnar, F.; Bernhart, V.; Eberhardt, R.; Rieger, B., *Chem. Eur. J.* **2005,** *11*, 6298-314.
29. Wu, T.; Wang, T.; Sun, L.; Deng, K.; Deng, W.; Lu, R., *ChemistrySelect* **2017,** *2*, 4533-4537.
30. Santiago-Rodríguez, Y.; Curet-Arana, M. C., *React. Kinet. Mech. Catal.* **2015,** *116*, 351-370.
31. Offermans, W. K.; Bizzarri, C.; Leitner, W.; Muller, T. E., *Beilstein J. Org. Chem.* **2015,** *11*, 1340-51.
32. Drees, M.; Cokoja, M.; Kühn, F. E., *ChemCatChem* **2012,** *4*, 1703-1712.
33. Adhikari, D.; Nguyen, S. T.; Baik, M. H., *Chem. Commun.* **2014,** *50*, 2676-8.
34. Liu, Z.; Torrent, M.; Morokuma, K., *Organometallics* **2002,** *21*, 1056-1071.
35. Singer, F. N.; Deacy, A. C.; McGuire, T. M.; Williams, C. K.; Buchard, A., *Angew. Chem. Int. Ed.* **2022,** *61*, e202201785.
36. Deacy, A. C.; Kilpatrick, A. F. R.; Regoutz, A.; Williams, C. K., *Nat. Chem.* **2020,** *12*, 372-380.
37. Kissling, S.; Lehenmeier, M. W.; Altenbuchner, P. T.; Kronast, A.; Reiter, M.; Deglmann, P.; Seemann, U. B.; Rieger, B., *Chem. Commun.* **2015,** *51*, 4579-4582.
38. Kissling, S.; Altenbuchner, P. T.; Lehenmeier, M. W.; Herdtweck, E.; Deglmann, P.; Seemann, U. B.; Rieger, B., *Chem. Eur. J.* **2015,** *21*, 8148-8157.

Chapter 3

Effect of Catalyst Ligand Backbone in Heterodinuclear Catalysts for PO/CO_2 ROCOP

3.1 Introduction and Aims

Elucidation of structure-activity relationships is central to catalysis, materials science, drug efficacy, sensing and many more applications.[1-5] It is the underpinning ethos of polymerisation catalysis but, partly because such catalysts must be applied at very low loadings, deconvoluting these relationships remains very demanding. Studies of catalysts in the solid state or more concentrated solutions often fail to reveal catalyst structure-activity, -selectivity, -stereoselectivity, or polymer composition relationships.

Structural activity relationships have been studied throughout the history of chemistry. One of the most widely used and applied, particularly to organic chemistry reactions, is the Hammett Parameter.[6] Its foundations lay in the ionization of aromatic organic acids to establish the substituent effect on pK_a of the acid. The change in pK_a can then be correlated to the effect the substituent has on the electronics of the system and hence its potential effect on reactions.[6] A refinement of this approach is the Swain-Lupton equation which splits the contribution of substituents into field and resonance effect allowing for more detailed understanding of the individual effects.[7] Others have looked more towards the effect on ligand binding to metals. The Tolman electronic parameter is a measure of the electron donating or withdrawing ability of a ligand. It is determined by measuring the frequency of C-O vibration of carbon monoxide bound to a Ni(0) complex with the effect of various ligands on this vibrational mode relative to the tetra-carbonyl complex.[8] A related method, the Guntmann-Beckett method, measures the Lewis acidity of the molecular species. This is done by using triethylphosphine oxide as a probe molecule and evaluating the resulting complex by ^{31}P-NMR spectroscopy.

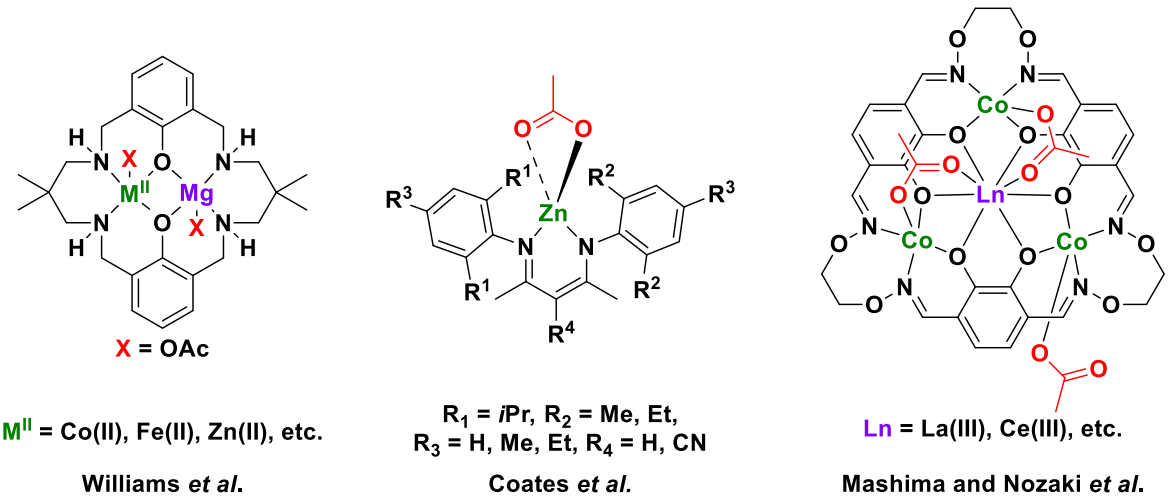


Figure 3.1 Structures of selected literature catalysts.[6-10]

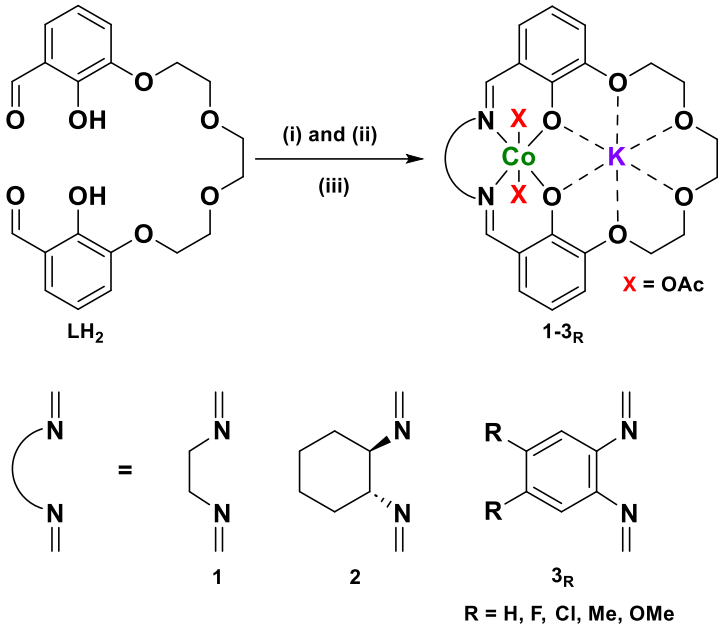
Focussing on CO_2/epoxide ROCOP catalysis, our team investigated heterodinuclear catalysts M(II)Mg(II), where M= first row transition metals(II) from Cr(II) to Zn(II); these showed a range of activities but there were no correlations between physical parameters, such as active site metal salt ionic radius, Lewis acidity or ligand substituent Hammett parameters, and catalytic performance (Fig. 3.1).[10] Similarly, Mashima, Nozaki and co-workers efficient Ln_3(III)/Co(II) catalysts, where Ln(III) = La(III), Ce(III), etc., but without any clear trends in catalyst structures/properties and polymerisation activity (Fig. 3.1).[11-12] Coates and co-workers established one type of structure-activity relationship – the importance of dinuclear active sites. Investigations of the ground-breaking Zn(II)-diiminate catalysts for cyclohexene oxide/CO_2 ROCOP revealed that the best catalysts were loosely associated dimers in solution; this important discovery motivated many subsequent investigations of dinuclear catalysts (Fig. 3.1).[13] Rieger and co-workers investigated heterogeneous zinc carboxylate catalysts: activity was computed to depend upon Zn-Zn separations on the catalyst surface, although care must be taken since heterogeneous surfaces and crystallinities are highly variable.[15] Our team introduced heterodinuclear catalysts to this field and in 2020 reported upon the physical chemistry underpinning heterodinuclear synergy using Co(II)Mg(II) catalysts for carbon dioxide/cyclohexene ROCOP. Eyring analyses revealed that the metals act together but with different functions: Co(II) reduces the transition state enthalpy barrier and Mg(II) reduces the transition state entropy barrier (Fig. 3.1).[14] Aside from targeting (hetero)dinuclear catalyst structures there is not yet any detailed structure-activity understanding in this field of polymerisation catalysis. The best process for catalyst design involves combing experimental

polymerisation kinetics with DFT calculations to propose a polymerisation mechanism. There have been attempts to correlate activity with computed catalyst parameters. A stand-out example, from Nozaki, Mori and co-worker, is the discovery of a linear correlation between computed difference between bond dissociation energies of metal-carbonate and metal-epoxide intermediates and activity.[16] These relationships, however, only applied to a specific class of (planar, tetradentate ligand)M/PPNCl catalyst systems, where M = Cr(III), Co(III), Ti(IV), Ge(IV). Several researchers have examined structure-activity relationships in tethered borane-'onium' catalysts and there is agreement that the 'tether' length is important, with a C5 linker emerging as the best.[17-21] Nonetheless, Lin and co-workers did not find any correlation between the measured Lewis acidity (of the borane) and the catalytic activity in cyclohexene oxide/carbon dioxide ROCOP; rather activity was dependent upon careful balancing of enthalpic and entropic factors.[17] Thus, there remains a clear need to better understand the steric and electronic features of the catalyst that result in the highest activity and selectivity

The aim of this work is to explore the electronic impact of the ligand, by the introduction of various substituents, including conventionally 'termed' electron withdrawing groups (EWG), like F and Cl, or electron donating groups (EDG), such as Me and OMe. The goal is to understand the influences on the ROCOP catalysis.

A series of heterobimetallic Co(III)K(I) complexes featuring a macrocyclic ligand with two distinct binding moieties were synthesised. The ligand features a tetradentate Schiff base to coordinate the Co(III) and a tetracrown-ether moiety for selective binding of the K(I). In this chapter, complexes featuring different ligand backbones are prepared and are characterised *via* NMR, IR spectroscopy and cyclic voltammetry (CV) and, where possible, X-ray crystallography. The backbones were chosen to vary the electronic properties of the ligand whilst being readily accessible in 1-2 synthesis steps.[22-23] Note that complex **1** has been previously reported and was discussed in Chapter 2.[24] These complexes will be investigated for ROCOP of PO and CO_2, both to benchmark them and allow for investigation of the effect of the electronics on catalysis.

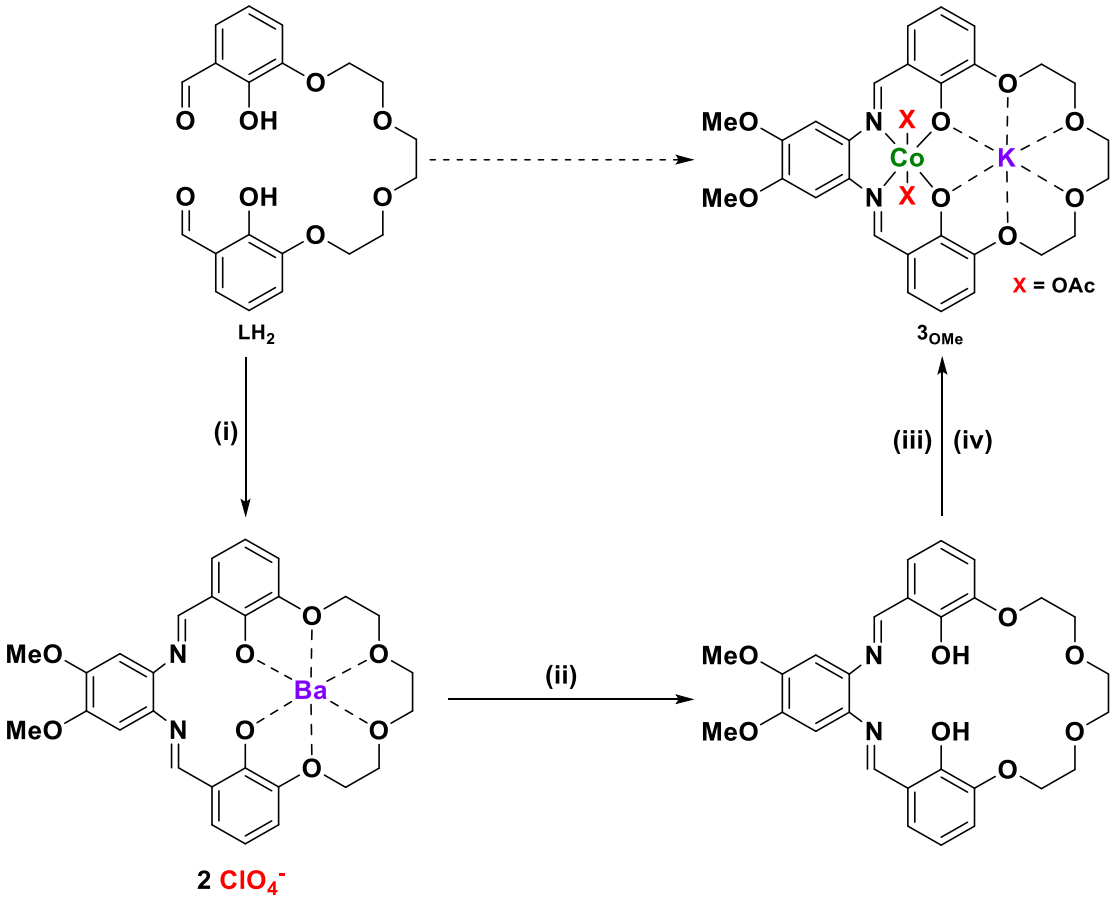
3.2 Synthesis and Characterisation of Heterobimetallic Co(III)K(I) Complexes



Complex	Yield (%)
1	74
2	68
3_{Me}	52
3_{OMe}	27
3_{H}	42
3_{F}	9
3_{Cl}	45

Scheme 3.1 Synthesis of complexes **1-3$_R$** from **LH$_2$**. (i) KOAc, $Co(OAc)_2$, MeCN, 25 °C, 30 min, N_2 (ii) Diamine, MeCN, 25 °C, 16 h, N_2 (iii) AcOH, air, MeCN, 48 h. **3$_{OMe}$**: (i) $Ba(ClO_4)_2$, MeCN, 25 °C then diamine, 24 h (ii) Guanidinium Sulfate, $H_2O/CHCl_3$, 25 °C, 16 h (iii) KOAc, $Co(OAc)_2$, MeCN, 25 °C, 16 h, N_2 (iv) AcOH, air, MeCN, 48 h.

The ligand precursor, LH_2, was purchased commercially and is a light-yellow powder. Complexes **1-3$_R$** were synthesized by modification of the previously reported procedure (Scheme 3.1).[24] An equivalent of potassium(I) acetate and cobalt(II) acetate were added to a solution of the ligand precursor (**LH$_2$**). The mixture was stirred for 30 min, at room temperature, before the addition of the appropriate diamine. The solution was then left to stir for 16 h, exposed to air and an equivalent of acetic acid was added to oxidize the Co(II) centre to Co(III). The Co(III)K(I) complexes (**1-3$_R$**) were isolated good yields (Scheme 2.1 and experimental section, chapter 5, for more details on the syntheses). The fluorine substituents on the phenylene ring of **3$_F$** disfavour the Co(II) oxidation. Catalyst **3$_F$** had a particularly low yield due to its Co(II) oxidation and hence required separation of the product from the Co(II)K(I).



Scheme 3.2 Synthesis of complexes $\mathbf{3_{OMe}}$ from $\mathbf{LH_2}$. (i) $Ba(ClO_4)_2$, MeCN, 25 °C then diamine, 24 h (ii) Guanidinium Sulfate, $H_2O/CHCl_3$, 25 °C, 16 h (iii) KOAc, $Co(OAc)_2$, MeCN, 25 °C, 16 h, N_2 (iv) AcOH, air, MeCN, 48 h.

For complex $\mathbf{3_{OMe}}$, on the other hand, the starting diamine and aldehyde react very slowly and only reach low conversions of the macrocycle using the method for the other complexes (Scheme 3.1). To circumvent this issue the free macrocyclic ligand was isolated first, using a previously reported procedure, where barium perchlorate is used as a templating agent to drive the ring-closure (Scheme 3.2). The isolated macrocycle was then reacted sequentially with the metal salts forming the desired complex.[25]

All complexes were diamagnetic due to the octahedral coordination with low spin d^6 electron configuration adopted by Co(III). Thus, the novel complexes were all characterized by solution-phase NMR spectroscopy. The complexes were all further characterised by IR spectroscopy and cyclic voltammetry. As complex **1** has been previously reported, the characterisation data will not be presented here.[24]

3.2.1 NMR Spectroscopy

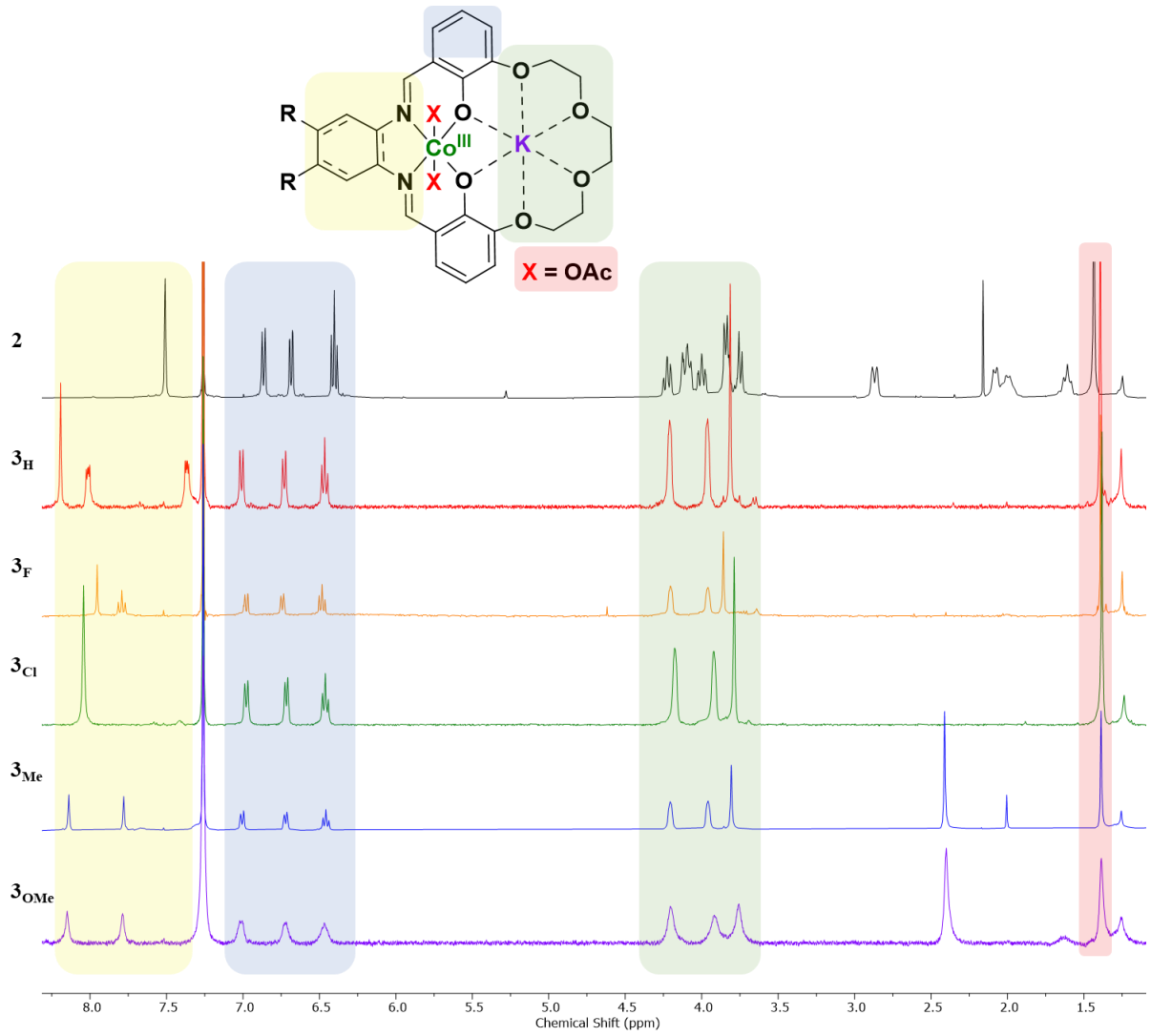


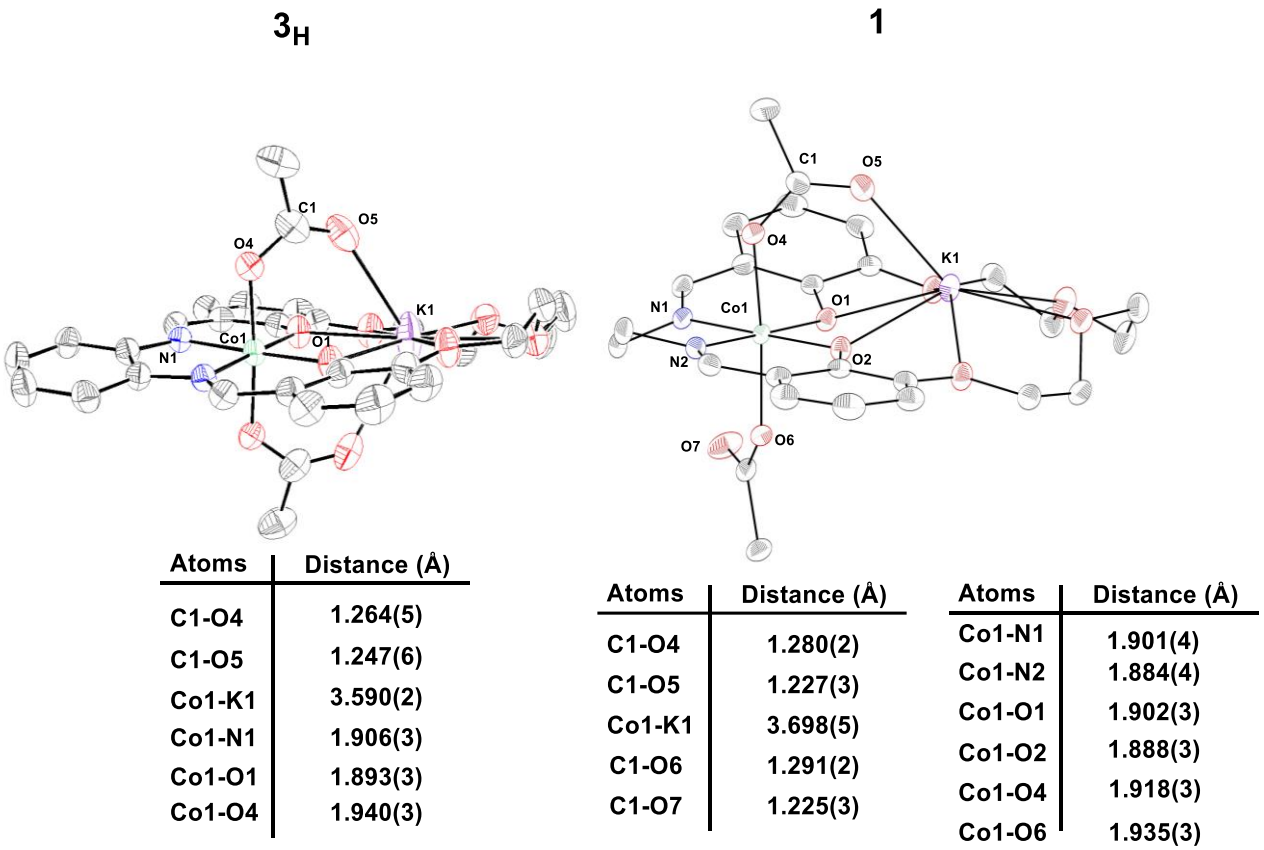
Figure 3.2 ^{1}H NMR spectra ($CDCl_3$, 298 K) spectra of **2-3$_R$** (integrated individual spectra in appendix: Fig. S3.1–S3.31).

^{1}H NMR spectra showed diagnostic imine resonance with no aldehyde or alcohol species detected. This suggests the formation of the complexes (Fig. 3.2, S3.1-S3.31). Each complex has a characteristic imine chemical shift between 7.40 and 8.25 ppm.

The complexes have 4 characteristic regions: imine and backbone aromatic peaks (yellow), alkoxide aromatic peaks (blue), ether region (green) and acetate region (red) (Fig. 3.2). Differences between the complexes can be observed in all of these regions, especially in the imine chemical shift. The cyclohexene complex **2** has characteristic splitting in the ether region (green) as well as on its single enantiomer *R,R*-cyclohexane backbone, showing 8 multiplets in the region of 1.5-4.5 ppm.

Interestingly, **2** also has the lowest imine chemical shift, likely because there is no backbone ligand conjugation. In contrast, the complexes with phenylene backbones ($\mathbf{3_R}$) show an increased imine chemical shift and distinct aromatic peaks in the same region (yellow, Fig. 3.2). Their phenoxide, ether and acetate resonances are all virtually identical, presumably due to their distance from the phenylene substituents (Fig. 3.2). They all show two doublets and one asymmetrical pseudo triplet in the phenoxide region. Furthermore, the ether regions for these complexes are characterised by three singlets of equivalent integration showing the fluxionality of the crown ether and highlighting the C_2 symmetry in the complexes. Interestingly, in complex $\mathbf{3_{Cl}}$ the aromatic backbone peak overlaps with the imine peak leading to one singlet with a higher integration. For $\mathbf{3_F}$, the phenylene protons couple to the fluorines resulting in a triplet, in both the ^{1}H and ^{19}F NMR spectra (Fig. S21 and S26).

3.2.2 X-ray Crystallography



Atoms	Distance (Å)
C1-O4	1.264(5)
C1-O5	1.247(6)
Co1-K1	3.590(2)
Co1-N1	1.906(3)
Co1-O1	1.893(3)
Co1-O4	1.940(3)

Atoms	Distance (Å)
C1-O4	1.280(2)
C1-O5	1.227(3)
Co1-K1	3.698(5)
C1-O6	1.291(2)
C1-O7	1.225(3)

Atoms	Distance (Å)
Co1-N1	1.901(4)
Co1-N2	1.884(4)
Co1-O1	1.902(3)
Co1-O2	1.888(3)
Co1-O4	1.918(3)
Co1-O6	1.935(3)

Figure 3.3 Molecular structures (determined by X-ray diffraction, H-atoms omitted for clarity, thermal ellipsoids at 50% probability) of complexes **1** and $\mathbf{3_H}$. Selected bond lengths are shown with complete bond lengths and angles, with crystallographic refinement data, presented in Tables S3.1.[24]

Single crystals, suitable for X-ray diffraction, of complex $\mathbf{3_H}$ was obtained from slow evaporation of pentane into DCM. The crystal structure of complex **1** has been previously reported and is presented for clarity and comparison.[24]

The complexes possess monomeric structures in the solid state (Fig. 3.2). Complex **1** has C_1 symmetry, with a 6-coordinate, distorted octahedral geometry around the Co(III) centre. The asymmetrical acetate C-O bond lengths and the dative carbonyl-K(I) bond suggests the Co(III) is a 'cobalt-ate' type, i.e., formally negatively charged (Fig. 3.3). The K(I) centre in complex **1** is 7-coordinate, with a distorted hexagonal pyramid geometry. In comparison, complex $\mathbf{3_H}$ possesses C_2 symmetry, with the K(I) centre being 8-coordinate. The Co(III) centre also has 6-coordinate, distorted octahedral geometry, but does not have the same -ate character. This complex has two bridging acetates, while **1** has one bridging and one terminal acetate in its solid structure likely due to the rigidity of the phenyl backbone. By ^{1}H NMR spectroscopy, both complexes have a single acetate resonances showing fluxional binding modes when put in context of the crystallographic data. Furthermore, there are also varying intermetallic distances between the complexes, with complex $\mathbf{3_H}$ having the Co(III) and K(I) closer together (3.590(2) *versus* 3.698(5) Å).

3.2.3 Infrared Spectroscopy

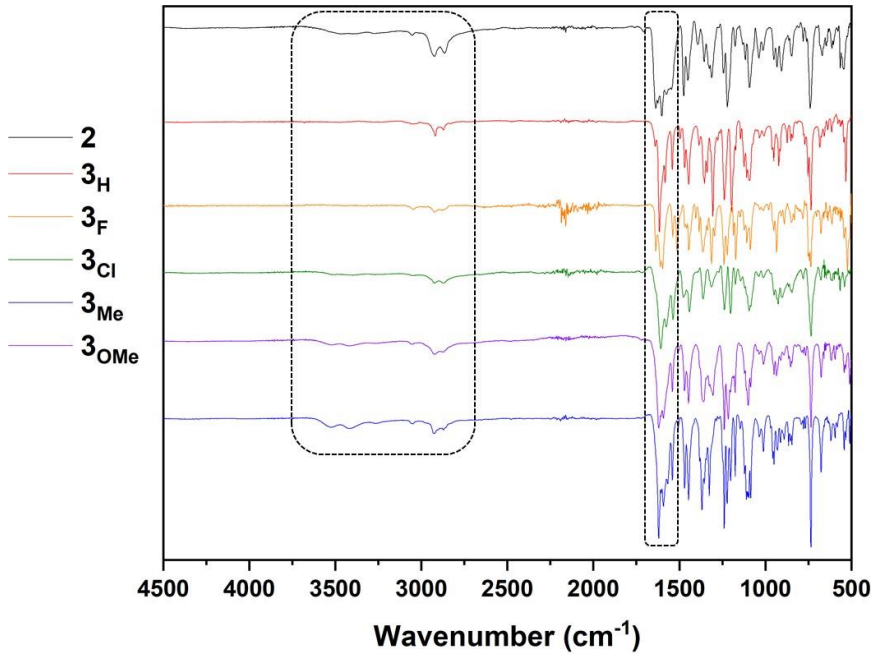


Figure 3.4 Stacked IR spectra of complexes **2**-$\mathbf{3_R}$ (Fig. S3.32).

The complexes show IR spectra consistent with the structures indicated by NMR spectroscopic- and XRD-data (Fig. 3.3). The complexes all show broad aromatic C-H stretches, between 3650 – 2800 cm^{-1}, and acetate C=O and imine C=N stretches, in the region of 1700 – 1500 cm^{-1}. Most complexes show three peaks in this region corresponding to the symmetric and asymmetric acetate stretch and imine resonance. The exception is **2**, which shows significant imine resonance broadening, perhaps as a result of the adjacent chiral centres on the ligand backbone.

3.2.4 Cyclic Voltammetry

Cyclic voltammetry measurements were obtained for all complexes, **2**-$\mathbf{3_R}$. All cyclic voltammetry (CV) experiments were performed in acetonitrile, in a glove box, under inert atmosphere and at ambient temperature. The concentration of the complexes were 1.6 mM and a scan rate of 0.1 V/s, from -1.5 to 1.5 V, was applied to all complexes. All spectra are referenced *versus* ferrocene.

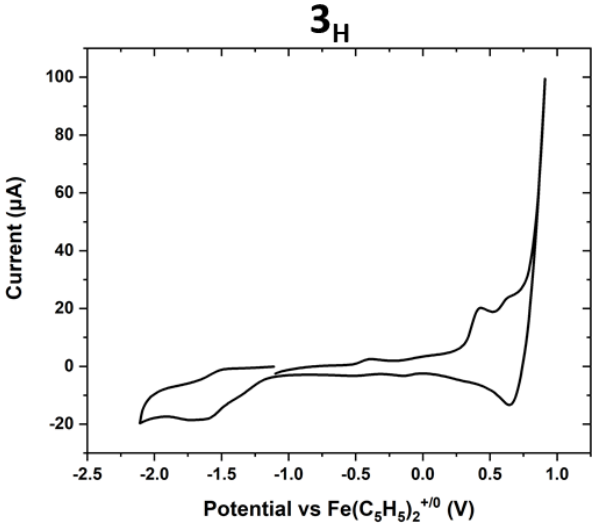


Figure 3.5 Cyclic voltammogram of $\mathbf{3_H}$.

All complexes show broadly similar data with Co(III/II) and Co(II/I) redox potential values consistent with other Co(III) complexes.[22] For example $\mathbf{3_H}$, shows two-metal based reversible transitions, at -1.65 V and -0.48 V, and an irreversible reduction just below 0.0 V, assigned to a ligand aromatic reduction, it's notable this transition is not observed in **1** and **2** (Fig. 3.5 and S3.33). The ligand reduction shifts and overlaps with the Co(III/II) transition for complexes $\mathbf{3_F}$ and $\mathbf{3_{Cl}}$ resulting in broadening of the peaks. $\mathbf{3_F}$ is the only complex which shows an irreversible Co(II/I) reduction.

Table 3.1 Summary of Electrochemical Data for Complexes **1-3$_R$**.[a]

Cat.	E_{Red} Co(II/I) (V)	$E_{1/2}$ Co(II/I) (V)	$E_{1/2}$ Co(III/II) (V)
1	-1.68	-1.65	-0.53
2	-1.70	-1.66	-0.46
3$_{Me}$	-1.61	-1.52	-0.37
3$_{OMe}$	-1.69	-1.64	-0.41
3$_H$	-1.72	-1.65	-0.48
3$_F$	-1.55	-	-0.16
3$_{Cl}$	-1.54	-1.49	-0.24

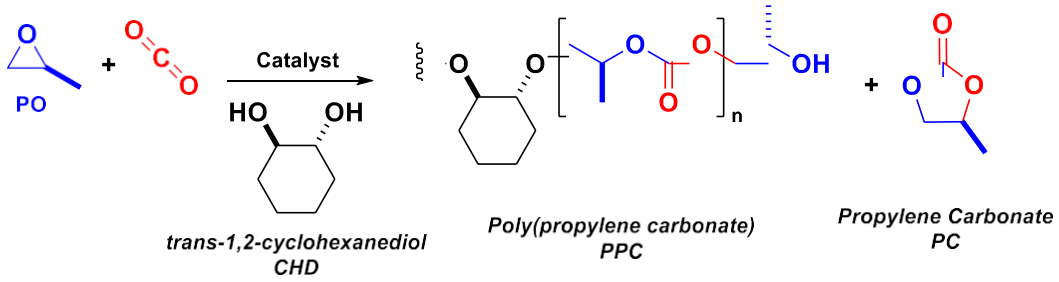
[a]Reduction potentials in acetonitrile referenced to ferrocene/ferrocenium.

Interestingly, of the phenylene series (**3$_R$**) **3$_H$** has the lowest Co(III/II) redox potential showing it has the most electron rich Co(III) (Table 3.1). This is contrary to what might be expected for these complexes using conventional ligand Hammett parameter. The -OMe and -Me groups are conventionally viewed as electron donating and thus might be expected to result in a more electron rich Co(III). However, in this system they appear to be weakly electron withdrawing resulting in a lower redox potential for the Co(III/II). The same trend is observed for the reduction potential of the Co(II/I) transition for these complexes. As expected, the -F and -Cl groups are still strongly electron withdrawing. Conversely, **1** has the lowest Co(III/II) redox potential, showing it too is very electron rich, with its Co(III/II) redox potential being 0.05 V higher than that of **3$_H$**.

When compared to similar complexes featuring the related ligand structures, reported by Yang and co-workers, the Co(II/I) redox potentials are slightly higher but broadly consitent.[26] The slight difference in redox potentials is likely due to changes to the ligand backbone, co-ligand and solvent effects.[26]

3.3 ROCOP of PO and CO_2, with Complexes 1-3$_R$

Following the successful synthesis and characterisation of the heterobimetallic complexes, studies of **1-3$_R$** as catalysts in PO/CO_2 ROCOP were carried out (Scheme 3.3).



Scheme 3.3 PO/CO_2 ROCOP to synthesise poly(propylene carbonate) (PPC) polyols and propylene carbonate (PC). The catalyst is applied using a chain transfer agent to ensure high selectivity for α,ω-hydroxyl telechelic polymer chains (catalyst: CTA, 1:20).

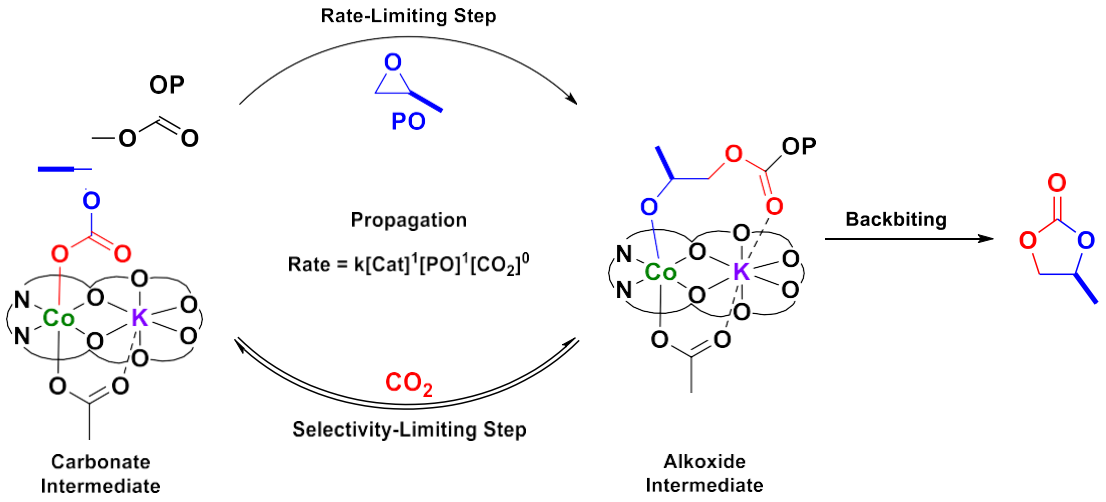
The complexes were tested under equivalent conditions of 1:20:4000 cat:CTA:PO, with the chain transfer agent (CTA) being *trans*-1,2-cyclohexanediol (CHD). The polymerisations were conducted in a 100 mL Parr reactor fitted with a DiComp sentinel probe, attached to an ATR-IR spectrometer, which allowed for continual monitoring of changes to absorptions, and hence to concentrations, of both polymer (PPC, 1750 cm^{-1}) and propylene carbonate (PC, 1810 cm^{-1}). These high-pressure polymerisations were run at 50 °C and 20 bar CO_2 pressure in 6mL of neat PO (14M). These conditions are equivalent to the best conditions identified in our earlier paper describing these complexes.[24] Furthermore, the conditions are demanding, but relevant to preparation of industrially relevant PPC polyols, because there is a large excess of diol (chain transfer agent) and a low catalyst loading; diols are used to control molar mass and many literature catalysts struggle to enchain under such conditions.[11, 27]

Table 3.2 ROCOP of CO_2/PO of Complexes **1-3**.[a]

Cat.	Time (h)	Conv. (%)[b]	CO_2 Selec. (%)[c]	PPC Selec. (%)[c]	TON[d]	TOF_{PPC} (h^{-1})[e]	$k_{p,PPC}$ *10^3 (dm^3 mol^{-1} s^{-1}) [f]	M_n [Đ] (g mol^{-1})[g]
1[h]	4.0	34	>99	98	1360 ± 68	333 ± 17	11.20 ± 0.56	5300 [1.08]
2	7.3	26	>99	81	1050 ± 53	117 ± 6	3.61 ± 0.18	4600 [1.10]
3$_H$	2.5	24	>99	>99	973 ± 49	389 ± 19	9.40 ± 0.47	4000 [1.06]
3$_{Me}$	11.7	34	>99	85	1402 ± 70	101 ± 6	4.40 ± 0.22	5500 [1.15]
3$_{OMe}$	7.5	37	>99	96	1494 ± 75	191 ± 10	7.25 ± 0.36	8900 [1.11]
3$_F$	13	30	>99	80	1196 ± 60	73 ± 4	1.78 ± 0.09	4400 [1.11]
3$_{Cl}$	12	24	>99	75	962 ± 48	62 ± 3	1.44 ± 0.07	4200 [1.13]

[a]Reaction conditions: Catalyst (0.025 mol %, 3.5 mM), PO (6 mL, 14 M), 1,2-cyclohexanediol (0.5 mol %, 70 mM), 20 bar CO_2, 50 °C. [b]PO conversion determined from the relative integrals in the ^{1}H NMR spectrum of PPC (4.92 ppm, 1H), CC (4.77 ppm, 1H), and PPO (3.46−3.64 ppm, 3H) using mesitylene as an internal standard (6.70 ppm). [c]PPC selectivity determined by the relative integrals in the ^{1}H NMR spectrum of PPC (4.92 ppm, 1H) compared with PC (4.77 ppm, 1H) and PPO (3.46−3.64 ppm, 3H). [d]Turnover number (TON) = number of moles of PO consumed/ number of moles catalyst. [e]Turnover frequency of PPC (TOF_{PPC}) = (TON*PPC selectivity)/time (h). [f]$k_p = k_{obs}/[cat]^1$; k_{obs} determined as the gradient of the plot of $\ln[PO]_t/[PO]_0$ vs time over the conversion range of 5% to 20% (Fig. 3.6 and S3.34-S3.38). [g]Determined by GPC analysis, in THF, calibrated with narrow-M_n polystyrene standards; dispersity values in parentheses (Fig. S3.39-S3.44). [h]Previously reported.[24]

All complexes were active for PO/CO_2 ROCOP, yet displayed a wide variety of activities and selectivities. All catalysts showed quantitative CO_2 uptake to form carbonates (without ether linkages) and with very high selectivity for hydroxyl telechelic PPC. The PPC samples all showed molar mass values consistent with theoretical values, in the target range for polycarbonate polyols, with monomodal, narrow dispersity distributions (Đ < 1.20). Within the series of catalysts there were significant differences: the activity values, as assessed by turn-over-frequency (TOF) varied from ~60-390 h^{-1} and the selectivity for PPC formation varied from 75-99%. For each individual catalyst, the selectivity was consistent throughout the reaction and independent of conversion, thereby suggesting that differences could be safely related to catalyst structural differences (Fig. S3.45).



Scheme 3.4 Cobaltate Dinuclear Mechanism for the PO/CO_2 Ring Opening Copolymerisation.

The rate law for **1** shows a first-order dependence on both PO and catalyst concentrations but is independent of carbon dioxide pressure.[20] The rate law is rationalised, and supported by DFT calculations, by the dinuclear metallate mechanism (Chapter 2). The rate-limiting step is proposed to be epoxide coordination and/or ring-opening by the cobalt-carbonate intermediate, with the two processes either both contributing or being indistinguishable using only the rate law (Scheme 3.4). Carbon dioxide insertion occurs rapidly but reversibly in the 'selectivity limiting step'. It is proposed that all new catalysts will follow the same rate law since all show related kinetic profiles and first order dependence on epoxide concentration. To analyse differences in rates, both the catalytic turn-over frequency value (TOF) and the initial rate constants (5-20% conversion range) were determined using *in situ* ATR-IR spectroscopy (Table 3.2, Fig. 3.6). It has previously been demonstrated in CO_2/epoxide

ROCOP catalysis that initial rates, determined in a similar manner, are within experimental error the same as those determined by an integrated rate treatment (20-80% conversion).[28] Also, since data are collected in the first stages of the reaction diffusion limitations are insignificant; these factors allow for proper correlation between catalyst structures and propagation rates.

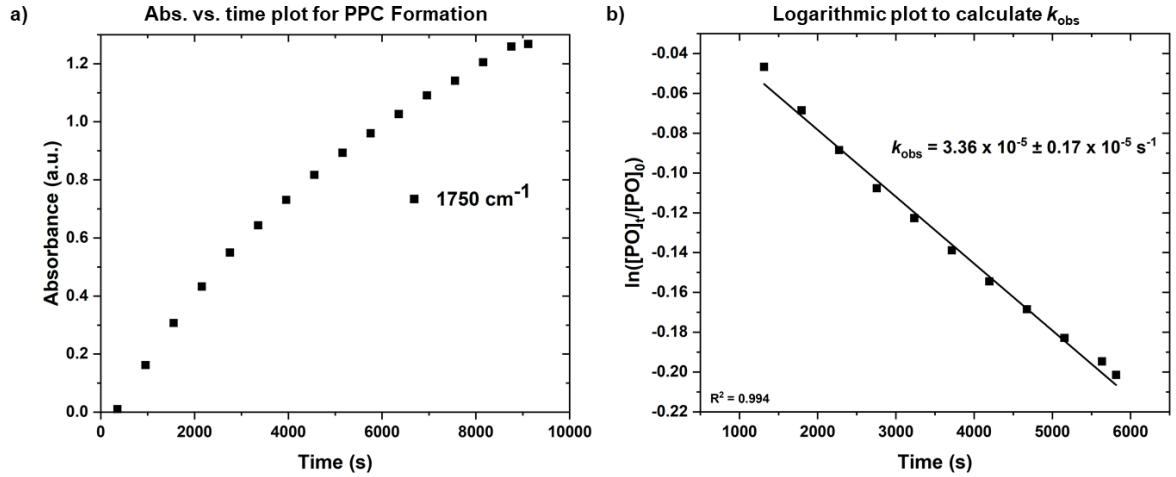


Figure 3.6 Exemplar Catalyst Activity Data for Catalyst $\mathbf{3_H}$. a) Plot showing changes to the absorbance at 1750 cm^{-1} (carbonyl stretch) versus time plot for PPC formation. b) Semi-logarithmic concentration vs. time plot used to determine k_{obs}.

For each catalyst, the absorbance versus time data was converted into semi-logarithmic [PO] *vs.* time plots by independent calibration of the starting and final PO concentrations (Fig. 3.6). The pseudo first-order rate coefficients, $k_{obs,\,PPC}$, were compared and also converted into propagation rate coefficients, $k_{p,\,PPC}$ by accounting for the catalyst concentration and following the rate law determined previously (equations 1).

$$\boldsymbol{k_{p,ppc}} = \frac{\boldsymbol{k_{obs,ppc}}}{[\boldsymbol{Cat.}]} \quad \text{(Equation 1)}$$

There were clear differences between the propagation rate constants with values from 9.40 ± 0.47 to 1.44 ± 0.07 $dm^3\ mol^{-1}\ s^{-1}$ (Table 3.2). Specifically, changing from ethylene (**1**) to cyclohexylene (**2**) linkers decreased the catalytic activity by about three-fold ($k_{p,\,PPC}$ = 11.20 ± 0.56 and 3.61 ± 0.18 $dm^3\ mol^{-1}\ s^{-1}$, respectively). It also resulted in reduced PPC selectivity (vs. CC) from 98% to 80% (Table 1). Changing back to a rigid phenylene linker, $\mathbf{3_H}$, restored the high activity and selectivity, with a TOF of 389 h^{-1} ($k_{p,\,PPC}$ = 9.40 ± 0.47 $dm^3\ mol^{-1}\ s^{-1}$) and >99 % PPC selectivity. The success using the phenylene linker is particularly promising since it allows for substitution of the aromatic rings with formally electron withdrawing or electron donating substituents, namely in catalysts $\mathbf{3_{H,\,Me,\,OMe,\,F,\,Cl}}$. Specifically, ligand substituents were added to the phenylene rings at sites opposite the two imine N atoms such that

each substituent is *para*- to one imine and *meta*- to the other. All the substituents selected are relatively small and the substitution sites are distant from the metals which should limit any steric influences. In all the experiments, the results are compared against the performance using the phenylene catalyst $\mathbf{3_H}$. Accordingly, the catalyst featuring two methyl substituents, $\mathbf{3_{Me}}$, showed a three-fold reduction in rate, TOF = 111 h^{-1} ($k_{p,\ PPC}$ = 4.40 ± 0.22 $dm^3\ mol^{-1}\ s^{-1}$) and lower selectivity (85% PPC) than $\mathbf{3_H}$. The catalyst featuring methoxy substituents $\mathbf{3_{OMe}}$ showed slightly better activity, TOF = 191 h^{-1} ($k_{p,\ PPC}$ = 7.25 ± 0.36 $dm^3\ mol^{-1}\ s^{-1}$) and greater selectivity at 96%, than $\mathbf{3_{Me}}$ but it was less effective than catalyst $\mathbf{3_H}$. Applying fluorine substituents $\mathbf{3_F}$ showed a significantly slower rate, with a TOF of 73 h^{-1} ($k_{p,\ PPC}$ = 1.78 ± 0.09 $dm^3\ mol^{-1}\ s^{-1}$) and lower selectivity, 80%, compared with $\mathbf{3_H}$. The catalyst featuring chlorine substituents $\mathbf{3_{Cl}}$ showed the lowest activity and selectivity of the series, with TOF = 62 h^{-1} (k_p= 1.44 ± 0.07 $dm^3\ mol^{-1}\ s^{-1}$) and 75% PPC selectivity, respectively. The results using the phenylene substituted catalysts clearly show that the best performances are from the unsubstituted catalyst, i.e. $\mathbf{3_H}$. Nonetheless, the substituted phenylene catalysts performances are important, even if less impressive, since they inform upon the influences over both rate and selectivity determining steps in the catalytic cycle.

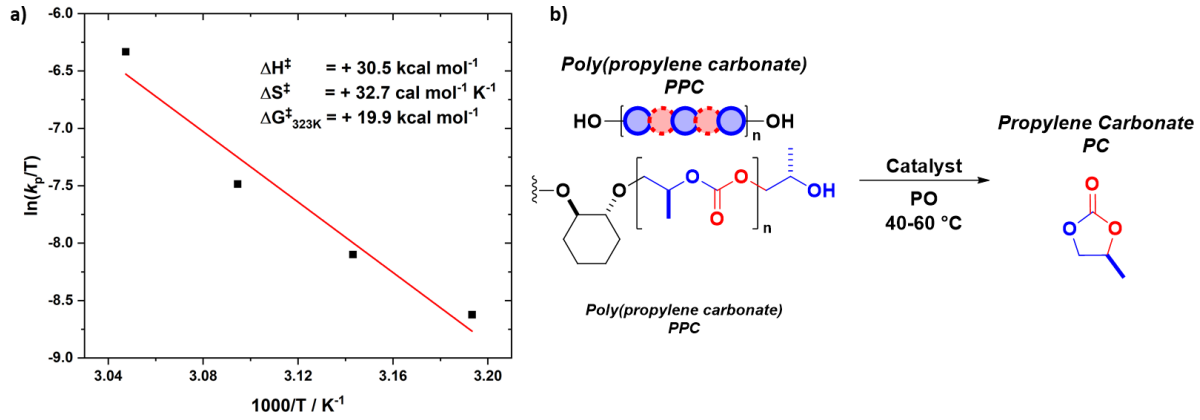


Figure 3.7 a) Eyring analysis of backbiting of PPC using $\mathbf{3_{Cl}}$. These experiments were conducted from 45 to 60 °C, using [$\mathbf{3_{Cl}}$] 3 mM and [PPC] 300 mM in neat PO (14 M) and were analysed to full conversion, where [PPC] is defined as the monomeric unit concentration. b) Reaction scheme showing consumption of PPC to PC.

To inform the changes in rate and selectivity, as second investigation into the side-reaction: the formation of PC was undertaken. The most and least selective catalyst (**1** and $\mathbf{3_{Cl}}$) were chosen since they feature the biggest difference in reactivity. As in Chapter 2, synthesised PPC was isolated and depolymerised to PC. The conditions were the same as the previous method in order to allow full comparison (Fig. 3.7b). The Eyring analysis showed that ΔG_{323K} = +19.9 kcal mol^{-1} for $\mathbf{3_{Cl}}$ which was

very similar to that observed for **1** (+19.5 kcal mol^{-1}). Therefore, the difference to the barrier to backbiting cannot explain changes in selectivity.

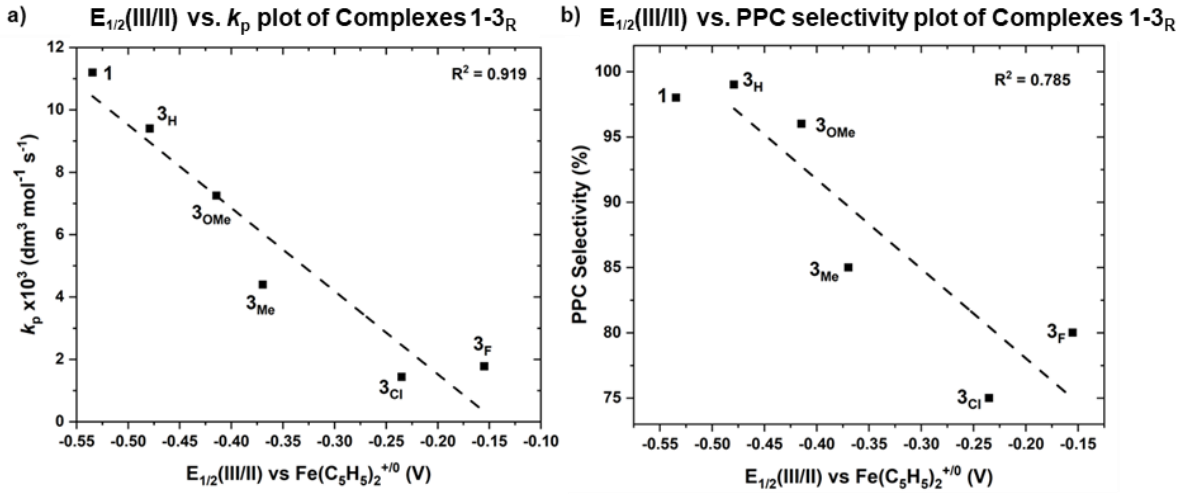


Figure 3.8 a) $E_{1/2}$(III/II) vs. k_p plot of complexes **3R**. b) $E_{1/2}$(III/II) vs. PPC selectivity plot of complexes **3R**. c) Summary of relationship between rate and selectivity and accuracy of the predicting method.

To understand the influences, if any, that the substituents exerted, multiple factors or 'probes' were investigated to see if any prediction and correlation of activity and selectivity can be made. It is critical these factors focus upon the metal active sites, i.e. the Co(III) centre. Perhaps the most accurate measure of the electron density at cobalt is its reduction potential and so CV experiments were conducted for all catalysts.

Plots of either the propagation rate constants (k_p) or PPC selectivity *versus* the redox/reduction potentials, $E_{1/2}$Co(III/II) or E_{Red}Co(II/I), showed linear fits and direct correlations (Fig. 3.8 and 3.9, Table 3.1, S3.33). E_{Red}Co(II/I) is used due to the irreversible nature of the **3F** Co(II/I) transition. In both cases, catalysts **1** and **3H** show the most negative reduction potentials, i.e. have the greatest electron density at cobalt of the series. The trends show that as electron density at Co(III) reduces, so does the activity and selectivity of all the catalysts in the series.

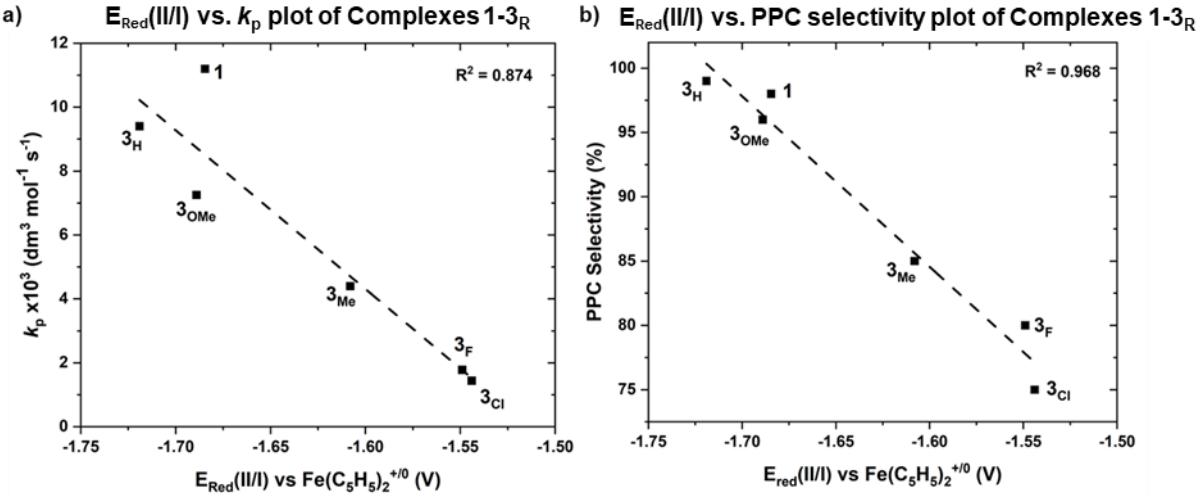


Figure 3.9 a) E_{Red}(II/I) vs. k_p plot of complexes **1** and $\mathbf{3_R}$. b) E_{Red}(II/I) vs. PPC selectivity plot of complexes **1** and $\mathbf{3_R}$.

With a successful probe for active site electronics in hand, attention turned to whether there was any correlation between the 'imine' donor chemistry and catalytic performance. It was notable that the catalysts showed slightly variable imine proton chemical shifts in the ^{1}H NMR spectra. Plotting the catalyst activity, or selectivity, against the imine chemical shifts showed a linear relationship but the correlation was less definitive (Fig. 3.10). Note that, catalysts **1** and **2** are not included in the data set as they feature very different backbones. The weaker correlation is likely related to the low sensitivity of NMR spectroscopy, as well as the greater distance of the 'probe' from the active site. Furthermore, chemical shift is not directly correlated with electron density at the active site.

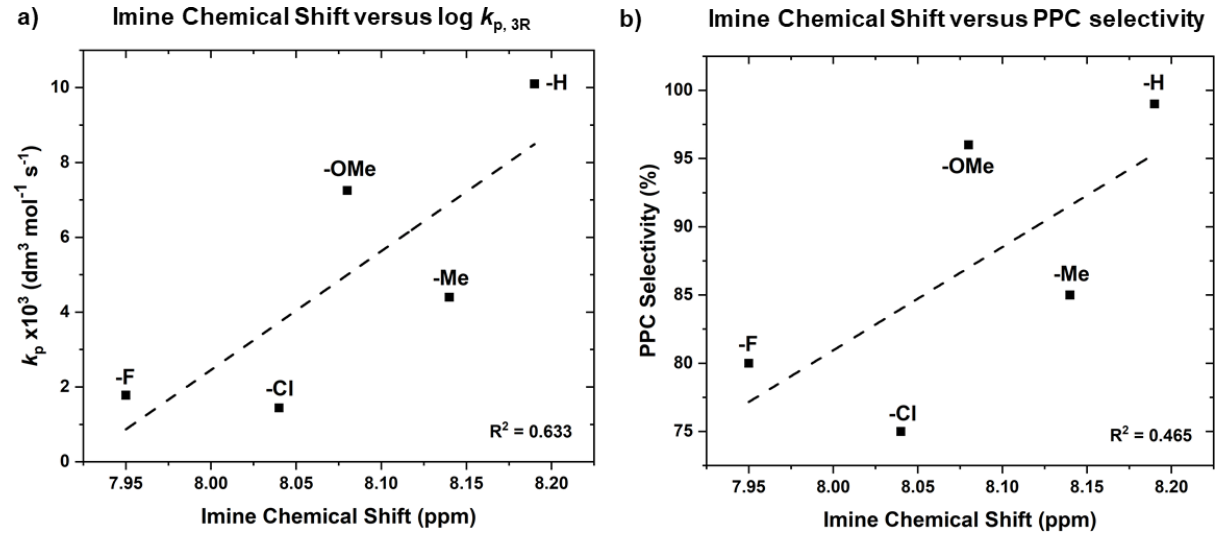


Fig. 3.10 a) Imine Chemical Shift versus log $k_{p,\,3R}$. b) Imine Chemical Shift versus PPC selectivity.

To demonstrate the importance of making direct measurements at the active site, plots of ligand substituent Hammett parameters, σ, were determined taking into account the respective meta- and para-

substituents. There was no obvious correlation between activity or selectivity, both Hammett plots showed apparent 'volcano' distribution between electron withdrawing and donating substituents (Fig. 3.11). Furthermore, one of the key limitations of the Hammett parameter is that it can only be applied to substituents on aromatic systems. It cannot be used to compare $\mathbf{3_R}$ series with **1** and **2**. Additionally, the Gutmann-Beckett method was determined to be ineffective due to the lower binding of nucleophiles at the K(I) and so not probing the Co(III) centre where the catalysis takes place.[9]

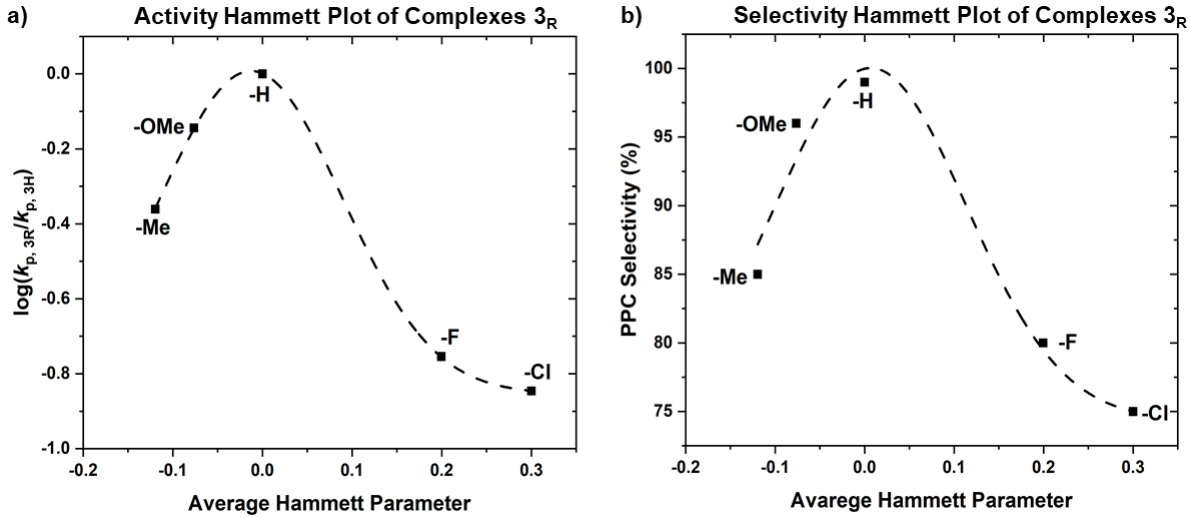


Figure 3.11 a) Activity Hammett plot of complexes $\mathbf{3_R}$. b) Selectivity Hammett plot of complexes $\mathbf{3_R}$.[6]

Overall, these findings are important for others investigating structure-activity relationships in catalysis and they demonstrate the perils of over-reliance of Hammett parameters or 'text-book assumptions' of the electronic properties of various aromatic ring substituents (Fig. 3.12). Substituents on aromatic rings assumed to be electron withdrawing/donation do not, in fact, result in those electronic effects at the metal active site. Rather, understanding electronic properties almost certainly requires consideration of the influences of substituents in the entire ligand system. Electrochemical measurements, such as reduction potentials, can be equally successfully applied to metals, main group elements or 'organic' active sites and are a rapid, unambiguous determinant of electron density. It is recommended they are applied more broadly in polymerisation catalyses even where redox processes are not occurring in propagation cycles.

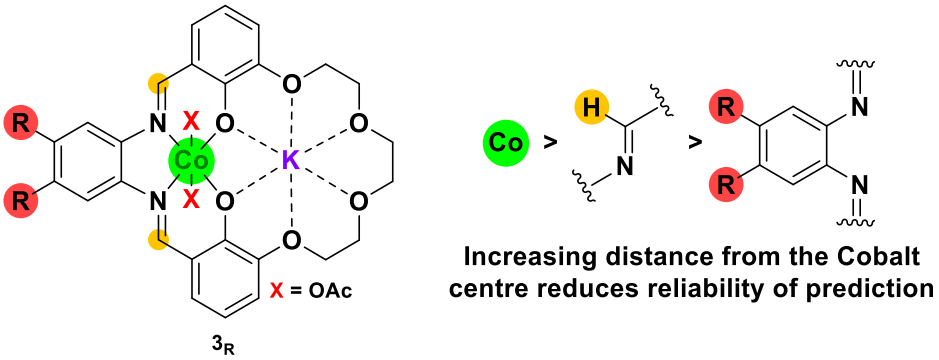


Figure 3.12 Summary of relationship between rate and selectivity and accuracy of the predicting method.

3.4 Discussion

3.4.1 Rate Limiting Step

The dinuclear metallate mechanism, supported by the rate law and DFT calculations using catalyst **1**, is used to rationalise the finding that the most active and selective catalyst is also the most electron rich at the Co(III) centre. The rate law shows a first-order dependence on both epoxide and catalyst concentrations. DFT calculations were used to probe the mechanism. Firstly, the mechanism involves a Co(III)-carbonate intermediate (formed by carbon dioxide insertion) that rapidly re-structures to provide a vacant site for epoxide coordination by generating a transient K(I)-carbonate species. Epoxide coordination occurs at Co(III) and is followed by K(I)-carbonate nucleophilic attack, passing through a high energy transition state (**TS_{I-II}**, Fig. 3.13). PO ring-opening occurs to generate a new Co(III)-alkoxide intermediate, **II**, which is stabilised by dative covalent bonds between the inserted carbonate and K(I). DFT calculations were completed on all complexes and suggest that the transition state barrier to the ring-opening of the epoxide is lowered for the more active catalysts as well as having a higher energy alkoxide intermediate. However, care must be taken not to over-interpret the data since the differences in the relative energies of intermediates and transition states are marginal (within DFT error of 2 kcal mol^{-1}).

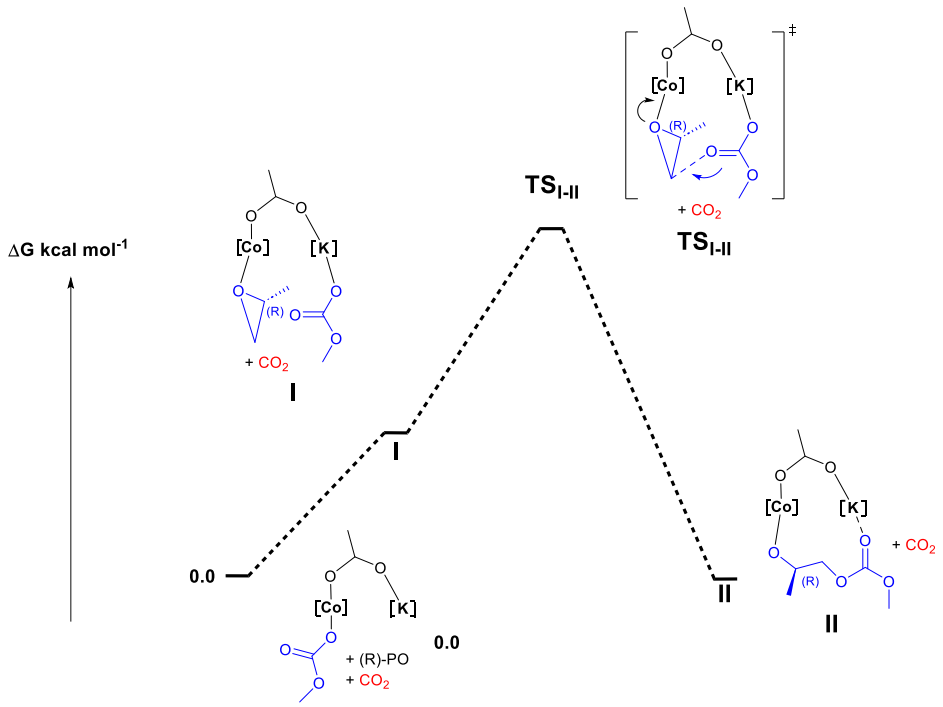


Figure 3.13 Rate determining step of **1-3$_R$**.

3.4.2 Selectivity Limiting Step

The catalytic selectivity for PPC *vs*. PC is also very important and depends upon the reactions of the Co-alkoxide intermediate (**II**). There are two processes that can occur: 1) Reaction with carbon dioxide, in an equilibrium process, to form Co(III)-carbonate intermediate, i.e. PPC propagation; or 2) Reaction with the polycarbonate chain, via an intramolecular nucleophilic attack, to form a new Co(III)-alkoxide and PC, i.e. by-product formation. Prior experiments using catalyst **1** suggest that the position of the carbon dioxide equilibrium dictates which pathway dominates (Fig. 3.14). Accordingly, higher carbon dioxide pressures and lower temperatures favour insertion and propagation. The current investigation clearly shows that under otherwise identical reaction conditions, different catalyst structures also affect the carbon dioxide insertion equilibrium.

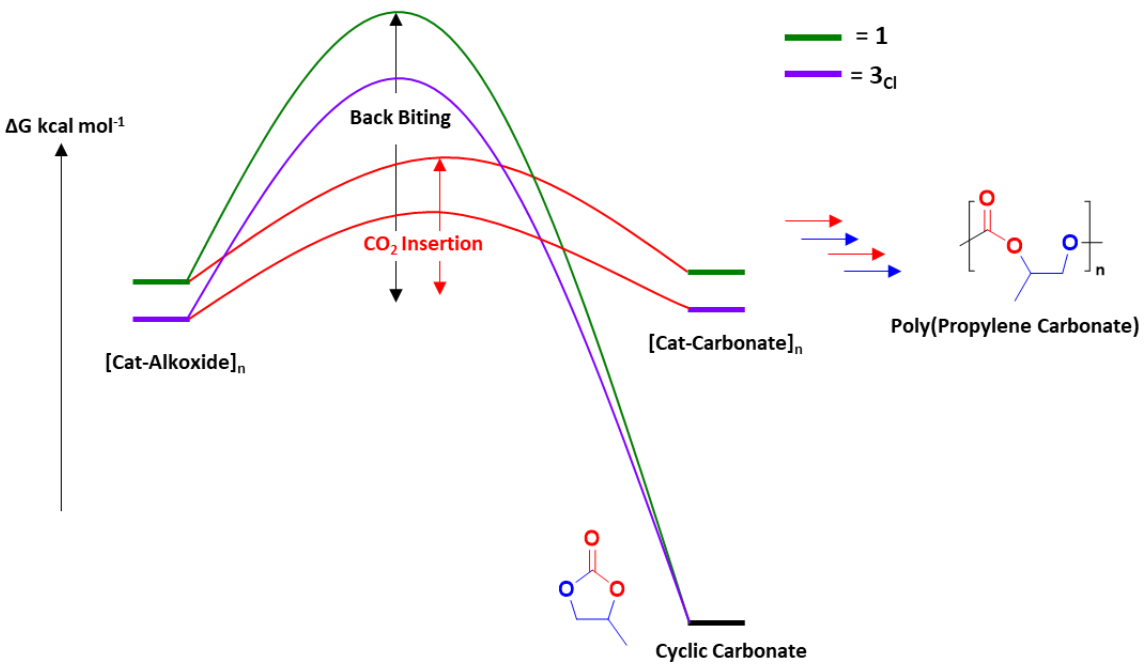


Figure 3.14 Schematic illutrating the selectivity limiting reactions of the Co(III)-alkoxide intermediate which can undergo either 1) Propagation by carbon dioxide insertion or 2) PC formation by intramolecular reactions. stability.

To test whether the catalysts showed different barriers to PC formation, deliberate depolymerisation of PPC using high (**1**) and low (**3**$_{Cl}$) activity catalysts was undertaken. PPC degradation reactions were undertaken in PO solution, without any carbon dioxide present, to provide the best model for only the PC formation process. Both catalysts resulted in PPC exponential decay to form PC and Eyring analyses of the rate constants showed nearly identical barriers to PC formation, with **1** having a slightly lower barrier (19.5 kcal/mol) compared with **3**$_{Cl}$ (+19.9 kcal mol^{-1}). This finding indicates that slight changes in the position of carbon dioxide insertion equilibria are responsible for the significant differences in selectivity (and rate). It is proposed that electron rich **3**$_{H}$ has an equilibrium lying further towards carbonate intermediate compared with **3**$_{Cl}$, which has reduced electron density. This might be rationalized by considering carbon dioxide insertion as a nucleophilic attack, where greater electron density facilitates the insertion process but such hypotheses remain speculative. The rationale is that a greater concentration of carbonate intermediate is useful since it reduces the alkoxide concentration and limits the extent of backbiting, even though the barrier to such processes should be accessible under the reaction conditions. The corollary is that a lower carbonate intermediate concentration results in a higher relative concentration of the alkoxide intermediate concentration, for **3**$_{Cl}$, and an accelerated rate of PC formation. The same rationale impacts the polymerisation rates, since greater carbonate concentration

should accelerate the propagation step (carbonate attack). Another consideration is the relative stability of the Co(III)-alkoxide intermediates: the electron rich intermediate from $\mathbf{3_H}$ is relatively destabilized compared with $\mathbf{3_{Cl}}$, this reduces the overall energy difference to access the key transition state barrier energies.

3.4.3 Polymerisation Catalysis Implications

Central to all catalysis is the need to understand how to moderate catalyst stability, activity and selectivity and hence structure-performance relationships are of great importance. Nonetheless, such studies are notoriously complex and in prior investigations of epoxide/CO_2 ROCOP have always failed to discover any correlation between any physical chemical parameter, measurable prior to catalysis, and performances. Thus, the finding that the electron density at the active site, in this case Co(III) centres, correlates with both activity and selectivity is significant both for improving catalysis and understanding how these reactions occur. One attraction of electrochemical method is its simplicity – an inexpensive cyclic voltammetry set-up is all that is required and there is no reliance on complex, operando spectroscopic techniques/methods. These factors and the ability to quickly 'predict' activity/selectivity trends is particularly relevant as these polymerisations typically require rather complex experimental processes and capital investment, including use of stainless-steel reactors/gas lines. As mentioned in the introduction section, all prior attempts to rationalise catalyst activity against parameters such as Lewis acidity, M-OR bond strength, water exchange constants or ligand Hammett parameters were unsuccessful. Consequently, the catalyst design has been underpinned by DFT and chemist instinct. This work clearly signals the importance of the ligand substituents in controlling the electron density at the metal centre, and highlights the need to directly measure electron density, since using ligand parameters data only is inaccurate. The findings are directly relevant to the broader families of other Co(III) catalysts, most notably those coordinated by salen or related Schiff base ligands.[29-32] The leading catalysts in the field for PO/CO_2 ROCOP are [Co(salen-PPNX)(X)] systems, containing co-catalysts tethered to the metal complex.[33-35] Much excellent work has been conducted to optimize structures and fine-tune performances but the complexity and the range of different mechanisms accessible has complicated structure-activity investigations. It is recommended that systematic structural

modifications should be conducted, using the electrochemical method to inform upon the electronic influences at the Co(III) centre. The methods and findings of this work could also be relevant to better understanding of the high-performance borane-ammonium/phosphonium catalysts which were reported to show good performances in CHO/CO_2 ROCOP but need development, both in terms of activity and selectivity, for the equivalent PO/CO_2 ROCOP. More broadly, it is also proposed that both the methods and findings that electron rich Co(III) centres are more active and selective will be relevant to other catalysts, both metal based and organic, and for other polymerisations operating by related mechanisms. These include the technologically important means to make bio-derived plastics such as heterocycle (lactone/cyclic carbonate) ring-opening polymerisation, epoxide/anhydride ROCOP and switchable catalyses.[36-40] All those polymerisations suffer equivalently from a lack of structure-activity insight and all require faster and more selective catalysts since the fields are relatively immature, particularly compared with alkene polymerisations. Future efforts must accelerate discovery of the best catalysts as decades of optimization will be too long to wait for the production of lower pollution and carbon recycled products. Since all mechanisms rely on the balance of active site-alkoxide Lewis acidity and lability, it is important to understand whether there are equivalent linear correlations between active site electron density and activity (as well as selectivity). Even more broadly, carbon dioxide utilization technologies are of central importance to the future of the chemical industry, yet there remain very few processes which can operate at scale and appropriate cost.[41] There is a real need for fundamental understanding of how carbon dioxide interacts with molecules; structure-activity studies are a rational driver for future discovery and implementation of these carbon dioxide transformation chemistries.

3.4.4 Comparison with Wider Field

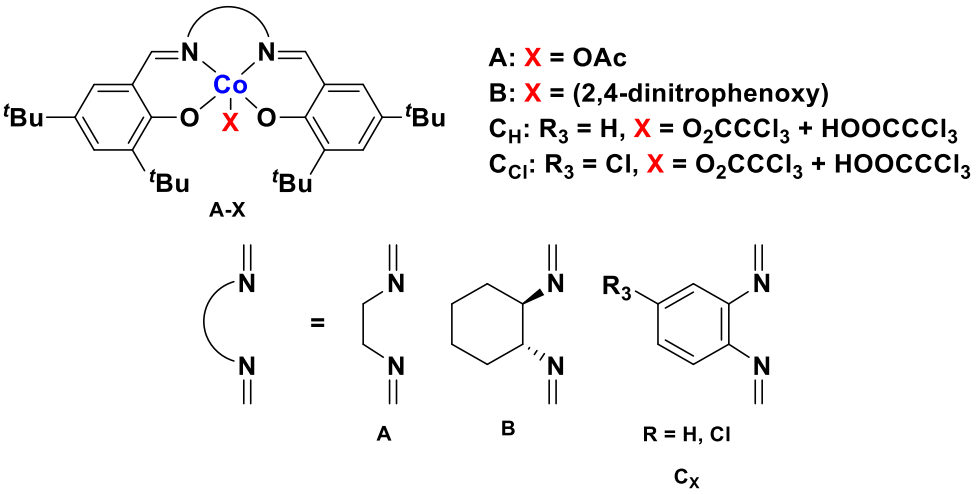


Figure 3.15 Literature PO/CO_2 salen catalysts.[22-23]

Although this study focuses on mechanistic aspects, it is relevant to set the performances of these catalysts in the context of the wider field. When comparing to the Co(III) catalyst/co-catalyst literature, there is only a limited exploration of electronic impact of the nitrogen linker on activity and selectivity of the Co(III)salen/PPNCl catalytic systems (Fig. 3.15). Surprisingly, there appears to be no report of Co(III)salen/co-catalyst systems with a simple unsubstituted ethylene backbone, analogous to complex **1**, reported for PO/CO_2 ROCOP (Fig. 3.12, **A**). However, other backbones have been reported, with the most explored featuring the cyclohexene analogous to complex **2** (Fig. 3.15, **B**). These [Co(III)salcy] complexes can show very high activity, e.g. [Co(III)Salcy(2,4-dinitrophenoxy)] (**B**), with PPNCl as a co-catalyst, has >99% selectivity for both CO_2 insertion and PPC and a TOF_{PPC} of 530 h^{-1} at 15 bar CO_2 and 25 °C with 0.05 mol% catalyst loading (Table 3.3, entry 1).[22] This is particularly interesting in light of **2** showing a reduced selectivity of 81% and a TOF of 117 h^{-1}. **B**, on the other hand, is amongst the best performing PO/CO_2 Co(III)salen catalysts. This highlights the significant change in reactivity of these bimetallic complexes and the need to study each system to understand its reactivity. $\mathbf{3_H}$, on the other hand, compares favorably to **B**, showing a TOF of 389 h^{-1} and the same selectivity (>99%). It should also be noted that the catalysts in this thesis operated at lower catalyst loadings (0.025 mol%) than **B** or other Co(III)salen/PPNCl catalyst systems reported. This is because bicomponent systems suffer from dramatic rate loss at comparative loadings. Furthermore, $\mathbf{3_R}$ complexes are able to operate at higher temperatures and show better thermal stability than **B** and related complexes.[42-43]

Table 3.3 Literature PO/CO_2 salen catalysts.[22-23]

Entry	Cat.	co-cat.	Cat. Loading (mol%)	CO_2 Pressure (bar)	Temp. (°C)	CO_2 Selec. (%)	PPC Selec. (%)	TOF_{PPC} (h^{-1})
1[22]	B	PPNCl	0.05	15	25	>99	>99	530
2[22]	B	18-crown-6/KI	0.05	15	25	>99	41	75
3[23]	C_H	PPNCl	0.05	10	50	>99	81	456
4[23]	C_{Cl}	PPNCl	0.05	10	50	>99	84	386

When the co-catalyst is changed to 18-crown-6/KI, **B** shows a selectivity for PPC of 41%, but retains full selectivity for CO_2 insertion (Table 3.3, entry 2). This is accompanied by a decrease in rate to TOF_{PPC} 75 h^{-1}, at 15 bar CO_2, 25 °C and with 0.05 mol% catalyst loading.[22] This shows the importance of the incorporation of the 18-crown-6 moiety into the macrocycle to obtain the desired metallic synergy.

Another common backbone features the phenylene linker, analogous to $\mathbf{3_H}$ (Fig. 3.15, $\mathbf{C_H}$). These complexes are often referred to as [Co(III)salphen] and showed appreciable rates, but poorer selectivities than the Co(III)salcy counterparts. This is in contrast to the trends observed in this thesis. For example, [Co(III)salphen(O_2CCCl_3)]/PPNCl showed selectivity for PPC of 81%, was fully selective for CO_2 insertion and showed a TOF_{PPC} of 456 h^{-1} (10 bar CO_2, 50 °C, PPNCl, 0.05 mol% catalyst) (Table 3.3, entry 3).[23] The rate is very similar to that of $\mathbf{3_H}$, but its selectivity is significantly lower under comparable conditions. In the same study, the chloro-phenylene ligand ($\mathbf{C_{Cl}}$), showed slightly greater selectivity for PPC to 84%, but a decrease in TOF_{PPC} to 386 h^{-1} (Fig. 3.15, Table 3.3, entry 3).[23] This trend deviates from that observed for $\mathbf{3_H}$ and $\mathbf{3_{Cl}}$, where the chloride substitution leads to a significant decrease in selectivity of almost 25% and a reduction in rate from 389 to 62 h^{-1}. The macrocyclic ligand appears to be more sensitive to electronic effects perhaps as it operates by a simpler mechanism.

Further studies focused on different linker sizes or introducing chirality on C_2 backbones, but these generally show similar or lower activity than **B**.[44-45] The nitrogen linker chemistry remains under

explored for Co(III)salen catalysis with the studies being split over many publications, with no one study systemically changing the nitrogen linker electronics.

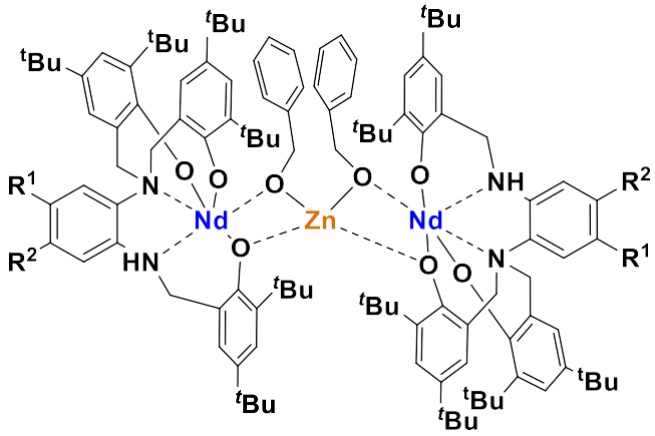


Fig. 3.16 Neodynium-zinc catalyst for CHO/CO_2 ROCOP.[46]

Interestingly, a recent structural activity study on heterometallic neodynium-zinc catalysts for cyclohexene oxide (CHO)/CO_2 ROCOP showed that substituents on the phenylene, such as -Me and -OMe (assumed to be electron donating groups), had a negative impact on rate (TOF) whilst groups such as -F, -Cl and -CF_3 (assumed to be electron withdrawing groups) accelerated rates (Fig. 3.16).[46] These findings contrast to those observed in this thesis. The ROCOP of CHO/CO_2 ROCOP is more selective, due to the higher barrier to backbiting and the thermodynamic instability of the corresponding cyclic carbonate. This means the polymerisation can be easily performed at elevated temperatures >80 °C, resulting in significant increases in rate.

3.5 Conclusions and Outlook

A series of novel heterodinuclear Co(III)/K(I) catalysts, differing by the imine backbone linker group were compared for PO/CO_2 ROCOP. A promising catalyst featuring a phenylene backbone group was systematically substituted, with -OMe, -Cl, -F and -Me groups. The data show a linear relationship with Co(III/II) or Co(II/I) reduction potentials and polymerisation activity and selectivity. The best performing catalyst was the catalyst featuring an unfunctionalized phenylene, which showed the greatest electron density at Co(III). The differences in activity are at the limit of the errors in DFT analysis preventing predictions and analysis using computation. Experimental kinetics and Eyring analyses for cyclic carbonate formation were compared for the catalysts showing highest and lowest activity and selectivity. These findings implicate a mechanism were a pre-rate limiting equilibrium involving carbon dioxide insertion is critical to controlling both catalytic activity and selectivity. The findings are expected to be useful for future catalyst design, both within this field of carbon dioxide copolymerisation and also for other carbon dioxide utilizations, specifically the importance of controlling/driving the carbonation/decarbonation equilibrium in determining selectivity. Overall, this demonstrates the utility of metal redox potential in predicting and understanding catalyst performance.

Future work, should focus on catalysts showing significant electron density at the Co(III) centre as assed by redox potentials since this should improve activity and selectivity.

3.6 References

1. Pardridge, W. M., *J. Cereb. Blood Flow Metab.* **1997,** *17*, 713-731.
2. Farhadi, F.; Khameneh, B.; Iranshahi, M.; Iranshahy, M., *Phytother. Res.* **2019,** *33*, 13-40.
3. Sahariah, P.; Masson, M., *Biomacromolecules* **2017,** *18*, 3846-3868.
4. Penzien, J.; Haeßner, C.; Jentys, A.; Köhler, K.; Müller, T. E.; Lercher, J. A., *J. Catal.* **2004,** *221*, 302-312.
5. Chen, E. Y.-X.; Marks, T. J., *Chem. Rev.* **2000,** *100*, 1391-1434.
6. Hansch C., Leo, A., and Taft R.W., *Chem. Rev.* **1991** *91*, 165-195. DOI: 10.1021/cr00002a004
7. Williams S.G. and Norrington F.E., *J. Am. Chem. Soc.* **1976** *98*, 508-516 DOI: 10.1021/ja00418a030
8. Tolman, C.A., *Chem. Rev.* **1977** *77*, 313-348 DOI: 10.1021/cr60307a002
9. P. Erdmann, L. Greb, *Angew. Chem. Int. Ed.* **2022**, *61*, e202114550.
10. Reis, N. V.; Deacy, A. C.; Rosetto, G.; Durr, C. B.; Williams, C. K., *Chem. Eur. J.* **2022,** *28*, e202104198.
11. Nagae, H.; Aoki, R.; Akutagawa, S. N.; Kleemann, J.; Tagawa, R.; Schindler, T.; Choi, G.; Spaniol, T. P.; Tsurugi, H.; Okuda, J.; Mashima, K., *Angew. Chem. Int. Ed.* **2018,** *57*, 2492-2496.
12. Asaba, H.; Iwasaki, T.; Hatazawa, M.; Deng, J.; Nagae, H.; Mashima, K.; Nozaki, K., *Inorg. Chem.* **2020**, 0- 5.
13. Moore, D. R.; Cheng, M.; Lobkovsky, E. B.; Coates, G. W., *J. Am. Chem. Soc.* **2003,** *125*, 11911-11924.
14. Deacy, A. C.; Kilpatrick, A. F. R.; Regoutz, A.; Williams, C. K., *Nat. Chem.* **2020,** *12*, 372-380.
15. Klaus, S.; Lehenmeier, M. W.; Herdtweck, E.; Deglmann, P.; Ott, A. K.; Rieger, B., *J. Am. Chem. Soc.* **2011,** *133*, 13151-13161.
16. Ohkawara, T.; Suzuki, K.; Nakano, K.; Mori, S.; Nozaki, K., *J. Am. Chem. Soc.* **2014,** *136*, 10728-10735.
17. Schaefer, J.; Zhou, H.; Lee, E.; Lambic, N. S.; Culcu, G.; Holtcamp, M. W.; Rix, F. C.; Lin, T.-P., *ACS Catal.* **2022,** *12*, 11870-11885.
18. Zhang, D.; Boopathi, S. K.; Hadjichristidis, N.; Gnanou, Y.; Feng, X., *J. Am. Chem. Soc.* **2016,** *138*, 11117-11120.
19. Yang, G.-W.; Zhang, Y.-Y.; Wu, G.-P., *Acc. Chem. Res.* **2021,** *54*, 4434-4448.
20. Yang, G. W.; Zhang, Y. Y.; Xie, R.; Wu, G. P., *J. Am. Chem. Soc.* **2020,** *142*, 12245-12255.
21. Yang, G. W.; Xu, C. K.; Xie, R.; Zhang, Y. Y.; Zhu, X. F.; Wu, G. P., *J. Am. Chem. Soc.* **2021,** *143*, 3455-3465.
22. Lu, X.-B.; Shi, L.; Wang, Y.-M.; Zhang, R.; Zhang, Y.-J.; Peng, X.-J.; Zhang, Z.-C.; Li, B., *J. Am. Chem. Soc.* **2006,** *128*, 1664-1674.
23. Hošťálek, Z.; Mundil, R.; Císařová, I.; Trhlíková, O.; Grau, E.; Peruch, F.; Cramail, H.; Merna, J., *Polymer* **2015,** *63*, 52-61.
24. Deacy, A. C.; Moreby, E.; Phanopoulos, A.; Williams, C. K., *J. Am. Chem. Soc.* **2020,** *142*, 19150-19160.
25. Brianese, N.; Casellato, U.; Tamburini, S.; Tomasin, P.; Vigato, P. A., *Inorg. Chim. Acta* **1999,** *293*, 178-194.
26. Reath, A. H.; Ziller, J. W.; Tsay, C.; Ryan, A. J.; Yang, J. Y., *Inorg. Chem.* **2017,** *56*, 3713-3718.
27. Darensbourg, D. J.; Wu, G. P., *Angew. Chem. Int. Ed. Engl.* **2013,** *52*, 10602-6.
28. Trott, G.; Garden, J. A.; Williams, C. K., *Chem. Sci.* **2019**, 4618-4627.
29. Lu, X. B.; Wang, Y., *Angew. Chem. Int. Ed. Engl.* **2004,** *43*, 3574-7.
30. Qin, Z.; Thomas, C. M.; Lee, S.; Coates, G. W., *Angew. Chem. Int. Ed.* **2003,** *42*, 5484-5487.
31. Kember, M. R.; Jutz, F.; Buchard, A.; White, A. J. P.; Williams, C. K., *Chem. Sci.* **2012,** *3*, 1245-1255.
32. Cohen, C. T.; Chu, T.; Coates, G. W., *J. Am. Chem. Soc.* **2005,** *127*, 10869-10878.
33. Cyriac, A.; Lee, S. H.; Varghese, J. K.; Park, E. S.; Park, J. H.; Lee, B. Y., *Macromolecules* **2010,** *43*, 7398-7401.
34. Lu, X.-b.; Ren, W.-m.; Wu, G.-p., *Acc. Chem. Res.* **2012,** *45*, 1721−1735.
35. Nakano, K.; Kamada, T.; Nozaki, K., *Angew. Chem. Int. Ed.* **2006,** *45*, 7274-7277.
36. Dechy-Cabaret, O.; Martin-Vaca, B.; Bourissou, D., *Chem. Rev.* **2004,** *104*, 6147-6176.
37. Longo, J. M.; Sanford, M. J.; Coates, G. W., *Chem. Rev.* **2016,** *116*, 15167-15197.
38. Zhang, X.; Fevre, M.; Jones, G. O.; Waymouth, R. M., *Chem. Rev.* **2018,** *118*, 839-885.
39. Gandini, A.; Lacerda, T. M.; Carvalho, A. J. F.; Trovatti, E., *Chem. Rev.* **2016,** *116*, 1637-1669.
40. Deacy, A. C.; Gregory, G. L.; Sulley, G. S.; Chen, T. T. D.; Williams, C. K., *J. Am. Chem. Soc.* **2021,** *143*, 10021-10040.
41. Hepburn, C.; Adlen, E.; Beddington, J.; Carter, E. A.; Fuss, S.; Mac Dowell, N.; Minx, J. C.; Smith, P.; Williams, C. K., *Nature* **2019,** *575*, 87-97.
42. Ren, W.-M.; Liu, Z.-W.; Wen, Y.-Q.; Zhang, R.; Lu, X.-B., *J. Am. Chem. Soc.* **2009,** *131*, 11509-11518.
43. Xia, W.; Salmeia, K. A.; Vagin, S. I.; Rieger, B., *Chem. Eur. J.* **2015,** *21*, 4384-90.
44. Niu, Y.; Li, H.; Chen, X.; Zhang, W.; Zhuang, X.; Jing, X., *Macromol. Chem. Phys.* **2009,** *210*, 1224-1229.
45. Niu, Y.; Zhang, W.; Pang, X.; Chen, X.; Zhuang, X.; Jing, X., *J. Polym. Sci., Part A: Polym. Chem.* **2007,** *45*, 5050-5056.
46. Yao, Q.; Wang, Y.; Zhao, B.; Zhu, X.; Luo, Y.; Yuan, D.; Yao, Y., *Inorg. Chem.* **2022,** *61*, 10373-10382.

Chapter 4

Heterobimetallic Co(III)K(I) catalyst for the Switchable Copolymerisation of Epoxides, CO_2 and Lactide

4.1 Introduction and Aims

Switchable polymerisation catalyses are reactions where mixtures of monomers and a single catalyst, able to access different catalytic cycles, are used to produce block sequence-selective copolymers.[1-3] In this catalysis, 'switches' refer to the ability to direct the catalyst between different polymerisations while simultaneously selecting for particular monomers.[4] This chapter investigates new catalyst for this reaction and targets ABA polymer structures as thermoplastic elastomers and plasticizers for PLLA/PLA.

Thermoplastic elastomers (TPEs) combine elasticity, straightforward thermal processing and recyclability. Unlike conventional rubbers, TPEs are re-processable and amenable to manufacture in large volumes *via* melt extrusion or injection moulding.[5-7] TPEs find application in electronics, packaging, automotive components, medical devices, coatings, fibres, tyres, sporting goods, footwear and as pressure-sensitive adhesives.[5, 7] The majority of commercial TPEs are petroleum-based, have a limited upper service temperature and have no end-of-life degradability.[8-10] As such, there is an opportunity for further research to maximize their performances.

An important class of TPEs are ABA block copolymers, where the 'B' block is a soft rubbery polymer with a glass transition temperature (T_g) below the operating temperature. The outer blocks, 'A', are glassy or semi-crystalline polymers with a T_g or T_m above the operating temperature.[7] When the relative volume fractions and $\overline{DP}$ of A and B are optimised, microphase separation of the blocks may occur yielding hard domains located within the soft matrix. For TPEs, the flexibility and extensibility of the overall material then arises from the soft B-blocks upon stretching and elastic recovery is provided by the physical crosslinking of the hard A-blocks.[11] Since the phase separation is a physical chain-linking, these TPEs can be recycled by thermal re-processing and, in the case, where ester/carbonate blocks are applied can be fully degraded after use.

For use as plasticizers, the lactide blocks allow for increased miscibility and reduction in leaching of the polymer.[12] Using blends, the properties of PLLA can be widely varied and improved. Giving access to materials with high impact strength, tensile strength and good heat resistance, especially when the

blends are highly miscible and compatible.[13-16] PLA is a commercial material with an annual demand in 2019 of 400,000 tones, improving the properties of this material will only help develop and grow the market further.[17]

The aim of this chapter is to apply the Co(III)K(I) catalysts to 'switch' catalysis to access new ABA-block copolymers. Catalyst **1**, described in Chapter 2 and 3, will be applied to switchable catalysis using allyl glycidyl ether (AGE), carbon dioxide and *L*-lactide.[18] First two polymerisations will be extensively explored i.e. AGE/CO_2 ROCOP to form poly(allyl glycidyl ether carbonate) (PAGEC) and *L*-LA ring-opening polymerisation (ROP) to form poly(*L*-lactic acid) (PLLA) using **1** (Fig. 4.1). The block polymer design targets poly(L-lactide acid) (PLLA) as the A-block since it should have a high T_m (151 °C) and a moderate T_g (around 58 °C).[19] The B-block poly(AGE-*co*-CO_2) (PAGEC), with a T_g of -12 °C.[20] If the molar mass or $\overline{DP}$ block can be maximized, these block polymers may undergo phase separation and show TPE performances.

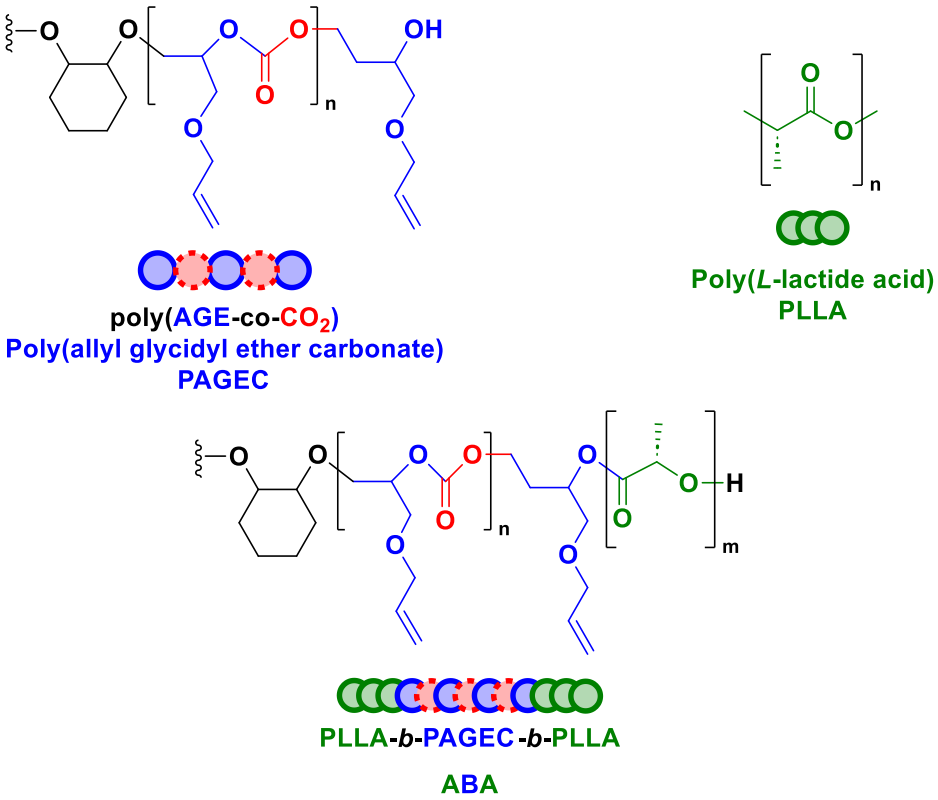
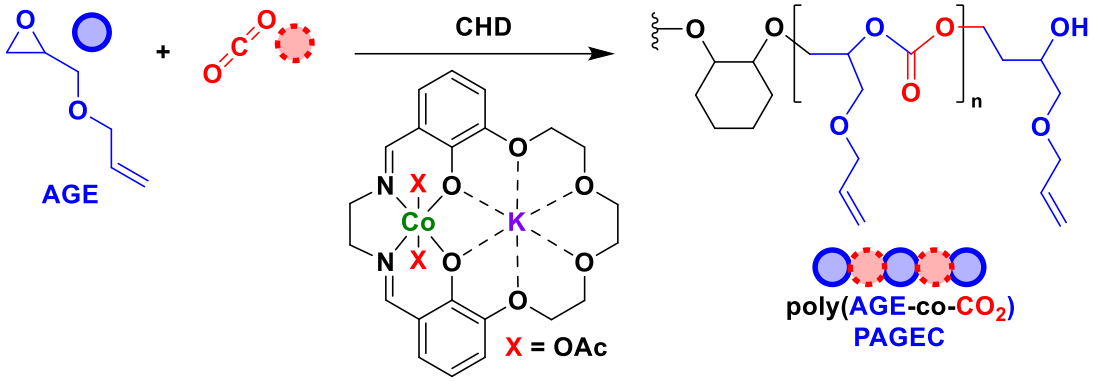


Figure 4.1 Polymer Structures.

4.2 Allyl Glycidyl Ether (AGE) and Carbon Dioxide Copolymerisation



Scheme 4.1 Allyl Glycidyl Ether (AGE) and Carbon Dioxide ROCOP (20 bar CO_2 pressure, neat AGE).

Catalyst **1** was first reported to be active for AGE/CO_2 ROCOP in 2020, with a TOF of 219 h^{-1}, >99% polycarbonate selectivity with a 1:4000 ratio of catalyst to monomer (0.025 mol% catalyst, 6 mL AGE (neat), 20 bar, 50 °C) (Scheme 4.1).[18] Although these results were very promising, a lower catalyst loading is needed to produce high molar mass PAGEC. High molar mass is expected to be required to access phase separated block polymers. Therefore, first an investigation of AGE/CO_2 ROCOP was undertaken to test the limits of the catalysis.

4.2.1 AGE/CO_2 ROCOP Optimisation

Table 4.1 Data for AGE/CO_2 ROCOP using **1**.[a]

#	CTA	Temp. (°C)	Conv. (%)[b]	TON[c]	PAGEC Selec. (%)[d]	TOF (h^{-1})[e]	M_n (kDa) [$Đ$][f]
1	CHD	50	40	4002	76	167	29.0 [1.06] 12.7 [1.05]
2	CHD	60	36	3602	79	150	50.8 [1.05] 24.4 [1.05] 10.7 [1.06]
3	BDM	50	42	4196	71	175	34.4 [1.06] 15.1 [1.06]
4	BDM	60	38	3753	57	156	20.6 [1.08] 8.7 [1.09]

Reaction conditions: Catalyst (0.01 mol %, 0.85 mM), AGE (10 mL, Neat), CTA (0.1 mol %, 8.5 mM), 20 bar CO_2, all polymerisations run for 24h. Cat:CTA:AGE = 1:10:10,000. [b]AGE conversion determined from the relative integrals in the ^{1}H NMR spectrum of PAGEC (4.96 ppm, 1H), CC (4.75 ppm, 1H), and PAGE (3.40-3.60 ppm, 3H) relative to the integral of allyl proton on all products and starting material (5.83 ppm, PAGEC 1H, CC 1H, PAGE 1H, AGE 1H) (Fig. 4.2). [c]Turnover number (TON) = number of moles of AGE consumed/ number of moles catalyst. [d]PAGEC selectivity determined by the relative integrals in the ^{1}H NMR spectrum of relative integrals in the ^{1}H NMR spectrum of PAGEC (4.96 ppm, 1H), CC (4.75 ppm, 1H), and PAGE (3.40-3.60 ppm, 3H). [e]Turnover frequency (TOF) = TON/time (h). [f]Determined by SEC analysis, in THF, calibrated with narrow-M_n polystyrene standards; dispersity values in parentheses (Fig. S4.1-S4.4).

The process of each reaction was assessed using the crude product and an example AGE/CO_2 crude product ^{1}H NMR spectrum in shown in Figure 4.2. When comparing the reactions, increasing the temperature, from 50 to 60 °C, unexpectedly had no effect on selectivity or rate (Table 4.1, entries 1 and 2). At lower catalyst loadings, the rate of polymerisation was retained, although a small decrease in polymer selectivity was observed. Nevertheless, overall the catalyst showed excelled activity and selectivity at low loadings (0.01 mol%, i.e. 1:10,000 cat:AGE). Furthermore, the catalyst retained selectivity and activity at higher temperature (60 °C).

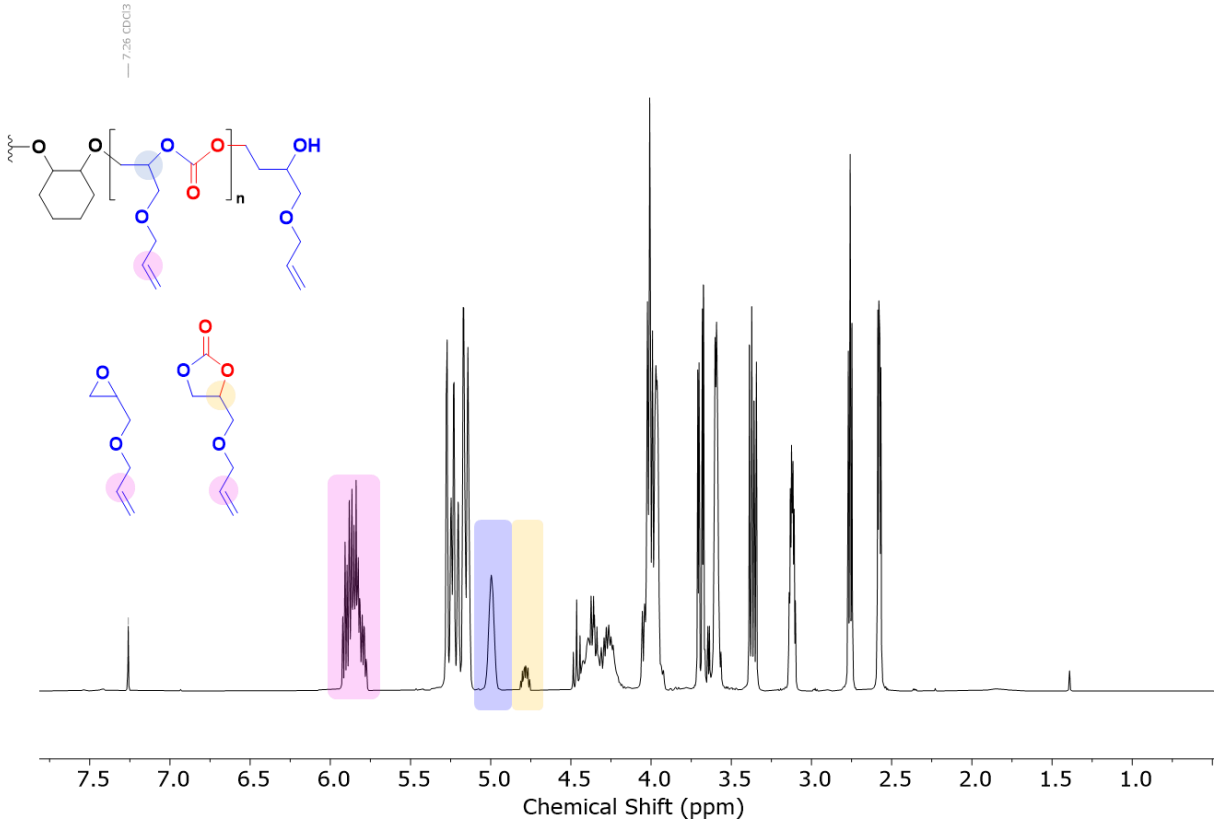


Figure 4.2 ^{1}H NMR spectrum ($CDCl_3$, 298K) of the crude product AGE/CO_2 polymerisation (Table 4.2, Entry 3).

Changing the chain transfer agent from *trans*-1,2-cyclohexanediol (CHD) to 1,4-benzene dimethanol (BDM) resulted in little to no change in activity, with a small drop in selectivity (Table 4.1, entry 1 and 3). The selectivity change could be due to the higher acidity of the primary BDM alcohols, further supported by the large reduction in selectivity observed with increasing temperature to 60 °C (entry 3 and 4). It is also possible that during the initiation period a larger quantity of cyclic carbonate is formed, thereby reducing overall selectivity.

Table 4.2 Catalyst loading and solvent assessment for AGE/CO_2 ROCOP using **1**.[a]

#	AGE Equiv.	Conv. (%)[b]	TON[c]	PAGEC Selec. (%)[d]	TOF (h^{-1})[e]	M_n (kDa) [$Đ$][f]
1	10,000	20	1962	89	49	10.4 [1.05]
2[g]	10,000	64	6354	82	132	57.7 [1.04] 29.9 [1.04] 13.0 [1.06]
3	20,000	46	9107	84	130	62.4 [1.04] 34.5 [1.03] 15.1 [1.07]
4[g]	20,000	18	3585	87	59	15.8 [1.05] 6.7 [1.03]
5	20,000	32	6481	89	135	29.8 [1.05] 13.3 [1.04]

[a]Reaction conditions: Catalyst, AGE (10 mL, Neat), 20 bar CO_2. Cat:CTA = 1:20. [b]AGE conversion determined from the relative integrals in the ^{1}H NMR spectrum of PAGEC (4.96 ppm, 1H), CC (4.75 ppm, 1H), and PAGE (3.40-3.60 ppm, 3H) relative to the integral of allyl proton on all products and starting material (5.83 ppm, PAGEC 1H, CC 1H, PAGE 1H, AGE 1H) (Fig. 4.2). [c]Turnover number (TON) = number of moles of AGE consumed/ number of moles catalyst. [d]PAGEC selectivity determined by the relative integrals in the ^{1}H NMR spectrum of relative integrals in the ^{1}H NMR spectrum of PAGEC (4.96 ppm, 1H), CC (4.75 ppm, 1H), and PAGE (3.40-3.60 ppm, 3H). [e]Turnover frequency (TOF) = TON/time (h). [f]Determined by SEC analysis, in THF, calibrated with narrow-M_n polystyrene standards; dispersity values in parentheses (Fig. S4.5-S4.9).[g] 20 v/v% THF used.

It was subsequently found that at lower conversions a higher polymer selectivity was observed (Table 4.2, entry 1). The increased viscosity at higher epoxide conversions may hinder intermolecular reactions, thereby promoting intramolecular backbiting to cyclic carbonate. At lower conversion only bimodal, and even monomodal, SEC traces were observed, while at conversions at or above 35% (in neat epoxide) a trimodal distribution was observed (Table 4.1 and 4.2, Fig. 4.3). The highest molar mass peak is tentatively ascribed to minor crosslinking of the allyl group. This was supported by findings that chains undergo rapid cross-linking in light and air, producing insoluble samples, which swelled upon addition of solvent. Attempts to lower the reaction mixture viscosity through dilution with THF failed, with multimodal SEC traces still observed at high conversion (Table 4.2, entry 2).

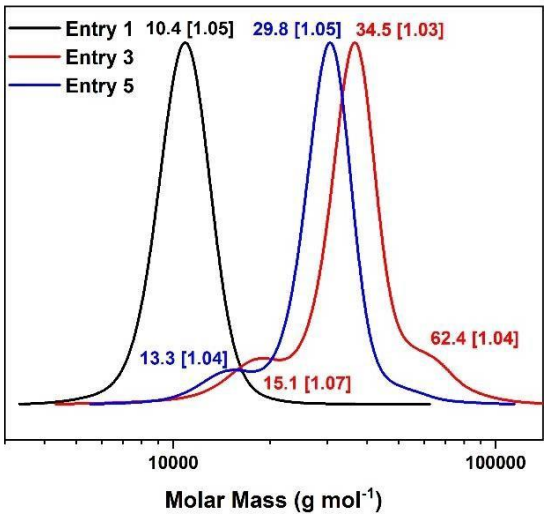


Figure 4.3 SEC traces of AGE/CO_2 ROCOP corresponding to entries 1, 3 and 5 from Table 4.2.

At 1:20,000 loadings, the activity of the catalyst was retained, with only a small decrease in selectivity (Table 4.2, entry 1 and 3). Dilution with THF at this loading resulted in a decrease in activity. In both neat and dilute experiments, multimodal molar mass distributions were observed, suggestive of chain cross-linking (Table 4.2, Entry 3 and 4). Finally, to mitigate alkene cross-linking, lower convesions of the AGE were targeted. Thus at 1:20,000 loading, the best selectivity (89%), activity (TOF 135 h^{-1}) and molar mass distributions were observed. These were the conditions used subsequently for block copolymer syntheses.

4.2.2 PAGEC Characterisation

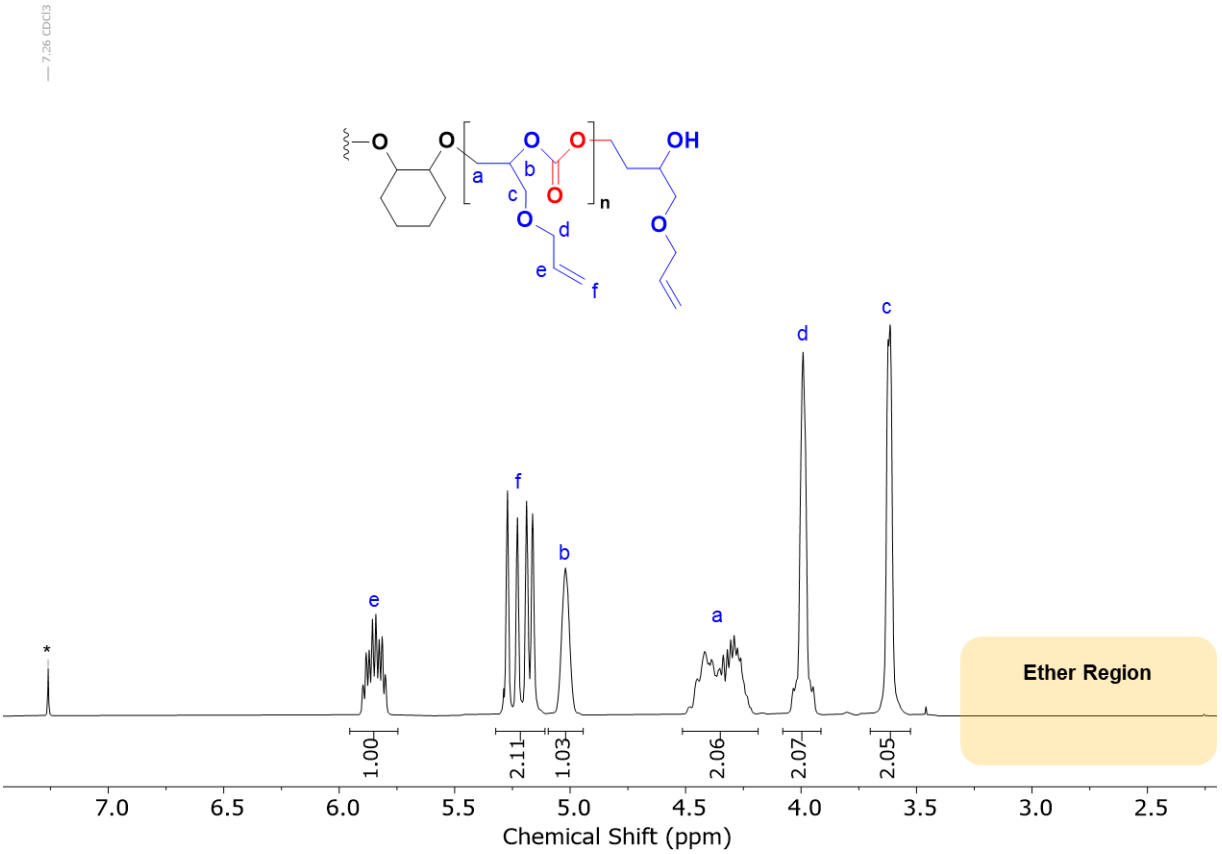


Figure 4.4 ^{1}H NMR spectrum ($CDCl_3$) of pure PAGEC. $CHCl_3$ marked by *.

The polycarbonate, PAGEC, was characterised using NMR, SEC and thermal methods. The polymer was purified by triple precipitation in methanol to yield a viscoelastic clear liquid. The ^{1}H NMR showed perfectly alternating PAGEC (Fig. 4.4). Notably, no ether resonances are observed, consistent with very high CO_2 selectivity with signals consistent with the proposed structure.

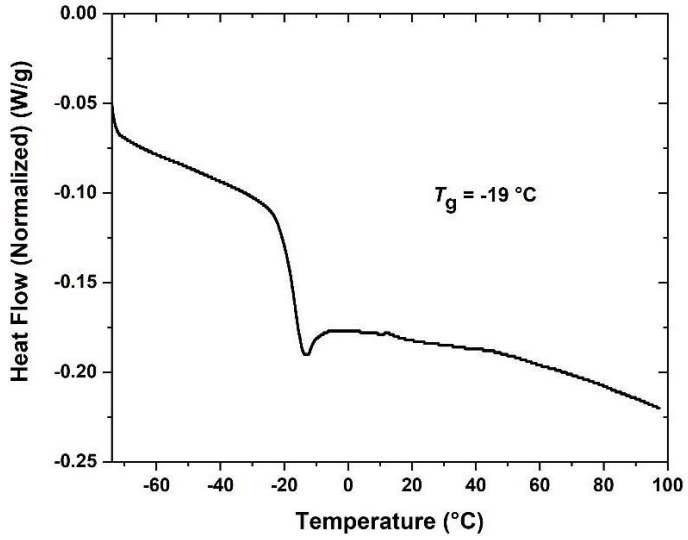


Figure 4.5 DSC performed on PAGEC (3rd heating cycle), showing its T_g = -19 °C (M_n = 27.8 kg mol-1, $Đ$ = 1.17).

The differential scanning calorimetry (DSC) trace shows a single glass transition temperature (T_g) at -19 °C, slightly lower than that reported (T_g of -12 °C) likely because of the low molecular weight of the sample (Fig. 4.5).[20] If phase separation can be achieved, this low T_g makes PAGEC an ideal soft block for thermal plastic elastomer (TPE) applications. Thermal gravimetric analysis (TGA) showed rapid thermal degradation with an onset temperature ($T_{d,\ onset}$) of 213 °C, giving a 200 °C processing window for the material (Fig. 4.6). These data are similar to PPC which showed a $T_{d,\ onse}$ of 217 °C (Chapter 2).

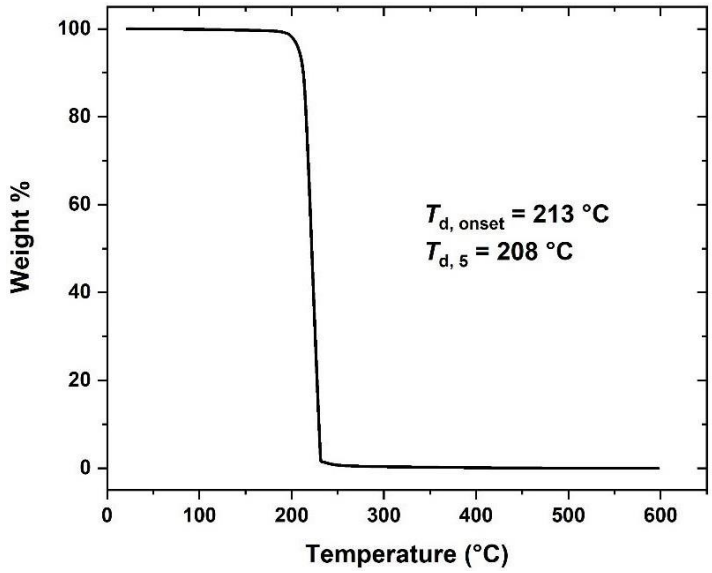
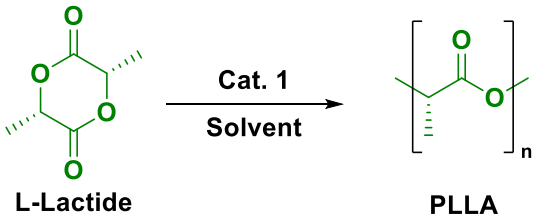


Figure 4.6 TGA data for PAGEC (M_n = 27.8 kg mol-1, $Đ$ = 1.17).

4.3 *L*-Lactide Ring-Opening Polymerisation



Scheme 4.2 Ring-opening polymerisation of *L*-lactide.

Although, ring-opening polymerisation (ROP) of *L*-lactide has been extensively studied, **1** has not been applied in this catalysis and so needs benchmarking (Scheme 4.2).[21]

4.3.1 Polymerisation Catalysis

1 was inactive with or without a small amount of epoxide present (Table 4.3, entry 1 and 2). It was previously reported that acetate ligands (on the catalyst) cannot initiate *L*-LA ROP.[22] Rather, when the epoxide is present it should be ring-opened by the acetate to form an alkoxide, which can initiate *L*-LA ROP. When conducting the ROP in neat AGE, at 50 °C, high lactide conversion (93%) was observed in 10 min resulting in a *L*-LA TOF of 558 h^{-1} (Table 4.3, entry 2).

Table 4.3 ROP of *L*-lactide with alternating solvents and temperature using cat. **1**.[a]

#	Solvent	Time (min)	Temp. (°C)	Conv. (%)[b]	TON[c]	TOF (h^{-1})[d]	M_n (kDa) [$Đ$][e]	$M_{n,\ Theoretical}$ (kDa)
1	PC (10 equiv. of AGE)	10	50	0	0	0	-	-
2	AGE	10	50	93	93	558	6.7 [1.09] 2.4 [1.15]	6.7
3	PC/AGE 1:1	10	50	89	89	534	2.4 [1.07] 1.0 [1.16]	6.4
4	PC/AGE 1:1	5	60	90	90	1080	3.0 [1.08] 1.0 [1.16]	6.5

[a]Reaction conditions: Catalyst (1 mol%, 6 mM), AGE, *L*-lactide (0.6 M). [b]*L*-lactide conversion determined from the relative integrals in the ^{1}H NMR spectrum of *L*-Lactide (1.64 ppm, 3H) and PLLA (1.56 ppm, 3H). [c]Turnover number (TON) = number of moles of lactide consumed/ number of moles catalyst. [d]Turnover frequency (TOF) = TON/time (h). [e]Determined by SEC analysis, in THF, calibrated with narrow-M_n polystyrene standards; dispersity values in parentheses and molar mass corrected using 0.58 correction factor (Fig. S4.10-S4.12).[23]

Upon dilution of the reaction mixture with propylene carbonate (PC) the activity remained very high but a significant drop in PLA molar mass was observed. This is most likely caused by the difficulty in drying PC, a very hydroscopic solvent, with water functioning as a CTA (by reacting with epoxide to generate diols). When increasing the temperature to 60 °C, higher rates were observed, TOF = 1080 h^{-1}.

All further polymerisations were conducted in neat AGE which was triply distilled, i.e. drier than most solvents. The catalyst loading was reduced to target higher molar mass PLLA and understand the limits of the catalysis. These reactions were conducted under reduced concentrations to allow the *L*-lactide to dissolve at the start of the reaction as well as limit viscosity effects on rate.

Table 4.4 *L*-Lactide polymerisations with **1** with different *L*-Lactide loadings.[a]

#	*L*-Lactide equiv.	Time (min)	Conv. (%)[b]	TON[c]	TOF (h^{-1})[d]	M_n (kDa) [$Đ$][e]	$M_{n,\ Theoretical}$ (kDa)
1	100	60	83	83	83	1.2 [1.14]	1.0
2	200	60	87	174	174	2.7 [1.26]	2.1
3	500	130	93	465	215	4.5 [1.25]	5.6
4[f]	1000	180	96	960	320	6.8 [1.12]	6.6

[a]Reaction conditions: Catalyst (2 mM), CHD (20 mM), AGE (4.5 mL, neat), *L*-lactide. [b]*L*-lactide conversion determined from the relative integrals in the ^{1}H NMR spectrum of *L*-Lactide (1.64 ppm, 3H) and PLLA (1.56 ppm, 3H). [c]Turnover number (TON) = number of moles of lactide consumed/ number of moles catalyst. [d]Turnover frequency (TOF) = TON/time (h). [e]Determined by SEC analysis, in THF, calibrated with narrow-M_n polystyrene standards; dispersity values in parentheses and molar mass corrected using 0.58 correction factor (Fig. S4.13-S4.16).[23] [f]CHD concentration increased to 40 mM.

Adding CHD to the polymerisation resulted in a reduction of the molar mass and ensured close agreement between the theoretical and measured PLLA molar mass (Table 4.3 and 4.4). Increasing concentration of *L*-lactide (0.2 M - 2 M) increased the catalytic activity as expected (Table 4.4). Doubling the concentration from 0.2M to 0.4M increased the rate, from 83 to 174 h^{-1} (Table 4.4, entry 1 and 2). Reactions using 500 equiv. of *L*-lactide resulted in a smaller increase in activity, but the PLLA molar mass was in good agreement with theoretical molar mass (Table 4.4, entry 3). At the lowest

loading, 1000 equiv. of *L*-lactide, the catalyst maintained high activity and good agreement between experimental and theoretical molar mass (Table 4.4, entry 4). These conditions represent a low loading for the field and demonstrate that catalyst **1** is suitable to use in 'switchable' polymerisations.

4.3.2 PLLA Characterisation

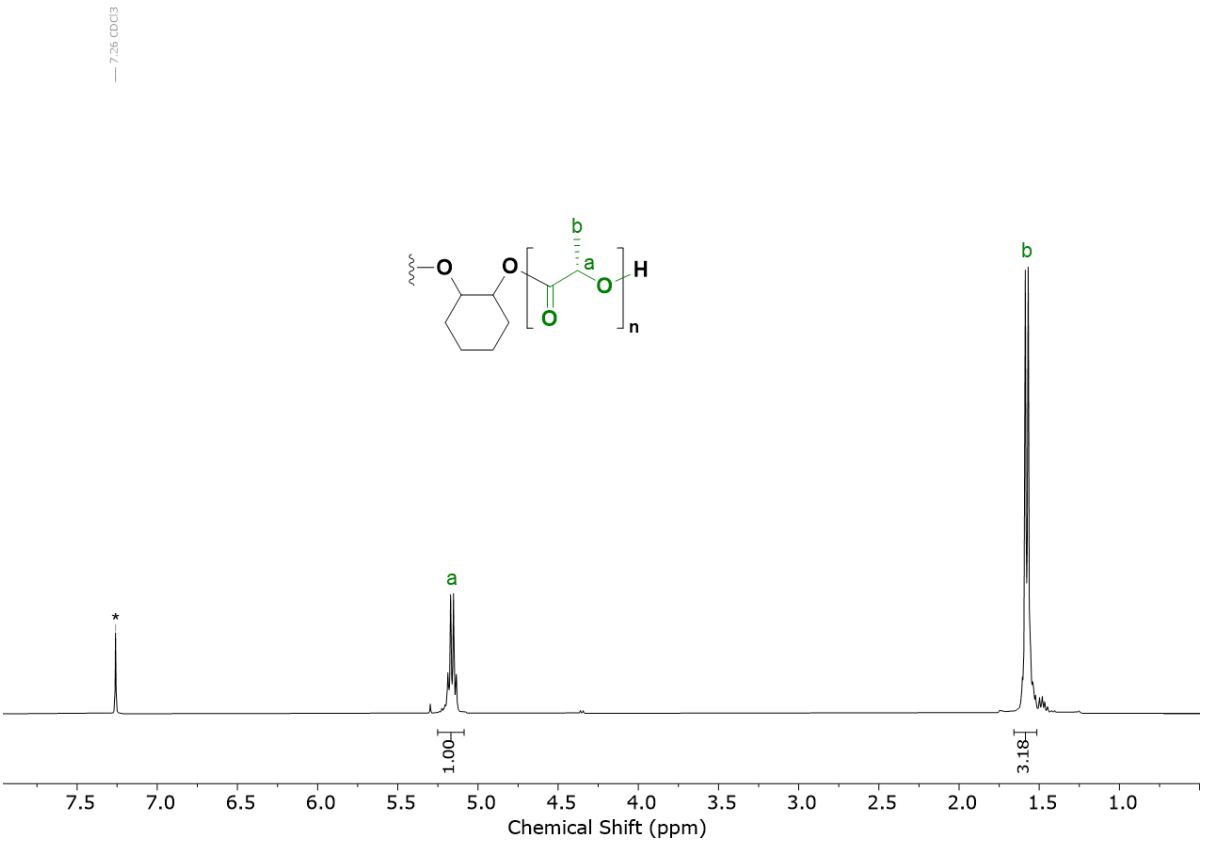


Figure 4.7 ^{1}H NMR spectrum ($CDCl_3$, 298K) of pure PLLA. $CHCl_3$ marked by *.

The crude PLLA dissolved DCM and triply precipitated from MeOH. The ^{1}H NMR of the purified PLLA shows the expected quartet for the α proton at 5.16 ppm (1H) and a doublet for the β protons at 1.58 ppm (3H, Fig. 4.7).

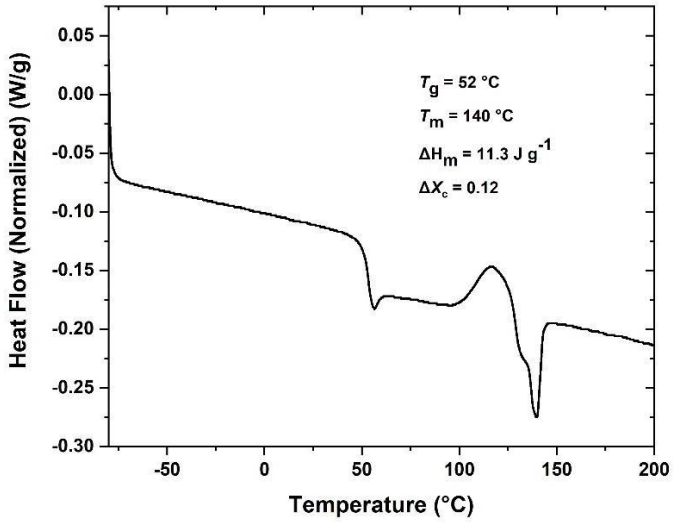


Figure 4.8 DSC of PLLA (3rd heating cycle), showing T_g = 52 °C and T_m = 140 °C (M_n = 6.8 kg mol^{-1}, $Đ$ = 1.12).

The DSC shows a T_g of 52 °C, consistent with literature samples (Fig. 4.8).[19, 24] Additionally, crystallisation and melt transition are observed. The T_m is 140 °C, which is consistent with other PLLA samples of this molar mass.[19, 24] The enthalpy of metling (ΔH_m), measured from the area of the metling peak, was 11.3 J g^{-1}. Fully crystalline PLLA has a ΔH_m of 93.1 J g^{-1}, giving a degree of crystallinity of 0.12.[24] The crystallinity of PLLA tends to be rather dependent on its processing, molar mass and dispersity.[25-26] The samples have moderate/low molar mass likely leading to low crystallinity. Furthermore, processing conditions have not been optimised to crystallinity.

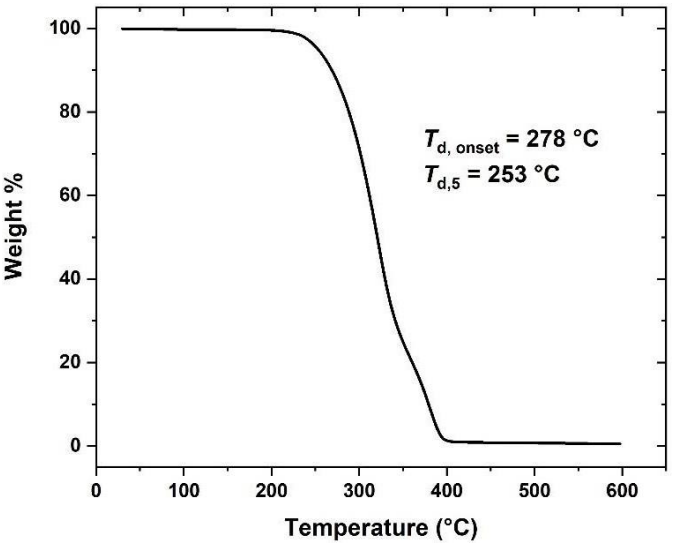
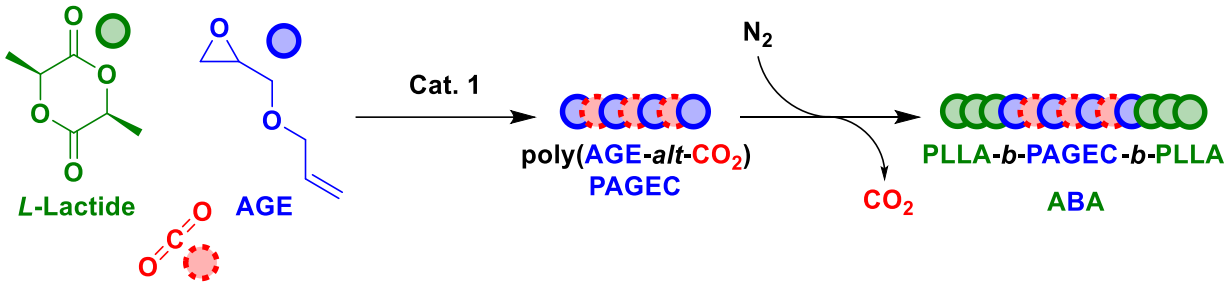


Figure 4.9 TGA of PLLA (M_n = 6.8 kg mol^{-1}, $Đ$ = 1.12).

TGA showed that the $T_{d, onset}$ was 278 °C, indicating the high thermal stability of the PLLA, compared to PAGEC (Fig. 4.9).

4.4 'Switchable' Catalysis using of AGE, CO_2 and *L*-Lactide



Scheme 4.3 Synthesis of block copolymers of AGE, CO_2 and *L*-Lactide, by 'switch' catalysis.

The synthesis of new block-copolymers featuring lactide and carbonates has been reported, but the syntheses either apply two separate catalysts or require isolation of first block before polymerisation of the second block.[12, 27] Here, a method is targeted allowing the synthesis of PAGEC-PLLA-PAGEC polymers with a single catalyst (**1**) using 'switchable' catalysis. To conduct these reactions requires an experimental protocol that allows switching between high pressure CO_2 gas, N_2 and vacuum (Scheme 4.3).

4.4.1 Building triple-manifold steel Schlenk line for high pressure CO_2 reactions

The experiments required a new Schlenk line which needed to be compatible with 25 and 100 mL Parr reactors and to allow switching between CO_2, N_2 and vacuum, easily and safely. A steel line was designed and all pieces had to be graded for both high pressure (up to 100 bar) and vacuum, adding further complexity to the design. Furthermore, safety features were incorporated.

The final design ensured vacuum and CO_2 gas flow could not occur simultaneously, this was achieved by introduction of a three-way valve. This valve also prevents accidental exposure of the cold trap and vacuum pump to high pressure CO_2 (Fig. 4.10 and 4.11). Furthermore, burst discs/emergency pressure release valves were installed in both the nitrogen and vacuum line, in case of accidental exposure to high-pressure gas. The steel Schlenk line also allows for the reaction vessels to be exposed to vacuum cycles to allow safe degassing of the reaction mixture.

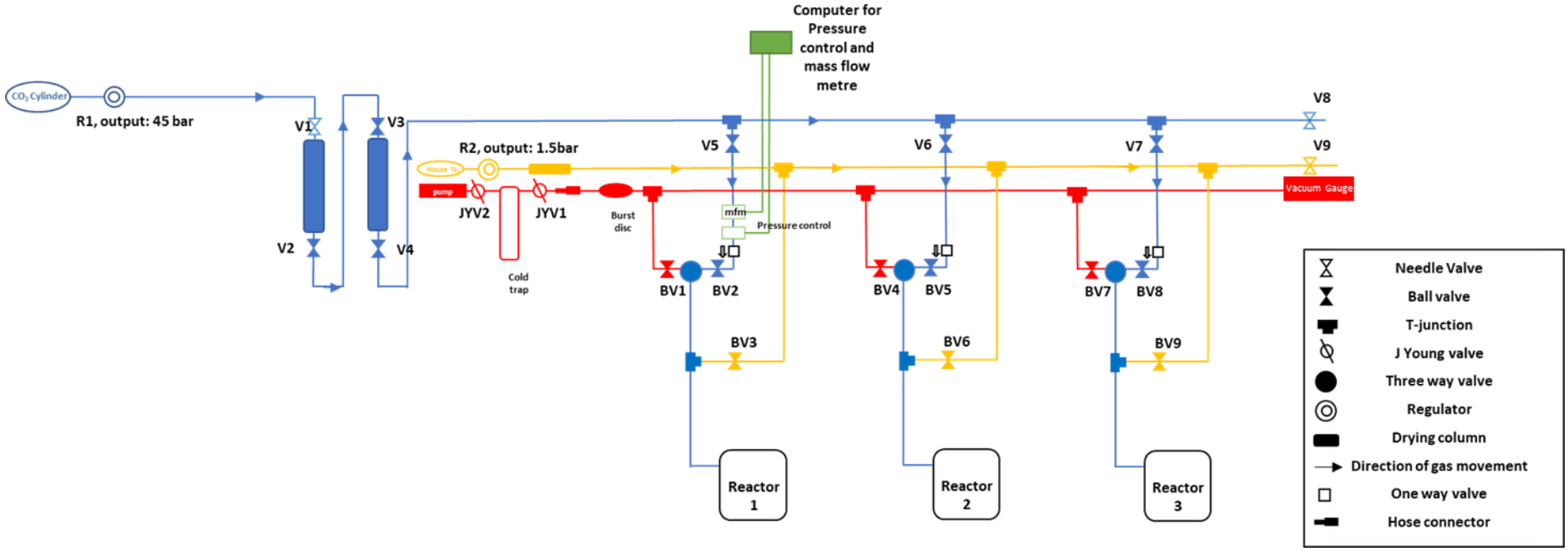


Figure 4.10 Diagram of triple-manifold steel Schlenk line for high pressure CO_2 reactions.



Figure 4.11 Picture of triple-manifold steel Schlenk line for high pressure CO_2 reactions.

4.4.2 Use of PAGEC chain transfer agent for *L*-lactide ROP

With a new set-up in hand and extensive exploration of the polymerisations of the two blocks separately, initial attempts were made to perform the 'switch' to form the block-copolymer. First the attempted use the PAGEC was tested as a macroinitiator for the *L*-lactide polymerisation.

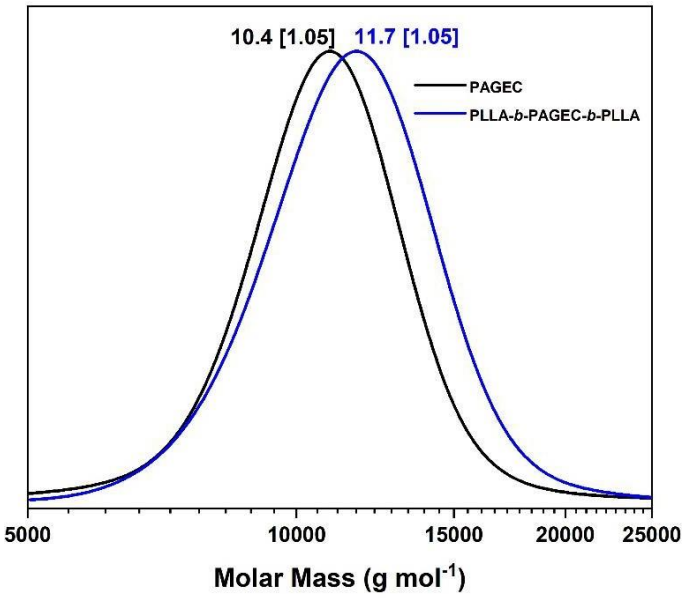


Figure 4.12 SEC traces of PAGEC and PLLA-*b*-PAGEC-*b*-PLLA of initial switch attempt.

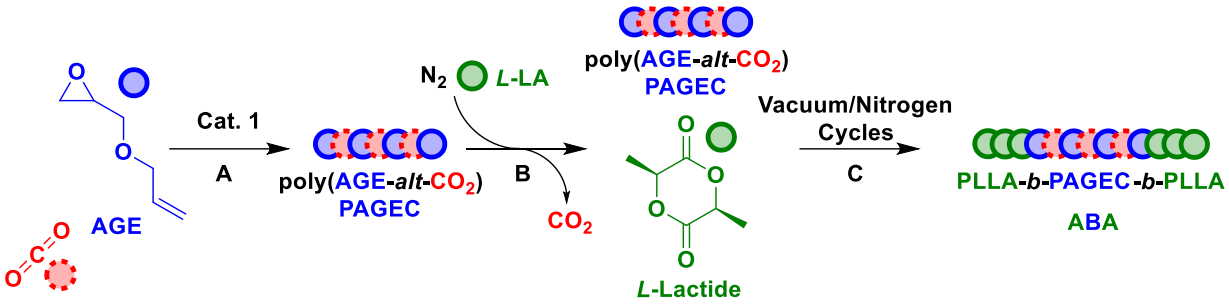
10 equiv. of PAGEC (10.4 kg mol^{-1}) was used as an initiator in the reaction, and reacted with 500 equiv. of *L*-lactide in 4.5 mL AGE at 50 °C and 115.5 mM *L*-LA concentration for 2 hours (Fig. 4.12, Table 4.5). The crude product was characterised by SEC and showed an increase in molar mass to 11.7 kg mol^{-1} (Fig. 4.12, Table 4.5). This data gives good evidence that the PAGEC block can initiate *L*-LA ROP and suggests 'switch' catalysis should be feasible.

Table 4.5 Data for the PAGEC initiated block polymer formation.[a]

PAGEC $M_{n,\,SEC}$ (KDa) [Đ][e]	Solvent	*L*-Lactide equiv.	Time (min)	Conv. (%)[b]	TON[c]	TOF (h^{-1})[d]	Overall $M_{n,\,SEC}$ (kDa) [Đ][e]
10.4 [1.05]	AGE	500	120	43	215	108	11.7 [1.05]

[a]Reaction conditions: Catalyst (0.5 mM), PAGEC (10 equiv., 5 mM), AGE (4.5 mL, neat), *L*-lactide (500 equiv., 115.6 mM. [b]*L*-lactide conversion determined from the relative integrals in the ^{1}H NMR spectrum of *L*-Lactide (1.64 ppm, 3H) and PLLA (1.56 ppm, 3H). [c]Turnover number (TON) = number of moles of PO consumed/ number of moles catalyst. [d]Turnover frequency (TOF) = TON/time (h). [e]Determined by SEC analysis, in THF, calibrated with narrow-M_n polystyrene standards; dispersity values in parentheses.

4.4.3 Switch Catalysis



Scheme 4.4 Detailed synthesis of block copolymers of AGE, CO_2 and *L*-Lactide, by 'switch' catalysis, 1:20:1,000:10,000 Cat:CHD:*L*-LA:AGE, 7.5 mL (initial) AGE (neat), 50 °C, 20 bar CO_2. Split into **A** ROCOP of AGE/CO_2, **B** addition of *L*-LA and **C** vacuum/nitrogen cycles and *L*-LA ROP.

Next, the 'switch' reaction was investigated by first charging the reactor with AGE (7.5 mL), **1** and CHD (1:20 cat:CHD) (scheme 4.4). The reactor was pressurised with 20 bar CO_2 and heated to 50 °C. After 17.5 h, 11% conversion of AGE was observed and the CO_2 was released (PAGEC selec. 83%). Then a solution of *L*-lactide (1000 equiv.), in AGE (4 mL), was injected and the solution was degassed by 10 vacuum/nitrogen cycles. Given that the rate law for ROCOP using **1** has a zero-order CO_2 pressure dependence, indicating rapid CO_2 insertion rates, the solution must be thoroughly degassed in order to ensure an alkoxide chain-end present (as the carbonate cannot initiate) to initiate the *L*-LA ROP. The reaction was undertaken using SEC, NMR spectroscopy, DSC and TGA to establish block polymer formation.[1, 4, 28-29]

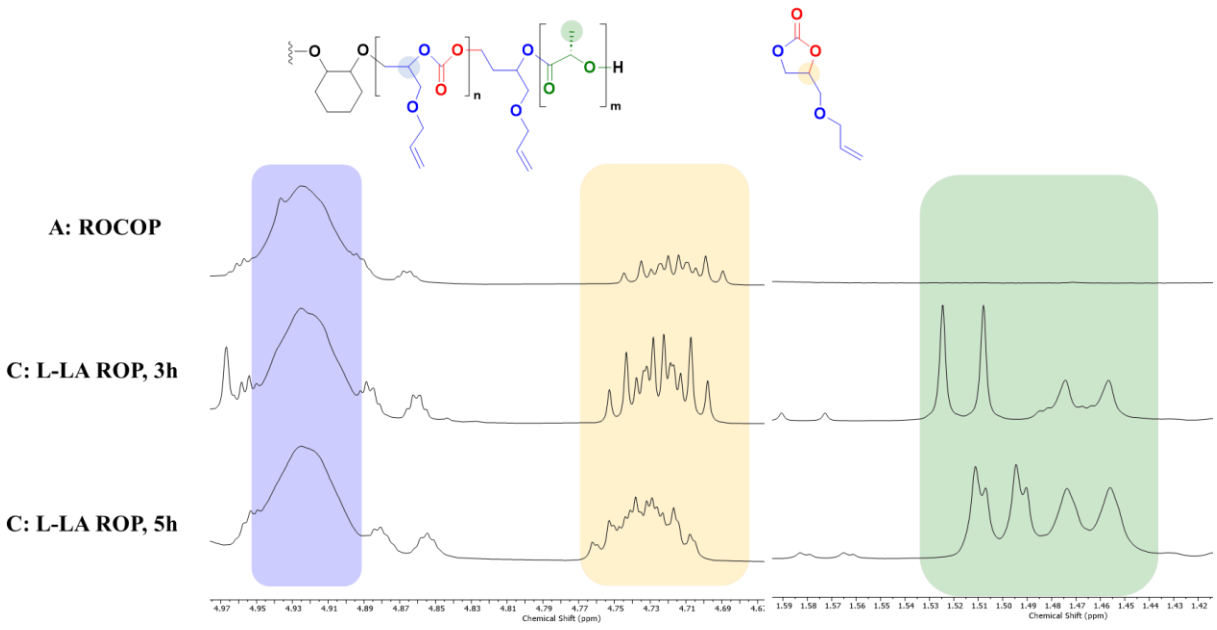


Figure 4.13 ^{1}H NMR spectra ($CDCl_3$) showing PAGEC and then PLLA-PAGEC-PLLA formation.

The ^{1}H NMR spectrum of aliquots taken throughout the reaction confirm the initial formation of the polycarbonate (Fig. 4.13). After 17.5 h, the *L*-lactide was added and its conversion was observed over the next 5 h, before the reaction is quenched and the polymer isolated (Fig. 4.13). *L*-LA conversion was 55% compared to 11% AGE conversion, giving a theoretical molar ratio of 61:39 PAGEC:PLLA.

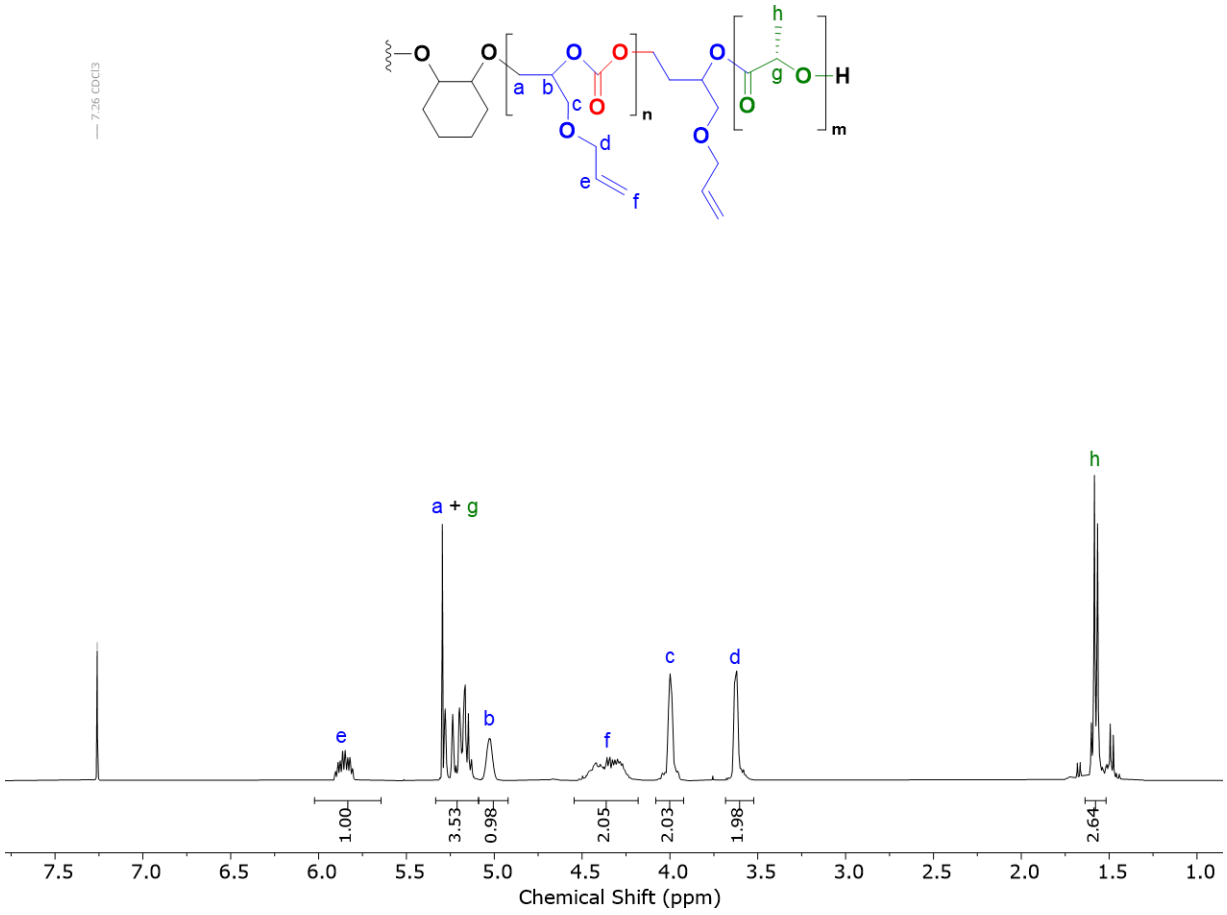


Figure 4.14 ^{1}H NMR spectrum of pure PLLA-*b*-PAGEC-*b*-PLLA with peak assignments.

The block-polymer was isolated by triple precipitation from methanol. Its ^{1}H NMR is consistent with resonances for both PAGEC and PLLA blocks (Fig. 4.4, 4.7 and 4.14). The ^{1}H NMR shows that the one of the PAGEC carbonate resonances overlap with the ester resonance of the PLLA block at 5.22 ppm (Fig. 4.7 and 4.14, a + g). The other carbonate resonance of the PAGEC remains a broad singlet at 5.03 ppm and all the side chain resonances also remain unchanged (Fig. 4.4 and Fig. 4.14). The methyl group in the PLLA is a doublet at 1.56 ppm, as expected. By NMR, the PLLA content of the overall material is 47 mol% corresponding to 38 weight%. This is higher than expected when compared to the conversions of the monomers (39 mol% PLLA), indicating some of the PAGEC chains may not have initiated the ROP and been removed during purification of the PLLA-PAGEC-PLLA.

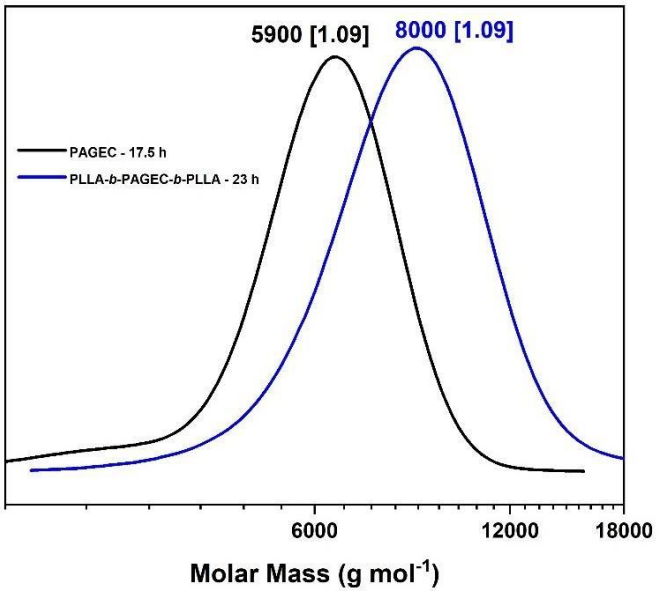


Figure 4.15 SEC traces of 'switch' before and after addition of *L*-lactide.

The SEC traces also showed an increase in molar mass after the addition of *L*-lactide, indicating block polymer formation (Fig. 4.15). This data provides strong evidence for block formation as there is no CO_2 present so further polycarbonate formation would be unfeasible. The SEC data shows a lower increase in molar mass than expected based on both the conversion and the PLLA content of the pure block polymer. The lower weight% PLLA by SEC likely arises from the inherent inaccuracy of the SEC as it is calibrated with a polystyrene standard and is generally found to be poor at determining accurate molar masses for block polymers. Both techniques support the formation of a block polymer.

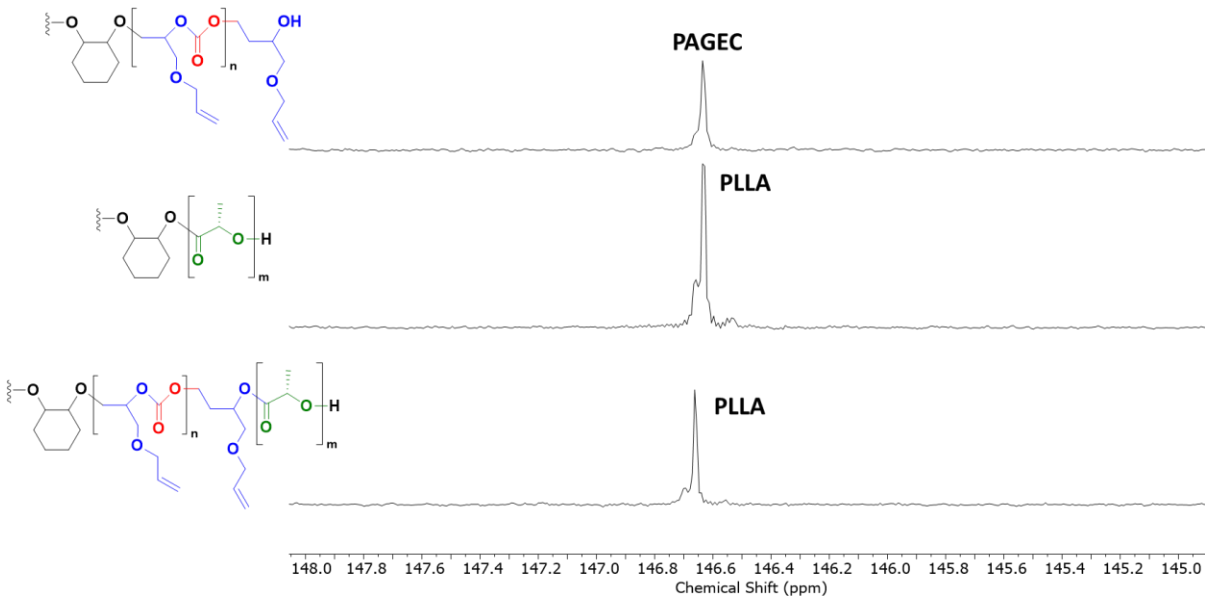


Fig. 4.16 ^{31}P NMR spectrum ($CDCl_3$, 298K) of phosphorous end-group titration of PAGEC, PLLA and the block-copolymer.

The ^{31}P NMR end-group titration experiment was conducted using PAGEC, PLLA and the block polymer to characterise the end-group chemistry.[30] The phosphorous end-group titration involves the reaction of the polymer end-groups with excess solution of 2-chloro-4,4,5,5-tetramethyldiozaphospholane. A solution of Bisphenol A (BPA) is added as a calibrant to allow accurate comparison between different spectra.[30] The ^{31}P NMR spectra show distinctive single signals for the polymers (Fig. 4.16). Comparison of the PAGEC and PLLA chemical shifts shows that both occur at equivalent values (146.65 ppm) and so cannot be distinguished by this method (Fig. 4.16). The PLLA signal has a distinct lower intensity shoulder at slightly higher chemical shift which is not observed for PAGEC (Fig. 4.16). This same PLLA shape for the block polymer.

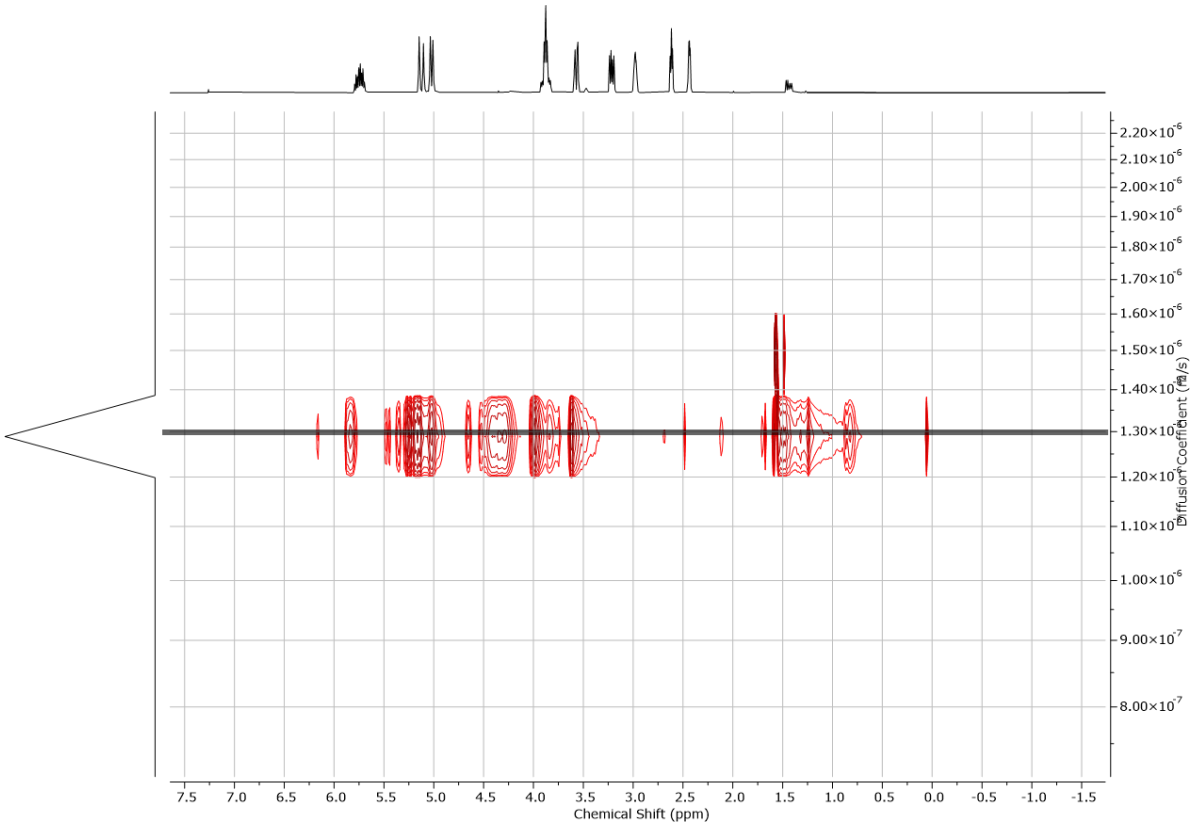


Fig. 4.17 ^{1}H DOSY NMR spectrum ($CDCl_3$, 298K) the PLLA-PAGEC-PLLA.

Final evidence for the block formation comes from the DOSY spectrum which shows a single diffusion coefficient for all polymer resonances, meaning a single chain is present containing both PLLA and PAGEC blocks (Fig. 4.17).

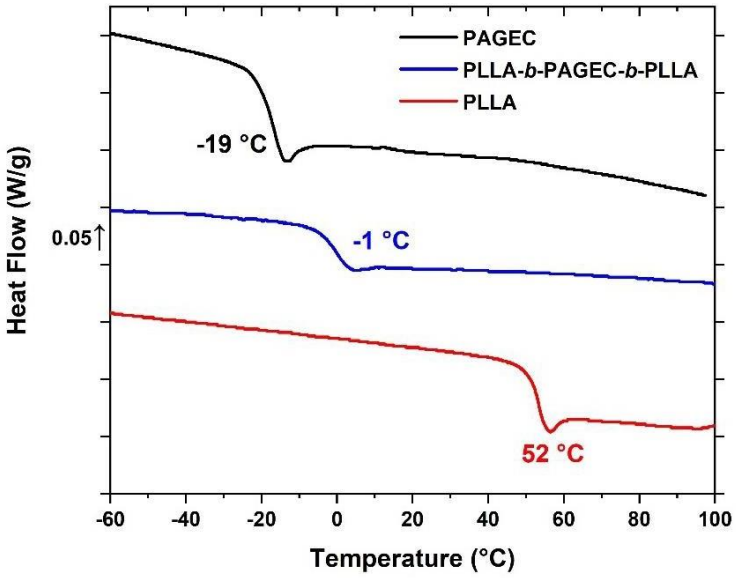


Figure 4.18 DSC traces for PAGEC, PLLA-*b*-PAGEC-*b*-PLLA triblock-copolymer and PLLA (third cycles).

The T_g for PLLA-PAGEC-PLLA is -1 °C (Fig. 4.18). This is in between the T_gs of the individual blocks, indictive of block miscibility, which most likely occurs due to the low overall polymer molar mass. The T_g corresponds well with that predicted by the Fox equation, -0.4 °C *versus* -1 °C, giving further evidence for block miscibility.[31] The TGA of the block-polymer shows a $T_{d,\ onset}$ of 232 °C, again between the two homopolymers, it also highlights the increased thermal stability after addition of the PLLA end-blocks (Fig. 4.19).

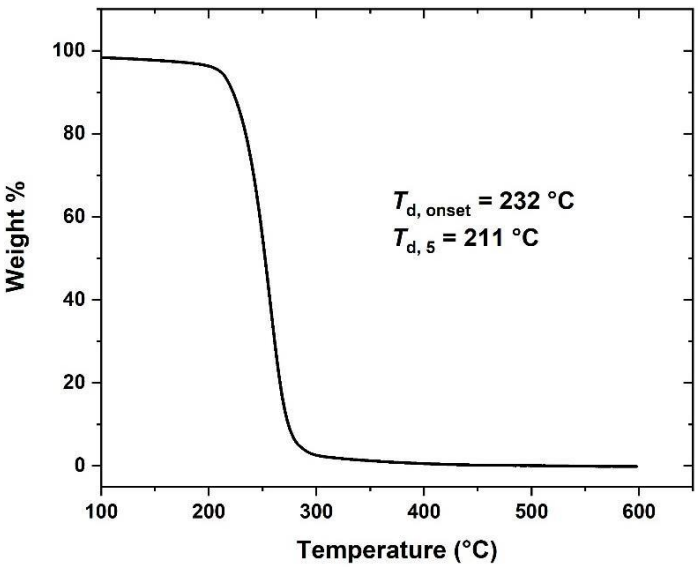


Figure 4.19 TGA of PLLA-*b*-PAGEC-*b*-PLLA triblock-copolymer.

4.5 Discussion

The copolymerisation AGE/CO_2 has been previously reported, with selectivity for polymer over cyclic carbonate being a key issue.[20] For example, Feng and co-workers explored a wide range of polycarbonates by the ROCOP of various epoxides and CO_2.[20] They were able to synthesis PAGEC of M_n = 45 kg mol^{-1}, with a T_g of -12 °C. This molar is higher than that reported here, and correlates with a higher T_g. They were subsequently able to make a block polycarbonate thermoplastic elastomer, by the sequential polymerisation of 1-octene oxide (OO) with CO_2, followed by CHO/CO_2. Wu and co-workers reported a ABA block polymer synthesis, featuring PAGEC and PCHC blocks.[32]

These prior experiments highlight the potential for PAGEC as a 'soft block' and in copolymers. To access high molar mass polymers requires dry monomers (both CO_2 and AGE) and efficient catalysis. In this thesis, the CO_2 was dried through two carbon dioxide purifiers (VICI Metronics carbon dioxide purifier) in series, with the ROCOP furnishing moderate molar mass PAGEC. In contrast, Feng and Wu used CO_2 dried by reaction with triisobutylaluminum (TiBA), a significant safety risk to handle. They also distilled their AGE 5 times and applied catalysts without initiators allowing for both molar mass and end-group control. In this thesis, the acetate initiators in catalyst **1** are responsible for bimodal molar mass distributions. Furthermore, **1** needs more development for 'switch' catalysis.

As stated previously, few catalysts function in ROCOP with PO and alkylene oxides and lactide ROP.[12, 27, 33] In this thesis, a single catalyst was discovered for 'switch' catalysis, functioning well for both alkylene oxide/CO_2 ROCOP and lactide ROP.

The rules of 'switch' catalysis determine that lactone ROP generally occurs after CO_2/epoxide ROCOP.[4, 34] The selectivity arises from the fast rates of CO_2 insertion and stabilised carbonate relative to alkoxide intermediates.[18, 35-37] Even low concentrations of CO_2 drives carbonate intermediate formation and prevents lactide ROP. One practical implication is that even switches using CO_2/anhydride/epoxide do not suffer the same problem, as rates of anhydride insertion are faster than CO_2.[38]

Here a new triple manifold steel Schlenk line allows for the switching to be conducted using CO_2 and high-pressure reactors. Furthermore, the set-up allows for vacuum-nitrogen cycles to be applied to the solution with stirring and at elevated temperatures. As CO_2 solubility decreases with temperature, this set-up allows for efficient degassing of the solution and the 'switch' in mechanism to take place. The degassing is key to the 'switch' in mechanism and it was found that 10 cycles of vacuum/nitrogen were necessary to remove the CO_2.

The block polymer produced showed low molar mass, resulting in miscibility of the blocks. The copolymer shows low T_g which could lead to applications in PLLA toughening or blend compatibilization.[39-40] The lactide monomer should allow for good miscibility with PLLA. Using polymeric plasticizer useful to prevent leaching. The goal would be to increase the elasticity and hence reduce brittleness.[12-16] It is also important to maintain impact strength, tensile strength and heat resistance. PLA is a commercial material with an annual demand in 2019 of 400,000 tones, improving properties should help develop its applications.[17] For the copolymers in this work, the PLLA block should be tuned, perhaps targeting greater PLLA content to increase miscibility with PLA. This objective could be achieved by increasing the loading of lactide as the catalyst has been shown to be highly loading tolerant.

A further application, could be to make ABA block polymer thermoplastic elastomers. Soft mid-block polycarbonates from epoxide/CO_2 ROCOP are rare due to limitations in the catalysis and lack of selectivity for many catalysts.[41-42]

4.6 Conclusion and Outlook

In summary, a new catalyst (**1**) and switch methodology were discovered using AGE/CO_2 ROCOP and lactide ROP. First, the two separate polymerisations were explored and then the 'switch' was optimised. Proofs of the 'switch' and block polymer formation were obtained using spectroscopy, GPC and thermal methods. The new block polymer showed M_n of 8000 g mol^{-1} and T_g of -1 °C.

There is significant promise in this method and future work should focus on expanding the range of polymers produced. Post functionalisation reactions on the PAGEC blocks should be feasible by reactions at the allyl group, e.g. thiol-ene click. This would also prevent allyl cross-linking reactions, which were a significant issue.

Further investigation should prioritise investigation using 1-hexene oxide, 1-octene oxide or butyl glycidyl ether (Fig. 4.20). These are all known to produce polycarbonates with low T_g's, which would be good candidates for soft blocks in polymers.[20] Feng also showed that these epoxides give better selectivities for polymer over cyclic carbonate and cross-linking side reactions not possible. Of these butyl glycidyl ether is similar to AGE so would make a suitable replacement. Catalyst **1** should be able to polymerise all these epoxides with CO_2, making them preferred candidates for investigation.

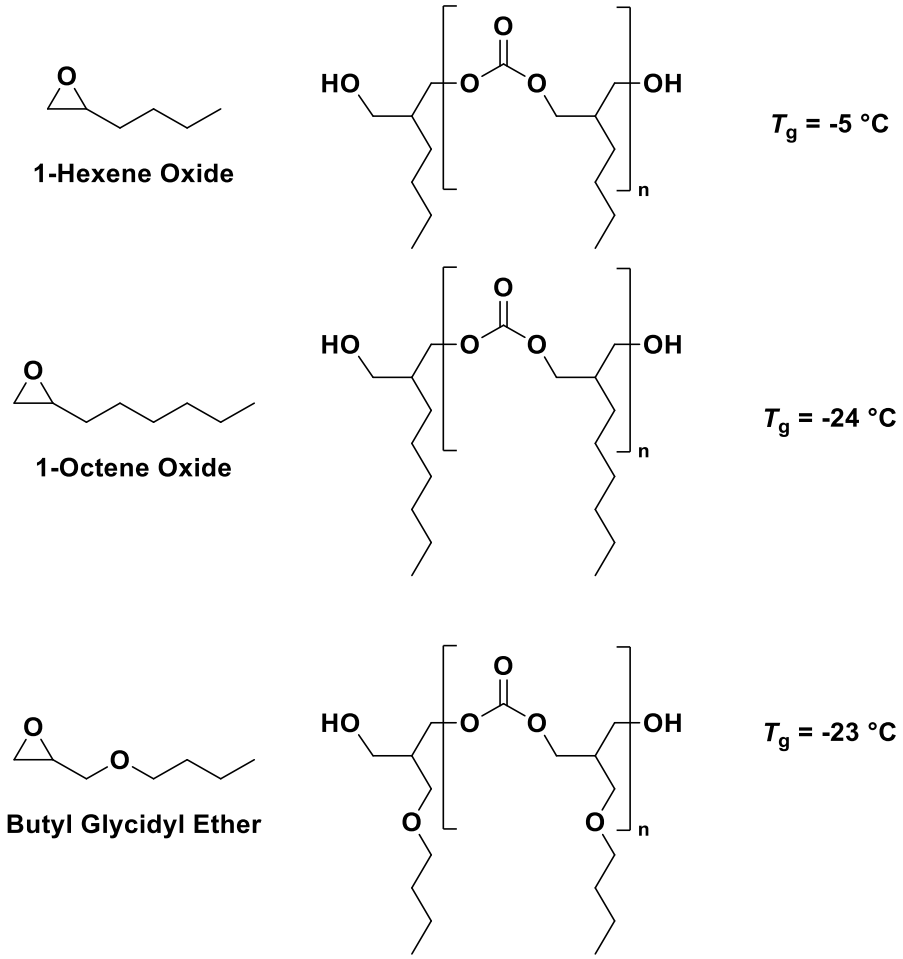


Figure 4.20 Alternative epoxides/polycarbonates and the T_gs.

Further investigation of the low molar mass polymers as plasticizers and tougheners PLA or PCHC could be performed. This investigation should target difference epoxides to block-copolymer in PLA blends could also be performed. This could be done in combination with the exploration of different epoxides understand structure-performance relationships.

4.7 References

1. Yuntawattana, N.; Gregory, G. L.; Carrodeguas, L. P.; Williams, C. K., *ACS Macro Lett.* **2021,** *10*, 774-779.
2. Kernbichl, S.; Reiter, M.; Adams, F.; Vagin, S.; Rieger, B., *J. Am. Chem. Soc.* **2017,** *139*, 6787-6790.
3. Romain, C.; Williams, C. K., *Angew. Chem. Int. Ed.* **2014,** *53*, 1607-1610.
4. Deacy, A. C.; Gregory, G. L.; Sulley, G. S.; Chen, T. T. D.; Williams, C. K., *J. Am. Chem. Soc.* **2021,** *143*, 10021-10040.
5. Schneiderman, D. K.; Hillmyer, M. A., *Macromolecules* **2017,** *50*, 3733-3749.
6. Wang, W.; Lu, W.; Goodwin, A.; Wang, H.; Yin, P.; Kang, N.-G.; Hong, K.; Mays, J. W., *Prog. Polym. Sci.* **2019,** *95*, 1-31.
7. Bates, F. S.; Hillmyer, M. A.; Lodge, T. P.; Bates, C. M.; Delaney, K. T.; Fredrickson, G. H., *Science* **2012,** *336*, 434-440.
8. Fagnani, D. E.; Tami, J. L.; Copley, G.; Clemons, M. N.; Getzler, Y. D. Y. L.; McNeil, A. J., *ACS Macro Lett.* **2021,** *10*, 41-53.
9. Zhu, Y.; Romain, C.; Williams, C. K., *Nature* **2016,** *540*, 354-362.
10. Coates, G. W.; Getzler, Y. D. Y. L., *Nature Reviews Materials* **2020,** *5*, 501-516.
11. DiCiccio, A. M.; Coates, G. W., *J. Am. Chem. Soc.* **2011,** *133*, 10724-7.
12. Darensbourg, D. J.; Wu, G. P., *Angew. Chem. Int. Ed. Engl.* **2013,** *52*, 10602-6.
13. Wang, Y.; Chiao, S. M.; Hung, T. F.; Yang, S. Y., *J. Appl. Polym. Sci.* **2012,** *125*.
14. Phuong, V. T.; Coltelli, M.-B.; Cinelli, P.; Cifelli, M.; Verstichel, S.; Lazzeri, A., *Polymer* **2014,** *55*, 4498-4513.
15. Lin, L.; Deng, C.; Lin, G.-P.; Wang, Y.-Z., *Ind. Eng. Chem. Res.* **2015,** *54*, 5643-5655.
16. Yuryev, Y.; Mohanty, A. K.; Misra, M., *Composites, Part B* **2017,** *130*, 158-166.
17. Mehmood, A.; Raina, N.; Phakeenuya, V.; Wonganu, B.; Cheenkachorn, K., *Mater. Today: Proc.* **2022**.
18. Deacy, A. C.; Moreby, E.; Phanopoulos, A.; Williams, C. K., *J. Am. Chem. Soc.* **2020,** *142*, 19150-19160.
19. Srithep, Y.; Pholharn, D.; Morris, J., *AIP Conf. Proc.* **2019,** *2065*, 030019.
20. Jia, M.; Zhang, D.; de Kort, G. W.; Wilsens, C.; Rastogi, S.; Hadjichristidis, N.; Gnanou, Y.; Feng, X., *Macromolecules* **2020,** *53*, 5297-5307.
21. Dechy-Cabaret, O.; Martin-Vaca, B.; Bourissou, D., *Chem. Rev.* **2004,** *104*, 6147-6176.
22. Pholharn, D.; Srithep, Y.; Morris, J., *IOP Conference Series: Materials Science and Engineering* **2017,** *213*, 012022.
23. Baran, J.; Duda, A.; Kowalski, A.; Szymanski, R.; Penczek, S., *Macromol. Rapid Commun.* **1997,** *18*, 325-333.
24. Ahmed, J.; Rahman, M. S.; Roos, Y. H., *Glass Transition and Phase Transitions in Food and Biological Materials*. Wiley: 2017.
25. Kawai, T.; Rahman, N.; Matsuba, G.; Nishida, K.; Kanaya, T.; Nakano, M.; Okamoto, H.; Kawada, J.; Usuki, A.; Honma, N.; Nakajima, K.; Matsuda, M., *Macromolecules* **2007,** *40*, 9463-9469.
26. Hernández Sánchez, F.; Molina Mateo, J.; Romero Colomer, F. J.; Salmerón Sánchez, M.; Gómez Ribelles, J. L.; Mano, J. F., *Biomacromolecules* **2005,** *6*, 3283-3290.
27. Zhang, Y.-Y.; Zhang, X.-H.; Wei, R.-J.; Du, B.-Y.; Fan, Z.-Q.; Qi, G.-R., *RSC Adv.* **2014,** *4*, 36183-36188.
28. Stosser, T.; Mulryan, D.; Williams, C. K., *Angew. Chem. Int. Ed. Engl.* **2018,** *57*, 16893-16897.
29. Stößer, T.; Chen, T. T. D.; Zhu, Y.; Williams, C. K., *Phil. Trans. R. Soc. A* **2017,** *376*, 20170066.
30. Spyros, A.; Argyropoulos, D. S.; Marchessault, R. H., *Macromolecules* **1997,** *30*, 327-329.
31. Fox T, G., *Bull. Am. Phys. Soc.* **1956,** *1*, 123.
32. Yang, G.-W.; Wu, G.-P., *ACS Sustainable Chem. Eng.* **2019,** *7*, 1372-1380.
33. Li, X.; Duan, R.-l.; Hu, C.-y.; Pang, X.; Deng, M.-x., *Polym. Chem.* **2021,** *12*, 1700-1706.
34. Sulley, G. S.; Gregory, G. L.; Chen, T. T. D.; Pena Carrodeguas, L.; Trott, G.; Santmarti, A.; Lee, K. Y.; Terrill, N. J.; Williams, C. K., *J. Am. Chem. Soc.* **2020,** *142*, 4367-4378.
35. Darensbourg, D. J.; Yarbrough, J. C., *J. Am. Chem. Soc.* **2002,** *124*, 6335-6342.
36. Lindeboom, W.; Fraser, D. A. X.; Durr, C. B.; Williams, C. K., *Chem. Eur. J.* **2021,** *27*, 12224.
37. Trott, G.; Garden, J. A.; Williams, C. K., *Chem. Sci.* **2019,** *10*, 4618-4627.
38. Rosetto, G.; Deacy, A. C.; Williams, C. K., *Chem. Sci.* **2021,** *12*, 12315-12325.
39. Deeraj, B. D. S.; Jayan, J. S.; Saritha, A.; Joseph, K., 8 - PLA-based blends and composites. In *Biodegradable Polymers, Blends and Composites*, Mavinkere Rangappa, S.; Parameswaranpillai, J.; Siengchin, S.; Ramesh, M., Eds. Woodhead Publishing: 2022; pp 237-281.
40. Luinstra, G. A., *Polymer Reviews* **2008,** *48*, 192-219.
41. Trott, G.; Saini, P. K.; Williams, C. K., *Phil. Trans. R. Soc. A* **2016,** *374*, 20150085.
42. Liu, Z.; Torrent, M.; Morokuma, K., *Organometallics* **2002,** *21*, 1056-1071.

Chapter 5

Thesis Conclusion and Outlook

5.1 Thesis Summary

This thesis has detailed the development and investigation of Co(III)K(I) catalysts for the ROCOP of epoxides and CO_2. Application of these catalysts to the ROP of *L*-lactide, and hence switchable catalysis, was also explored. The work presented focused on two areas:

1) Heterobimetallic catalysts for PO/CO_2 ROCOP.

   Prior to this work our group discovered the first heterodinuclear catalysts for PO/CO_2 ROCOP. The mechanism was unknown, so a detailed investigation into the kinetics and mechanism by which the Co(III)K(I) complex operates in PO/CO_2 ROCOP was conducted (Fig. 5.1). It was proposed that the rate determining step was the ring-opening of the epoxide, occuring *via* coordination of the epoxide at the Co(III) centre with the nucleophilic carbonate coordinated to the K(I) centre. Furthermore, the CO_2 insertion was found to be reversible under the reaction conditions, with the position of the equilibrium being key to selectivity for PPC over cyclic carbonate formation. A detailed study of the formation of cyclic carbonate using catalyst **1** revealed that the cyclic carbonate formation occurred exclusively from the alkoxide intermediate, likely through a combination of chain-end 'unzipping' and random chain scission mechanism.

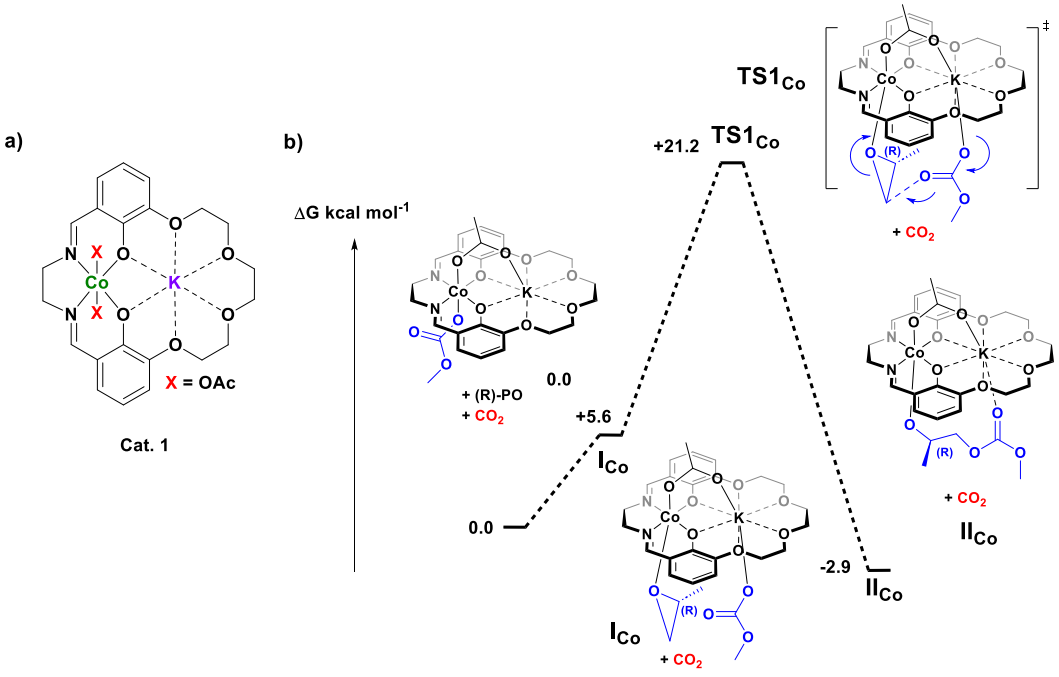


Figure 5.1 Structure of catalyst **1** and proposed RDS (by DFT).

The mechanism was used to support the synthesis of 6 new catalysts for PO/CO_2 ROCOP. The ligand was substituted with the objective of altering the electron density at the Co(III) centre and the effects of these changes on catalysis were investigated. A linear relationship between the Co(III/II) redox potential and the activity of the complexes was observed. The most electron rich complex (**1**) exhibits the highest activity. This discovery is very unusual since all prior structure-activity relationships, using many different catalysts, were inconclusive. This highlights that this direct measure of electron density at the Co(III) centre also provides a useful tool in future to predict catalyst activity. Furthermore, reversible CO_2 insertion must be considered in future catalyst design.

2) New heterodinuclear catalyst for 'switchable' CO_2, epoxide, lactide catalysis.

   A new catalyst system (**1**) was successfully applied in 'switch' using AGE, CO_2 and lactide. Catalyst **1** was active and selective for both AGE/CO_2 ROCOP and *L*-lactide ROP. It was used to make new block polymer and its properties were outlined. This discovery should allow future access to a wide variety of new block and even multiblock polymers.

5.2 Outlook

5.2.1 Future Catalyst Design

The work in this thesis primarily focussed on understanding heterodinuclear catalysts for PO/CO_2 ROCOP. Following from this work, modifications to the ligand could be useful to improve catalyst activity and selectivity (Fig. 5.2).

The structure-activity study suggests that increased electron density at Co(III) would lead to higher rates. To try to achieve this, various new imine backbones are proposed. The ether linker was successful in catalysis for CHO/CO_2 ROCOP and is proposed to give increased electron density at the cobalt centre (Fig. 5.2).[1]

The other (*R*)-(+)-1,1′-binaphthyl and (1*R*,2*R*)-(+)-1,2-diphenylethylene backbones should provide chirality close to the active site. These linkers were previously reported to give high stereochemical control in PO/CO_2 ROCOP and lactide ROP using LCoX/PPNX systems.[2-3] The new catalysts should

can also be applied to CHO/CO_2 ROCOP and other polycarbonates. Targeting tacticity controlled PPC could produce crystalline materials and maybe even stereocomplexes

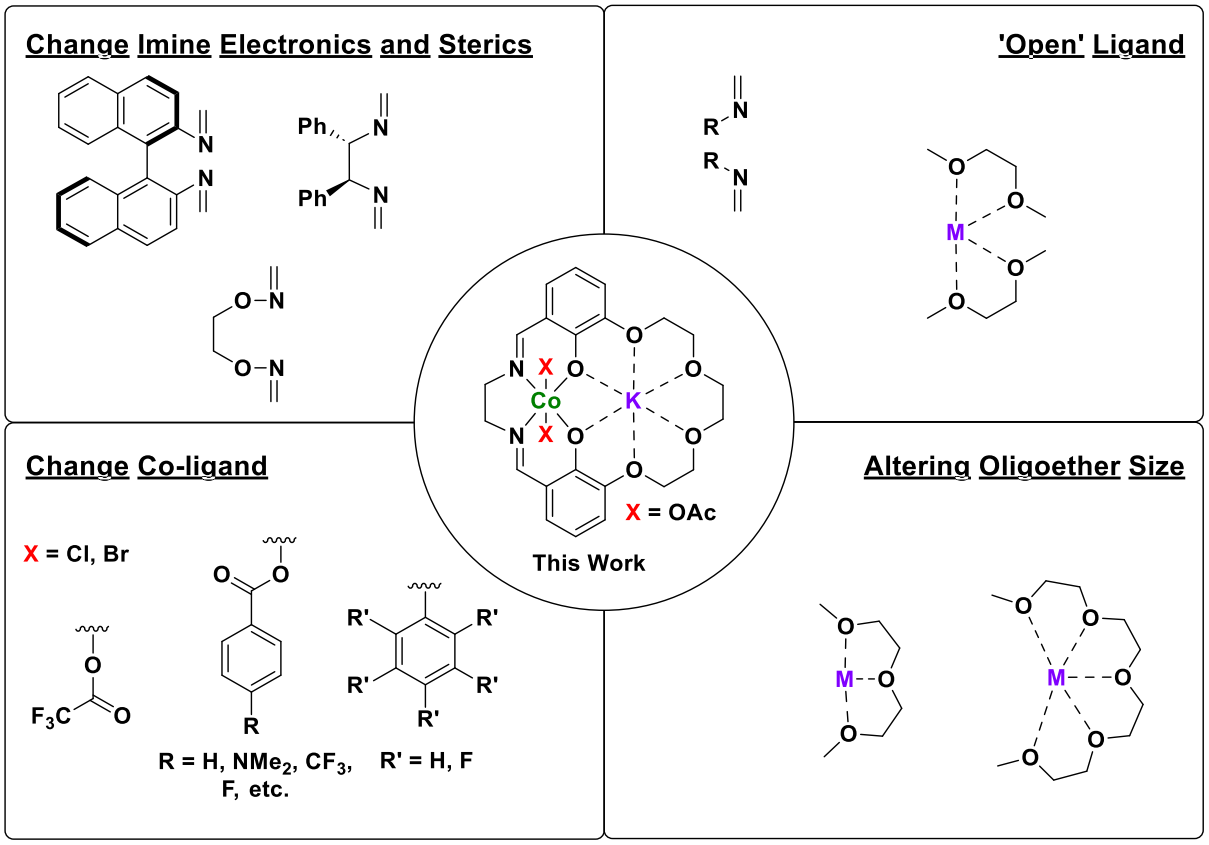


Figure 5.2 Proposed Future Catalyst Design Targets.

A further ligand modification would be to change the linker length of the ether group (Fig. 5.2). This would allow for selective binding of different metals, such as Na(I) in a smaller tri-ether macrocycle, and Rb(I) and Cs(I) in 5-ether. In the initial report of catalyst **1**, the binding affinity of the Group 1 metal was proposed to be key to the high activity of the Co(III)K(I) metal combination.[4]

The third ligand alteration which should be investigated is the 'opening' of the macrocycle. This should increase ligand flexibility and may facilitate access to the transition state for the ring-opening of the epoxide. The synthesis of such ligands is known and their complexation with Co(III) and K(I) is a priority for this catalyst.[5-6]

Finally, changing the co-ligand could be explored since such changes should influence the catalysis if the 'chain-shuttling' mechanism, proposed by Williams and co-workers, is occuring.[7] Furthermore, the

co-ligand in these heterobimetallic complexes has a significant effect on initiation time and rate, making this a worthwhile exploration to undertake.[8]

5.2.2 Future for 'Switch' Catalysis with 1

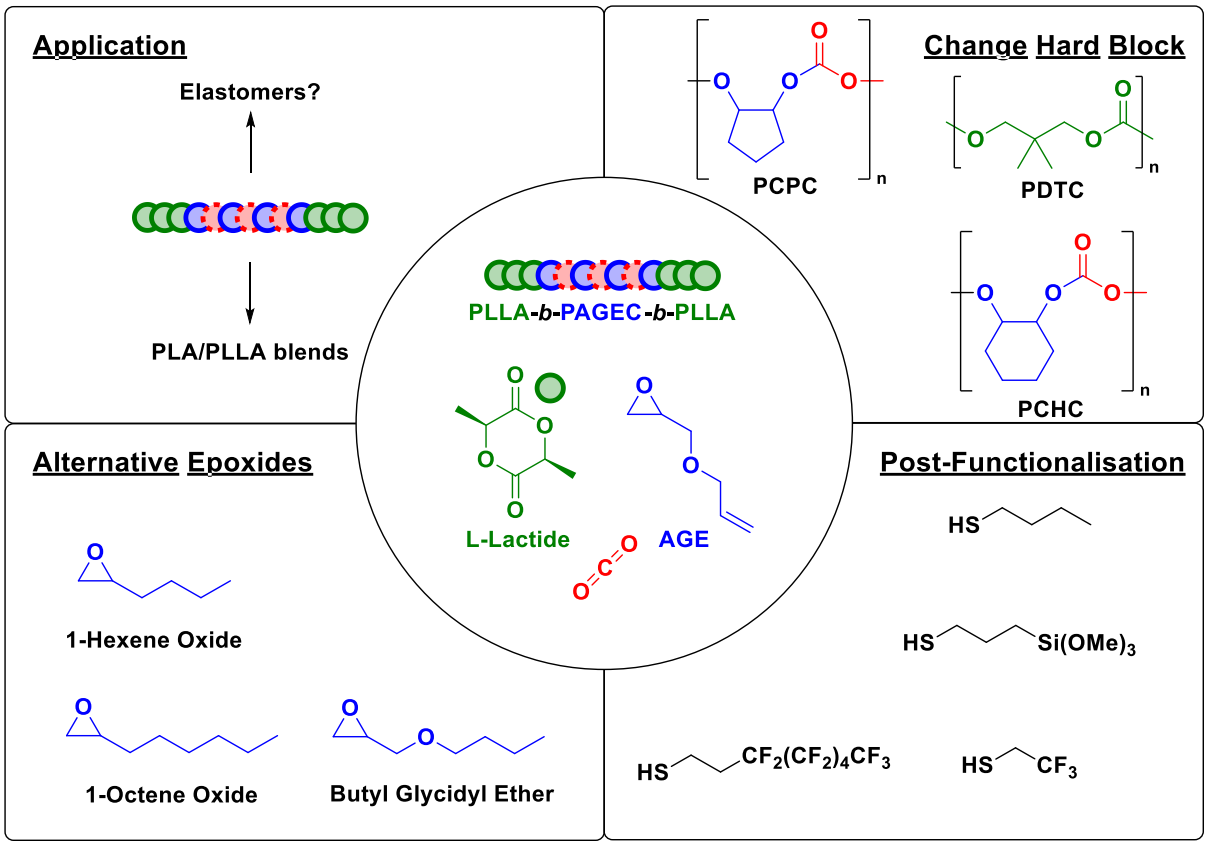


Figure 5.3 Proposed Future 'Switch' Catalysis and Polymers.

Chapter 4 shows the potential for the catalyst to be applied in 'switch' catalysis to make new block polymers. The great potential in this work lies in making blocks using alkylene oxides (such as AGE) and combining them effectively with other polyesters and polycarbonates (prepared ROP and ROCOP).

1-Hexene Oxide (HO), 1-Octene Oxide (OO) and Butyl Glycidyl Ether (BGE) have all been reported to produce polycarbonate with low T_gs. As such these monomers should be good candidates for polycarbonate 'soft' blocks in TPEs (Fig. 5.3).[9] Additionally, these polymers would not be susceptible to alkene cross-linking, significantly easing characterisation and processing.

The reaction of the alkene moieties of PAGEC could be used to improve properties and processibility. For example, using thiol-ene reactions it should be feasible to add functionality to the carbonate blocks

(Fig. 5.3). The suggested moieties to introduce are alkanes, silanes and fluoro-alkanes since these should decrease T_g, reduce the polarity of the soft-block and increase phase separation.

Additionally, other hard blocks should be explored, including ROP of 2,2-dim trimethylene carbonate (DTC), which yields highly crystalline polycarbonate with T_m = 110 °C.[10] Furthermore, polycarbonate hard blocks like PCHC or PCPC could also be used as they show high T_g values and have precedent with catalyst **1**.

Finally, applications for the polymers should be explored. One potential application could be to use the block polymers as plasticizers for in PLLA formulations.[11-12] The PLLA block should improve miscibility and reduce leaching in blends with PLLA.[13] The properties of PLA need to be improved as it is very brittle. Plasticizers give access to materials with high impact strength, tensile strength and good head resistance.[14-17]

5.3 References

1. Asaba, H.; Iwasaki, T.; Hatazawa, M.; Deng, J.; Nagae, H.; Mashima, K.; Nozaki, K., *Inorg. Chem.* **2020**, *59* (12), 7928-7933.
2. Che, C., *Coord. Chem. Rev.* **2003,** *242*, 97-113.
3. Lu, X.-B. B.; Darensbourg, D. J., *Chem. Soc. Rev.* **2012,** *41*, 1462-1484.
4. Deacy, A. C.; Moreby, E.; Phanopoulos, A.; Williams, C. K., *J. Am. Chem. Soc.* **2020,** *142*, 19150-19160.
5. Casellato, U.; Tamburini, S.; Tomasin, P.; Vigato, P. A., *Inorg. Chim. Acta* **2004,** *357*, 4191-4207.
6. Ho, X. L.; Shao, H.; Ng, Y. Y.; Ganguly, R.; Lu, Y.; Soo, H. S., *Inorg. Chem.* **2019,** *58*, 1469-1480.
7. Buchard, A.; Jutz, F.; Kember, M. R.; White, A. J. P. P.; Rzepa, H. S.; Williams, C. K., *Macromolecules* **2012,** *45*, 6781-6795.
8. Trott, G.; Garden, J. A.; Williams, C. K., *Chem. Sci.* **2019,** *10*, 4618-4627.
9. Jia, M.; Zhang, D.; de Kort, G. W.; Wilsens, C.; Rastogi, S.; Hadjichristidis, N.; Gnanou, Y.; Feng, X., *Macromolecules* **2020,** *53*, 5297-5307.
10. Kricheldorf, H. R.; Dunsing, R.; Albet, A. S. i., *Die Makromolekulare Chemie* **1987,** *188*, 2453-2466.
11. Deeraj, B. D. S.; Jayan, J. S.; Saritha, A.; Joseph, K., 8 - PLA-based blends and composites. In *Biodegradable Polymers, Blends and Composites*, Mavinkere Rangappa, S.; Parameswaranpillai, J.; Siengchin, S.; Ramesh, M., Eds. Woodhead Publishing: 2022; pp 237-281.
12. Luinstra, G. A., *Polymer Reviews* **2008,** *48*, 192-219.
13. Darensbourg, D. J.; Wu, G. P., *Angew. Chem. Int. Ed. Engl.* **2013,** *52*, 10602-6.
14. Wang, Y.; Chiao, S. M.; Hung, T. F.; Yang, S. Y., *J. Appl. Polym. Sci.* **2012,** *125*.
15. Phuong, V. T.; Coltelli, M.-B.; Cinelli, P.; Cifelli, M.; Verstichel, S.; Lazzeri, A., *Polymer* **2014,** *55*, 4498-4513.
16. Lin, L.; Deng, C.; Lin, G.-P.; Wang, Y.-Z., *Ind. Eng. Chem. Res.* **2015,** *54*, 5643-5655.
17. Yuryev, Y.; Mohanty, A. K.; Misra, M., *Composites, Part B* **2017,** *130*, 158-166.

Chapter 6

Experimental Details

6.1 General Considerations

All experimental manipulations were performed using a dual-manifold nitrogen-vacuum Schlenk line or in a nitrogen filled glovebox, unless stated otherwise. All solvents and reagents were obtained from commercial sources and used as received, unless stated otherwise. Acetonitrile, pentane and toluene were obtained from an SPS system, degassed by several freeze-pump-thaw cycles, further dried with 3 Å molecular sieves and stored under N_2.

All reagents were purchased from Sigma Aldrich, unless stated otherwise. Potassium acetate was dried under dried under vacuum for 16 hours before use. All materials were stored under a nitrogen atmosphere, except the diamines which were stored at ambient temperature and pressure in air. The dialdehyde pro-ligand (LH_2) was purchased from Enamine.

Propylene oxide (PO) was dried over CaH_2, overnight, and fractionally distilled prior to use. Allyl glycidyl ether (AGE) was first dried over CaH_2, overnight, and fractionally distilled, it was further dried of *n*-butyl lithium (1.6 M in Hexanes) at 0 °C and the solution was left to warm up slowly to room temperature. It was subsequently fractionally distilled. Finally, AGE was fractionally distilled to remove any solvent and *n*-butyl lithium remaining. *L*-Lactide was purchased from Purac and was recrystallised three times from dry toluene under inert atmosphere. The recrystallised lactide was sublimed three times under vacuum.

CP grade carbon dioxide (BOC, 99.995 %) was dried by passing it through two drying columns (VICI Metronics carbon dioxide purifier) in series, at 50 bar pressure, before use at lower pressures in the copolymerization. Catalyst **1** was synthesised according to literature procedure.[1]

6.2 General PO/CO_2 Copolymerisation Procedure

A solution of catalyst (13 mg, 0.02 mmol), cyclohexene diol (46 mg, 0.4 mmol) and mesitylene (30 µL. 0.2 mmol, internal standard) in PO (6 mL, 85.7 mmol) was injected into a 100 mL Parr reactor, under a stream of dry CO_2. The reactor was also fitted with a DiComp sentinel probe, attached to an ATR-IR spectrometer, which allowed for continual monitoring of PPC formation. The reactor was then

pressurized with CO_2 to the target reaction pressure and allowed to reach the required temperature. Upon reaction completion, the reactor vessel was cooled to room temperature and depressurized with the catalyst quenched by the addition of a 1 M solution of benzoic acid, in $CHCl_3$. A sample of the crude reaction mixture was removed for analysis. The polymer was precipitated by dropwise addition into methanol, the solution was decanted and polymer dried in vacuo.

6.3 General PPC to PC Procedure

Note PPC must have hydroxyl end-groups (as assessed by 31P NMR spectroscopy). Here PPC has M_n of 15.3 kg mol^{-1} and $Đ$ = 1.03. A 100 mL Parr reactor was charged with catalyst (11.3 mg, 0.018 mmol) as a solid and a solution of poly(propylene carbonate) (0.184 g, 1.8 mmol) in propylene oxide (6 mL, 85.7 mmol). The reactor was also fitted with a DiComp sentinel probe, attached to an ATR-IR spectrometer, which allowed for continual monitoring of PPC consumption and PC formation. The reactor was then heated to the desired temperature. Upon reaction completion (as judged by IR spectroscopy), the reactor vessel was cooled to room temperature and a sample of the crude reaction mixture removed for NMR spectroscopy.

6.4 General AGE/CO_2 Copolymerisation Procedure

The base of a 25 mL Parr reactor was dried overnight at 140 °C and the reactor was then taken into the glovebox overnight (under vacuum). The reactor was charged with 6 – 15 mL of AGE, **1** and *trans*-1,2-cyclohexanediol, at the desired loadings and ratios. The reactor was sealed and charged to 20 bar with CO_2 and then heated to 50 or 60 °C. After the desired amount of time, the reactor was cooled to 30 °C and the CO_2 vented. The reaction was quenched by addition of 20 equiv. benzoic acid and 20 equiv. of butylated hydroxytoluene (BHT) and subsequently precipitated three times from methanol. Finally, the polymer was dried in vacuo.

6.5 General L-Lactide Polymerisation Procedure

Under anaerobic conditions, **1**, CHD, *L*-lactide and AGE (1 – 4.5 mL) were added to a flame-dried vial and stirred at 50 – 60 °C for the desired time. The reaction was quenched by exposure to air and a crude

sample was analysed by ^{1}H NMR spectroscopy. SEC analysis (THF, 1 mL min^{-1}, 30 °C) of a crude sample was performed on removal of residual polymerisation solvent. The PLLA was purified by precipitation from a solution of DCM or THF (< 1 g mL^{-1}) into cold methanol (200-300 mL) and subsequently dried *in vacuo* to a constant weight.

6.6 General Switch Polymerisation of AGE, CO_2 and *L*-Lactide

The reactor was charged with AGE (7.5 mL, 63.70 mmol), **1** (4.0 mg, 6.37 μmol) and CHD (14.8 mg, 0.13 mmol) (1:20:10,000 cat:CHD:AGE). The reactor was subsequently pressurised 20 bar CO_2 and heated to the reaction temperature (50 °C). After 17.5 h, 11% conversion of AGE was observed and the CO_2 was released. Subsequently, a solution of *L*-lactide (727 mg, 6.37 mmol, 1:1,000 cat:*L*-LA), in AGE (4 mL), was injected. Next, the solution is degassed *via* 10 rapid vacuum/nitrogen cycles. After another 5 h reaction (55% conversion of *L*-LA) was quenched by addition 20 equiv. benzoic acid and 20 equiv. of butylated hydroxytoluene. The polymer was precipitated from MeOH three times before being dried *in vacuo*.

6.7 End Group Titration and Analysis by $^{31}P\{^{1}H\}$ NMR Spectroscopy

Analysis of the hydroxyl polymer end groups was carried out following a reported procedure.[2] In an NMR tube, the polymer (40 mg), purified via precipitation from methanol, was added to a stock solution (40 μL) of pyridine (10 mL), bisphenol A (400 mg) and $Cr(acac)_3$ (5.5 mg) and 2-chloro-4,4,5,5-tetramethyldioxaphospholane (40 mg), in $CDCl_3$ (0.5 mL). The mixture was allowed to react at room temperature for 6 hours, before $^{31}P\{^{1}H\}$ NMR spectra were recorded.

6.8 Methods

NMR Spectroscopy: ^{1}H and ^{31}P NMR spectra were obtained using a Bruker AV III HD 400 instrument. ^{13}C NMR spectra were obtained using either a Bruker AV III 500. All spectra were recorded at 298 K.

IR Spectroscopy: Carried out on a Shimadzu IRSpirit FT-IR spectrometer equipped with a single reflection ATR (attenuated total reflectance) accessory, in a nitrogen filled glovebox.

Elemental Analysis: Carried out by either at London Metropolitan University or Elemental Microanalysis Ltd., 1 Hameldown Road, Okehamptom, Devon, EX20 1UB.

X-Ray Crystallography: Crystallographic data were collected, and structures solved, by Dr. Andreas Phanopolous. Air sensitive samples were isolated in a nitrogen filled glovebox and immersed in fluorinated oil before analysis. Crystalline samples were mounted on a MiTeGen Micromount and cooled to 150 K with dry nitrogen using an Oxford Cryostream.[3] Data was collected with an Oxford Diffraction Supernova diffractometer using Cu K_α (λ = 1.5417 Å) or Mo K_α (λ = 0.7107 Å) radiation. The resulting reflection data was processed with CrysAlis Pro.[4] Structures were solved using the SHELXT program and least-square refined using the SHELXL program within the Olex2 system suite.[5-7]

SEC analysis: Carried out on a Shimadzu LC-20AD instrument, equipped with a Refractive Index (RI) detector and two PSS SDV 5 μm linear M columns, with an eluent of HPLC-grade THF, heated to 30 °C and with a flow rate of 1.0 mL min^{-1}. Glass transition temperatures were taken from the mid-point of the curves.

Differential Scanning Calorimetry (DSC): Carried out using either a TA discovery 25 auto DSC. For samples described in chapter 4 the following procedure was applied: samples were first cooled -80 °C, before heating and cooling from -80 °C to 100 - 200 °C at a rate of 5 °C min^{-1}. Each sample was run for three heating and cooling cycles. Glass transition temperatures (T_g) and melting temperatures (T_m) were recorded from the midpoint of the transition during the third heating curve.

Thermal Gravimetric Analysis (TGA): Carried out using a TA TGA 5500 instrument. Samples were heated from 30 °C to 500 °C, under continuous N_2 flow, at a rate of 5 °C min^{-1}.

Cyclic Voltammetry: Carried out using a PalmSens EmStat Blue potentiostat under computer control with three electrodes: Au disc (2.0 mm2) as the working electrode, Graphite wire as the counter electrode and a Ag wire as the pseudo-reference electrode. The measurements were performed with a solution of 1.6 mM complex with 0.1 M [^{n}Bu$_4$N][PF_6] in 10mL of MeCN. Potentials are referenced to ferrocene.

6.9 Characterisation Data for Chapter 2

Density Functional Theory Calculations

Note conducted in collaboration with Dr. Andreas Phanopoulos and Dr. Antoine Buchard.

Computational Methods

DFT calculations were run using Gaussian 16 (Revision C.01).[8] The reaction free energies were calculated using the hybrid exchange-correlation ωB97X-D functional, which includes D2 dispersion corrections described by Grimme.[9-10] A functional screening was undertaken on key transition states for both pathways, with the surveyed functionals including B3LYP[11-12] with Grimme's D3 dispersion correction including Becke-Johnson damping (GD3BJ),[13-14] M06[15] with Grimme's D3 dispersion correction (GD3)[16] and PBE0[17-18] with GD3BJ.[13-14] NBO analysis was performed using NBO 6.0.[19] QTAIM analysis was conducted using the AIMAll package.[20] Data are presented from *very fine* mesh calculations. Standard cut-offs for plotting the data with AIMAll were used. Non-covalent interactions were analysed using the NCIPLOT 3.0 program.[21]

The split valence 6-31+g(d,p) basis sets were used for carbon and hydrogen. This lower basis set was chosen as these elements do not bind directly to either catalytic metal centre, but extra diffuse functions were added to capture more mid- and long-range interactions, for instance with growing polymer chains. The triple-ζ 6-311+g(d) basis set was used for potassium and all heteroatoms. Cobalt centres were described with the Stuttgart SDD ECP and associated basis sets.

Geometry optimisation calculations were performed without symmetry constraints and using an "ultrafine" grid for numerical integration. All structures are optimized using the self-consistent reaction field (SCRF) approach with conductor-like polarisable continuum model (CPCM).[22] In polymerization reactions, the propylene oxide (PO) monomer also serves as the solvent but is not implemented as a standard solvent in Gaussian16. A CPCM model for PO was therefore implemented by using the built-in non-polar parameters of tetrahydrofuran, modified with the polar parameters of propylene oxide (ε=16, n^2=1.867) ([SCRF=(cpcm,solvent=tetrahydrofuran),read] and [eps=16/epsinf=1.867)].

Free enthalpies were corrected using Goodvibes software,[23] with Grimme's quasiharmonic approximation applied with a frequency cut-off value of 100.0 wavenumbers, a frequency scale factor = 1.0. To account for experimental conditions, a temperature of 323.15 K and concentrations of 14.1156 mol L^{-1} (for neat PO), 4.787 mol L^{-1} (for CO_2 dissolved in PO at 50 bar and 313.15 K)[24] and 0.003 mol L^{-1} (for any metal complex species) were also applied.

All intermediates and transition states were characterised by normal coordinate analysis revealing either precisely zero or one imaginary frequency, respectively. In the case of transition states, the imaginary frequency corresponds to the mode of the intended reaction step. Full coordinates for all the calculated stationary points are included as part of the supplementary information (.xyz).

Full coordinates for all structures, together with computed energies and vibrational frequency data, are available via the corresponding Gaussian 16 output files and calculation spreadsheet, stored in the open-access digital repository, DOI: 10.6084/m9.figshare.20026409.

6.10 Characterisation Data for Chapter 3

Synthesis of 3_H

A Schlenk tube was charged with LH_2 (300 mg, 0.77 mmol), $Co(OAc)_2$ (136 mg, 0.77 mmol), KOAc (74 mg, 0.77 mmol) and dry MeCN (40 mL) under a nitrogen atmosphere. The solution was stirred for 2 hours before adding 1,2-phenylenediamine (83 mg, 0.77 mmol) and left to stir overnight, after which the reaction was exposed to air and AcOH (44 μL, 0.77 mmol). The solution was stirred for a further 48 hours and then filtered and solvent removed under vacuum. The solid was triturated with toluene (3 x 50 mL) and pentane (3 x 50 mL) to remove excess acetic acid, resulting in pure product (219 mg, 68% yield).

^{1}H NMR (400 MHz, $CDCl_3$, 298K). δ(ppm): 8.19 (2H, s, –**H**C=N–), 8.01 (2H, dd, HC–**H**C=C–N–, $^3J_{H-H}$ = 6.1, 3.4 Hz), 7.37 (2H, dd, **H**C–HC=C–N–, $^3J_{H-H}$ = 6.2, 3.4 Hz), 7.01 (2H, d, Ar–$\mathbf{H}_{meta}$, $^3J_{H-H}$ = 8.1 Hz), 6.73 (2H, d, Ar–$\mathbf{H}_{meta}$, $^3J_{H-H}$ = 7.5 Hz), 6.47 (2H, t, Ar–$\mathbf{H}_{para}$, $^3J_{H-H}$ = 7.5 Hz), 4.24-3.78 (12H, m, –O–C$\mathbf{H}_2$–), 1.36l (6H, s, $\mathbf{H}_3$C–C(O)O). ^{13}C NMR (125 MHz, $CDCl_3$, 298K). δ(ppm): 179.50 (–**C**(O)O), 158.88 (–H**C**=N–), 157.20 (Ar–$\mathbf{C}_{ipso}$–O^-, Ar–$\mathbf{C}_{ortho}$–O/CH), 151.91 (Ar–$\mathbf{C}_{ipso}$–O^-, Ar–$\mathbf{C}_{ortho}$–O/CH), 147.05 (Ar–**C**–N), 127.32 (H**C**–HC=C–N–, Ar–$\mathbf{C}_{Meta}$), 118.55 (Ar–$\mathbf{C}_{ipso}$–O^-, Ar–$\mathbf{C}_{ortho}$–O/CH), 115.62 (HC–H**C**=C–N–), 113.16 + 113.04 (Ar–$\mathbf{C}_{para}$, Ar–$\mathbf{C}_{meta}$), 70.22 (–O–$\mathbf{C}H_2$–), 69.53 (–O–$\mathbf{C}H_2$–), 66.21 (–O–$\mathbf{C}H_2$–), 24.88 ($H_3\mathbf{C}$–C(O)O). Calculated; C, 53.3; H, 4.5; N, 4.1 %. Found; C, 51.3; H, 4.4; N, 4.0 %.

Synthesis of 3_{Cl}

A Schlenk tube was charged with LH_2 (300 mg, 0.77 mmol), $Co(OAc)_2$ (136 mg, 0.77 mmol), KOAc (74 mg, 0.77 mmol) and dry MeCN (40 mL) under a nitrogen atmosphere. The solution was stirred for 2 hours, before adding 4,5-dichloro-1,2-phenylenediamine (136 mg, 0.77 mmol) and left to stir overnight, after which the reaction was exposed to air and AcOH (44 μL, 0.77 mmol). The solution was stirred for a further 48 hours and then filtered and solvent removed under vacuum. The solid was triturated with toluene (3 x 50 mL) and pentane (3 x 50 mL). The resulting solid dissolved in a minimum

methanol and precipitated with diethyl ether. The solution was filtered and solvent removed under vacuum to collect the product (258 mg, 45% yield).

^{1}H NMR (400 MHz, $CDCl_3$, 298K). δ(ppm): 8.04 (4H, s, –**H**C=N–, ClC–**H**C=C–N–), 6.98 (2H, d, Ar–$\mathbf{H}_{meta}$, $^{3}J_{H\text{-}H}$ = 8.1 Hz), 6.72 (2H, d, Ar–$\mathbf{H}_{meta}$, $^{3}J_{H\text{-}H}$ = 7.5 Hz), 6.46 (2H, t, Ar–$\mathbf{H}_{para}$, $^{3}J_{H\text{-}H}$ = 7.8 Hz), 4.24-3.82 (12H, m, –O–C$\mathbf{H}_2$–), 1.38 (6H, s, $\mathbf{H}_3$C–C(O)O). ^{13}C NMR (125 MHz, $CDCl_3$, 298K). δ(ppm): 179.38 (–**C**(O)O), 158.90 (–H**C**=N–), 157.21 (Ar–$\mathbf{C}_{ipso}$–O^-, Ar–$\mathbf{C}_{ortho}$–O/CH), 151.64 (Ar–$\mathbf{C}_{ipso}$–O^-, Ar–$\mathbf{C}_{ortho}$–O/CH), 146.15 (Ar–**C**–Cl, Ar–**C**–N), 130.67 (Ar–**C**–Cl, Ar–**C**–N), 127.04 (Ar–$\mathbf{C}_{meta}$), 117.78 (Ar–ClC=**C**H–), 116.36 (Ar–$\mathbf{C}_{ipso}$–O^-, Ar–$\mathbf{C}_{ortho}$–O/CH), 113.36 + 113.25 (Ar–$\mathbf{C}_{para}$, Ar–$\mathbf{C}_{meta}$), 69.90 (–O–**C**H_2–), 69.03 (–O–**C**H_2–), 66.10 (–O–**C**H_2–), 24.46 (H_3**C**–C(O)O). Calculated; C, 48.3; H, 3.8; N, 3.8 %. Found; C, 48.0; H, 4.1; N, 3.7 %.

Synthesis of 3_F

A Schlenk tube was charged with LH_2 (300 mg, 0.77 mmol), $Co(OAc)_2$ (136 mg, 0.77 mmol), KOAc (74 mg, 0.77 mmol) and dry MeCN (40 mL) under a nitrogen atmosphere. The solution was stirred for 2 hours before adding 4,5-Difluoro-1,2-phenylenediamine (111 mg, 0.77 mmol) and left to stir overnight, after which the reaction was exposed to air and AcOH (44 μL, 0.77 mmol). The solution was stirred for a further 48 hours and then filtered and solvent removed under vacuum. The solid was dissolved in a minimum methanol and precipitated with diethyl ether. The resulting solid was triturated with toluene (3 x 50 mL) and pentane (3 x 50 mL). The solution was filtered and solvent removed under vacuum to collect the product (50 mg, 9% yield).

^{1}H NMR (400 MHz, $CDCl_3$, 298K). δ(ppm): 7.95 (2H, s, –**H**C=N–), 7.79 (2H, t, FC–**H**C=C–N–, $^{3}J_{H\text{-}F}$ = 9.1 Hz), 6.98 (2H, d, Ar–$\mathbf{H}_{meta}$, $^{3}J_{H\text{-}H}$ = 7.8 Hz), 6.74 (2H, d, Ar–$\mathbf{H}_{meta}$, $^{3}J_{H\text{-}H}$ = 7.5 Hz), 6.48 (2H, t, Ar–$\mathbf{H}_{para}$, $^{3}J_{H\text{-}H}$ = 7.8 Hz), 4.20-3.82 (12H, m, –O–C$\mathbf{H}_2$–), 1.38 (6H, s, $\mathbf{H}_3$C–C(O)O). ^{13}C NMR (125 MHz, $CDCl_3$, 298K). δ(ppm): 179.45 (–**C**(O)O), 158.77 (–H**C**=N–), 157.18 (Ar–$\mathbf{C}_{ipso}$–O^-, Ar–$\mathbf{C}_{ortho}$–O/CH), 151.88 (Ar–$\mathbf{C}_{ipso}$–O^-, Ar–$\mathbf{C}_{ortho}$–O/CH), 143.16 (Ar–**C**–F, Ar–**C**–N), 127.27 (Ar–$\mathbf{C}_{meta}$), 118.13 (Ar–$\mathbf{C}_{ipso}$–O^-, Ar–$\mathbf{C}_{ortho}$–O/CH), 113.51 + 113.45 (Ar–$\mathbf{C}_{para}$, Ar–$\mathbf{C}_{meta}$), 103.86 (Ar–FC–**C**H–), 70.14 (–O–**C**H_2–), 69.38 (–O–**C**H_2–), 66.33 (–O–**C**H_2–), 24.85 (H_3**C**–C(O)O). Calculated; C, 50.6; H, 4.0; N, 3.9 %. Found; C, 50.2; H, 3.9; N, 4.2 %.

Synthesis of 3_{Me}

A Schlenk tube was charged with LH_2 (300 mg, 0.77 mmol), $Co(OAc)_2$ (136 mg, 0.77 mmol), KOAc (74 mg, 0.77 mmol) and dry MeCN (40 mL) under a nitrogen atmosphere. The solution was stirred for 2 hours before adding 4,5-dimethyl-1,2-phenylenediamine (111 mg, 0.77 mmol) and left to stir for two days after which the reaction was exposed to air. After a further two days AcOH (44 μL, 0.77 mmol) was added and the solution was stirred for a further 48 hours. The solution was then filtered and solid precipitate was shown to be the desired complex. It was dried under vacuum to collect the product 280 mg, 52% yield).

^{1}H NMR (400 MHz, $CDCl_3$, 298K). δ(ppm): 8.14 (2H, s, –**H**C=N–), 7.78 (2H, s, MeC–**H**C=C–N–), 7.01 (2H, d, Ar–$\mathbf{H}_{meta}$, $^{3}J_{H\text{-}H}$ = 8.0 Hz), 6.72 (2H, d, Ar–$\mathbf{H}_{meta}$, $^{3}J_{H\text{-}H}$ = 7.5 Hz), 6.46 (2H, t, Ar–$\mathbf{H}_{para}$, $^{3}J_{H\text{-}H}$ = 7.8 Hz), 4.20-3.80 (12H, m, –O–C$\mathbf{H}_2$–), 2.41 (6H, s, $\mathbf{H}_3$C–C(O)O) 1.39 (6H, s, $\mathbf{H}_3$C–C=HC). ^{13}C NMR (125 MHz, CD_3OD, 298K). δ(ppm): 160.87 (–H**C**=N–), 158.64 (Ar–$\mathbf{C}_{ortho}$–O/CH), 153.03 (Ar–$\mathbf{C}_{para}$), 144.43 (Ar–**C**–N), 139.39 (Ar–**C**–Me), 128.58 (Ar–$\mathbf{C}_{meta}$), 119.75 (Ar–$\mathbf{C}_{ipso}$–O^-), 118.26 (Ar–**C**H–C–N), 115.92 + 115.69 (Ar–$\mathbf{C}_{para}$, Ar–$\mathbf{C}_{meta}$), 71.28 (–O–**C**H_2–), 70.13 (–O–**C**H_2–), 68.33 (–O–**C**H_2–), 49.45 (H_3**C**–C(O)O), 20.04 (Ar-**C**H_3). Calculated; C, 54.5; H, 4.9; N, 4.0 %. Found; C, 52.3; H, 5.0; N, 4.0 %.

Synthesis of 3_{OMe}

A round bottom flask was charged with LH_2 (300 mg, 0.77 mmol), $Ba(ClO_4)_2$ (258 mg, 0.77 mmol) and methanol (300 mL) and left to stir for 1 h. 1,2-diamino-4,5-dimethoxybenzene (129 mg, 0.77 mmol) was added to the reaction mixture and it was left to stir overnight. The solution was concentrated under reduced pressure and dissolved in chloroform (250 mL). Deionized water (200 mL) and guanidine sulfate (831 mg, 7.69 mmol) were added to form a biphasic mixture and the mixture was stirred overnight. The layers were separated and extra product extracted with chloroform (3 x 50 mL). The organic layer was dried ($MgSO_4$) and the solvent was removed, under a reduced pressure, to yield an orange solid (250 mg, 0.46 mmol, 60%).

Next a Schlenk tube was charged with the produced macrocycle (200 mg, 0.38 mmol), $Co(OAc)_2$ (68 mg, 0.38 mmol), KOAc (38 mg, 0.38 mmol) and dry MeCN (40 mL) under a nitrogen atmosphere. The

solution was stirred, overnight, after which the reaction was exposed to air and AcOH (22 μL, 0.38 mmol). The solution was stirred for a further 48 hours and then filtered and solvent removed under vacuum. The resulting solid was triturated toluene (3 x 50 mL) and pentane (3 x 50 mL). The solution was filtered and solvent removed under vacuum to collect the product (75 mg, 27% yield).

^{1}H NMR (400 MHz, $CDCl_3$, 298K). δ(ppm): 8.15 (2H, s, –**H**C=N–), 7.79 (2H, s, MeOC–**H**C=C–N–), 7.01 (2H, s, Ar–$\mathbf{H}_{meta}$), 6.72 (2H, s, Ar–$\mathbf{H}_{meta}$), 6.47 (2H, s, Ar–$\mathbf{H}_{para}$), 4.20-3.80 (12H, m, –O–C$\mathbf{H}_2$–), 2.40 (6H, s, H_3C-O-Ar), 1.39 (6H, s, $\mathbf{H}_3$C–C(O)O). ^{13}C NMR (125 MHz, $CDCl_3$, 298K). δ(ppm): 179.47 (–**C**(O)O), 156.42 (–H**C**=N–), 151.91 (Ar–$\mathbf{C}_{ortho}$–O/CH), 145.13 (Ar–$\mathbf{C}_{ortho}$–O/CH), 136.26 (Ar–**C**–OMe, Ar–**C**–N), 127.24 (Ar–$\mathbf{C}_{meta}$), 118.67 (Ar–**C**–OMe, Ar–**C**–N), 116.38 (Ar–MeOC–**C**H–), 113.34 (Ar–$\mathbf{C}_{ipso}$–O^-), 112.94 + 112.83 (Ar–$\mathbf{C}_{para}$, Ar–$\mathbf{C}_{meta}$), 70.17 (–O–**C**H_2–), 69.50 (–O–**C**H_2–), 66.12 (–O–**C**H_2–), 24.95 (H_3**C**–C(O)O), 22.86 (–O–**C**H_3). Calculated; C, 52.2; H, 4.7; N, 3.8 %. Found; C, 51.2; H, 4.6; N, 4.1 %.

6.11 Characterisation Data for Chapter 4

Poly(Allyl Glycidyl Ether Carbonate) (PAGEC)

GPC: M_n = 27.8 kg mol^{-1}, M_w = 32.5 kg mol^{-1} and $Đ$ = 1.17.

DSC: T_g = -19 °C.

TGA: $T_{d,\ onset}$ = 213 °C and $T_{d,\ 5}$ = 208 °C.

^{1}H NMR (400 MHz, $CDCl_3$, 298K). δ(ppm): 5.85 (1H, m, CH_2–**H**C=CH_2), 5.23 (2H, m, –HC=C$\mathbf{H}_2$), 5.02 (1H, broad s, CH_2–**H**C–OC(O)O), 4.35 (2H, m, OC(O)O–C$\mathbf{H}_2$–HC–), 3.99 (2H, m, O–C$\mathbf{H}_2$–HC=CH_2), 3.62 (2H, s, OC(O)O–CH–C$\mathbf{H}_2$–O).

Poly(*L*-Lactide Acid) (PLLA)

GPC: M_n = 6.8 kg mol^{-1}, M_w = 7.6 kg mol^{-1} and $Đ$ = 1.12.

DSC: T_g = 52 °C, T_m = 140 °C, ΔH_m = 11.3 J g^{-1} and ΔX_c = 0.12.

TGA: $T_{d,\ onset}$ = 278 °C and $T_{d,\ 5}$ = 253 °C.

^{1}H NMR (400 MHz, $CDCl_3$, 298K). δ(ppm): 5.16 (1H, q, J, $^{3}J_{H\text{-}H}$ = 7.1 Hz, O–**H**C–CH_3), 1.58 (3H, d, $^{3}J_{H\text{-}H}$ = 7.1 Hz, O–HC–C$\mathbf{H}_3$).

PLLA-*b*-PAGEC-*b*-PLLA

GPC: M_n = 8.0 kg mol^{-1}, M_w = 8.7 kg mol^{-1} and $Đ$ = 1.09.

DSC: T_g = -1 °C.

TGA: $T_{d,\ onset}$ = 232 °C and $T_{d,\ 5}$ = 211 °C.

^{1}H NMR (400 MHz, $CDCl_3$, 298K). δ(ppm): 5.85 (1H, m, CH_2–**H**C=CH_2), 5.21 (4H, m, –HC=C**H**$_2$, O–**H**C–CH_3), 5.03 (1H, broad s, CH_2–**H**C–OC(O)O), 4.37 (2H, m, OC(O)O–C**H**$_2$–HC–), 4.00 (2H, m, O–C**H**$_2$–HC=CH_2), 3.60 (2H, s, OC(O)O–CH–C**H**$_2$–O), 1.58 (3H, d, $^3J_{H\text{-}H}$ = 7.1 Hz, O–HC–C**H**$_3$).

6.12 References

1. Deacy, A. C.; Moreby, E.; Phanopoulos, A.; Williams, C. K., *J. Am. Chem. Soc.* **2020,** *142*, 19150-19160.
2. Spyros, A.; Argyropoulos, D. S.; Marchessault, R. H., *Macromolecules* **1997,** *30*, 327-329.
3. Cosier, J.; Glazer, A. M., *J. Appl. Crystallogr.* **1986**, 106-107.
4. CrysAlisPRO, Oxford Diffraction /Agilent Technologies UK Ltd. Yarnton, England.
5. Sheldrick, G., *Acta Crystallogr., Sect. A* **2015,** *71*, 3-8.
6. SHELXTL v5.1. Bruker AXS: Madison, WI, 1998, 1998.
7. Dolomanov, O. V.; Bourhis, L. J.; Gildea, R. J.; Howard, J. A. K.; Puschmann, H., *J. Appl. Crystallogr.* **2009,** *42*, 339- 341.
8. Frisch, M. J.; Trucks, G. W.; Schlegel, H. B.; Scuseria, G. E.; Robb, M. A.; Cheeseman, J. R.; Scalmani, G.; Barone, V.; Petersson, G. A.; Nakatsuji, H.; Li, X.; Caricato, M.; Marenich, A. V.; Bloino, J.; Janesko, B. G.; Gomperts, R.; Mennucci, B.; Hratchian, H. P.; Ortiz, J. V.; Izmaylov, A. F.; Sonnenberg, J. L.; Williams; Ding, F.; Lipparini, F.; Egidi, F.; Goings, J.; Peng, B.; Petrone, A.; Henderson, T.; Ranasinghe, D.; Zakrzewski, V. G.; Gao, J.; Rega, N.; Zheng, G.; Liang, W.; Hada, M.; Ehara, M.; Toyota, K.; Fukuda, R.; Hasegawa, J.; Ishida, M.; Nakajima, T.; Honda, Y.; Kitao, O.; Nakai, H.; Vreven, T.; Throssell, K.; Montgomery Jr., J. A.; Peralta, J. E.; Ogliaro, F.; Bearpark, M. J.; Heyd, J. J.; Brothers, E. N.; Kudin, K. N.; Staroverov, V. N.; Keith, T. A.; Kobayashi, R.; Normand, J.; Raghavachari, K.; Rendell, A. P.; Burant, J. C.; Iyengar, S. S.; Tomasi, J.; Cossi, M.; Millam, J. M.; Klene, M.; Adamo, C.; Cammi, R.; Ochterski, J. W.; Martin, R. L.; Morokuma, K.; Farkas, O.; Foresman, J. B.; Fox, D. J. *Gaussian 16 Rev. C.01*, Wallingford, CT, 2016.
9. Chai, J. D.; Head-Gordon, M., *J. Chem. Phys.* **2008,** *128*, 084106.
10. Alipour, M.; Fallahzadeh, P., *Phys. Chem. Chem. Phys.* **2016,** *18*, 18431-18440.
11. Becke, A. D., *J. Chem. Phys.* **1993,** *98*, 5648-5652.
12. Lee, C.; Yang, W.; Parr, R. G., *Phys Rev B Condens Matter* **1988,** *37*, 785-789.
13. Grimme, S.; Ehrlich, S.; Goerigk, L., *J. Comput. Chem.* **2011,** *32*, 1456-1465.
14. Becke, A. D.; Johnson, E. R., *J. Chem. Phys.* **2005,** *123*, 154101.
15. Zhao, Y.; Truhlar, D., *Theor. Chem. Acc.* **2008,** *120*, 215-241.
16. Grimme, S.; Antony, J.; Ehrlich, S.; Krieg, H., *J. Chem. Phys.* **2010,** *132*, 154104.
17. Perdew, J. P.; Burke, K.; Ernzerhof, M., *Phys. Rev. Lett.* **1996,** *77*, 3865-3868.
18. Adamo, C.; Barone, V., *J. Chem. Phys.* **1999,** *110*, 6158-6170.
19. Glendening, E. D.; Landis, C. R.; Weinhold, F., *J. Comput. Chem.* **2013,** *34*, 2134-2134.
20. AIMAll (Version 13.10.19), Keith, T. A. TK Gristmill Software, Overland Park, KS, USA (2013) (aim.tkgristmill.com).
21. Johnson, E. R.; Keinan, S.; Mori-Sánchez, P.; Contreras-García, J.; Cohen, A. J.; Yang, W., *J. Am. Chem. Soc.* **2010,** *132*, 6498-6506.
22. Barone, V.; Cossi, M., *The Journal of Physical Chemistry A* **1998,** *102*, 1995-2001.
23. Luchini, G.; Alegre-Requena, J.; Funes-Ardoiz, I.; Paton, R., *F1000Research* **2020,** *9*.
24. Foltran, S.; Cloutet, E.; Cramail, H.; Tassaing, T., *J. Supercrit. Fluids* **2012,** *63*, 52–58.

Chapter 7

Appendix

List of Figures and Tables

Table S2.3 Depolymerization of PPC using Catalyst **1** under standard conditions. 3
Figure S3.1 ^{1}H NMR of **2** ($CDCl_3$, 298K). 3
Figure S3.2 $^{13}C\{^{1}H\}$ NMR of **2** ($CDCl_3$, 298K). 4
Figure S3.3 2D ^{1}H COSY NMR of **2** ($CDCl_3$, 298K). 4
Figure S3.4 2D ^{1}H-^{13}C HSQC NMR of **2** ($CDCl_3$, 298K). 5
Figure S3.5 2D ^{1}H-^{13}C HMBC NMR of **2** ($CDCl_3$, 298K). 5
Figure S3.6 ^{1}H NMR of $\mathbf{2_H}$ ($CDCl_3$, 298K). 6
Figure S3.7 $^{13}C\{^{1}H\}$ NMR of $\mathbf{2_H}$ ($CDCl_3$, 298K). 6
Figure S3.8 2D ^{1}H COSY NMR of $\mathbf{2_H}$ ($CDCl_3$, 298K). 7
Figure S3.9 2D ^{1}H-^{13}C HSQC NMR of $\mathbf{2_H}$ ($CDCl_3$, 298K). 7
Figure S3.10 2D ^{1}H-^{13}C HMBC NMR of $\mathbf{2_H}$ ($CDCl_3$, 298K). 8
Figure S3.11 ^{1}H NMR of $\mathbf{2_{Me}}$ ($CDCl_3$, 298K). 8
Figure S3.12 $^{13}C\{^{1}H\}$ NMR of $\mathbf{2_{Me}}$ (CD_3OD, 298K). 9
Figure S3.13 2D ^{1}H COSY NMR of $\mathbf{2_{Me}}$ (CD_3OD, 298K). 9
Figure S3.14 2D HSQC NMR of $\mathbf{2_{Me}}$ (CD_3OD, 298K). 10
Figure S3.15 2D ^{1}H-^{13}C HMBC NMR of $\mathbf{2_{Me}}$ (CD_3OD, 298K). 10
Figure S3.16 ^{1}H NMR of $\mathbf{2_{OMe}}$ ($CDCl_3$, 298K). 11
Figure S3.17 $^{13}C\{^{1}H\}$ NMR of $\mathbf{2_{OMe}}$ ($CDCl_3$, 298K). 11
Figure S3.18 2D ^{1}H COSY NMR of $\mathbf{2_{OMe}}$ ($CDCl_3$, 298K). 12
Figure S3.19 2D ^{1}H-^{13}C HSQC NMR of $\mathbf{2_{OMe}}$ ($CDCl_3$, 298K). 12
Figure S3.20 2D ^{1}H-^{13}C HMBC NMR of $\mathbf{2_{OMe}}$ ($CDCl_3$, 298K). 13
Figure S3.21 ^{1}H NMR of $\mathbf{2_F}$ ($CDCl_3$, 298K). 13
Figure S3.22 $^{13}C\{^{1}H\}$ NMR of $\mathbf{2_F}$ ($CDCl_3$, 298K). 14
Figure S3.23 2D ^{1}H COSY NMR of $\mathbf{2_F}$ ($CDCl_3$, 298K). 14
Figure S3.24 2D ^{1}H-^{13}C HSQC NMR of $\mathbf{2_F}$ ($CDCl_3$, 298K). 15
Figure S3.25 2D ^{1}H-^{13}C HMBC NMR of $\mathbf{2_F}$ ($CDCl_3$, 298K). 15
Figure S3.26 ^{19}F NMR of $\mathbf{2_F}$ ($CDCl_3$, 298K). 16
Figure S3.27 ^{1}H NMR of $\mathbf{2_{Cl}}$ ($CDCl_3$, 298K). 16
Figure S3.28 $^{13}C\{^{1}H\}$ NMR of $\mathbf{2_{Cl}}$ ($CDCl_3$, 298K). 17
Figure S3.29 2D ^{1}H COSY NMR of $\mathbf{2_{Cl}}$ ($CDCl_3$, 298K). 17
Figure S3.30 2D ^{1}H -^{13}C HSQC NMR of $\mathbf{2_{Cl}}$ ($CDCl_3$, 298K). 18
Figure S3.31 2D ^{1}H -^{13}C HMBC NMR of $\mathbf{2_{Cl}}$ ($CDCl_3$, 298K). 18
Table S3.1 Selected Atom Distances and Angles from Solid State Structure of $\mathbf{2_H}$. 19
Figure S3.32 IR spectra of **2** and $\mathbf{3_R}$. 20
Figure S3.33 CV Curves of **1** and $\mathbf{3_R}$. 21
Figure S3.34 a) Absorbance versus time plot for PPC Formation for **2**. b) Logarithmic plot to calculate k_{obs} for **2**. 22
Figure S3.35 a) Absorbance versus time plot for PPC Formation for $\mathbf{3_{Me}}$. b) Logarithmic plot to calculate k_{obs} for $3_{\mathbf{Me}}$. 22
Figure S3.36 a) Absorbance versus time plot for PPC Formation for $\mathbf{3_{OMe}}$. b) Logarithmic plot to calculate k_{obs} for $3_{\mathbf{OMe}}$. 22
Figure S3.37 a) Absorbance versus time plot for PPC Formation for $\mathbf{3_F}$. b) Logarithmic plot to calculate k_{obs} for $\mathbf{3_F}$. 23
Figure S3.38 a) Absorbance versus time plot for PPC Formation for $\mathbf{3_{Cl}}$. b) Logarithmic plot to calculate k_{obs} for $\mathbf{3_{Cl}}$. 23
Figure S3.39 GPC trace of PO/CO_2 polymerisation run from Table 1 of **2**. 23
Figure S3.40 GPC trace of PO/CO_2 polymerisation run from Table 1 of $\mathbf{3_{Me}}$. 24
Figure S3.41 GPC trace of PO/CO_2 polymerisation run from Table 1 of $\mathbf{3_{OMe}}$. 24
Figure S3.42 GPC trace of PO/CO_2 polymerisation run from Table 1 of $\mathbf{3_H}$. 24
Figure S3.43 GPC trace of PO/CO_2 polymerisation run from Table 1 of $\mathbf{3_F}$. 25
Figure S3.44 GPC trace of PO/CO_2 polymerisation run from Table 1 of $\mathbf{3_{Cl}}$. 25
Figure S3.45 Conversion versus Selectivity plot of PO/CO_2 polymerisation of $\mathbf{3_H}$ (0-20% conversion). 26
Figure 4.1 SEC trace of Entry 1 Table 4.1. 26
Figure 4.2 SEC trace of Entry 2 Table 4.1. 27
Figure 4.3 SEC trace of Entry 3 Table 4.1. 27
Figure 4.4 SEC trace of Entry 4 Table 4.1. 28
Figure 4.5 SEC trace of Entry 1 Table 4.2. 28
Figure 4.6 SEC trace of Entry 2 Table 4.2. 29
Figure 4.7 SEC trace of Entry 3 Table 4.2. 29
Figure 4.8 SEC trace of Entry 4 Table 4.2. 30
Figure 4.9 SEC trace of Entry 5 Table 4.2. 30
Figure 4.10 SEC trace of Entry 2 Table 4.3. Molar mass corrected using 0.58 correction factor. 31
Figure 4.11 SEC trace of Entry 3 Table 4.3. Molar mass corrected using 0.58 correction factor. 31
Figure 4.12 SEC trace of Entry 4 Table 4.3. Molar mass corrected using 0.58 correction factor. 32
Figure 4.13 SEC trace of Entry 1 Table 4.4. Molar mass corrected using 0.58 correction factor. 32
Figure 4.14 SEC trace of Entry 2 Table 4.4. Molar mass corrected using 0.58 correction factor. 33
Figure 4.15 SEC trace of Entry 3 Table 4.4. Molar mass corrected using 0.58 correction factor. 33
Figure 4.16 SEC trace of Entry 4 Table 4.4. Molar mass corrected using 0.58 correction factor. 34

7.1 Supplementary Figures and Data for Chapter 2

Table S2.4 Depolymerization of PPC using Catalyst **1** under standard conditions.[a]

Entry	T (°C)	k_{obs} (s^{-1})	k_p ($dm^3\ mol^{-1}\ s^{-1}$)	ln(k_p/T)	Average ln(k_p/T)	Standard Deviation
1	45	0.93	0.31	-6.94	-6.95	0.127
2	45	0.77	0.26	-7.13		
3	45	1.02	0.34	-6.84		
4	45	0.98	0.33	-6.88		
5	50	1.36	0.45	-6.57	-6.64	0.058
6	50	1.19	0.40	-6.71		
7	50	1.27	0.42	-6.64		
8	50	1.24	0.41	-6.66		
9	55	3.40	1.13	-5.67	-5.79	0.093
10	55	2.71	0.90	-5.89		
11	55	3.04	1.01	-5.78		
12	55	2.98	0.99	-5.80		
13	60	4.52	1.51	-5.40	-5.62	0.148
14	60	3.33	1.11	-5.70		
15	60	3.43	1.14	-5.68		
16	60	3.34	1.11	-5.70		

[a]Reaction Conditions: [cat] : [PPC] = 1 : 100 where [PPC] = 0.3 M in PO. All reactions were run to completion as determined by *in-situ* IR monitoring. All reactions resulted in the depolymerization of PPC to PC where no polyether linkages were detected by ^{1}H NMR spectroscopy.

7.2 Supplementary Figures and Data for Chapter 3

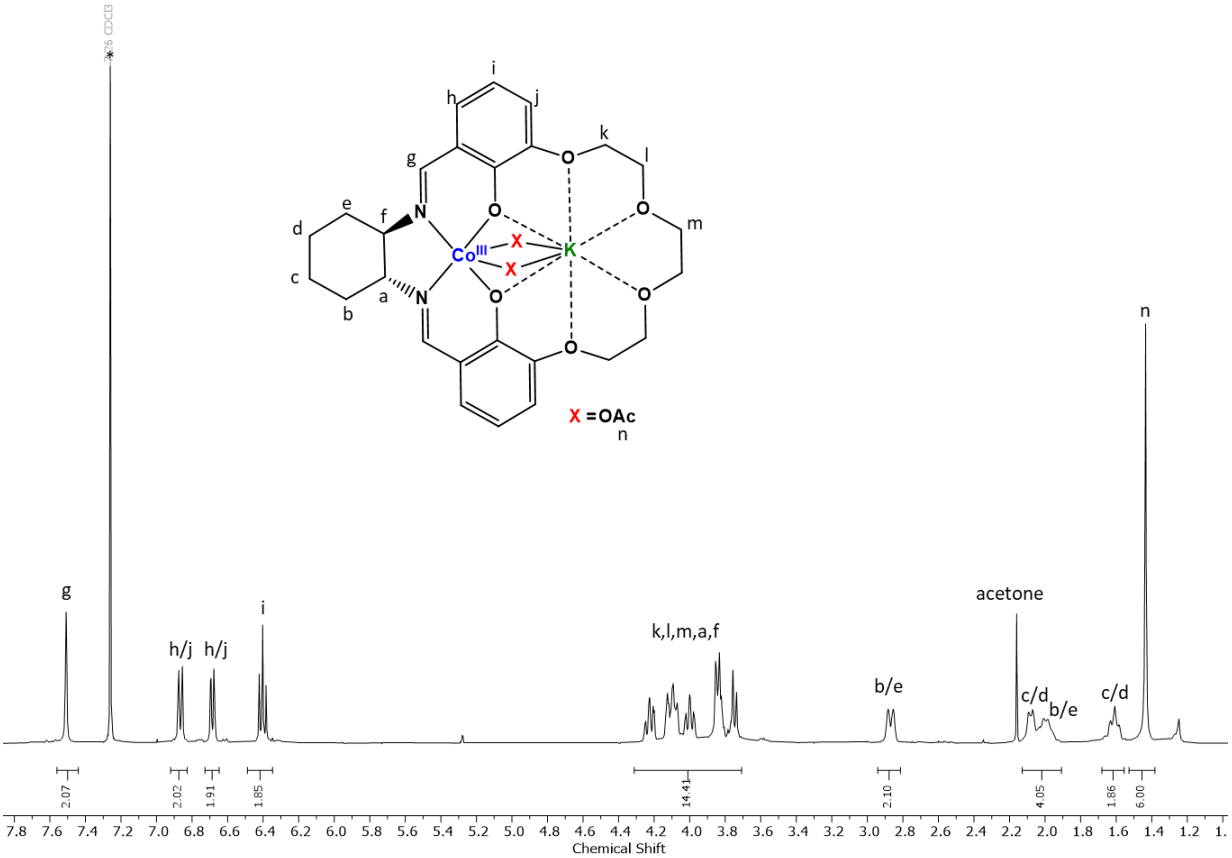


Figure S3.1 ^{1}H NMR of **2** ($CDCl_3$, 298K).

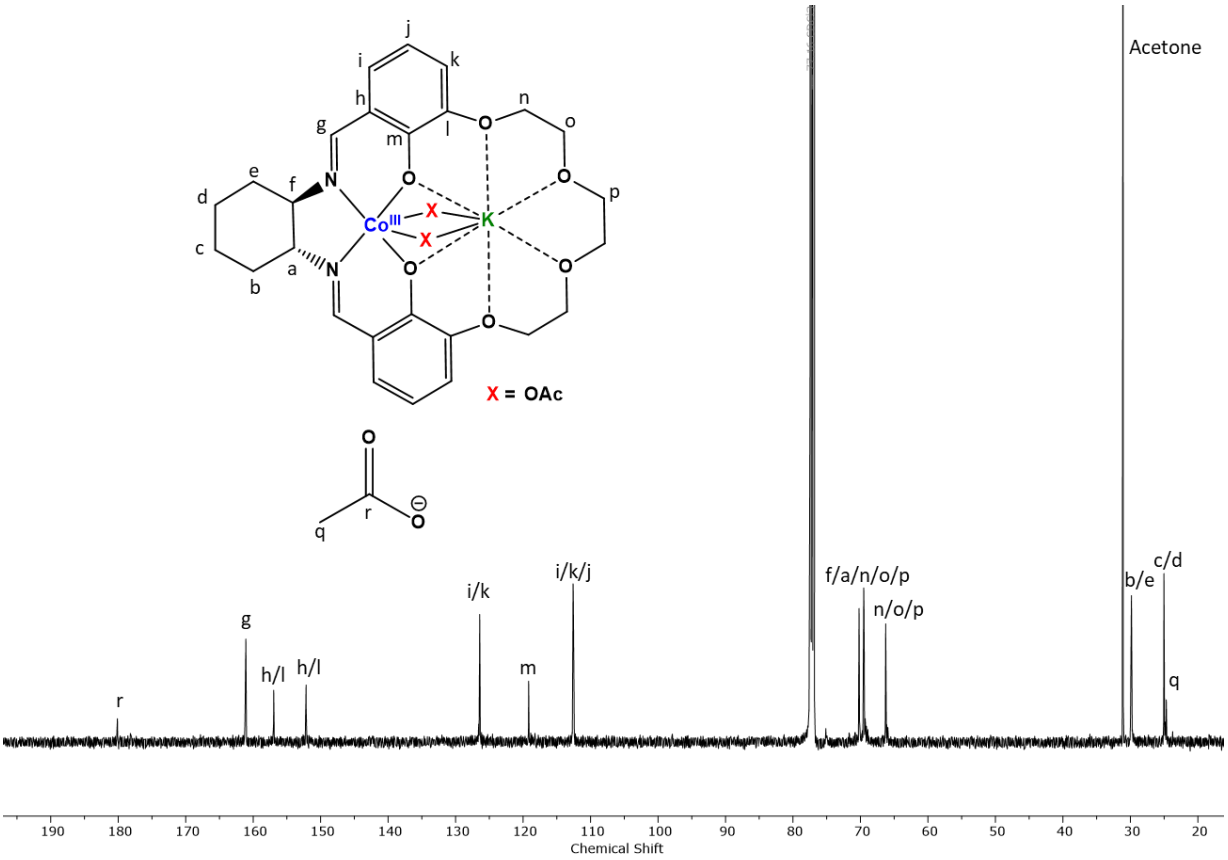


Figure S3.2 $^{13}C\{^{1}H\}$ NMR of **2** ($CDCl_3$, 298K).

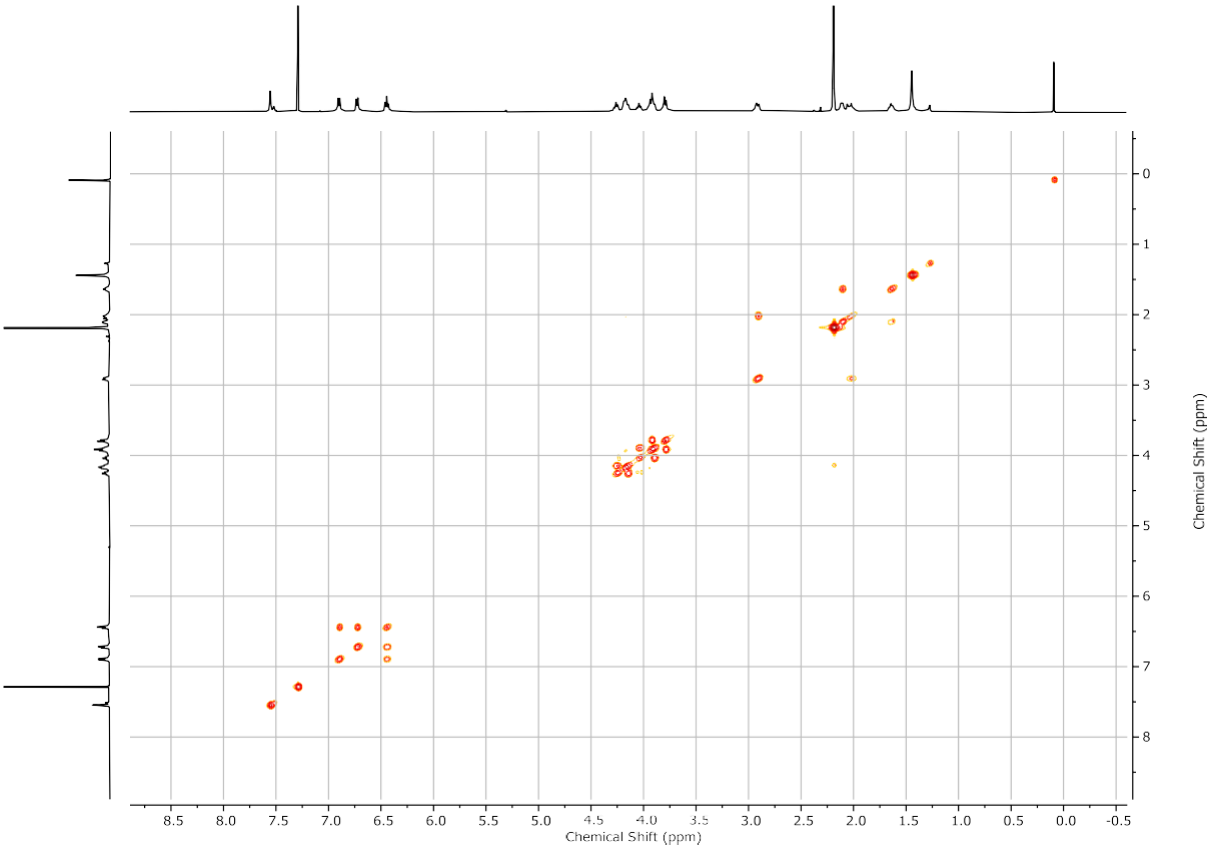


Figure S3.3 2D ^{1}H COSY NMR of **2** ($CDCl_3$, 298K).

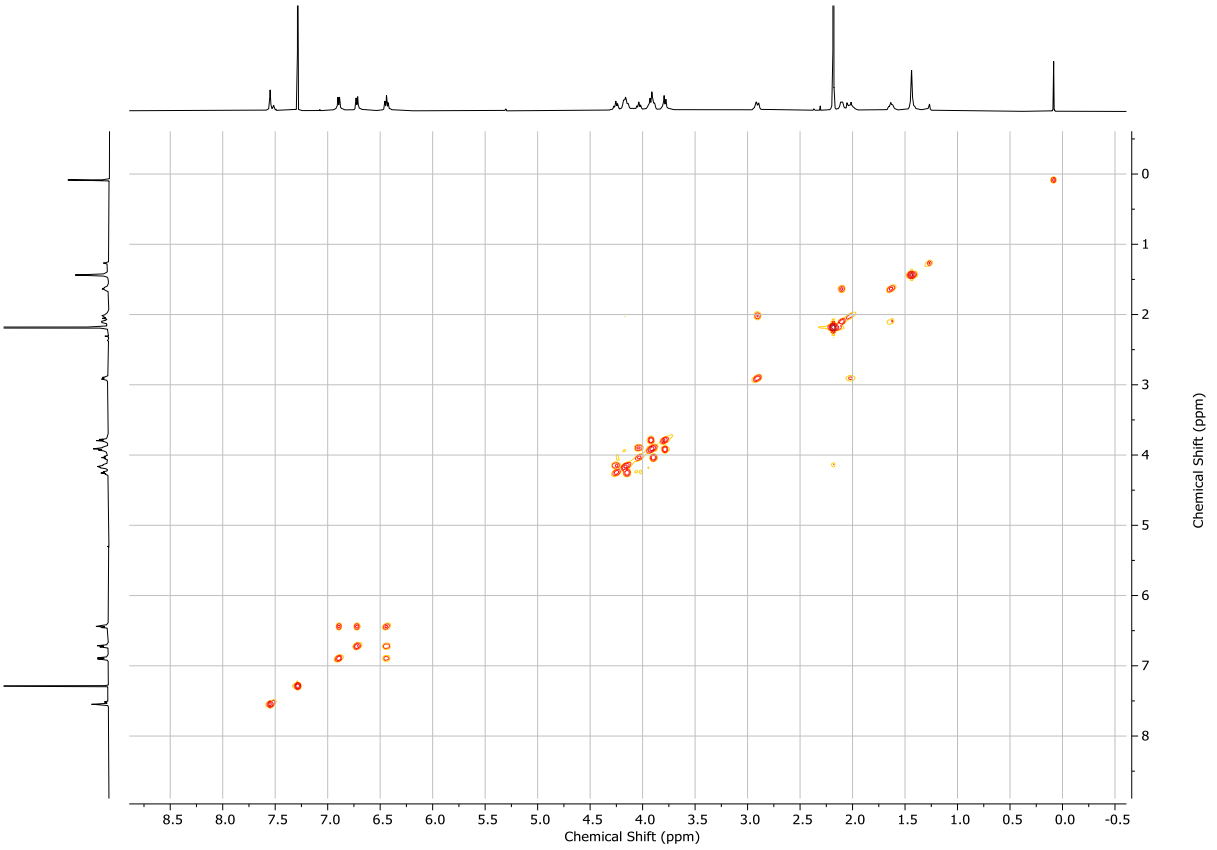


Figure S3.4 2D ^{1}H-^{13}C HSQC NMR of **2** ($CDCl_3$, 298K)

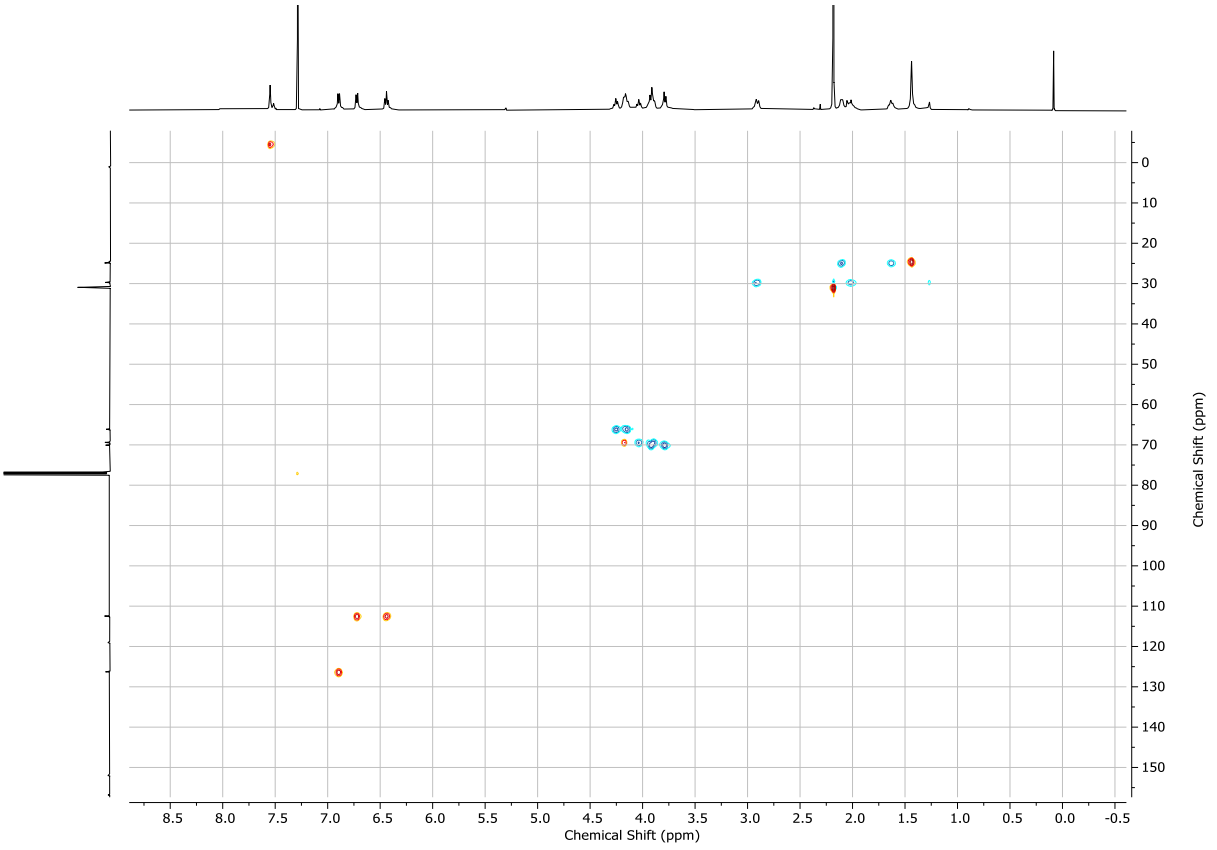


Figure S3.5 2D ^{1}H-^{13}C HMBC NMR of **2** ($CDCl_3$, 298K).

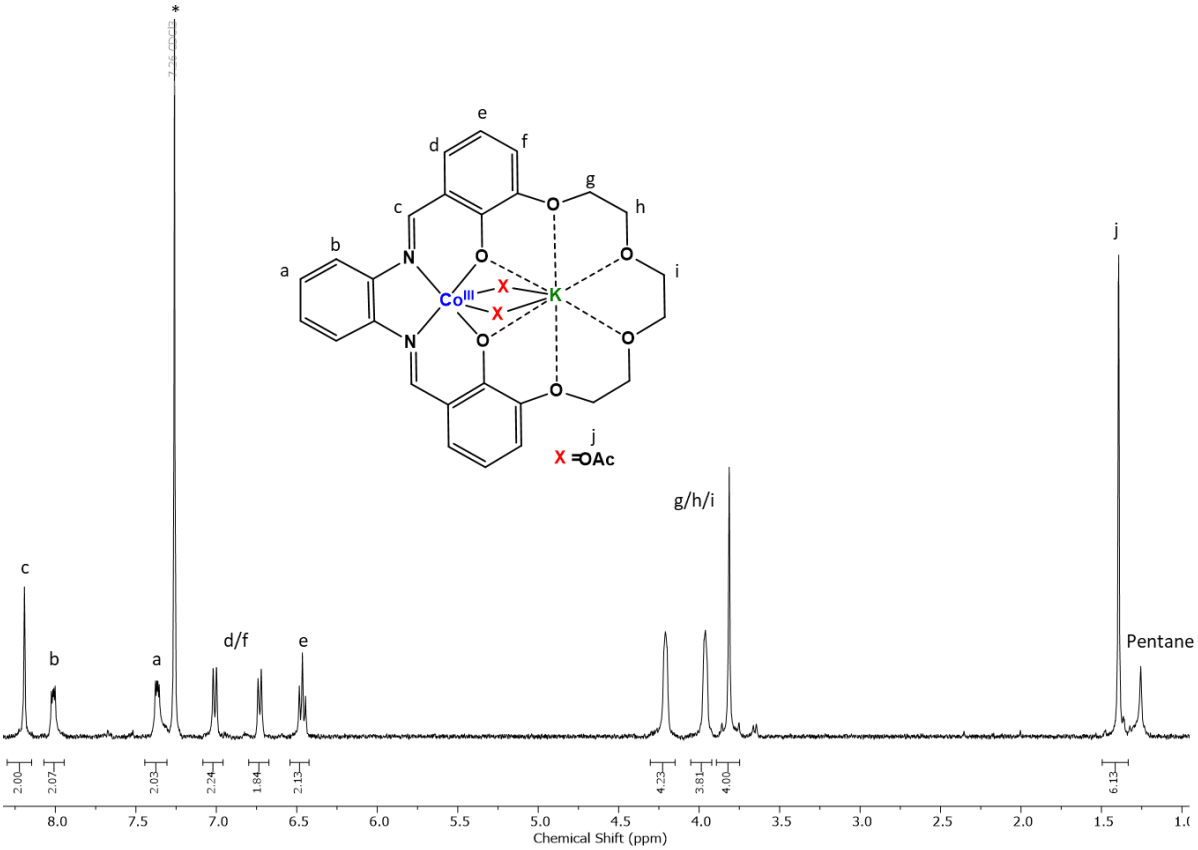


Figure S3.6 ^{1}H NMR of **3$_{H}$** ($CDCl_3$, 298K).

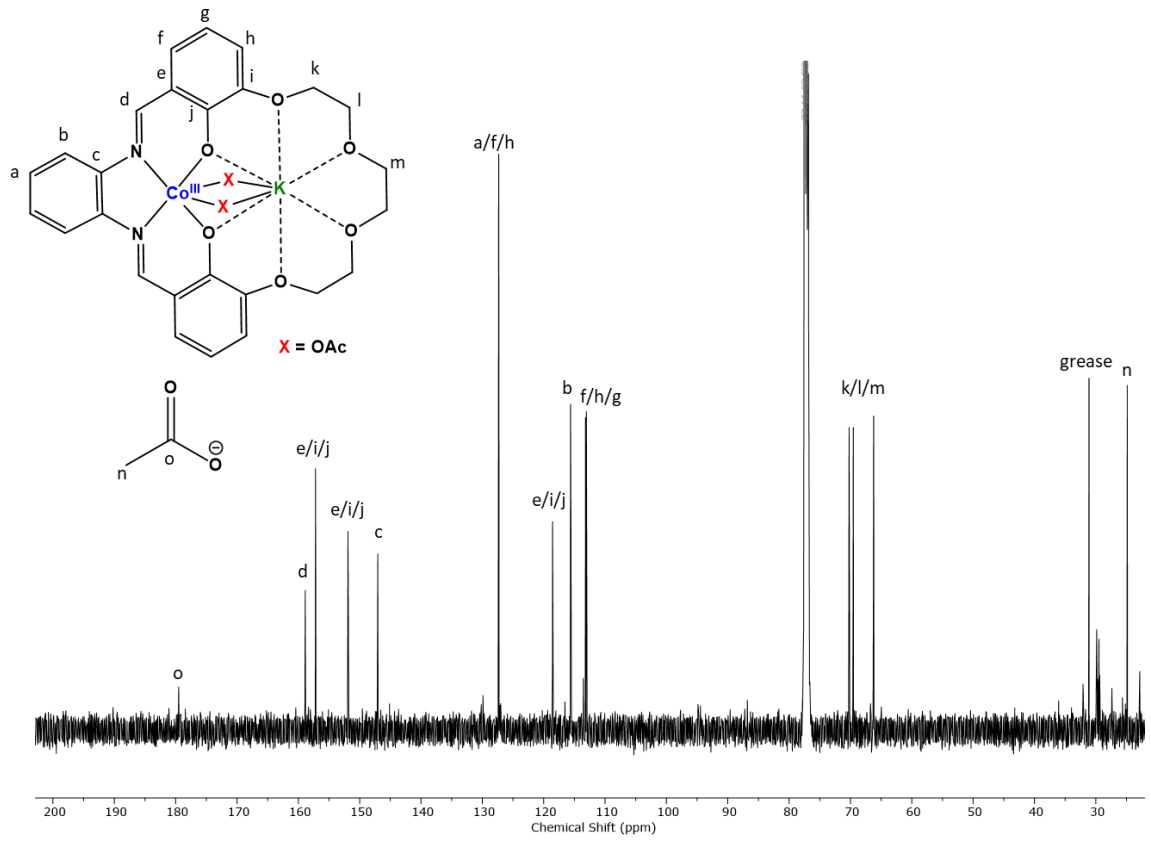


Figure S3.7 ^{13}C{^{1}H} NMR of **3$_{H}$** ($CDCl_3$, 298K).

Chemical Shift (ppm)

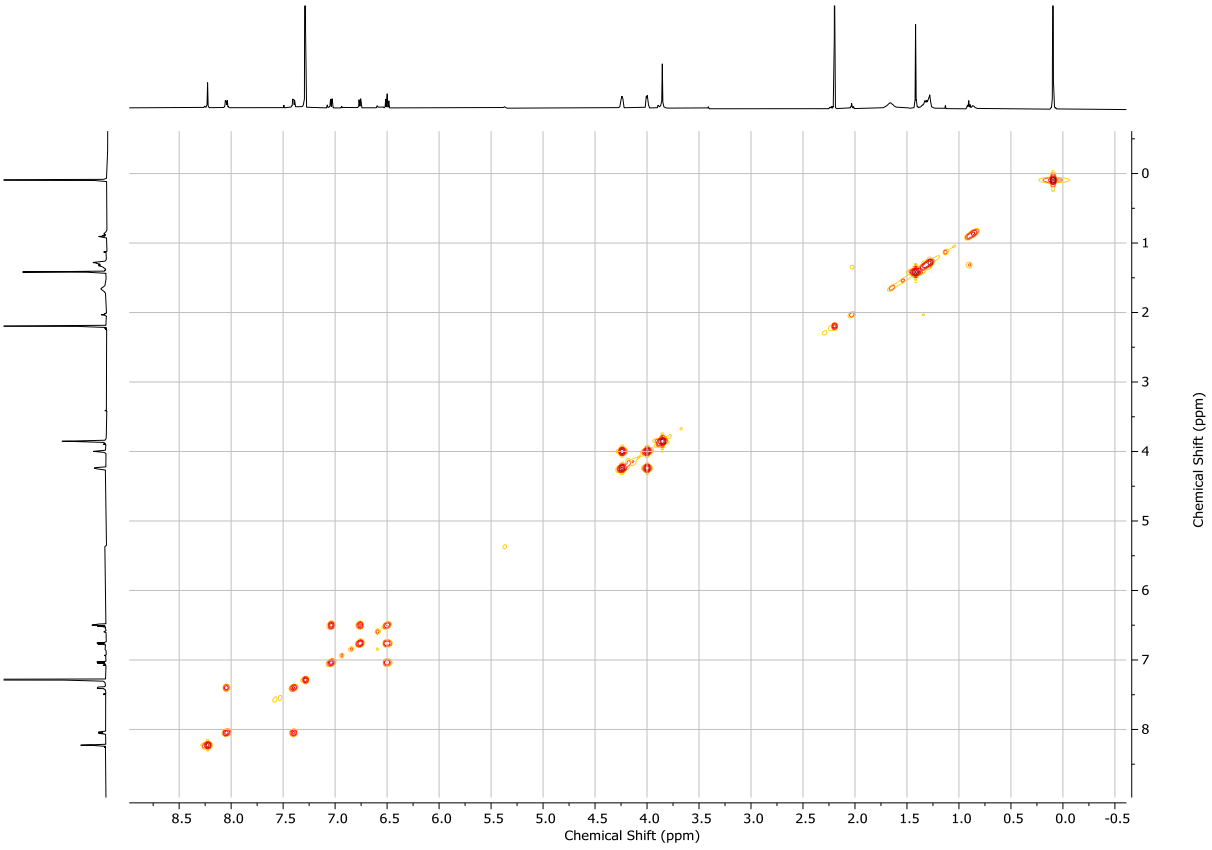


Figure S3.8 2D ^{1}H COSY NMR of **3$_{H}$** ($CDCl_3$, 298K).

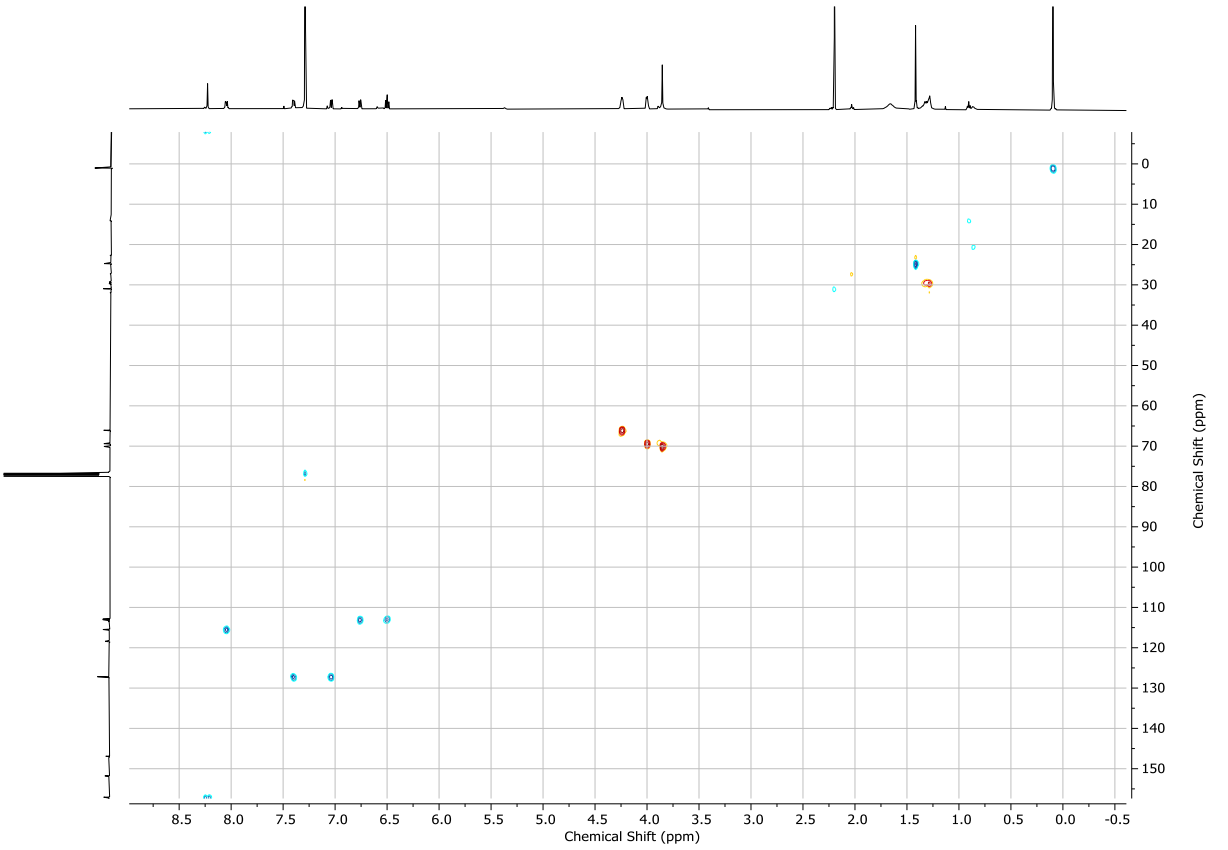


Figure S3.9 2D ^{1}H-^{13}C HSQC NMR of **3$_{H}$** ($CDCl_3$, 298K).

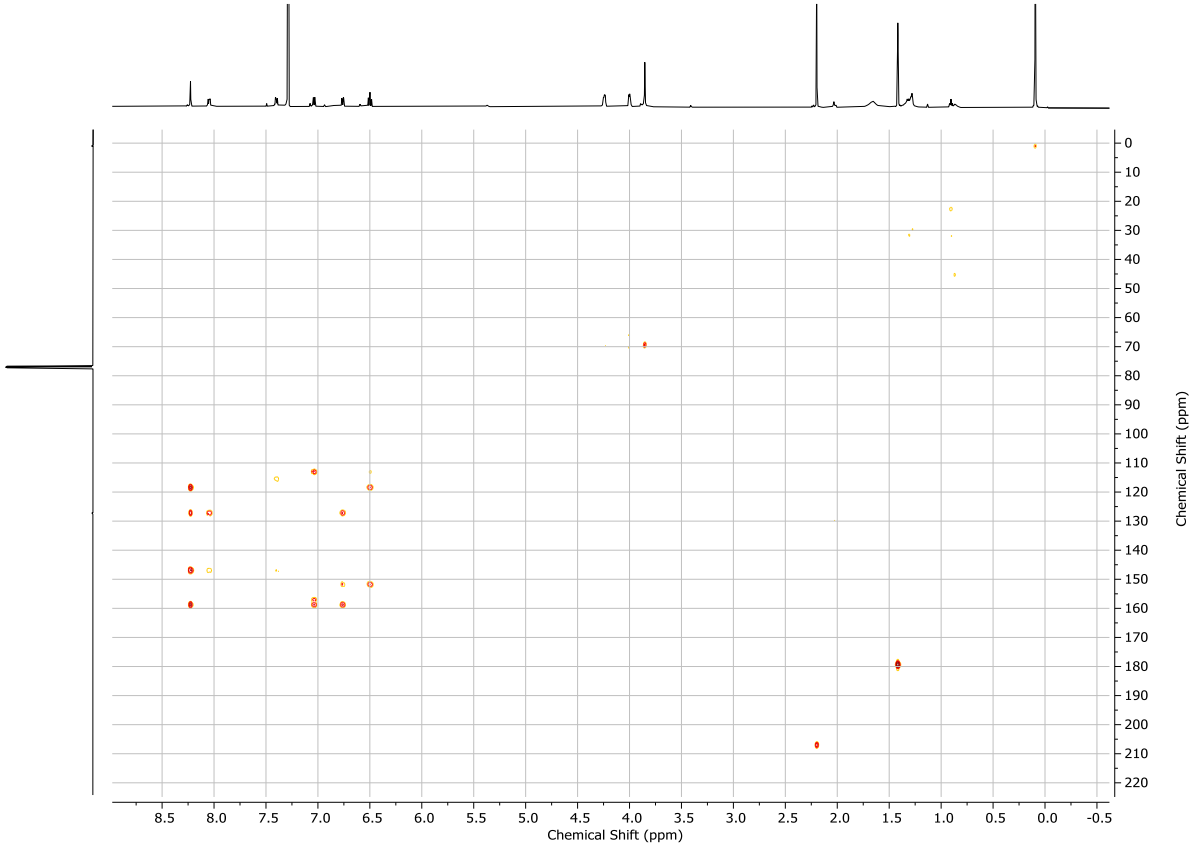


Figure S3.10 2D ^{1}H-^{13}C HMBC NMR of 3_{H} ($CDCl_3$, 298K).

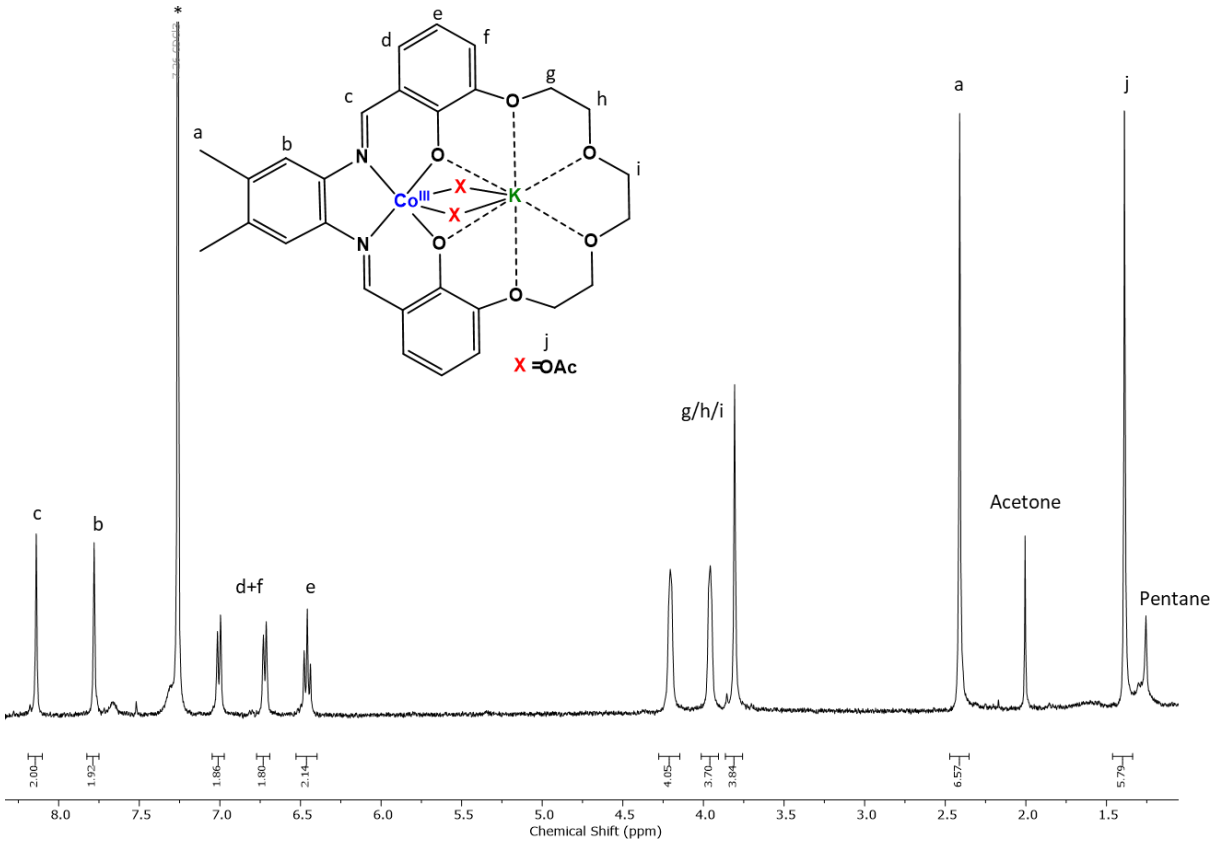


Figure S3.11 ^{1}H NMR of $\mathbf{3_{Me}}$ ($CDCl_3$, 298K).

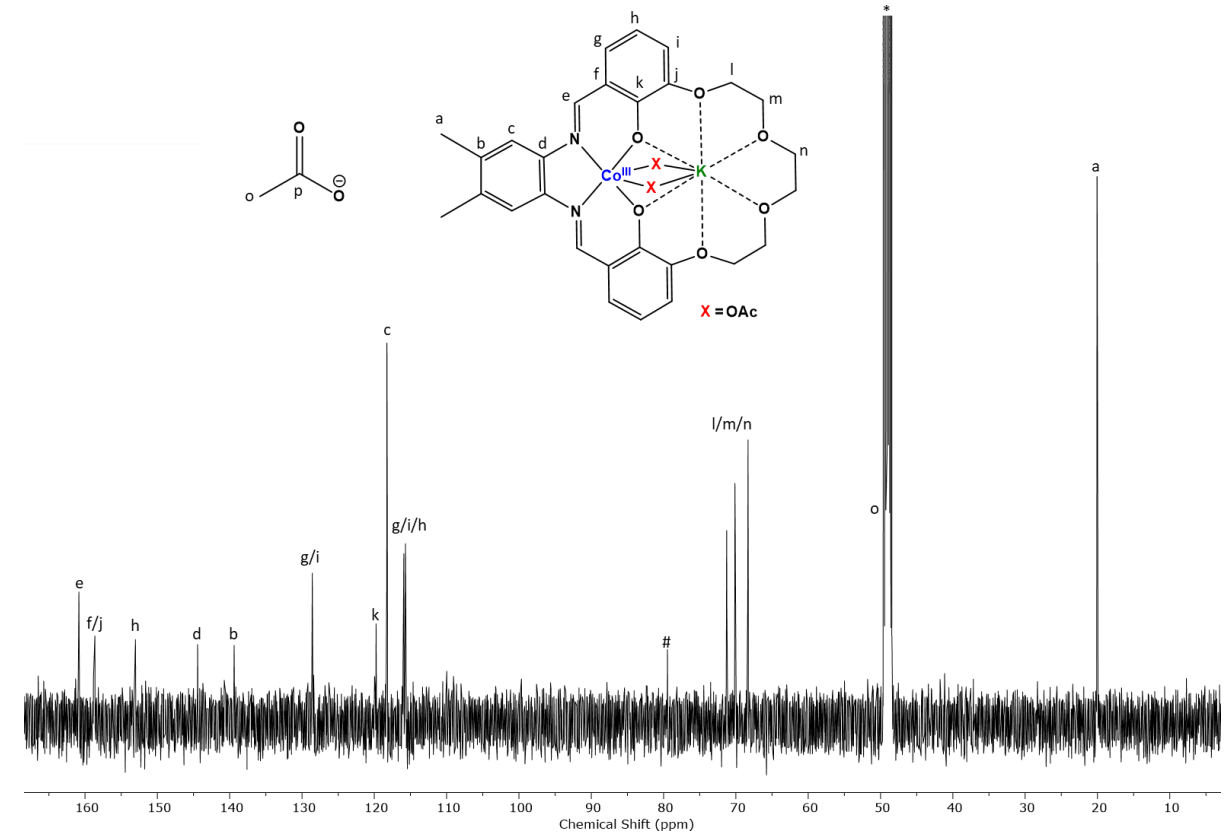


Figure S3.12 $^{13}C\{^{1}H\}$ NMR of $\mathbf{3_{Me}}$ (CD_3OD, 298K).

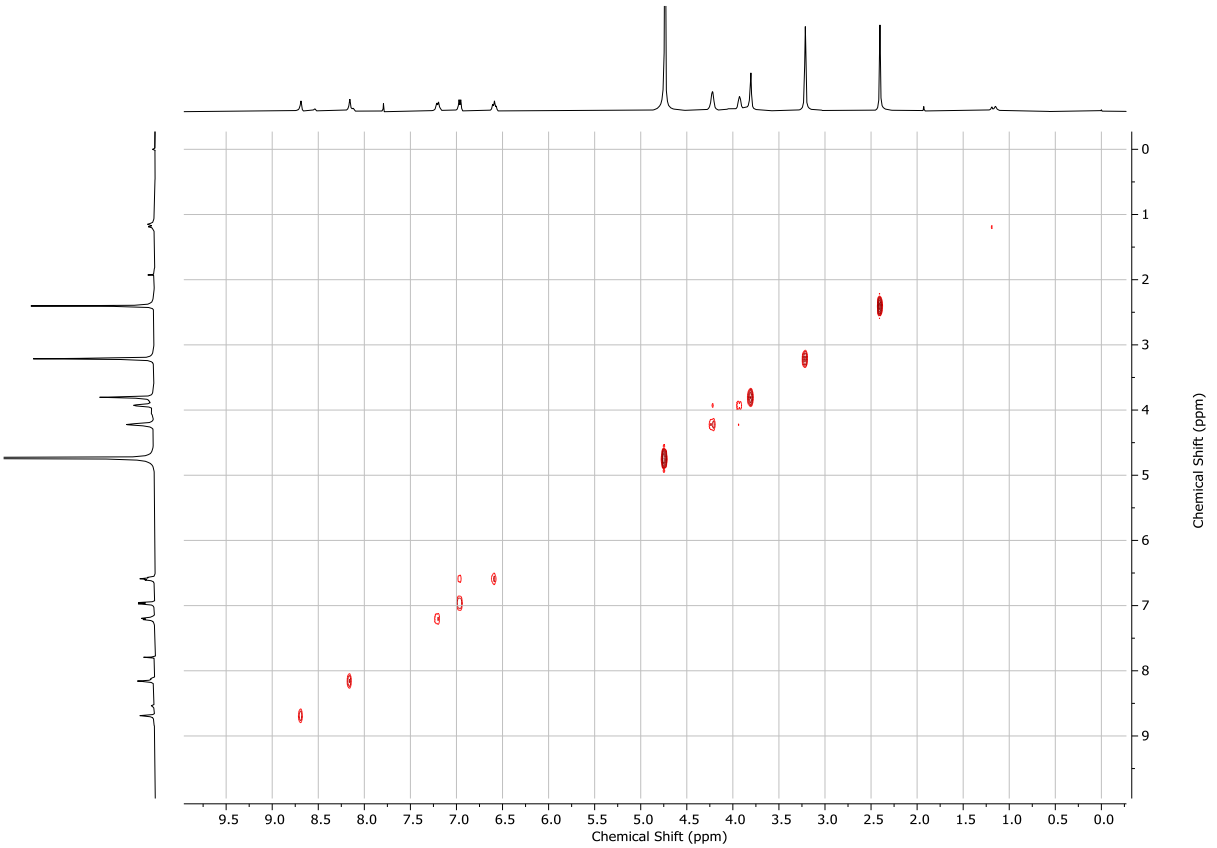


Figure S3.13 2D ^{1}H COSY NMR of $\mathbf{3_{Me}}$ (CD_3OD, 298K).

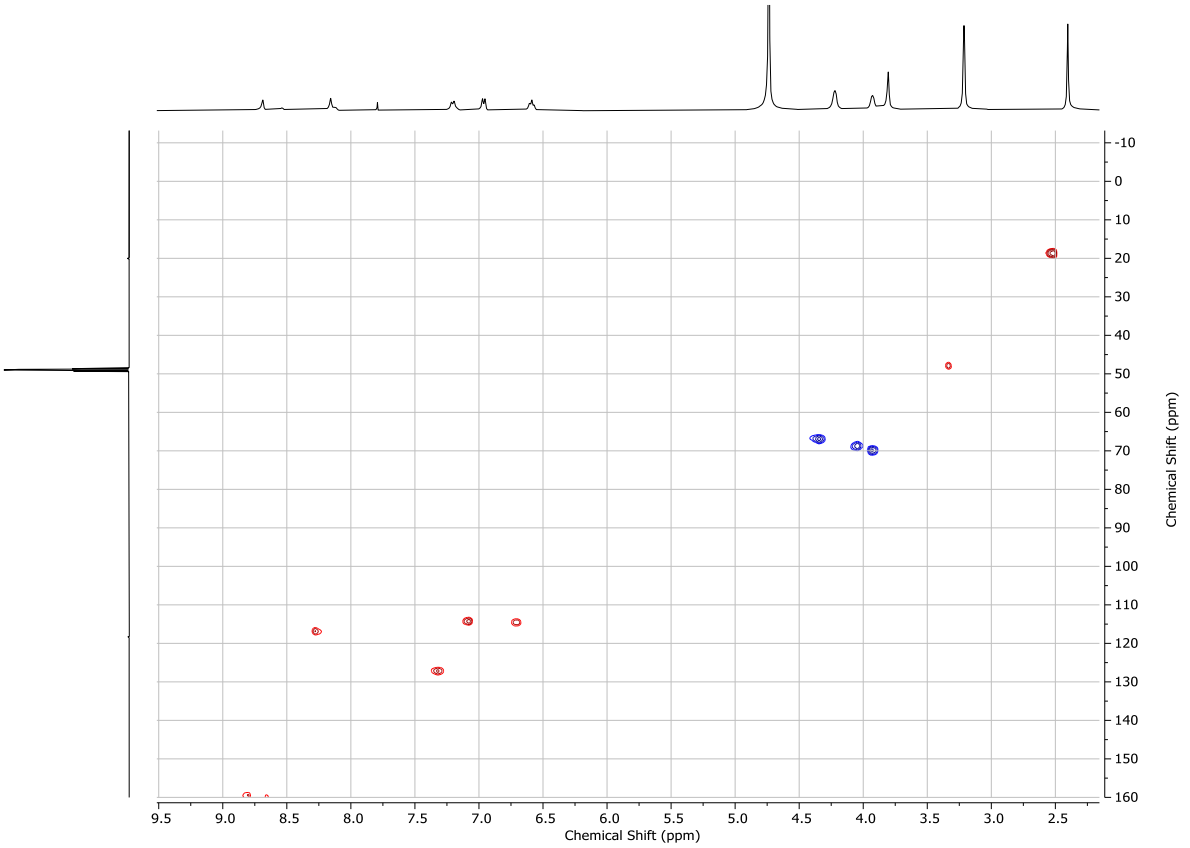


Figure S3.14 2D HSQC NMR of **3$_{Me}$** (CD_3OD, 298K).

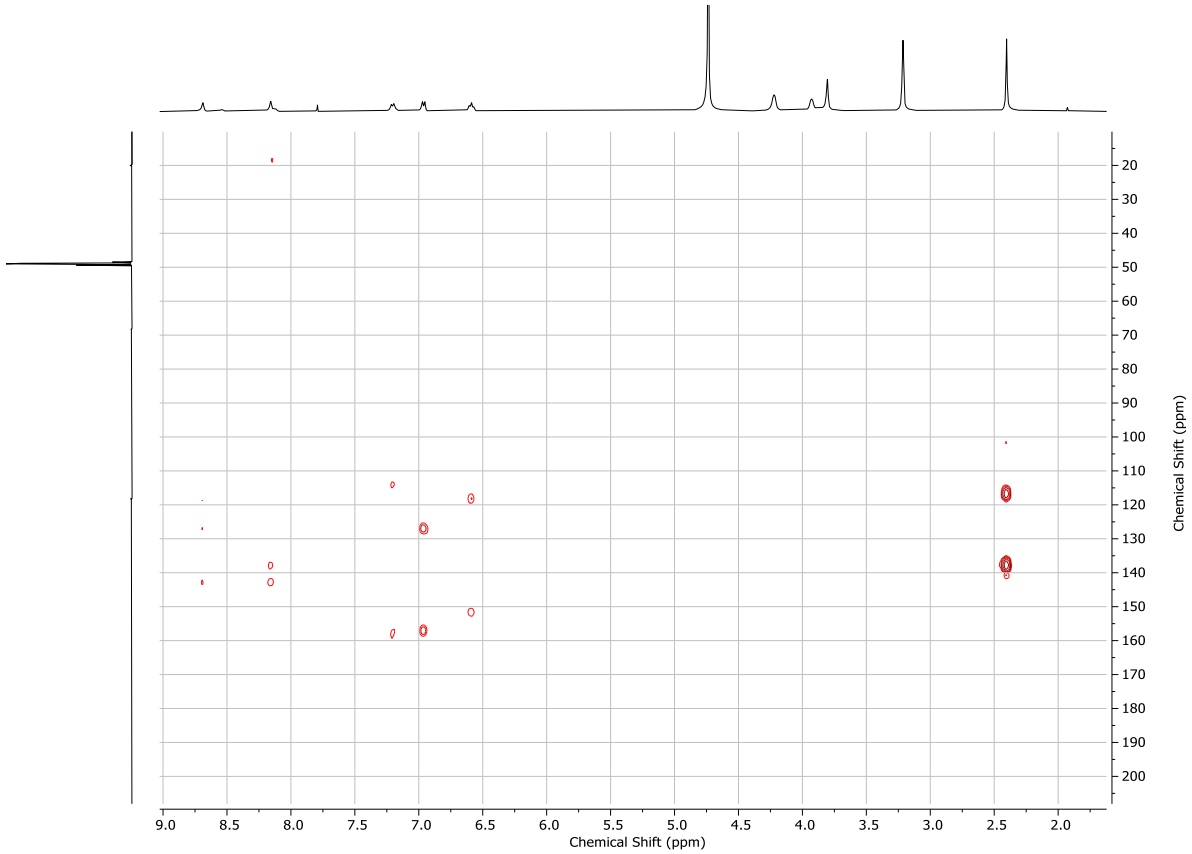


Figure S3.15 2D ^{1}H-^{13}C HMBC NMR of 3_{Me} (CD_3OD, 298K).

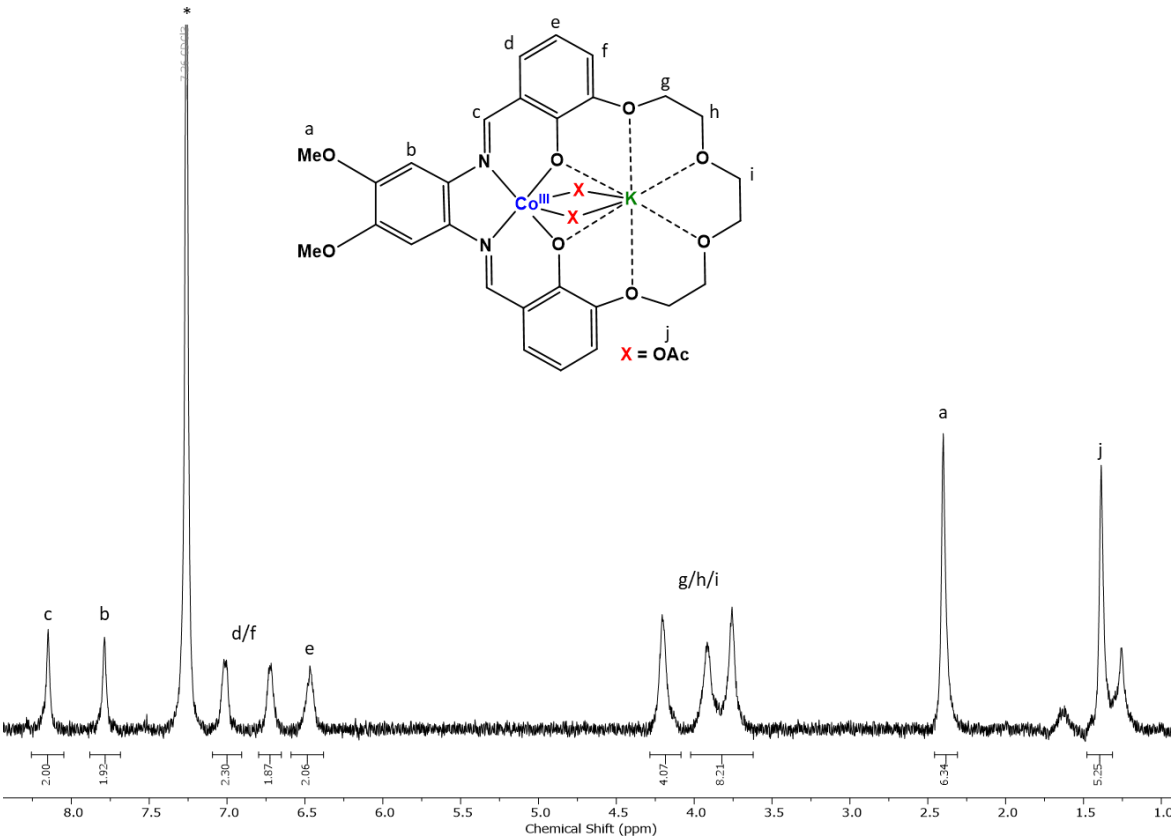


Figure S3.16 ^{1}H NMR of **3$_{OMe}$** ($CDCl_3$, 298K).

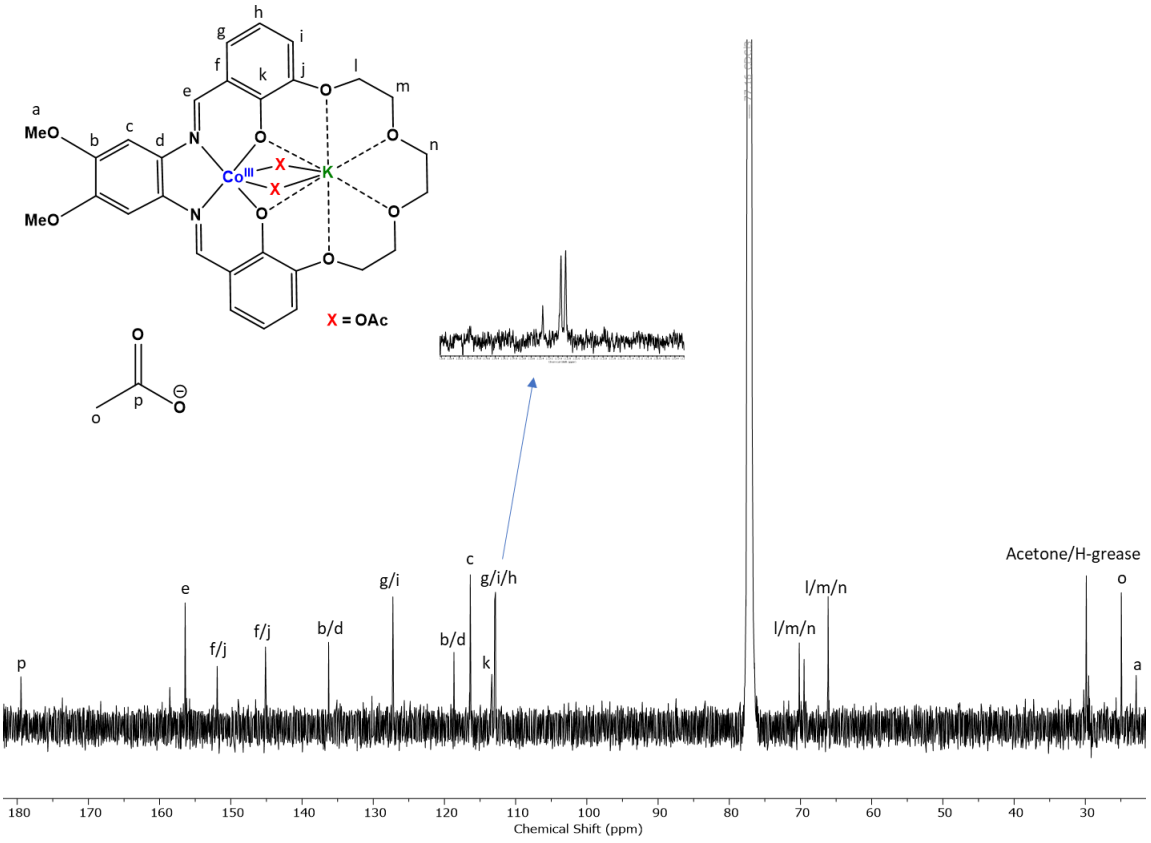


Figure S3.17 ^{13}C{^{1}H} NMR of **3$_{OMe}$** ($CDCl_3$, 298K

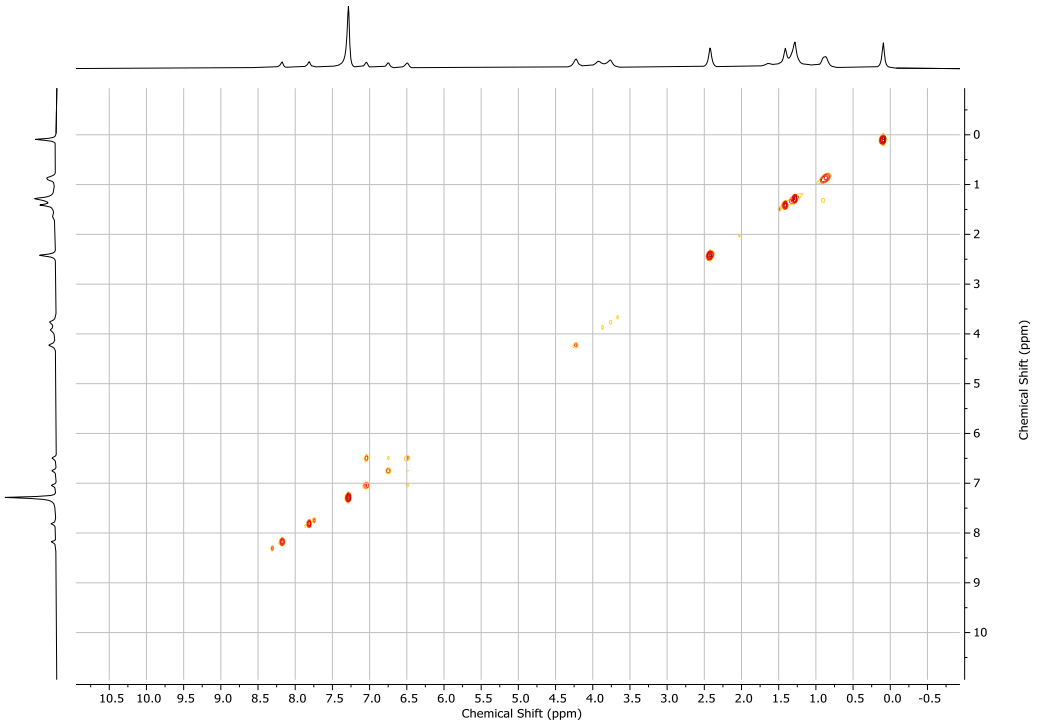


Figure S3.18 2D ^{1}H COSY NMR of **3$_{OMe}$** ($CDCl_3$, 298K).

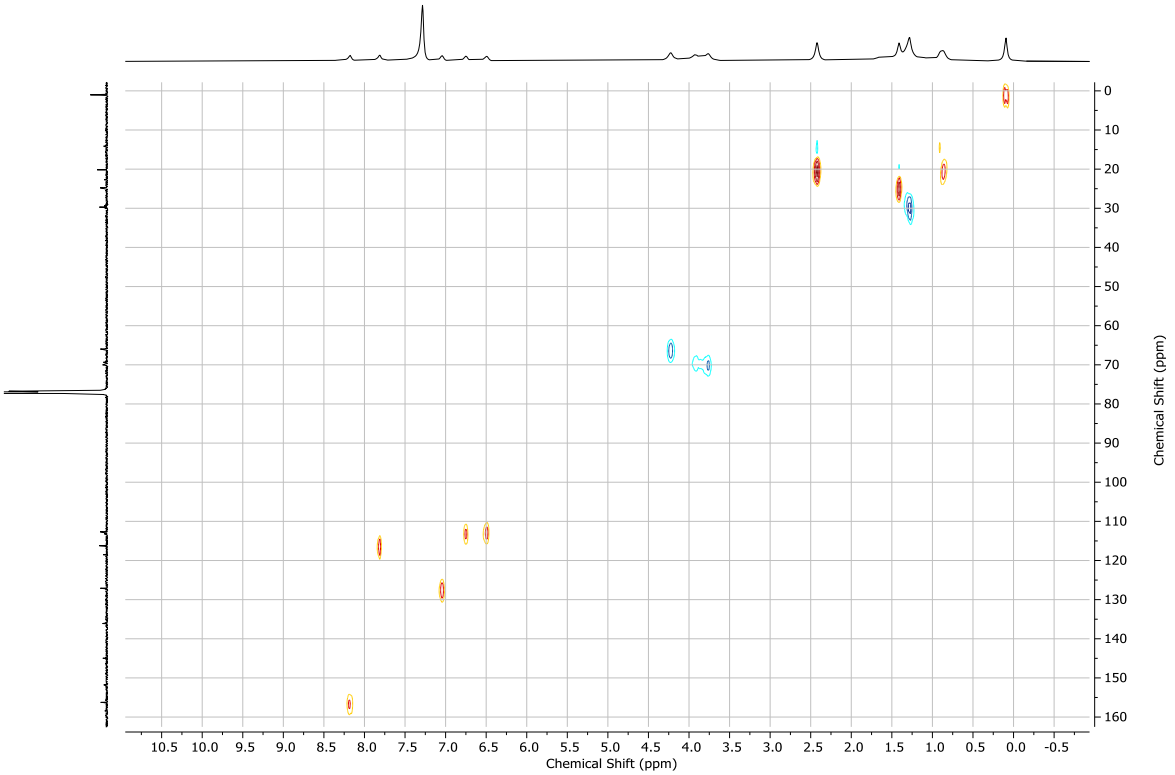


Figure S3.19 2D ^{1}H-^{13}C HSQC NMR of **3$_{OMe}$** ($CDCl_3$, 298K).

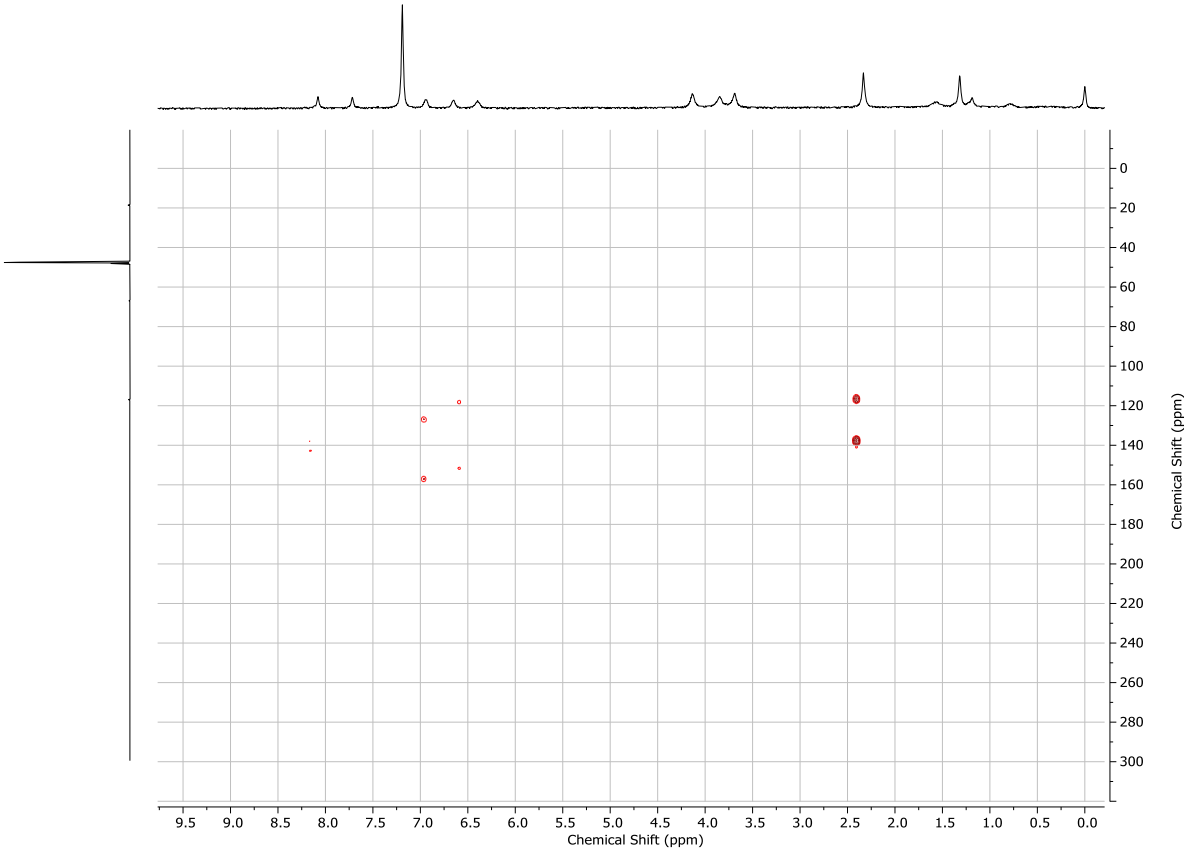


Figure S3.20 2D ^{1}H-^{13}C HMBC NMR of $\mathbf{3_{OMe}}$ ($CDCl_3$, 298K).

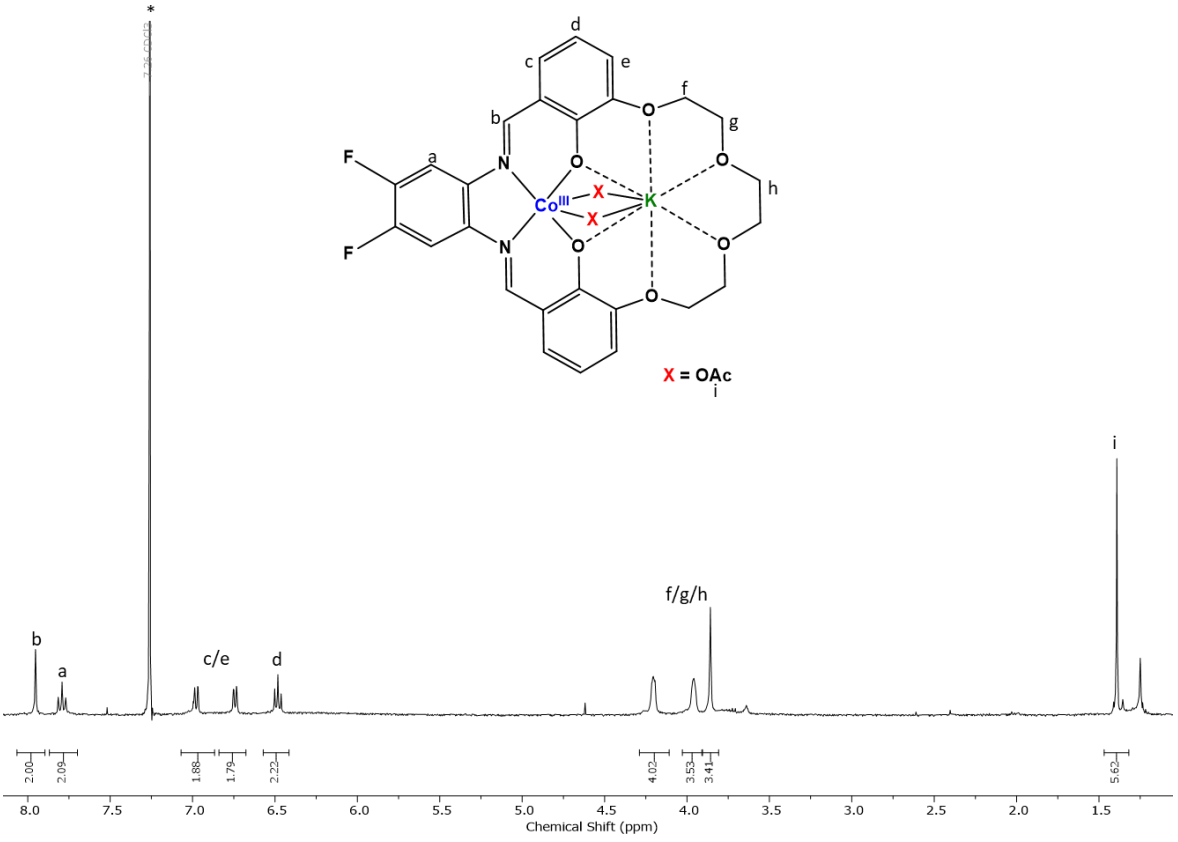


Figure S3.21 ^{1}H NMR of $\mathbf{3_F}$ ($CDCl_3$, 298K).

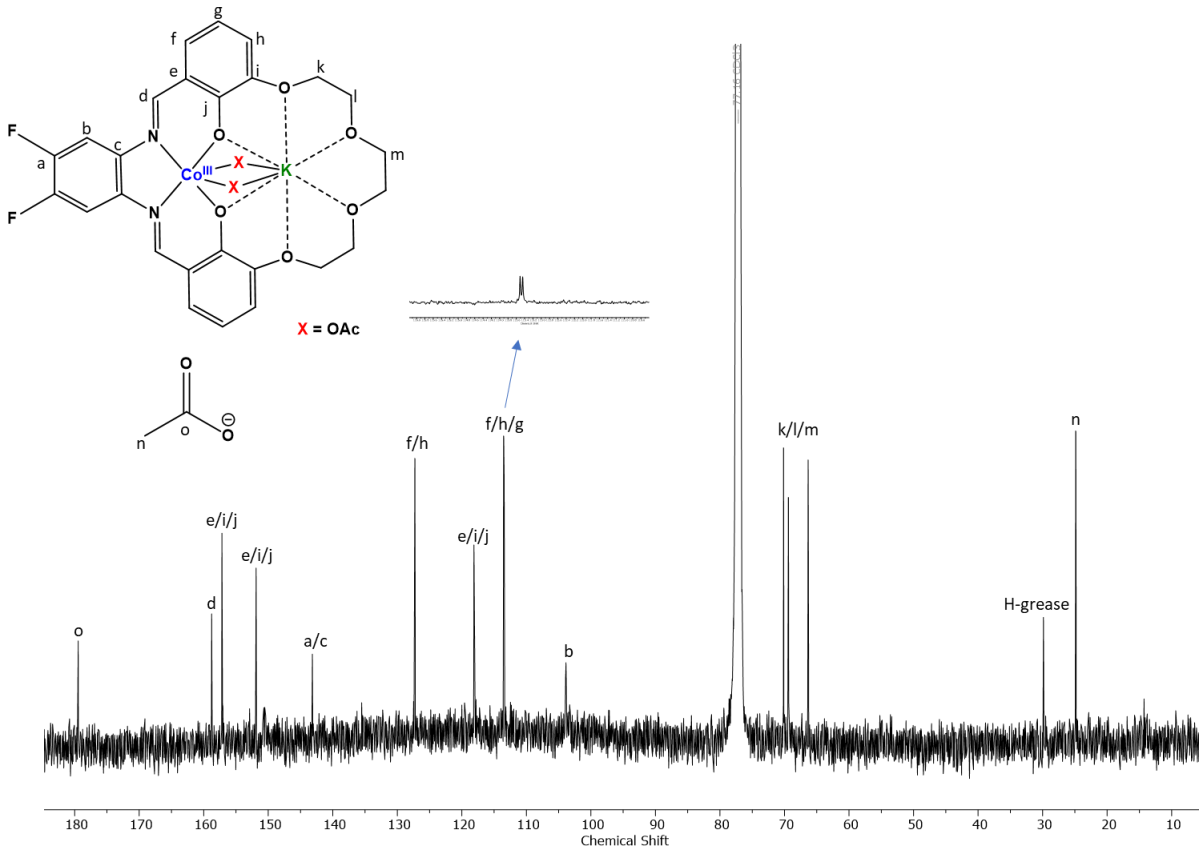


Figure S3.22 $^{13}C\{^{1}H\}$ NMR of $\mathbf{3_F}$ ($CDCl_3$, 298K).

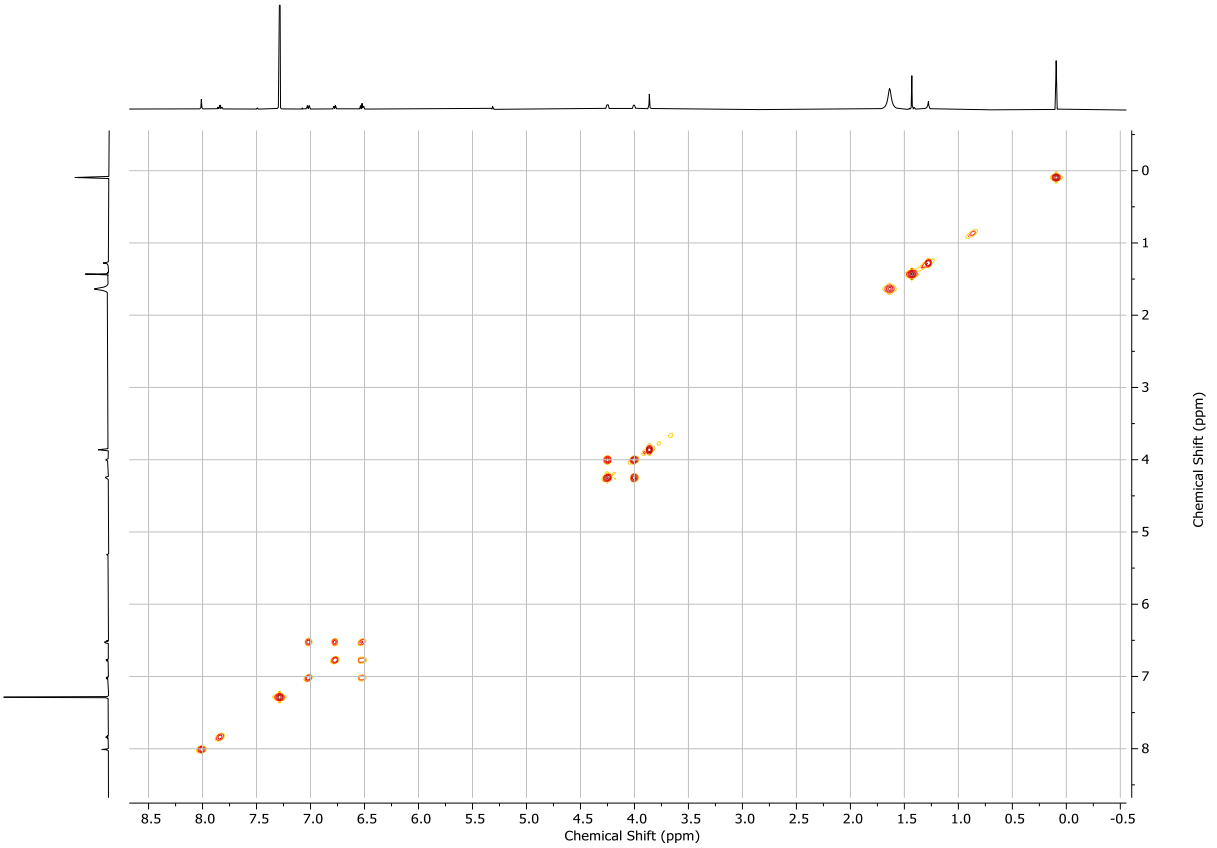


Figure S3.23 2D ^{1}H COSY NMR of $\mathbf{3_F}$ ($CDCl_3$, 298K).

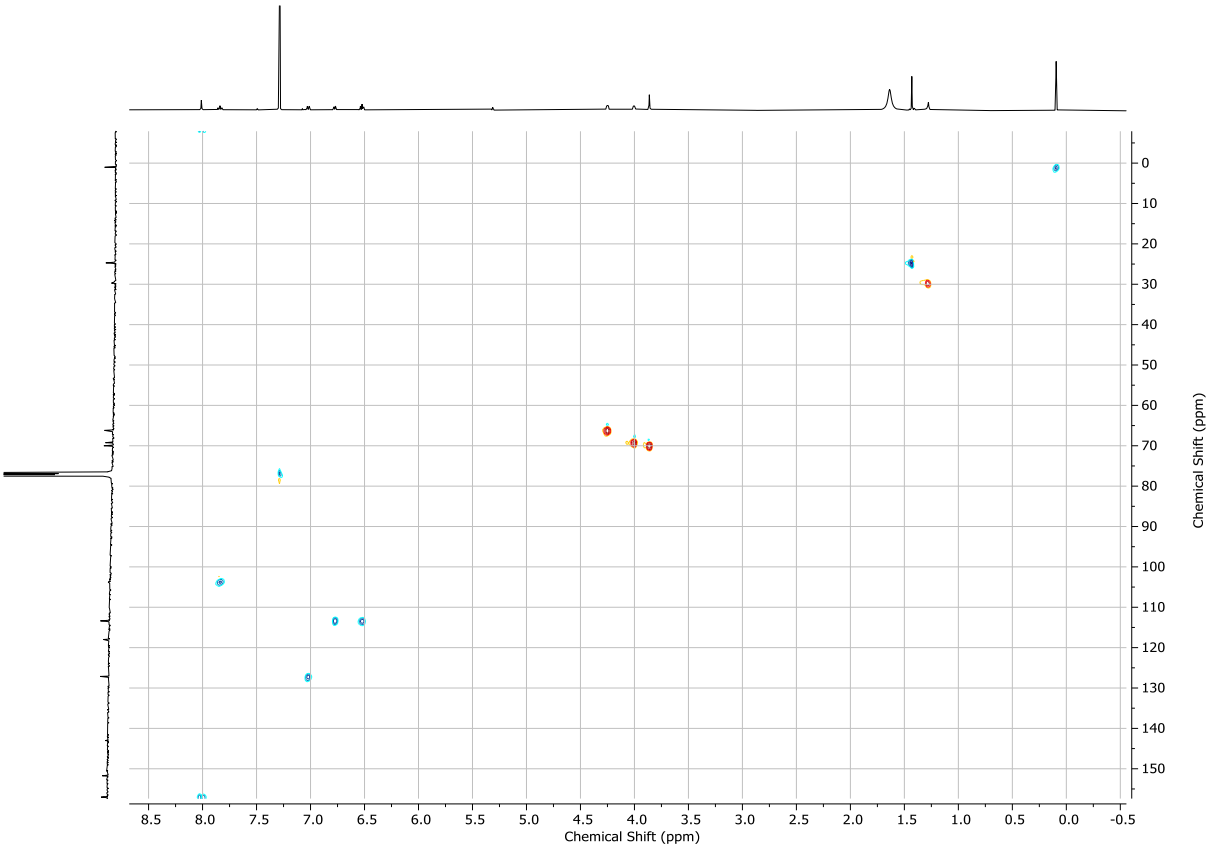


Figure S3.24 2D ^{1}H-^{13}C HSQC NMR of $\mathbf{3_F}$ ($CDCl_3$, 298K).

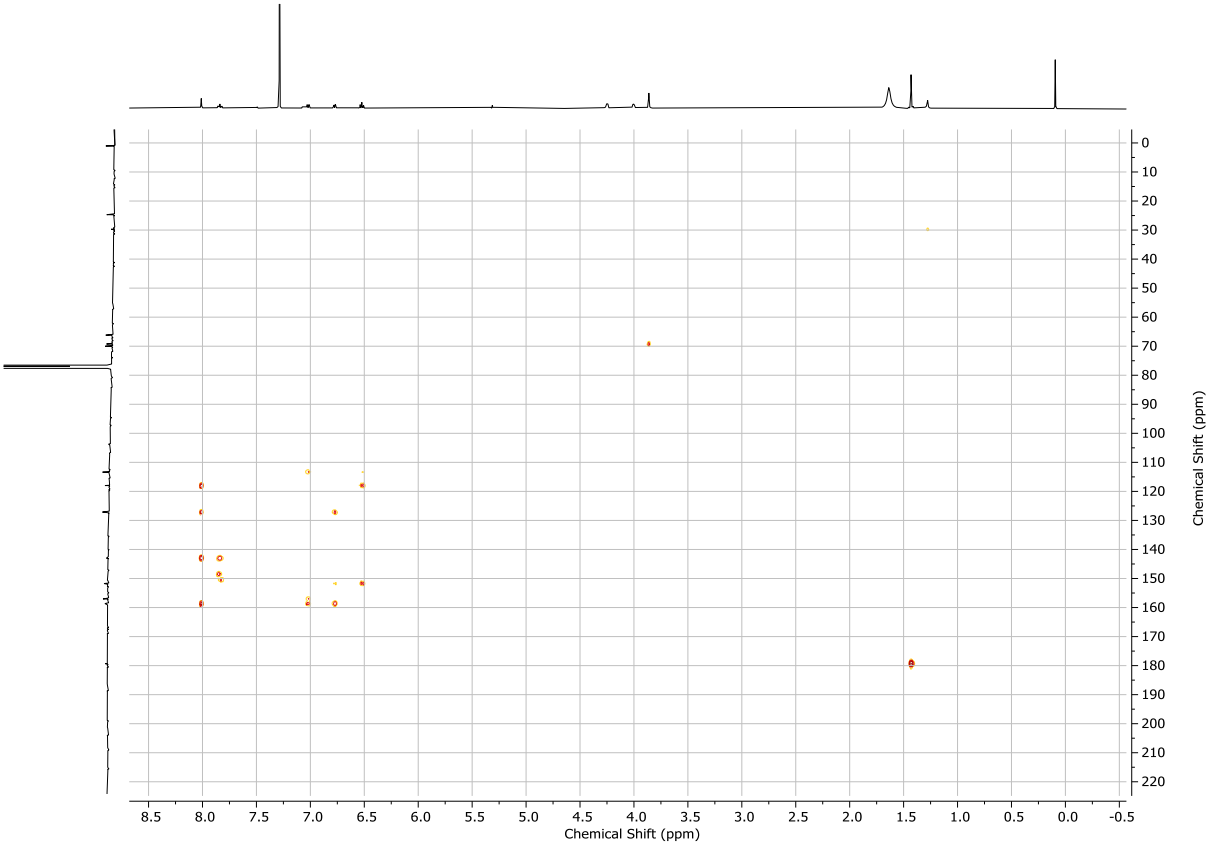


Figure S3.25 2D ^{1}H-^{13}C HMBC NMR of $\mathbf{3_F}$ ($CDCl_3$, 298K).

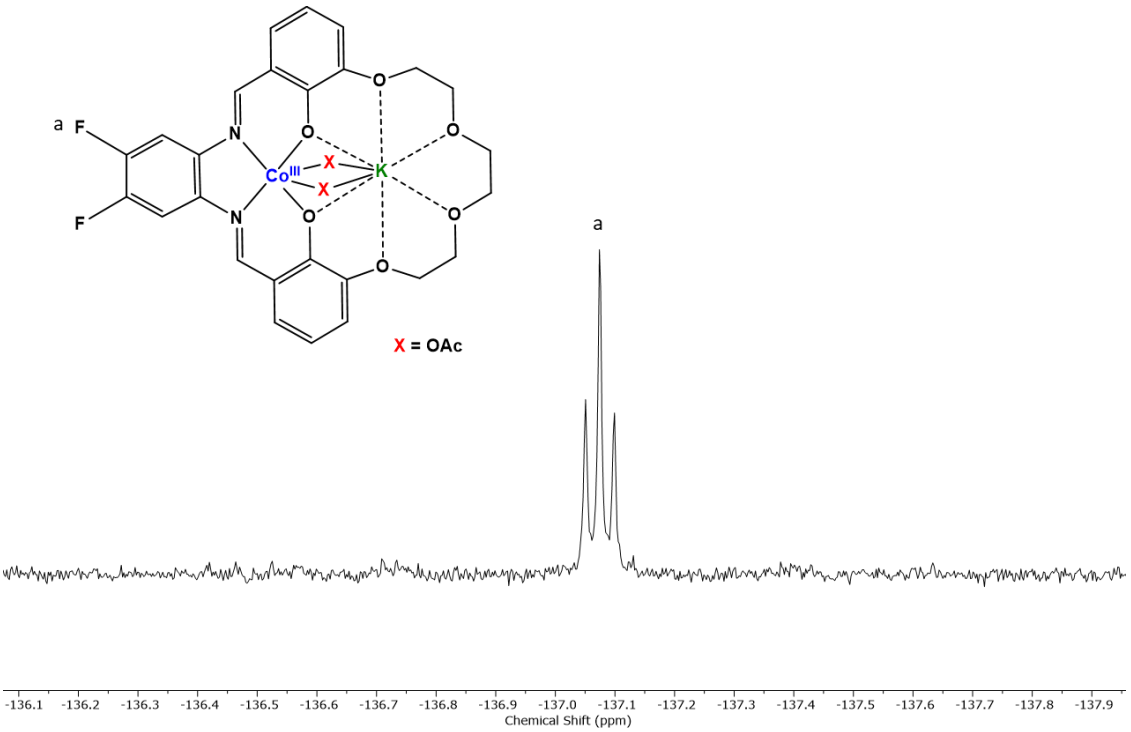


Figure S3.26 ^{19}F NMR of $\mathbf{3_F}$ ($CDCl_3$, 298K).

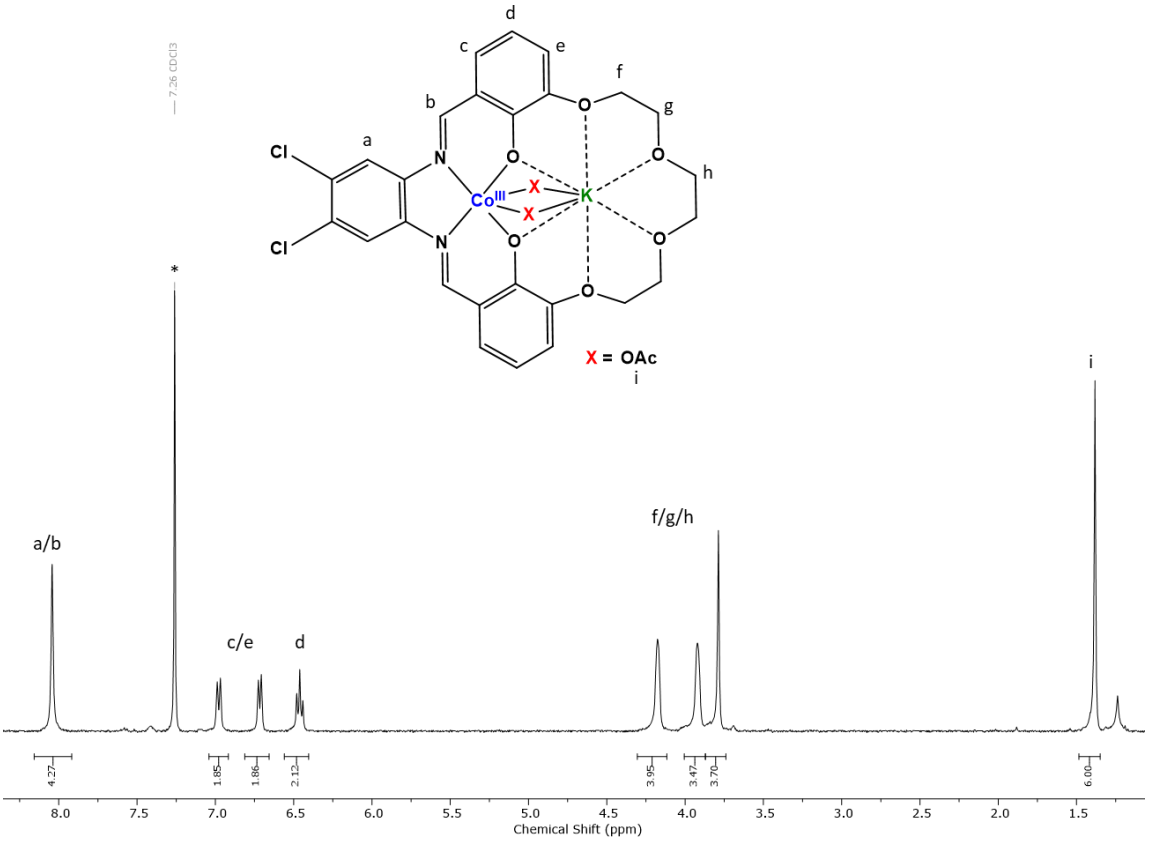


Figure S3.27 ^{1}H NMR of $\mathbf{3_{Cl}}$ ($CDCl_3$, 298K).

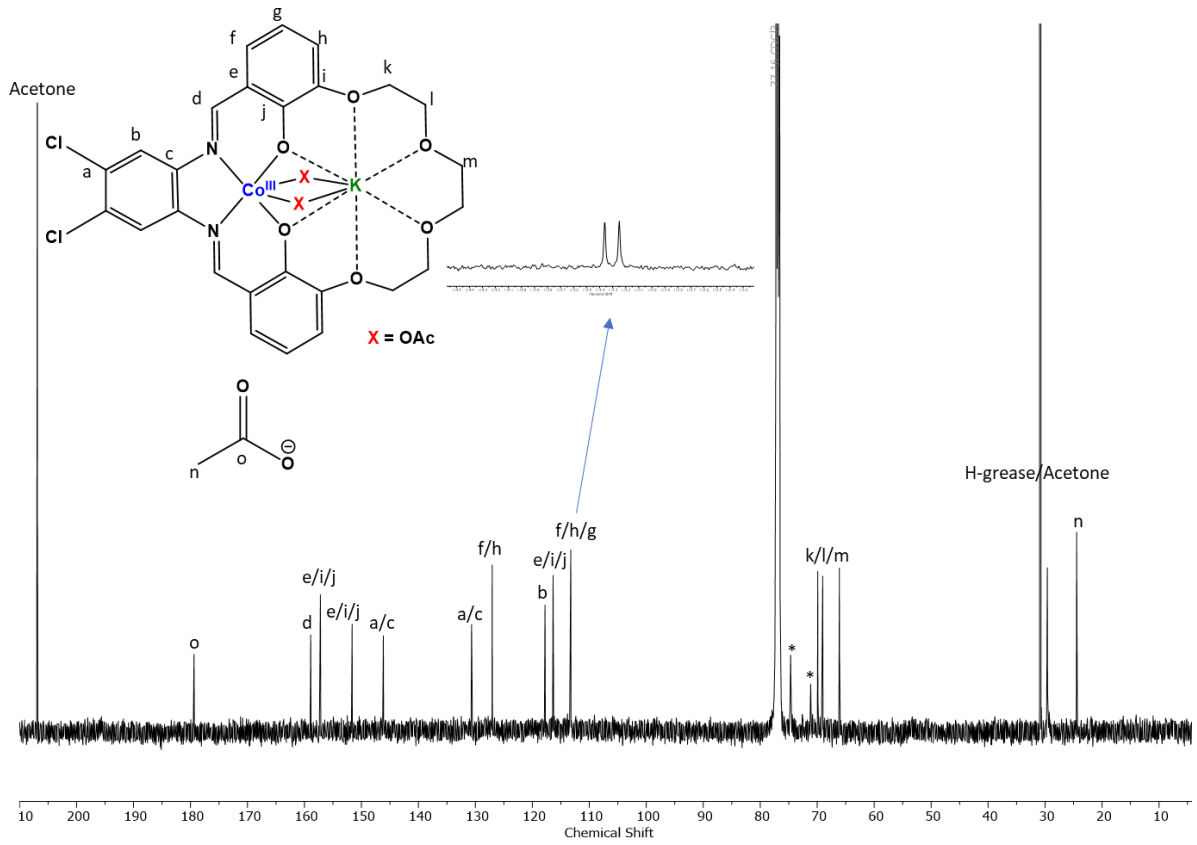


Figure S3.28 $^{13}C\{^{1}H\}$ NMR of $\mathbf{3_{Cl}}$ ($CDCl_3$, 298K).

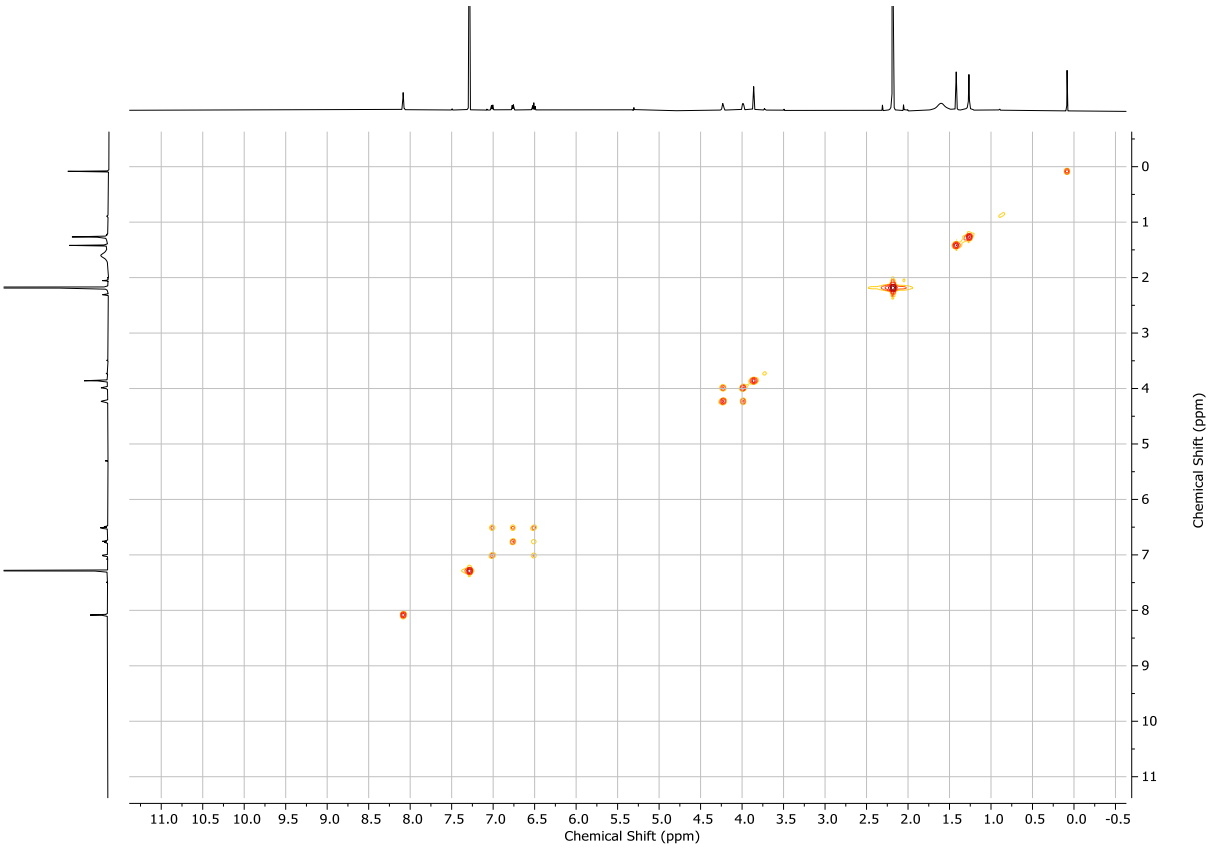


Figure S3.29 2D ^{1}H COSY NMR of $\mathbf{3_{Cl}}$ ($CDCl_3$, 298K).

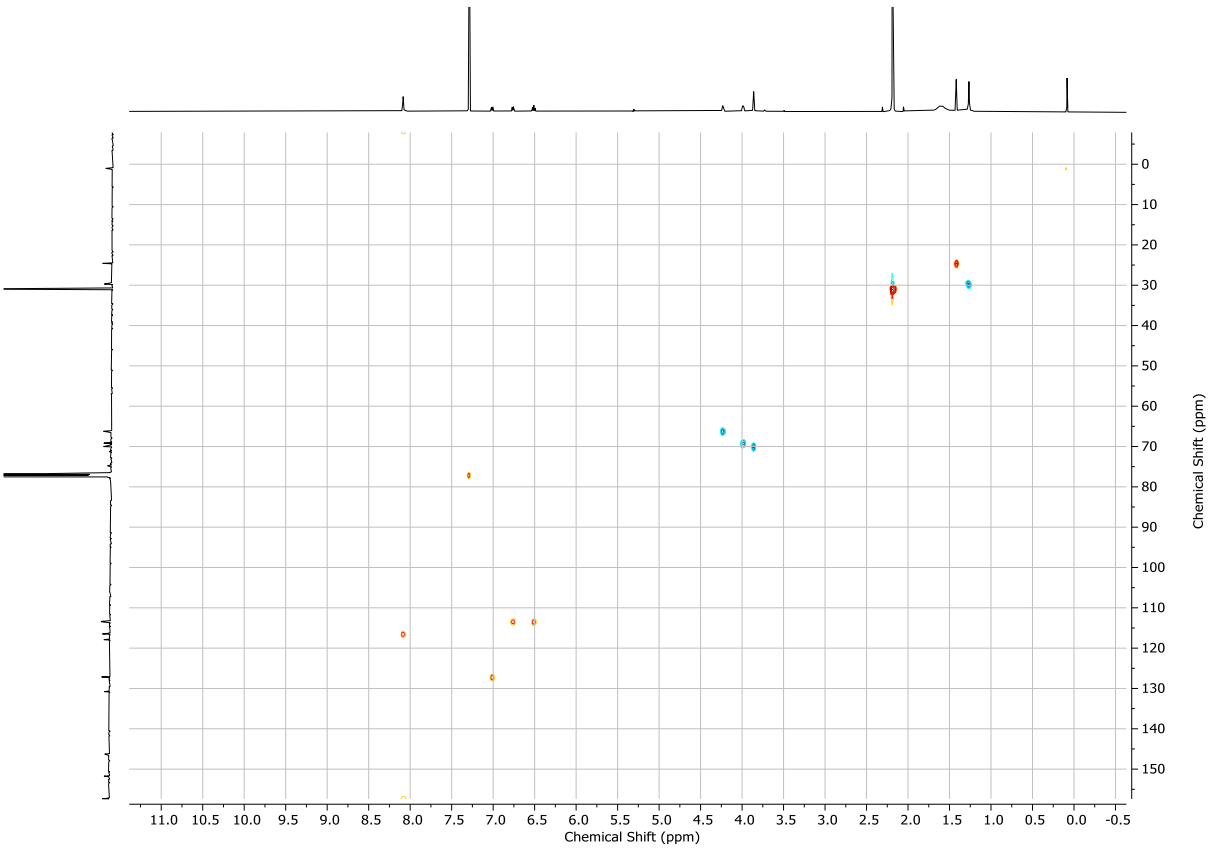


Figure S3.30 2D ^{1}H -^{13}C HSQC NMR of **2$_{Cl}$** ($CDCl_3$, 298K).

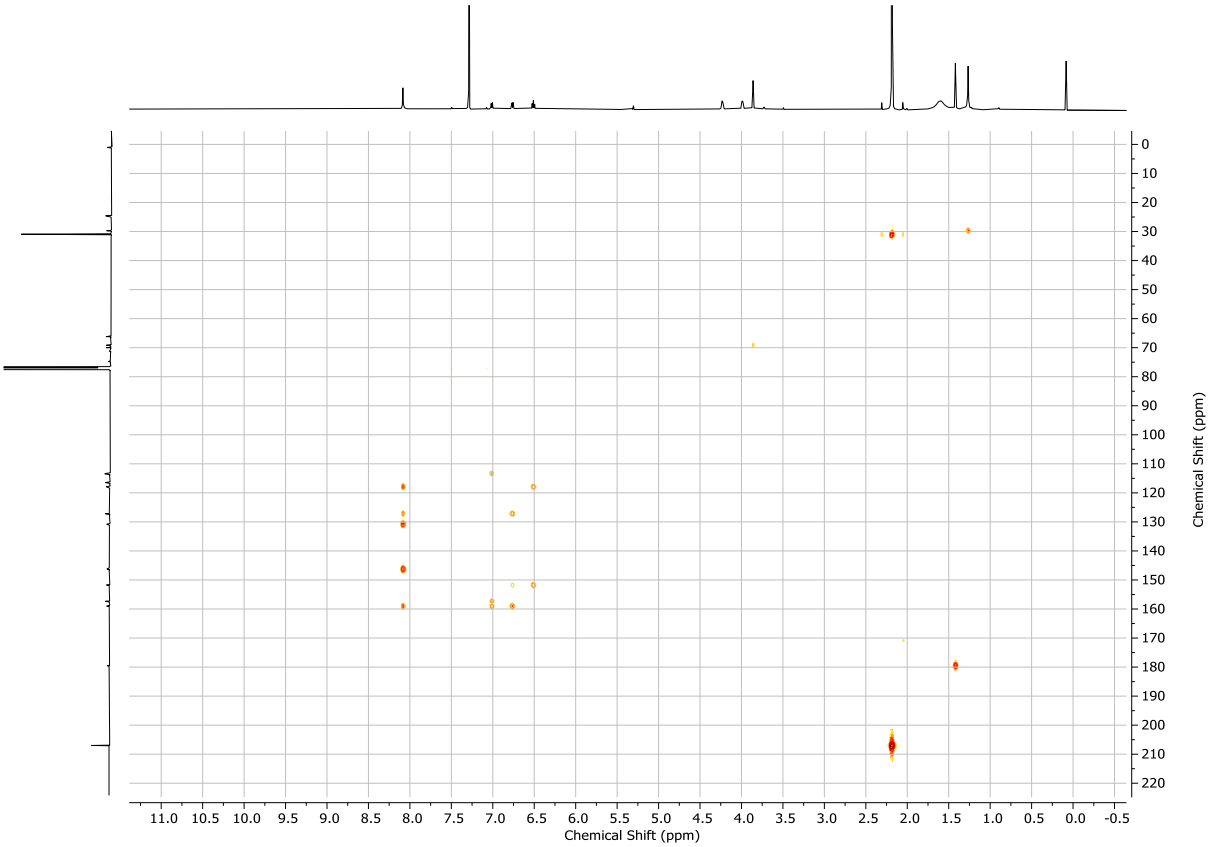


Figure S3.31 2D ^{1}H -^{13}C HMBC NMR of **3$_{Cl}$** ($CDCl_3$, 298K).

Table S3.1 Selected Atom Distances and Angles from Solid State Structure of $\mathbf{2_H}$.

Atoms	Distance (Å)	Atoms	Angles (°)
$K_1 - Co_1$	3.5904 (17)	$N_1 - Co_1 - O_4$	88.27 (12)
$Co_1 - N_1$	1.907 (3)	$N_1 - Co_1 - O_1$	93.70 (13)
$Co_1 - O_1$	1.892 (3)	$O_{1'} - Co_1 - O_1$	87.86 (17)
$Co_1 - O_4$	1.939 (3)	$O_4 - Co_1 - O_1$	94.28 (12)
$k_1 - O_1$	2.587 (3)	$N_1 - Co_1 - N_{1'}$	84.75 (19)
$K_1 - O_2$	2.713 (3)		
$K_1 - O_3$	2.819 (3)		
$K_1 - O_5$	2.875 (4)		
$C_1 - O_4$	1.264 (5)		

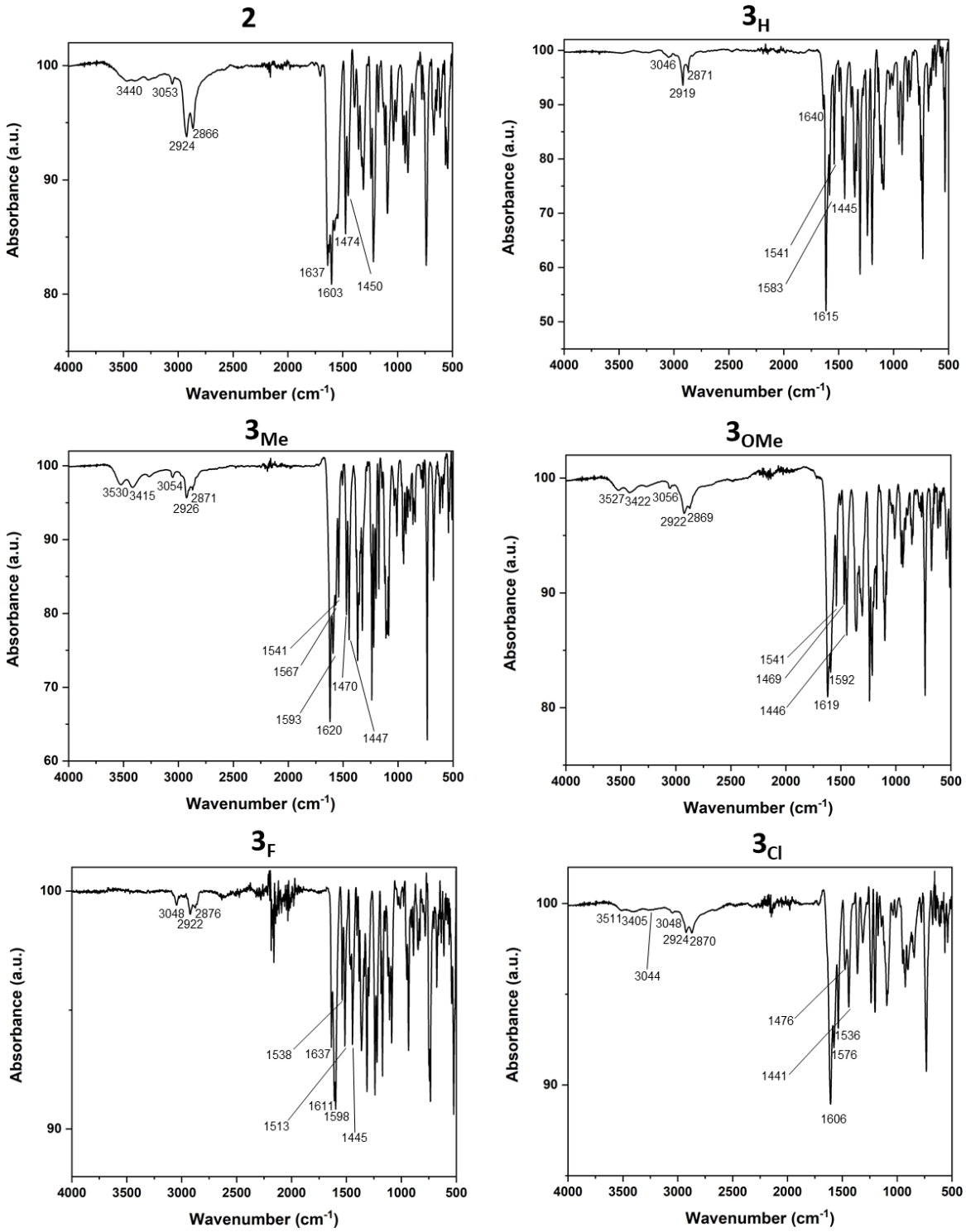


Figure S3.32 IR spectra of **2** and $\mathbf{3_R}$.

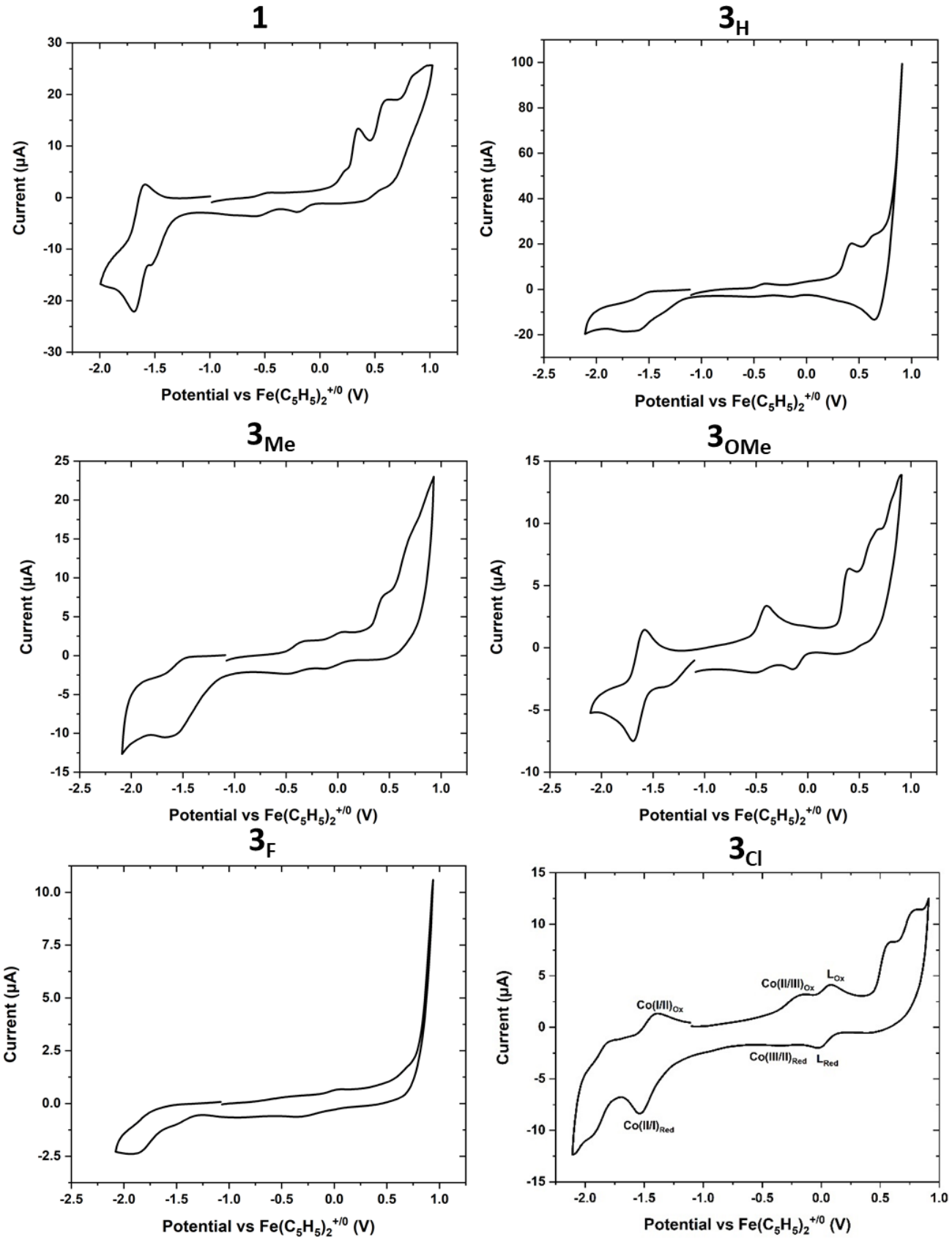


Figure S3.33 CV Curves of **1** and $\mathbf{3_R}$.

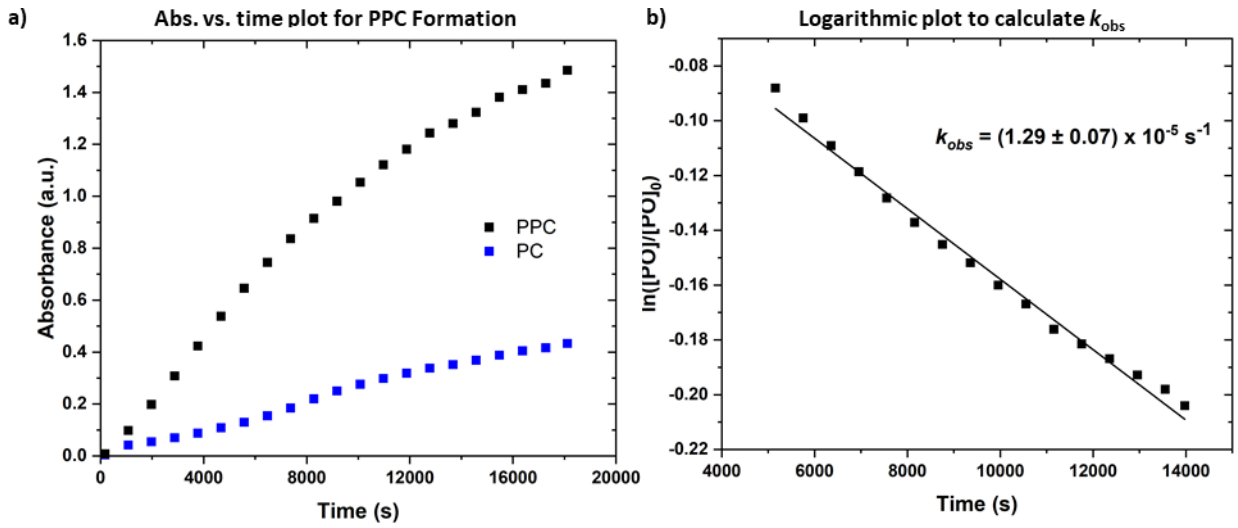


Figure S3.34 a) Absorbance versus time plot for PPC Formation for **2**. b) Logarithmic plot to calculate k_{obs} for **2**.

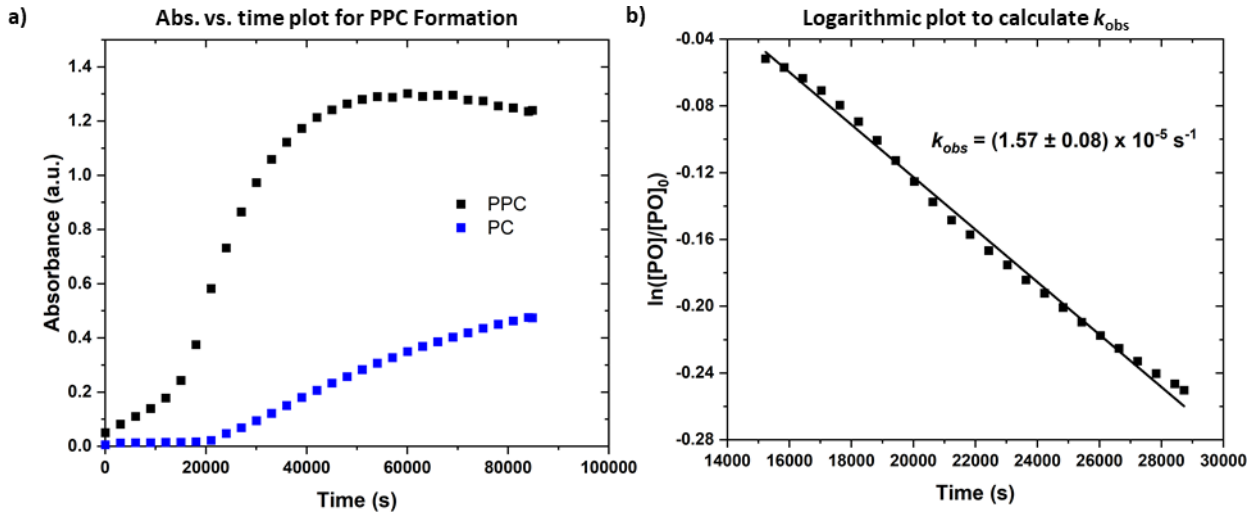


Figure S3.35 a) Absorbance versus time plot for PPC Formation for **3$_{Me}$**. b) Logarithmic plot to calculate k_{obs} for 3$_{Me}$.

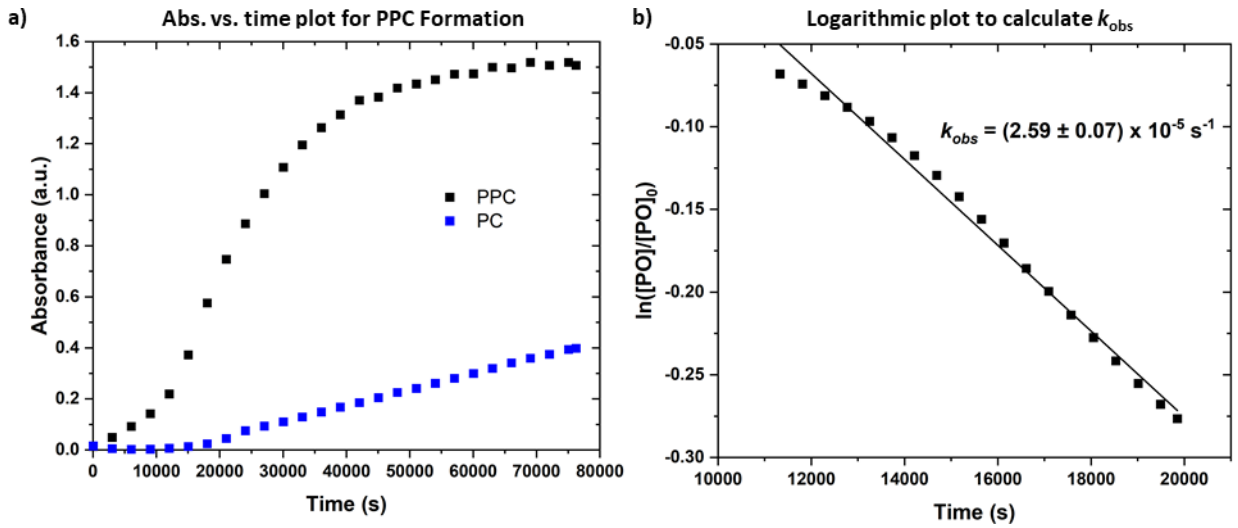


Figure S3.36 a) Absorbance versus time plot for PPC Formation for **3$_{OMe}$**. b) Logarithmic plot to calculate k_{obs} for 3$_{OMe}$.

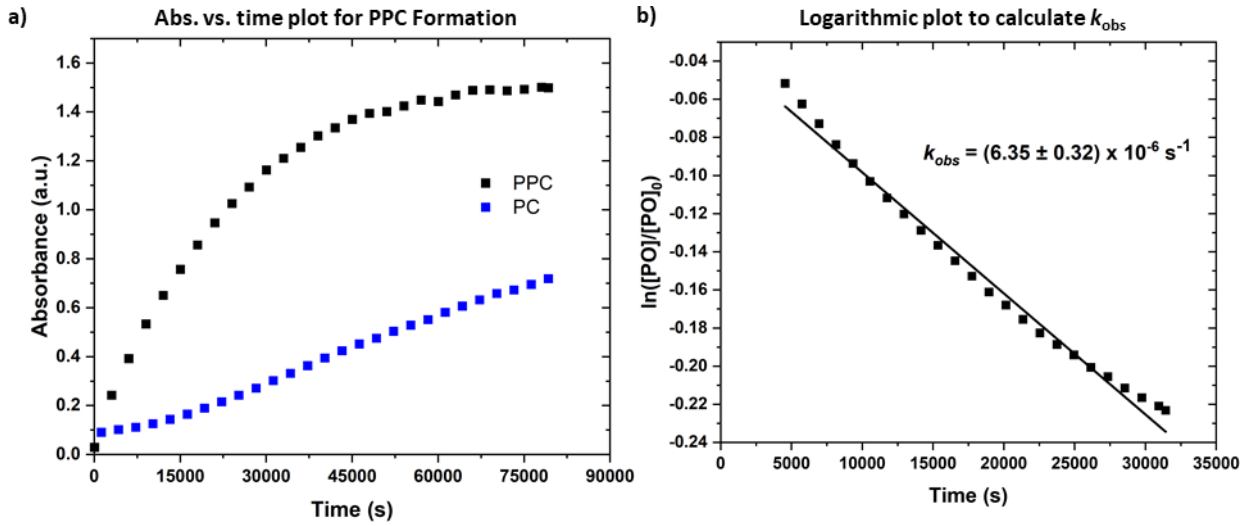


Figure S3.37 a) Absorbance versus time plot for PPC Formation for **3**$_F$. b) Logarithmic plot to calculate k_{obs} for **3**$_F$.

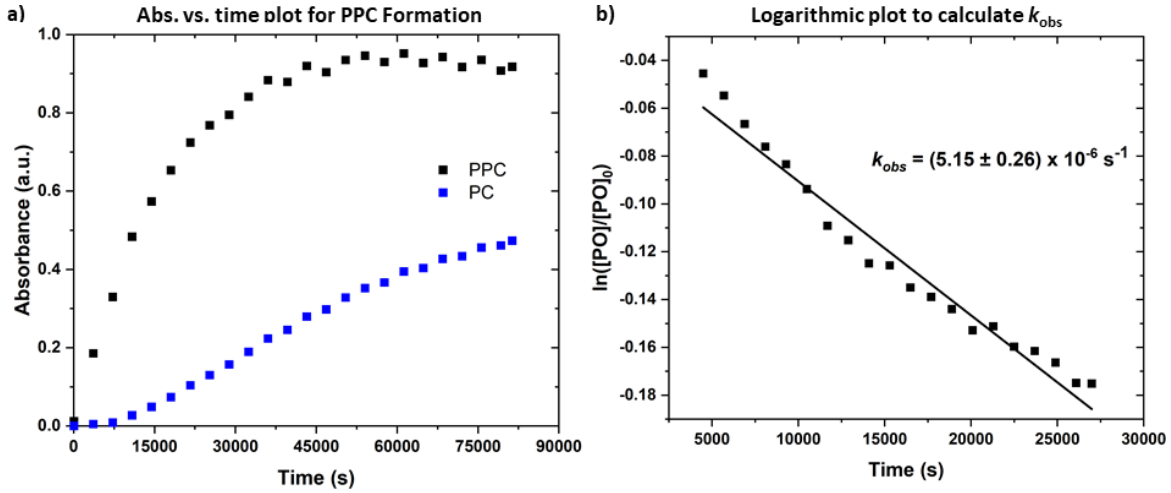


Figure S3.38 a) Absorbance versus time plot for PPC Formation for **3**$_{Cl}$. b) Logarithmic plot to calculate k_{obs} for **3**$_{Cl}$.

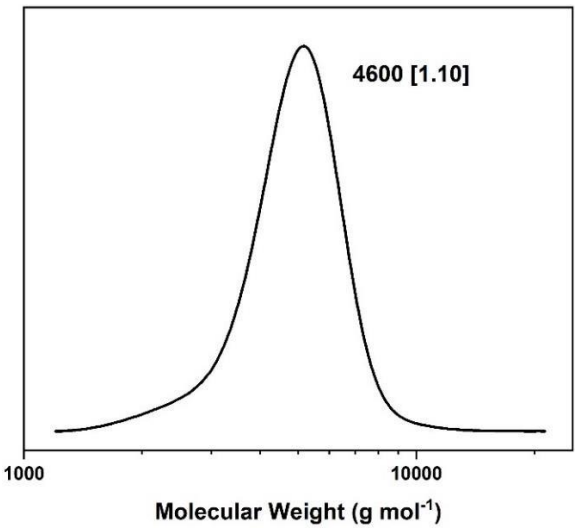


Figure S3.39 GPC trace of PO/CO_2 polymerisation run from Table 1 of **2**.

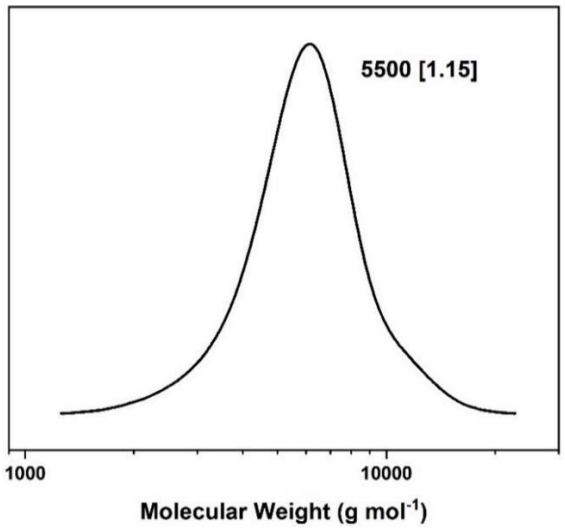


Figure S3.40 GPC trace of PO/CO_2 polymerisation run from Table 1 of $\mathbf{3_{Me}}$.

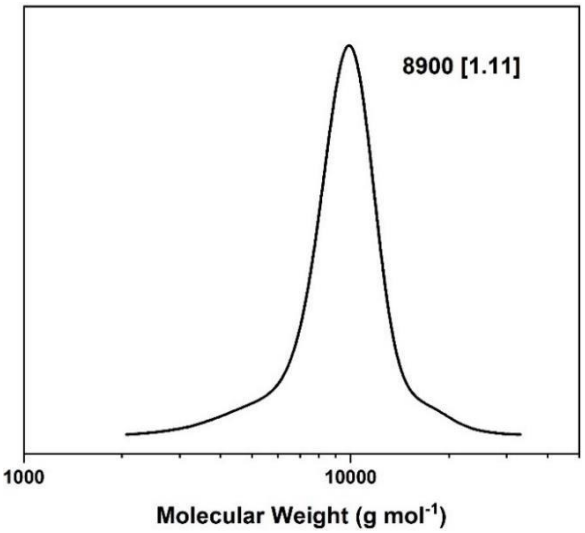


Figure S3.41 GPC trace of PO/CO_2 polymerisation run from Table 1 of $\mathbf{3_{OMe}}$.

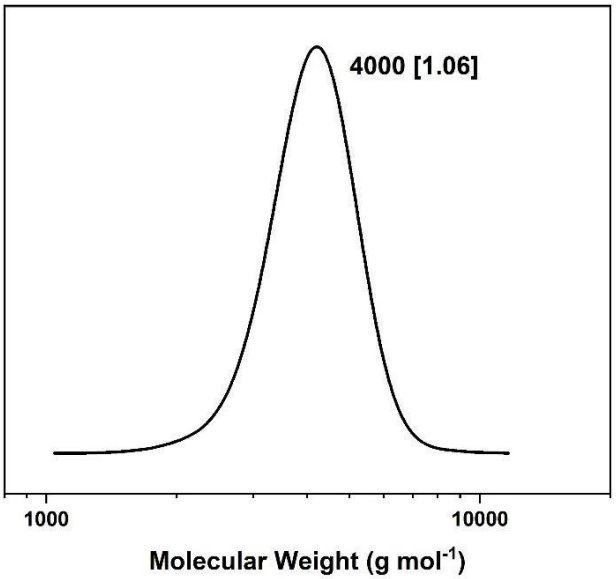


Figure S3.42 GPC trace of PO/CO_2 polymerisation run from Table 1 of $\mathbf{3_{H}}$.

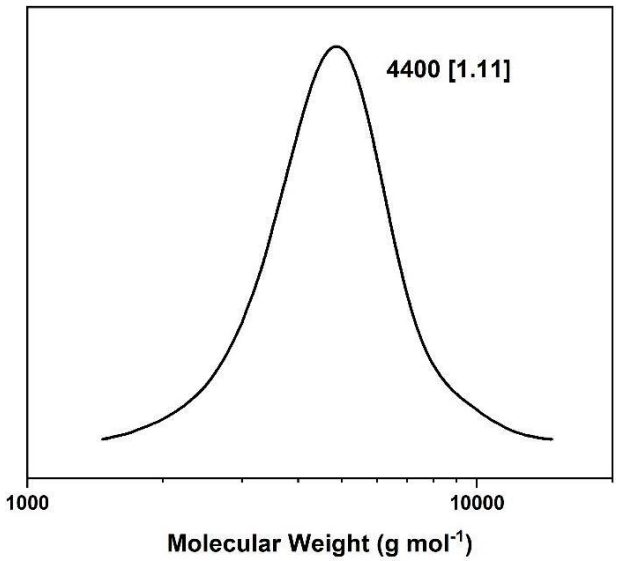


Figure S3.43 GPC trace of PO/CO_2 polymerisation run from Table 1 of $\mathbf{3_F}$.

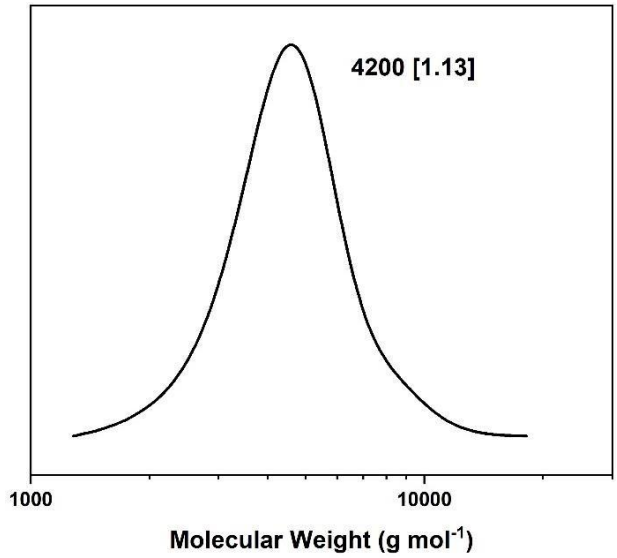


Figure S3.44 GPC trace of PO/CO_2 polymerisation run from Table 1 of $\mathbf{3_{Cl}}$.

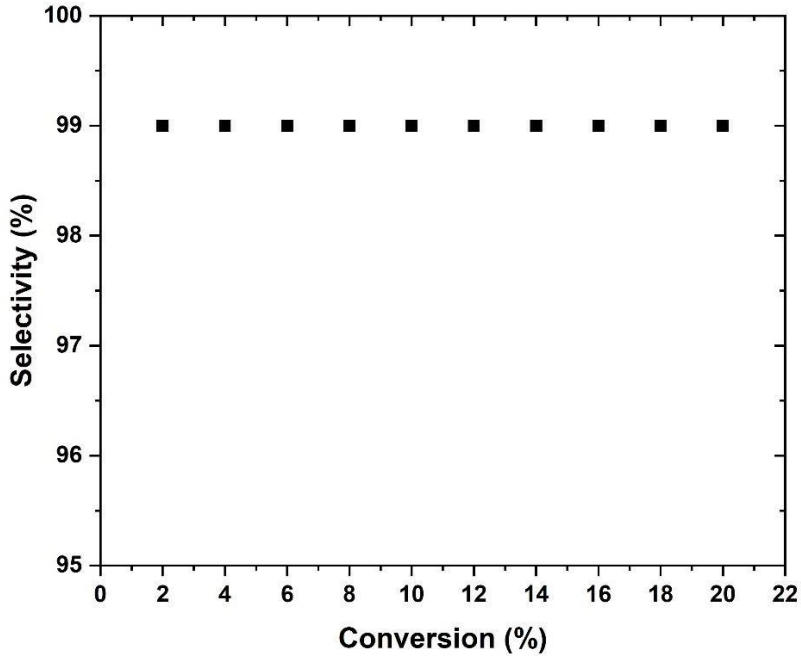


Figure S3.45 Conversion versus Selectivity plot of PO/CO_2 polymerisation of **3H** (0-20% conversion).

7.3 Supplementary Figures and Data for Chapter 4

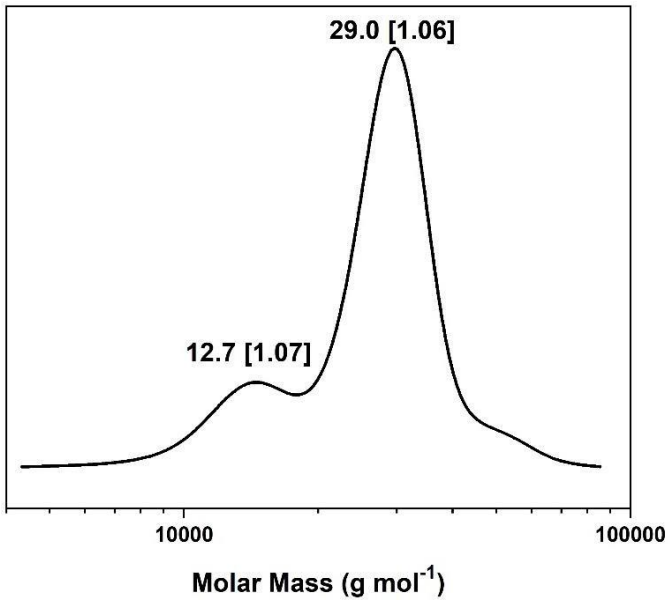


Figure 4.1 SEC trace of Entry 1 Table 4.1.

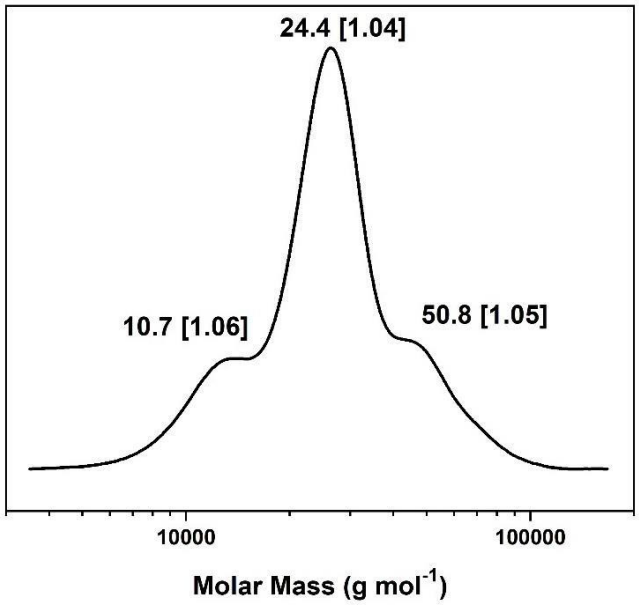


Figure 4.2 SEC trace of Entry 2 Table 4.1.

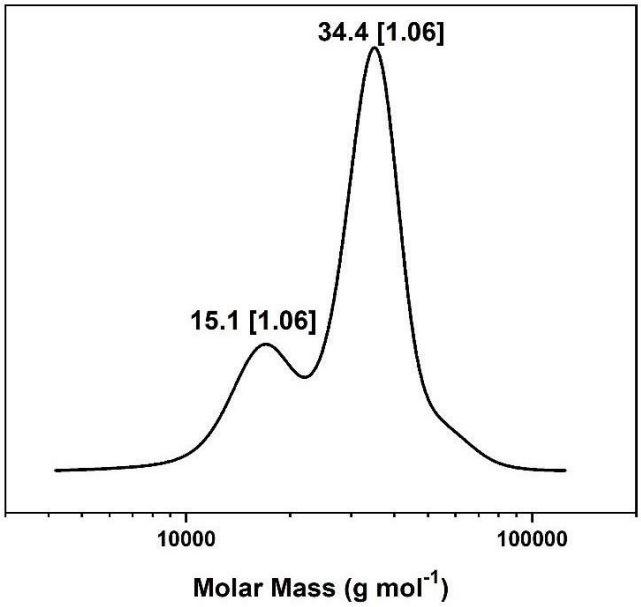


Figure 4.3 SEC trace of Entry 3 Table 4.1.

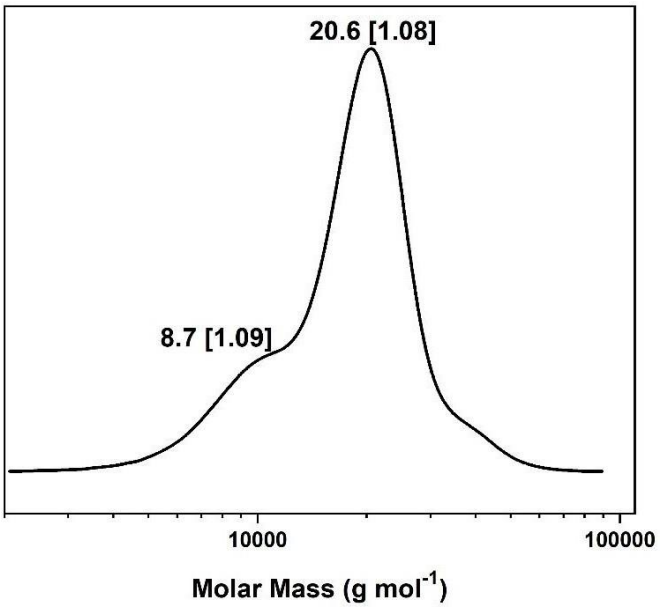


Figure 4.4 SEC trace of Entry 4 Table 4.1.

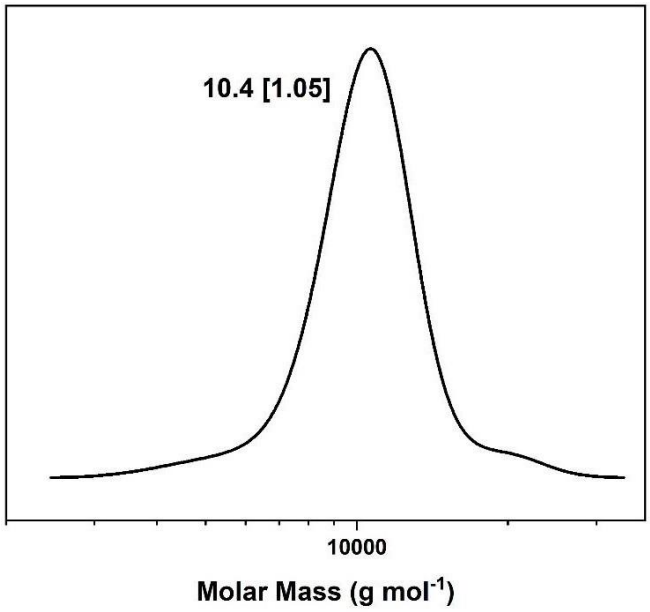


Figure 4.5 SEC trace of Entry 1 Table 4.2.

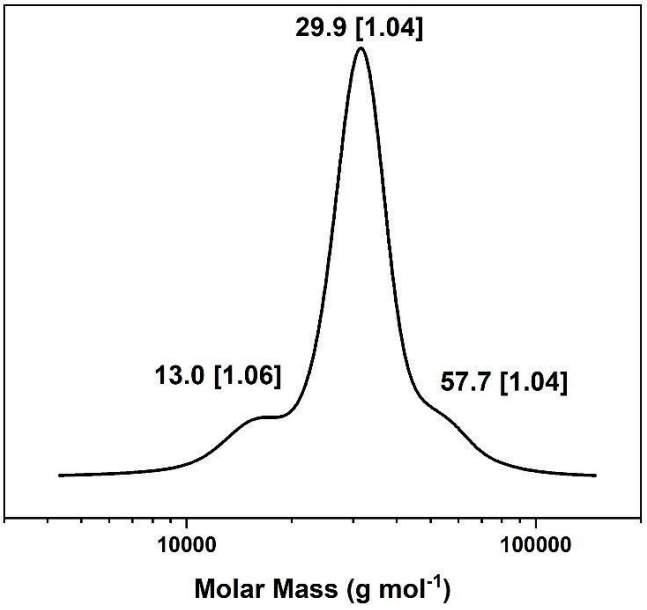


Figure 4.6 SEC trace of Entry 2 Table 4.2.

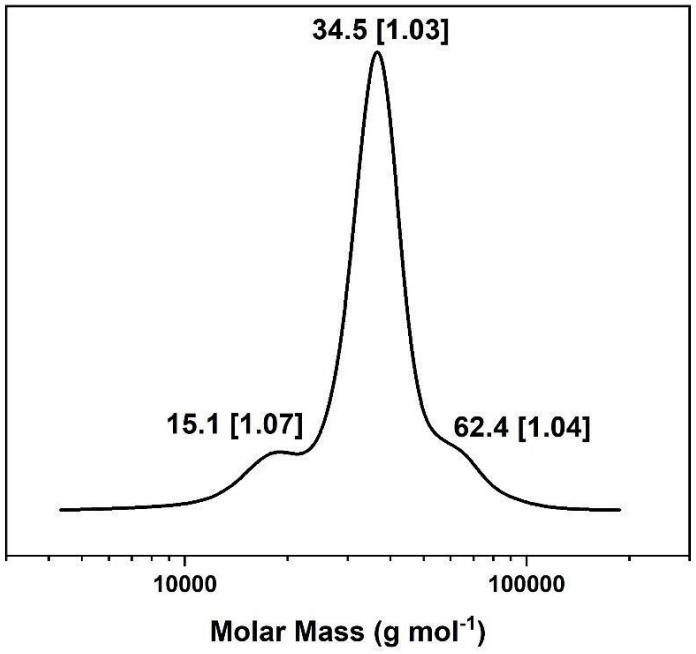


Figure 4.7 SEC trace of Entry 3 Table 4.2.

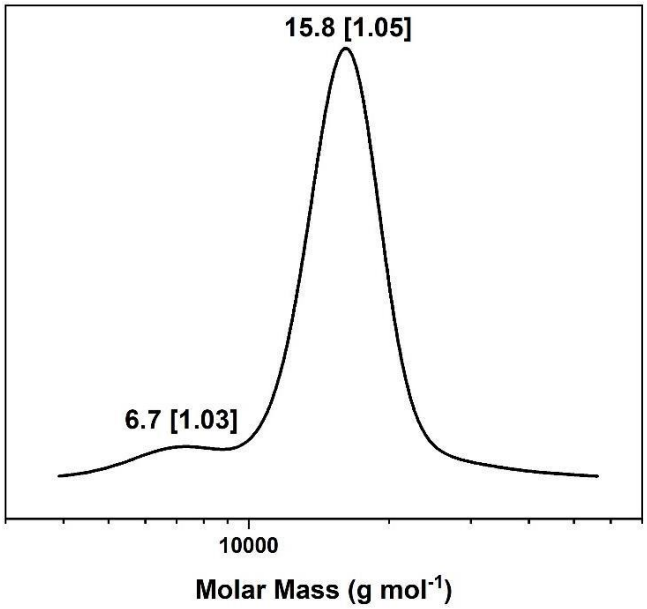


Figure 4.8 SEC trace of Entry 4 Table 4.2.

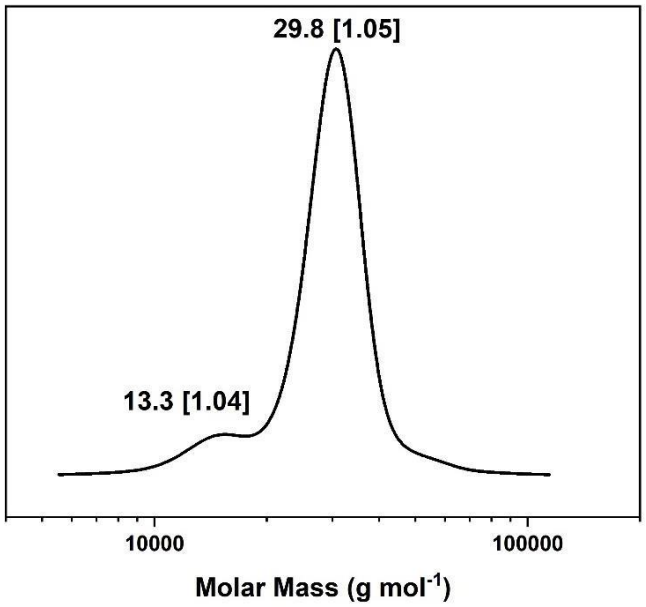


Figure 4.9 SEC trace of Entry 5 Table 4.2.

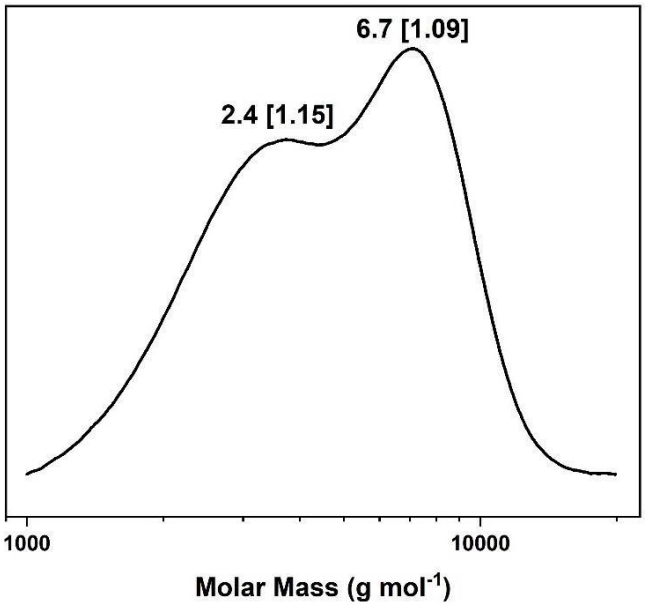


Figure 4.10 SEC trace of Entry 2 Table 4.3. Molar mass corrected using 0.58 correction factor.[1]

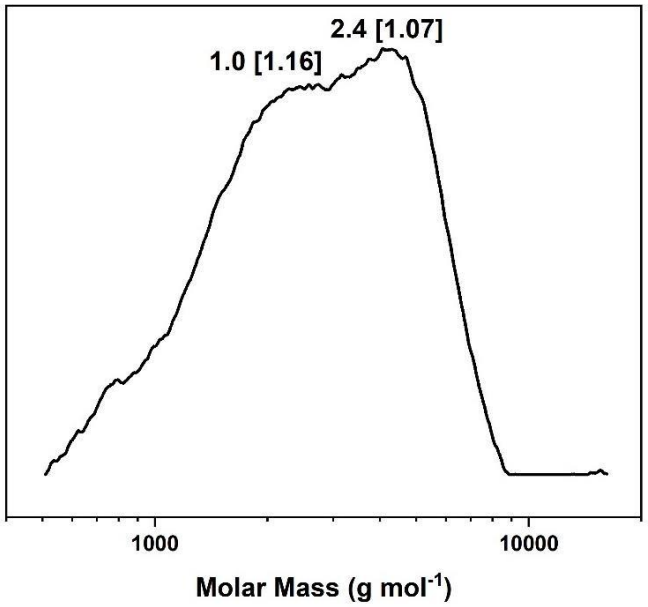


Figure 4.11 SEC trace of Entry 3 Table 4.3. Molar mass corrected using 0.58 correction factor.[1]

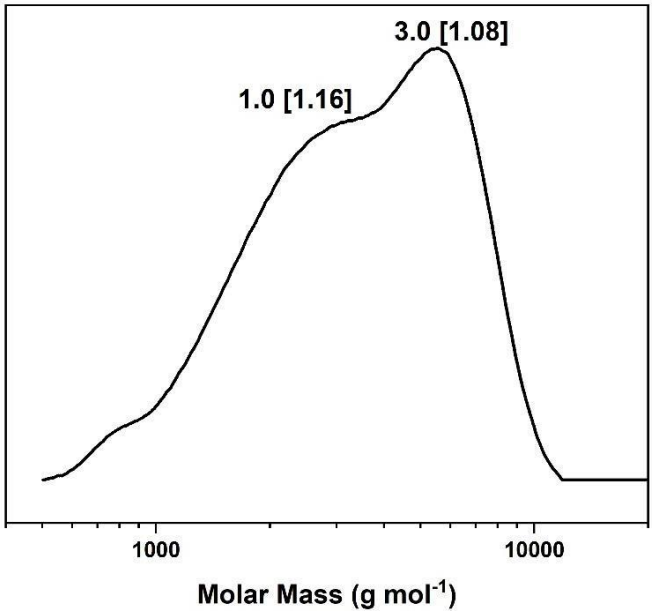


Figure 4.12 SEC trace of Entry 4 Table 4.3. Molar mass corrected using 0.58 correction factor.[1]

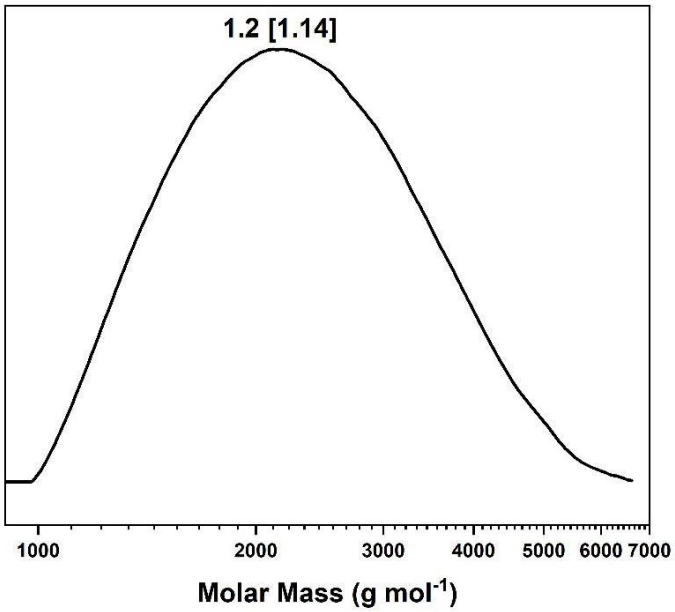


Figure 4.13 SEC trace of Entry 1 Table 4.4. Molar mass corrected using 0.58 correction factor.[1]

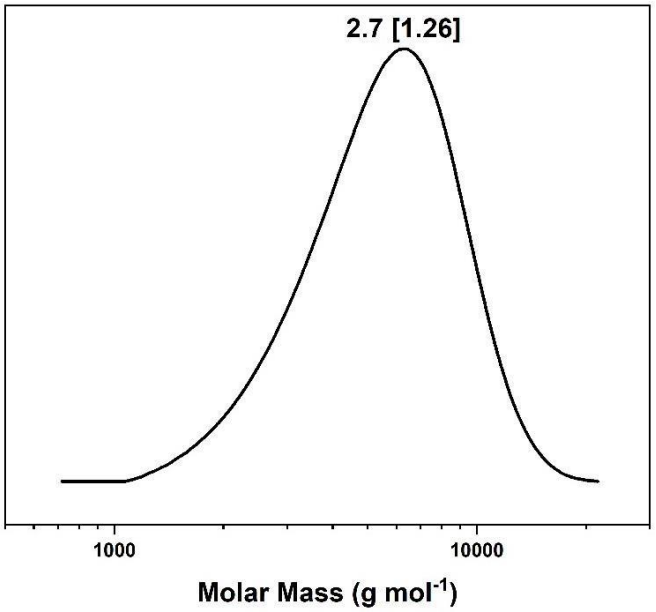


Figure 4.14 SEC trace of Entry 2 Table 4.4. Molar mass corrected using 0.58 correction factor.[1]

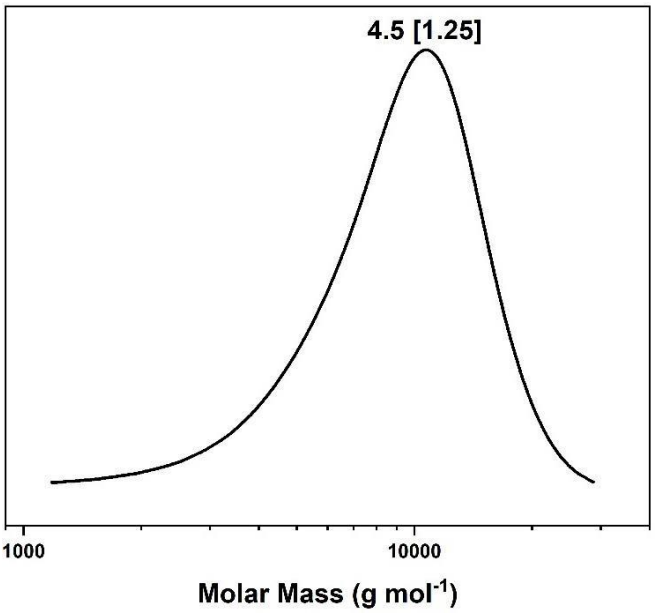


Figure 4.15 SEC trace of Entry 3 Table 4.4. Molar mass corrected using 0.58 correction factor.[1]

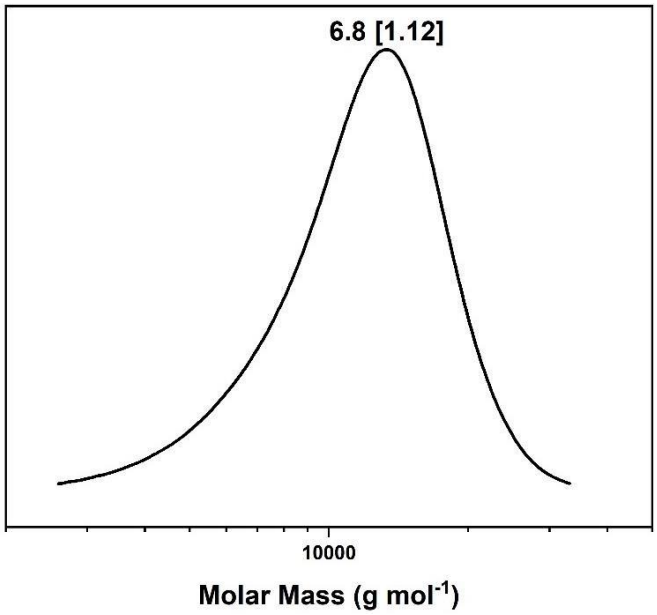


Figure 4.16 SEC trace of Entry 4 Table 4.4. Molar mass corrected using 0.58 correction factor.[1]

7.4 References

1. Baran, J.; Duda, A.; Kowalski, A.; Szymanski, R.; Penczek, S., *Macromol. Rapid Commun.*

This is an open access article published under a Creative Commons Attribution (CC-BY) License, which permits unrestricted use, distribution and reproduction in any medium, provided the author and source are cited.

ACS AUTHORCHOICE

JACS JOURNAL OF THE AMERICAN CHEMICAL SOCIETY

pubs.acs.org/JACS

Article

Co(III)/Alkali-Metal(I) Heterodinuclear Catalysts for the Ring-Opening Copolymerization of CO_2 and Propylene Oxide

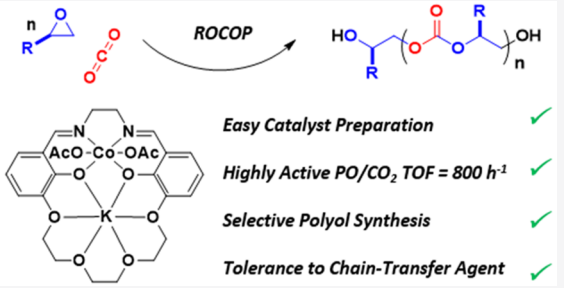
Arron C. Deacy, Emma Moreby, Andreas Phanopoulos, and Charlotte K. Williams*

Cite This: J. Am. Chem. Soc. 2020, 142, 19150−19160

Read Online

ACCESS | Metrics & More | Article Recommendations | Supporting Information

ABSTRACT: The ring-opening copolymerization of carbon dioxide and propene oxide is a useful means to valorize waste into commercially attractive poly(propylene carbonate) (PPC) polyols. The reaction is limited by low catalytic activities, poor tolerance to a large excess of chain transfer agent, and tendency to form byproducts. Here, a series of new catalysts are reported that comprise heterodinuclear Co(III)/M(I) macrocyclic complexes (where M(I) = Group 1 metal). These catalysts show highly efficient production of PPC polyols, outstanding yields (turnover numbers), quantitative carbon dioxide uptake (>99%), and high selectivity for polyol formation (>95%). The most active, a Co(III)/K(I) complex, shows a turnover frequency of 800 h^{-1} at low catalyst loading (0.025 mol %, 70 °C, 30 bar CO_2). The copolymerizations are well controlled and produce hydroxyl telechelic PPC with predictable molar masses and narrow dispersity ($Đ$ < 1.15). The polymerization kinetics show a second order rate law, first order in both propylene oxide and catalyst concentrations, and zeroth order in CO_2 pressure. An Eyring analysis, examining the effect of temperature on the propagation rate coefficient (k_p), reveals the transition state barrier for polycarbonate formation: $\Delta G^{‡}$ = +92.6 ± 2.5 kJ mol^{-1}. The Co(III)/K(I) catalyst is also highly active and selective in copolymerizations of other epoxides with carbon dioxide.



INTRODUCTION

Carbon dioxide utilization is a grand challenge for contemporary chemistry, and although several efficient reactions are known, few are viable or true utilizations when considered more broadly.[1,2] Many require esoteric, greenhouse gas emitting, and expensive stoichiometric reagents, while others yield products with no current large-scale application, or need unacceptably high catalyst loadings or operate under conditions, including carbon dioxide purity, incompatible with scale-up.[3] In contrast, epoxide and carbon dioxide ring-opening copolymerization (ROCOP) is well suited for large-scale deployment since it applies already commercial monomers, enables significant carbon dioxide sequestration, and produces valuable polymers whose properties allow for the replacement of existing petrochemicals.[3−5] This process can sequester up to 50 wt % carbon dioxide into the polymer and it is truly catalytic allowing for multiple turnovers and high converson of epoxide.[3−5] At the cutting-edge are carbon dioxide and propylene oxide derived polyols which are low molar mass, hydroxyl end-capped polypropylene carbonate (PPC) or polyethercarbonates. These polyols are applied to make polyurethanes to construct mattresses and furniture foams, insulation sheet foam, coatings, sealants, and elastomers.[4,6−8] Life-cycle assessment shows that polyols with just 20 wt % CO_2 content (i.e., imperfectly alternating polymers) display a ∼20% reduction in green-house gas emissions and fossil fuel consumption compared to currently used petrochemicals.[9] High molar mass polycarbonates are also explored as toughened plastics, elastomers, and adhesives.[10] In terms of polyols, the use of propylene oxide as the epoxide is particularly important because it is an inexpensive commodity chemical already used at large-scale in polyol manufacture,[11] and it delivers attractive material properties.[4,6−8] While tremendous advances have been made in high molar mass PPC catalysis,[12−24] the production of the desired low molar mass polyols from propylene oxide and carbon dioxide is challenging.[4,25,26] One difficulty is that any catalyst must tolerate a large excess of the protic starter or chain transfer agent (CTA), typically a diol or diacid, essential to control the chain end-group chemistry and ensure that polyols achieve the correct molar mass, even at high epoxide conversions (Figure 1).[4]

Among the most active high molar mass PPC catalysts are cobalt(III) salen complexes, [(salen)Co(III)X] where X = carboxylate or halide, and these compounds are best applied with an equimolar quantity of an ionic cocatalyst, typically

Received: August 3, 2020
Published: October 27, 2020



Downloaded via UNIV OF OXFORD on December 9, 2020 at 11:39:53 (UTC).
See https://pubs.acs.org/sharingguidelines for options on how to legitimately share published articles.

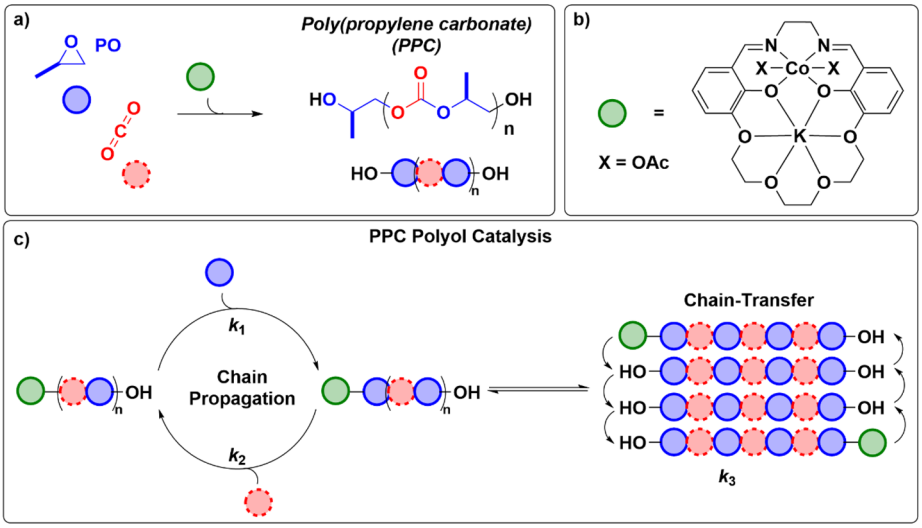


Figure 1. (a) PO/CO_2 ROCOP to make poly(propylene carbonate) (PPC) polyols. (b) Illustration of one of the heterodinuclear catalysts used in this investigation (2). (c) Catalytic cycle for PO/CO_2 ROCOP illustrating both propagation and chain transfer reactions (epoxide ring-opening k_1, CO_2-insertion k_2 and chain-transfer k_3).

bis(triphenyl phosphine)iminium chloride (PPNCl).[12−21] Although this type of catalyst can be used to prepare polyols, they usually show significantly compromised activity. For example, [(salen)CoX]/PPNX shows an activity, TOF, of just 10 h^{-1} when applied with the added water (as CTA) necessary to selectively produce polyols.[26] Another problem is the use of PPNX salts which are toxic, expensive, poorly soluble in many epoxides, and may be corrosive to steel. As the active catalyst comprises an ion pair, rapid deactivation occurs at the necessary low catalyst loading, which is another detraction.[14,15] To address these limitations, Nozaki and co-workers, and subsequently many others, reported modified [(salen[NR_3^+])-Co(III)X]X′ complexes, i.e., single component catalysts, where the salen ligand is modified to include a covalently bonded organic salt cocatalyst, most commonly an ammonium salt.[12,14,15,18] These catalysts show better turnover frequencies for low molar mass PPC, for example, achieving a TOF of 48 h^{-1} with excess methanol.[18] Detailed optimization resulted in a catalyst featuring four ammonium "arms", [(salen[NBu_3^+]$_4$)-Co(III)(OAc)](NO_2^-)$_4$, that achieved an impressive TOF of 10 300 h^{-1} (0.001 mol % catalyst, 80 °C, 20 bar CO_2) and importantly is stable to copious quantities of CTA (400 equiv).[27] Unfortunately, this catalyst is somewhat complex to prepare, requiring >8 synthetic steps, and has an ill-defined composition and unclear mechanism.[28,29] Very recently, the tethered cocatalyst strategy also significantly improved an Al(III)-porphyrin catalyst, but for CO_2/CHO ROCOP.[30]

Lewis acid−base pair catalysts, of the form Et_3B/*tetra*-butylammonium carbonate (TBAC), also successfully yielded PPC polyols, although with low TOF = 3 h^{-1} and requiring high catalyst loading (7.5 mol % BEt_3, 2.5 mol % TBAC, 40 °C, 10 bar).[31] Recently, recycling of this catalyst system has been reported with >95% catalyst recovery.[32] The stratagem of tethering the Lewis acid−base pair has significantly enhanced rates for CO_2/CHO ROCOP, but there are not yet reports of these catalysts for PPC polyol synthesis.[33]

Homogeneous dinuclear metal ROCOP catalysts operate without cocatalyst, show high activity and selectivity at low carbon dioxide pressures for CHO/CO_2 ROCOP, and retain performances when using chain transfer agents to selectively deliver PCHC polyols.[34−46] The most active are heterodinuclear catalysts which show synergy in CHO/CO_2 ROCOP.[43−49] Nonetheless, so far these dinuclear catalysts underperform in propylene oxide (PO)/carbon dioxide ROCOP: they either scarcely turnover to PPC or produce cyclic carbonate.[34,38,43] Motivated by the heterodinuclear synergy concept, this study targets heterodinuclear PO/CO_2 ROCOP catalysts. The catalyst selection is underpinned by the following guidelines: (1) The optimum internuclear separation should be ∼3−4 Å to provide for intermetallic "cooperation" in the ring-opening transition state and intermediate.[35,40,45,50] (2) The chain-shuttling mechanism, operative for other dinuclear catalysts, is accelerated by trans- disposed coligands and chain growth alternating between the two metals.[34−36,38,43−45] (3) For CHO/CO_2 ROCOP, the most effective metal combinations feature M(II)M′(II), where M = Co(II) and M′ = Mg(II).[43] Here, PO/CO_2 ROCOP, catalysts of the form M(III)/M′(I), where M = Co(III) and M′ = Na, K, Cs, Rb(I), are proposed to exploit the high nucleophilicity of Co(III)-propylene carbonate intermediates and the oxophilicity of Group 1 metals toward epoxide coordination. Additionally, Group 1 metals are attractive due to their abundance, low cost, lack of color, and low toxicity. Heterodinuclear complex formation is essential since prior work has established that ROCOP using mixtures of [(salen)Co(III)X] complexes and Group 1 crown ether additives yielded cyclic carbonates.[13] To make the heterodinuclear M(III)/M(I) complex, a macrocyclic ligand featuring differentiated binding cavities was selected, with a tetradentate Schiff base to coordinate the Co(III) and a "crown-ether" moiety for M(I) (Figure 2). The ligand features two bridging phenolate sites which could enhance electronic communication between Co(III) and M(I), which may increase electronic synergy in catalysis (Figure 1a).[34,36,43] Related transition metal/M(I) heterodinuclear complexes are successful magnetic resonances probes (Co(II)/Na(I)), CH oxidation catalysts (Fe(III)/K(I)), and epoxidation catalysts (Mn(III)/Na(I)).[51−56]

https://dx.doi.org/10.1021/jacs.0c07980
J. Am. Chem. Soc. 2020, 142, 19150−19160

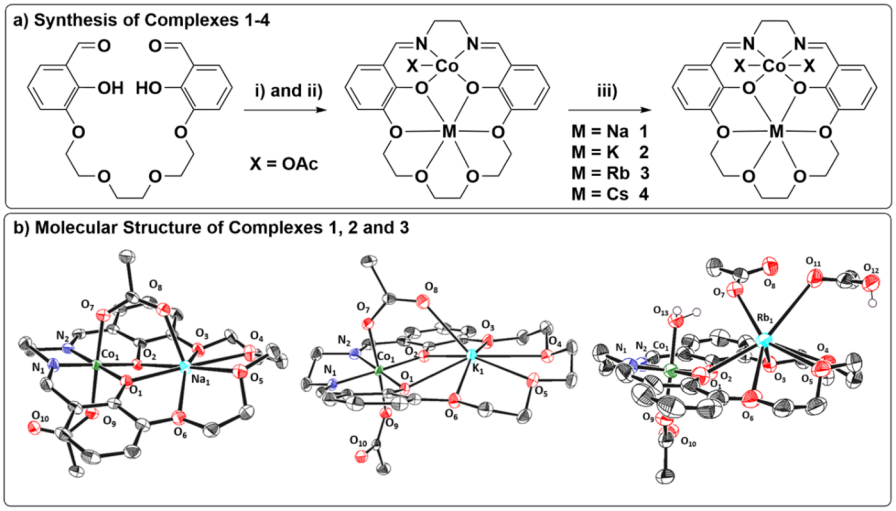


Figure 2. (a) Synthesis of the heterodinuclear complexes **1**−**4**. Reagents and conditions: (i) M(OAc) [M = Na, K, Rb, or Cs], $Co(OAc)_2$, MeCN, 25 °C, 30 min, N_2. (ii) Ethylenediamine, MeCN, 25 °C, 16 h, N_2. (iii) AcOH (2 equiv), MeCN, air, 72 h, >50% yield. (b) ORTEP representation of the molecular structures of complexes **1**−**3**, with hydrogen atoms and residual solvents omitted for clarity, and thermal ellipsoids are represented at 50% probability (see SI for experimental details).

RESULTS AND DISCUSSION

Complexes **1**−**4** were synthesized from the macrocycle ligand (SI for ligand synthesis) by the addition of an equivalent of the appropriate alkali-metal(I) acetate, followed shortly after by the addition of an equivalent of cobalt(II) acetate. The reaction mixture was stirred for 30 min, at 25 °C, and then ethylenediamine was added and the solution stirred for a further 16 h. The resulting solution was exposed to air and two equivalents of acetic acid added to oxidize the Co(II) center. The resulting Co(III)/M(I) complexes were isolated in >50% overall yield as pale brown solids. The complexes were characterized by NMR spectroscopy (Figure S2−S10), mass spectrometry (Figure S11−S13), IR spectroscopy (Figure S14), elemental analysis, and where possible, by single crystal X-ray diffraction (SI for details). For example, the NMR spectrum of **1** shows the disappearance of the phenolic protons, at ∼10.86 ppm in the free ligand, and the appearance after complexation of both ethylene (^{1}H: 4.31; ^{13}C: 59.4 ppm) and acetate (^{1}H: 1.45; ^{13}C: 179.5, 24.8 ppm) resonances, respectively. The transformation of the aldehyde to imine functional groups results in shifting of a singlet resonance from 9.94 to 7.70 ppm in the ^{1}H NMR spectrum. During the synthesis, both metals are added in short succession and yet there is selective formation of the heterodinuclear complex. This arises because the ligand binding "pockets" discriminate between the metals' coordination chemistry and ionic radii (Co(II) = 0.75 Å, Na(I) = 1.1 Å, K(I) = 1.5 Å, Rb(I) = 1.6 Å and Cs(I) = 1.7 Å vs binding sites N_2O_2 = 1.9 Å, 18C6 = 2.7 Å).[57]

The 2D DOSY NMR spectra show a single diffusion coefficient for complexes **1**−**4**, indicative of a single structure in solution (Figure S10). The solution hydrodynamic radii are 5.14, 5.17, 5.65, and 6.66 Å for **1**−**4**, respectively. For complexes **1** and **2**, values correlate well with those calculated from the solid state structures (vide infra) and indicate monomeric species. Complex **3** shows a smaller value (5.65 Å) than that calculated for the dimeric solid (6.45 Å) and correlates better to a "half-dimeric" structure (5.23 Å) suggesting it is monomeric in solution. Although the solid state structure of complex **4** was not obtained, its solution hydrodynamic radius (6.66 Å) falls in the expected range for a dimer. The change in complex nuclearity on descending Group 1 can be rationalized by increasing larger radii, e.g., of Rb(I) and Cs(I), enabling access to higher coordination numbers and facilitating complex aggregation.[58]

The MALDI-ToF mass spectra display molecular ions, at 495, 511, and 604 amu, for complexes **1**, **2**, and **4**, respectively, and values correspond to the molecular cation, $[LCo(II)M]^+$ (Figure S11−S13). The isotope distribution patterns match those expected. Crystals suitable for single crystal X-ray diffraction were obtained via vapor diffusion of pentane (**1**) or diethyl ether (**2**) into a saturated solution of each complex in dichloromethane. Structural elucidation confirmed the desired heterodinuclear complexes (Figure 2b). Catalysts **1** and **2** are isostructural, as both are monomeric with an octahedral cobalt(III) coordinated in the bis(iminophenol) ligand cavity, and the alkali metal(I) coordinated in the crown ether cavity. There is a measurable increase in Co−M separation (M = Na; 3.388 Å, K; 3.698 Å) consistent with the increase in radii. In each structure, one acetate ligand bridges (κ_2) between the Co(III) and M(I) and the other is coordinated only to cobalt (κ_1). The structures of complexes **1** and **2** are formally cobalt "ate" species; i.e., the Co(III) is anionic while the M(I) is cationic.

Catalysts **1**−**4** were each tested in CO_2/PO ROCOP, at 50 °C, using neat PO (14 M, 6 mL), 0.025 mol % catalyst, 20 bar CO_2 pressure and 0.5 mol % 1,2-cyclohexane diol (i.e., 20 equiv CTA vs catalyst) to deliver PPC polyols (Table 1). Under these polyol synthesis conditions, all catalysts showed very good activity and resulted in near quantitative CO_2 uptake. The reactions were also highly selective with catalysts **2** and **3**, in particular, showing very little cyclic carbonate byproduct. In all cases, the poly(propylene carbonate) formed without detectable ether linkages and with molar mass values consistent with theoretical values and within the desired polyol range. The PPC polyols show monomodal, narrow dispersity distributions ($Đ$ < 1.10) with excellent selectivity for hydroxyl end-groups (vide infra).

Catalyst **2**, i.e., Co(III)K(I), is the most active and has a turnover frequency (TOF) of 340 h^{-1} at 50 °C (k_p = 11.20

https://dx.doi.org/10.1021/jacs.0c07980
J. Am. Chem. Soc. 2020, 142, 19150−19160

Table 1. ROCOP of CO_2/PO of Catalysts 1−4[a]

#	Co(III)/M(I)	time (h)	conv. (%)[b]	CO_2 (%)[c]	polym. (%)[d]	TON[e]	TOF (h^{-1})[f]	k_p (mM^{-1} s^{-1})[g]	M_n [Đ] (g mol^{-1})[h]
1	Na = **1**	5.0	15	>99	79	600	120	2.09	2300 [1.08]
2	K = **2**	4.0	34	>99	98	1360	340	11.20	5900 [1.10]
3[i]	K = **2**	1.4	28	>99	93	1120	800	24.0	5800 [1.07]
4[j]	K = **2**	19.8	90	>99	98	1800	91	10.70	8800 [1.04]
5	Rb = **3**	23	31	>99	91	1240	54	1.77	6500 [1.07]
6	Cs = **4**	23	27	>99	84	1080	47	1.76	5600 [1.08]
7[k,13]	[(salen)Co(2,4-DNP)]/18C6/KI	3.0	27	>99	41	540	182	–	4700 [1.43]
8[l,26]	[(salcy)Co(O_2CCF_3)]PPN(O_2CCF_3) (20 equiv H_2O)	48	95	>99	>99	475	10	–	7800 [1.06]
9[m,18]	[(salen[Pip^+]$_2$)Co($OAc)_2$] (20 equiv MeOH)	20	95	>99	96	960	48	–	5100 [1.06]
10[n,27]	[(salen[NBu_3^+]$_4$)Co(OAc)]$(NO_2)_4$ (400 equiv adipic acid)	1	10	>99	>99	10 300	10 300	–	2600 [1.05]
11[o,31]	Et_3B:[NBu_4^+]$_2$[O_3C^{2-}]	14	95	91	95	37	3	–	4100 [1.10]
12[p,59]	Zn-Co-DMCC (15 equiv sebacic acid)	30	64	75	98	1280 g/g	43 g/g/h	–	1500 [1.10]

[a]Reaction conditions: Catalyst (0.025 mol %, 3.5 mM), PO (6 mL, 14 M), 1,2-cyclohexanediol (0.5 mol %, 70 mM), 20 bar CO_2, 50 °C. [b]PO conversion determined from the relative integrals in the ^{1}H NMR spectrum of PPC (4.92 ppm, 1H), PC (4.77 ppm, 1H), and PPO (3.46−3.64 ppm, 3H) using mesitylene as an internal standard (6.70 ppm). [c]CO_2 selectivity determined by the relative integrals in the ^{1}H NMR spectrum of PPC (4.92 ppm, 1H) and PC (4.77 ppm, 1H) compared with PPO (3.46−3.64 ppm, 3H). [d]Polymer selectivity determined by the relative integrals in the ^{1}H NMR spectra of PPC (4.92 ppm, 1H) against PC (4.77 ppm, 1H). [e]Turnover number (TON) = number of moles of PO consumed/number of moles catalyst. [f]Turnover frequency (TOF) = TON/time (h). [g]$k_p = k_{obs}/[cat]^1$; k_{obs} determined as the gradient of the plot of $\ln[PO]_t/[PO]_0$ vs time. [h]Determined by GPC analysis, in THF, calibrated with narrow-M_n polystyrene standards; dispersity values in parentheses. [i]Catalyst (0.025 mol %, 3.5 mM), PO (6 mL, 14 M), 1,2-cyclohexanediol (0.5 mol %, 70 mM), 30 bar CO_2, 70 °C. [j]Catalyst (0.05 mol %, 3.5 mM), PO (3 mL, 7 M), diethyl carbonate (3 mL), 1,2-cyclohexanediol (0.5 mol %, 70 mM), 20 bar CO_2, 50 °C. [k]Catalyst (0.05 mol %, 7.1 mM), PO (14 mL, 14 M), KI (0.05 mol %, 7.1 mM), 15 bar CO_2, 25 °C. [l]Catalyst (0.2 mol %, 10.0 mM), PO (0.5 mL, 4.6 M), toluene/chloroform (1 mL), PPNX (0.2 mol %, 10.0 mM), H_2O (2.0 mol %, 1 M), 15 bar CO_2, 25 °C. [m]Catalyst (0.1 mol %, 7.2 mM), PO (1 mL, 7 M), 1,2-dimethoxyethane (1 mL), methanol (1.0 mol %, 0.14 M), 14 bar CO_2, 25 °C. [n]Catalyst (0.001 mol %, 1.7 μM), PO (12 mL, 14 M), adipic acid (0.4 mol %, 0.68 M), 25 bar CO_2, 75 °C. [o]Catalyst (7.5 mol %, 0.25 M, 1 mL from a 1 M THF solution), tetra-butyl ammonium carbonate (TBAC) (2.5 mol %, 0.09 M), PO (2 mL, 7 M), THF (1 mL), 10 bar CO_2, 40 °C. [p]Catalyst (50 mg), PO (100 mL, 14 M), sebacic acid (95 mmol, 0.95 M), 40 bar CO_2, 50 °C. For illustrations of the literature catalyst structures, see Figure S15.

mM^{-1} s^{-1}, 98% PPC, 20 bar CO_2) which is increased to an impressive 800 h^{-1} at 70 °C (k_p = 24.0 mM^{-1} s^{-1}, 93% PPC, 30 bar CO_2). Catalysts **1**, **3**, and **4** are all considerably less active (k_p ∼ 2.00 mM^{-1} s^{-1}) and selective than **2**.

The outstanding performance of the potassium heterodinuclear complex, compared to the other Group 1 metals, likely arises from a combination of carefully balanced metal sizes and binding affinities. When the alkali metal is too small, e.g., Na(I) in complex **1**, it may be coordinatively saturated by the macrocycle crown ether which hinders propylene oxide coordination. When the alkali metal is too large, e.g., Rb(I) or Cs(I) in complexes **3** or **4**, coplanar metal coordination within the macrocycle is no longer possible and aggregates form, as indicated by the DOSY NMR data. Catalyst **2** also produced PPC polyols with excellent productivity, reaching >90% conversion of PO while maintaining high activity and selectivity (Table 1, Entry 2). This data is significant since it demonstrates the ability to use these catalysts to fully convert the epoxide into the target PPC polyols.

Compared against other literature catalysts, the performance of **2** stands out. For example, Lu and co-workers reported a catalyst mixture of [(salen)Co(III)X] (X = 2,4-dinitrophenolate) with an equimolar amount of 18-crown-6/KI (1:1) which formed mostly cyclic carbonate (41% selectivity for PPC) with only half the activity of **2** and without any polyol formation (Table 1, Entry 7).[13] Compared against the [(salen)Co(III)-X]/PPNX system, applied under polyol formation conditions where X = trifluoroactetate, catalyst **2** shows >30× higher activity, at 10× lower loading.[26] As mentioned in the Introduction, the tethered catalyst [(salen[Pip^+]$_2$)Co($OAc)_2$] is less effective in polyol synthesis, with **2** showing 8× higher activity at 2× lower catalyst loading and delivering better selectivity.[18] Catalyst **2** is less active than the highly optimized tetra-ammonium substituted catalyst [(salen[NBu_3^+]$_4$)Co-(OAc)]$(NO_2)_4$, but is substantially higher yielding compared to the 10% PPC conversion reported.[27] Beneficially, **2** is fully characterized and does not contain any salts or anion mixtures.

Heterogeneous double metal cyanide catalysts are used industrially to produce poly(propylene oxide-ran-propylene carbonate) polyols—they show excellent activity but much lower carbon dioxide uptake (carbonate linkages <20%). Unfortunately these heterogeneous catalysts also produce significant quantities of cyclic carbonate byproducts (Table 1, Entry 12).[60,61] Wang and co-workers reported conditions, specifically at lower temperatures and using specific acidic cocatalysts and starters, that increase carbon dioxide uptake (% carbonate <75%). Nonetheless, these conditions impact negatively upon catalyst activity (TOF = 43 g/g/h, 15 equiv sebacic acid, 50 °C, 40 bar CO_2).[59] In comparison, **2** displays an equivalent activity (35 g/g/h at 50 °C), but, unlike the DMC catalysts, it may be applied at higher temperature without loss of selectivity. Thus, at 70 °C, its activity increases to 83 g/g/h without significant compromise in polymer selectivity.

Using low loadings of catalyst **2**, the molar mass of the resulting PPC was easily controlled by varying the amount of chain-transfer agent used (0−250 equiv, Table 2). When the catalyst was applied without CTA, the resulting PPC showed bimodal molar mass distributions attributed to chains which are catalyst initiated (lower MW series) and chains initiated

https://dx.doi.org/10.1021/jacs.0c07980
J. Am. Chem. Soc. 2020, 142, 19150−19160

Table 2. Molecular Weight Control with Addition of Chain-Transfer Agent Using Catalyst 2[a]

#	CTA	conv. (%)[b]	CO_2 (%)[c]	polym. (%)[d]	TON[e]	M_n exp CHD [OAc] (kg mol^{-1})[f]	M_n theoCHD + OAc (kg mol^{-1})[g]	CHD:OAc[h]	$Đ$[i]
1[j]	0	21	>99	93	840	33.7 [14.4]	42.8	50:50	1.04 [1.10]
2	5	58	>99	94	5800	79.6 [38.9]	84.5	76:24	1.06 [1.05]
3	10	46	>99	96	4600	36.8 [15.4]	39.1	83:17	1.06 [1.08]
4	20	52	>99	97	5200	23.1 [10.7]	26.5	95:05	1.03 [1.03]
5	50	63	>99	97	6300	12.3	12.9	99	1.06
6	100	69	>99	94	6900	7.2	7.0	99	1.07
7	250	37	>99	97	3700	1.3	1.5	99	1.16

[a]Reaction conditions: Catalyst (0.01 mol %, 1.9 mM), PO (15 mL, 14 M, 290 mmol), CTA = 1,2-cyclohexanediol, 20 bar CO_2, 50 °C. [b]PO conversion determined from the relative integrals in the ^{1}H NMR spectrum of PPC (4.92 ppm, 1H), PC (4.77 ppm, 1H), and PPO (3.46−3.64 ppm, 3H) using mesitylene as an internal standard (6.70 ppm). [c]CO_2 selectivity determined by the relative integrals in the ^{1}H NMR spectrum of PPC (4.92 ppm, 1H) and PC (4.77 ppm, 1H) compared with PPO (3.46−3.64 ppm, 3H). [d]Polymer selectivity determined by the relative integrals in the ^{1}H NMR spectra of PPC (4.92 ppm, 1H) against PC (4.77 ppm, 1H). [e]Turnover number (TON) = number of moles of PO consumed/number of moles catalyst. [f]Determined by GPC analysis, in THF, calibrated with narrow M_n polystyrene standards. [g]Theoretical molar mass determined by (TON × 102 g mol^{-1})/number of initiators (CHD + OAc). [h]Determined by the relative ratios of the lower (OAc initiated) and upper (CHD initiated) molar mass distributions observed in GPC analysis. [i]Dispersity calculated by M_w/M_n. [j]0.025 mol % catalyst.

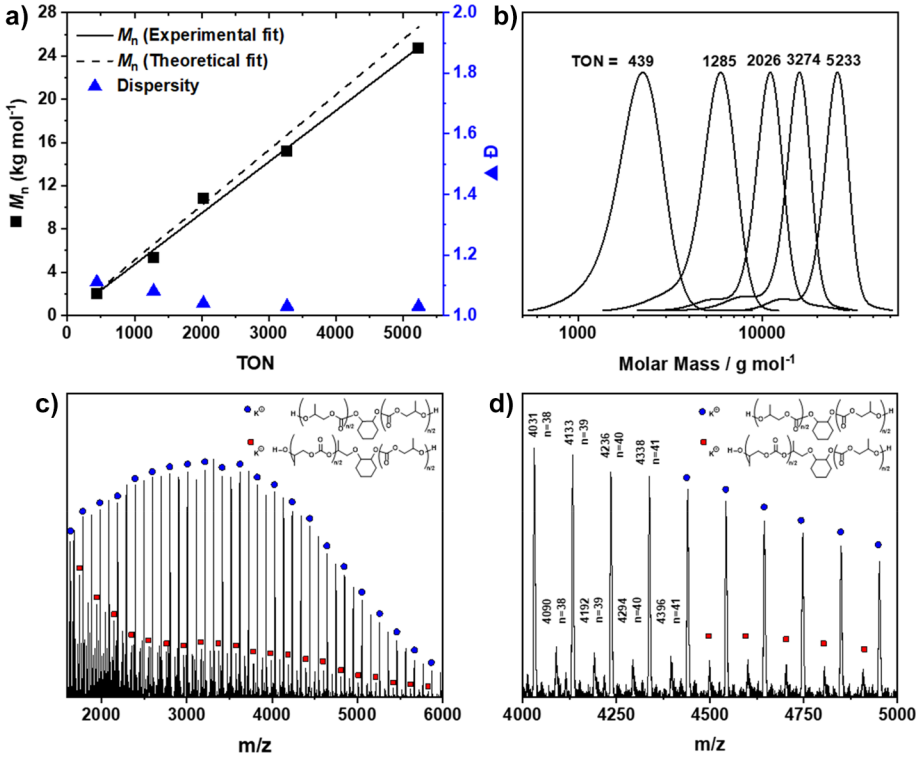


Figure 3. Polymerization data using catalyst **2** (Co(III)/K(I) for PO/CO_2 ROCOP (Table S1). (a) Plot of PPC molar mass (M_n: ■) and dispersity ($Đ$: ▲) versus turnover number (TON). (b) Evolution of the PPC molar masses showing an increase in molar mass (g mol^{-1}) with turnover number (TON) (note the low molar mass shoulder present in some cases arises from chains initiated from catalyst acetate groups). (c) MALDI-ToF spectrum (1000−6000 m/z) of poly(propylene carbonate) initiated from cyclohexanediol (●) and cyclohexane diol + one ether linkage (■). (d) Expanded region of the MALDI-ToF spectrum (4000−5000 m/z) showing both polymer distributions having a repeat unit of 102 g mol^{-1} consistent with the value expected for poly(propylene carbonate).

from 1,2-propane diol (upper series, note the diol evolves by ring opening of epoxide and trace water as discussed previously[25]). For polymerizations conducted with progressively greater numbers of equivalents of CTA, the quantity of catalyst initiated polymer chains decreases resulting in the desired monomodal GPC traces when >50 equiv of CTA are used. The molar mass of the resulting polymers are progressively reduced as the quantity of CTA used increases, allowing access to PPC with controllable M_n values spanning 79.6−1.3 kg mol^{-1} correlating well with theoretical values.

Catalyst **2** shows excellent absolute performance and so a more detailed examination of polymerization control is warranted. The PPC is regiorandom as indicated by quantitative ^{13}C{^{1}H} NMR spectroscopy with a head-to-tail proportion (HT) of 63% (Figure S16). A series of polymerizations conducted at systematically increasing catalyst loadings, from 0.05 to 0.01 mol % (Table S1), showed fast and highly selective catalysis in all cases and, as expected, allowed for good control over PPC molar mass. Plots of PPC molar mass vs turnover number (TON) are linear and there is close agreement between experimental and theoretical values.

https://dx.doi.org/10.1021/jacs.0c07980
J. Am. Chem. Soc. 2020, 142, 19150−19160

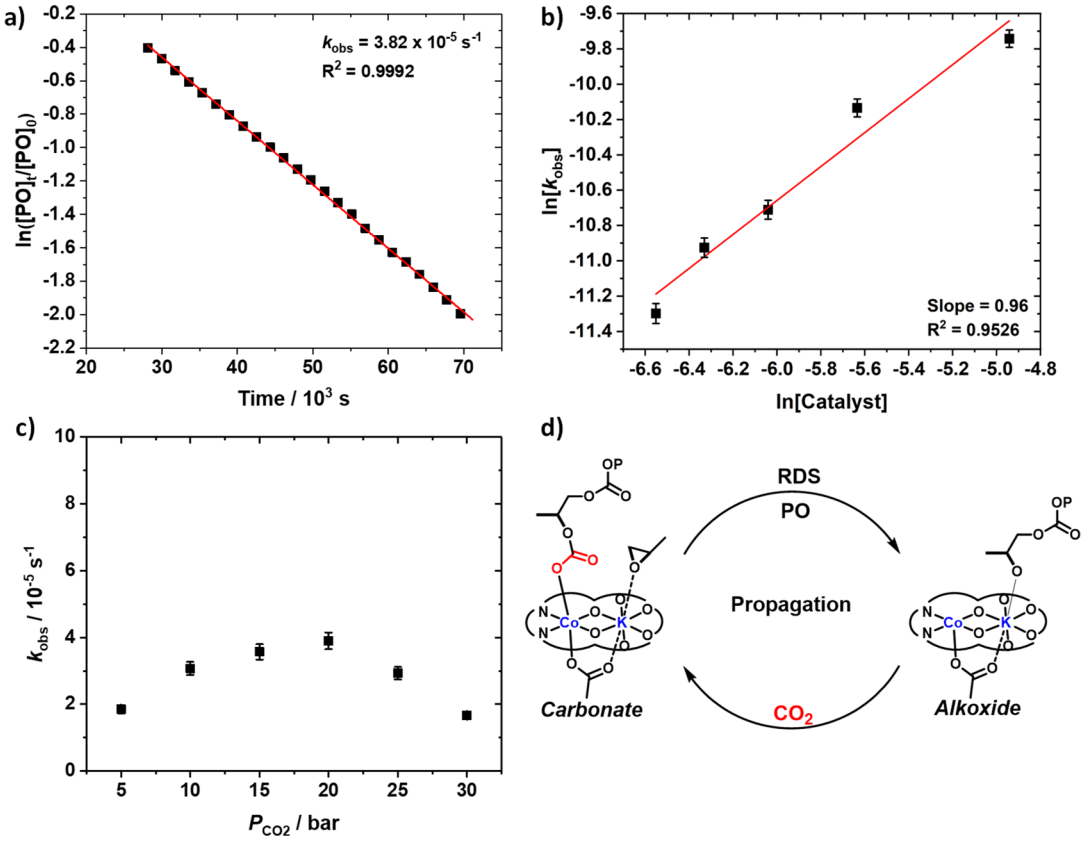


Figure 4. Kinetic data and pathway for catalyst **2** in PO/CO_2 ROCOP. (a) Semilogarithmic plot of $\ln[PO]_t/[PO]_0$ versus time (Table 1, Entry 4). (b) Plot of $\ln[k_{obs}]$ vs ln[**2**], where [**2**] = 1.56−7.13 mM (Table S1). (c) Plot of k_{obs} vs P_{CO_2} from 5 to 30 bar. (d) Illustration of polymerization pathway and rate-determining step. All errors are calculated from duplicate runs and there is an average error of ±5% on all data.

Both findings are consistent with controlled polymerizations, as are the observation that the molar mass distributions are monomodal, with consistently narrow dispersity values (Figure 3b). MALDI-ToF data show two distributions, both corresponding to PPC polyols and differing only in terms of one ether linkage. End group analysis, using $^{31}P\{^1H\}$ NMR spectroscopy, also confirms polyol formation (Figure 3c and d, Figure S17).

One puzzle for the previously reported [(salen)Co(III)-(X)]/PPNX catalysts is the complexity of the polymerization rate law. Reaction orders in [Co(III)] are typically between 1 and 2 and the optimal [PPNCl] loading lies from 0.5 to 2 (vs [Co]).[13−15,29,62] Authors have speculated regarding mono-, dinuclear, and ionic (i.e., off-metal) intermediates and mechanisms to rationalize this data.[13,14,16,17,22,29,45,62−65] Because the ionic cocatalyst performs multiple functions, including nucleophilic attack, coordination, and stabilizing free ionic polymer chains, it is very difficult to design better catalysts.[66]

Given the impressive performance of **2**, particularly as its structure is not yet optimized, it is important to establish its rate law and mechanism. To determine the order in propylene oxide concentration, catalyst **2** was dissolved in a 50:50 mixture of PO:diethyl carbonate (total volume 6 mL) with a resulting PO concentration of 7 M and heated to 50 °C, under 20 bar CO_2 pressure. Using a ReactIR instrument the concentration of PO vs time was evaluated and the data plotted. In the early stages of the reaction (0−30% PO conversion), the data shows a sigmoidal decrease in PO concentration, consistent with slow initiation. The semi-logarithmic plot shows a linear relationship (k_{obs} = 3.82 × 10^{-5} s^{-1}, R^2 = 0.9992) indicative of a first order in epoxide concentration (Figure 4a). To determine the order in catalyst concentration, a series of reactions were carried out in neat PO (14 M), 20 bar CO_2, at 50 °C using a range of concentrations of catalyst **2** (1.56−7.13 mM) (Table S1). All reactions afforded perfectly alternating PPC, without ether linkages, and without any significant cyclic carbonate (<5%). Plotting the logarithm of the observed rate coefficient vs the logarithm of catalyst concentration shows a linear fit, with a gradient of 0.96 (R^2 = 0.9526), indicating a first order in catalyst concentration. The rate dependence on CO_2 pressure was determined by measuring the observed rate coefficient (k_{obs}) over a range of CO_2 pressures from 5 to 30 bar, using 3.57 mM catalyst, neat PO (14 M) and at 50 °C (Table S2). The plot of the rate coefficient versus pressure (k_{obs} vs P_{CO_2}) resulted in a slightly curved fit to the data, but without significant rate changes over the range 10−25 bar. Slightly lower rates were observed at 5 bar and this is attributed to the increased formation of cyclic carbonate, perhaps resulting from the relatively low CO_2 concentration in solution. At higher CO_2 pressures (>20 bar) activity again slightly decreases likely due to gas expansion, prior to the critical point, reducing the overall catalyst and epoxide concentrations.[67] Overall, the reaction is proposed to operate via a second order rate law: first order in both catalyst and epoxide concentrations.

$$\text{Rate} = [\text{Cat}]^1[\text{PO}]^1[\text{CO}_2]^0$$

https://dx.doi.org/10.1021/jacs.0c07980
J. Am. Chem. Soc. 2020, 142, 19150−19160

The kinetic data could be interpreted by a rate-determining step (RDS) involving the ring-opening of the potassium-coordinated epoxide by a cobalt(III)−carbonate intermediate which would be in accordance with a dinuclear mechanism (Figure. 4d, Figure S18). In the solid state complex **2** exhibits a cobaltate structure, i.e., both acetate ligands are coordinated to cobalt (Figure 2b). Accordingly it is hypothesized that propylene oxide (PO) coordination occurs at the oxophilic cationic potassium (Figure S18). In related Ni(II)/Na(I) complexes an internal electric dipole is proposed to localize a positive electric field at Na(I).[55] By analogy, potassium may be electrostatically biased toward epoxide coordination. The mechanistic hypothesis involves propylene oxide coordination being followed by cobaltate acetate nucleophilic attack, during initiation, and by a cobaltate-carbonate intermediate, during propagation. The PO ring-opening results in the formation of a potassium coordinated alkoxide. Carbon dioxide insertion (re)generates the putative cobaltate carbonate intermediate and is proposed as the catalyst resting state. Chain propagation involves both metals and is proposed to occur by a "chain-shuttling" mechanism, akin to CHO/CO_2 ROCOP by dinuclear catalysts.[34,36,38,44,45,47,48,65]

To better understand the catalysis, the temperature dependence of rate and selectivity were investigated (Table S3). Polymerizations were conducted from 40 to 70 °C, using [**2**] of 3.57 mM, in neat PO (14 M), at 20 bar CO_2 pressure, and using 20 equiv of 1,2-cyclohexane diol. All polymerizations resulted in quantitative carbon dioxide uptake (>99%). Increasing the temperature increased the catalytic activity, from 134 to 834 h^{-1}, but the polymer selectivity only slightly decreased. The cyclic carbonate is proposed to form by chain backbiting reactions and these may occur from the alkoxide intermediate. The concentration of the alkoxide intermediate likely increases with temperature due to decreased carbon dioxide solubility. To test this hypothesis, a reaction was conducted at elevated temperature (and otherwise identical conditions) but with a greater CO_2 pressure (30 bar): these reaction conditions restore polymer selectivity to >90% while maintaining very high catalytic activity (TOF = 800 h^{-1}). All polymerizations resulted in molar mass values consistent with theoretical expectations and in monomodal distributions ($Đ$ < 1.1), i.e., catalyst **2** showed very high control and selectivity for polyol even at higher temperatures. Eyring analysis, i.e., a plot of $\ln(k_p/T)$ versus $1/T$, determined the transition state enthalpy, $\Delta H^{‡}$ = 56.0 ± 1.8 kJ mol^{-1}, and entropy, $\Delta S^{‡}$ = −112.7 ± 5.5 J mol^{-1} K^{-1} (Figure 5). Overall, the transition state Gibbs free energy was determined as $\Delta G^{‡}$ = 92.6 ± 2.5 kJ mol^{-1} (50 °C). To compare with ROCOP catalysts, which are often only analyzed by Arrhenius methods (Figure S19), simple activation energy values (E_a) were also determined. For PPC formation, **2** shows E_a = 58.9 ± 1.8 kJ mol^{-1}. Its activation energy is lower than [(salen)Cr(III)(Cl)]/*N*-MeIm (E_a = 67.6 kJ mol^{-1}),[68] but higher than [(salen)Co(X)]/PPNCl or tethered [(salen[NR_3^+])$Co(X)_2$], where E_a = 29−35 kJ mol^{-1}.[69−71]

Compared to M(II)M′(II) dinuclear catalysts, used in CHO/CO_2 ROCOP, it shows significantly lower Gibbs free energy, ΔG = 95−110 kJ mol^{-1}.[40,43] Given the outstanding performance of complex **2** in PO/CO_2 ROCOP, it was useful to observe that it was also an excellent catalyst for a range of other epoxides in ROCOP with CO_2 (Table 3, Figure S20). In all cases, the same conditions were applied as for PO/CO_2 ROCOP: 3.57 mM catalyst, neat epoxide (6 mL), 1,2-cyclohexene diol (71.4 mM), 50 °C, and 20 bar CO_2. Catalyst **2** shows impressive activity for most other epoxides and in all cases ensures high carbon dioxide uptake (>99%) without ether linkage formation. In most cases, the selectivity for polymer is very high (>95%) with only trace quantities of cyclic carbonate (<5%). All the polycarbonate polyols show molar mass values consistent with theoretical values and monomodal distributions, with narrow dispersity (>1.30 $Đ$), consistent with well-controlled polymerizations (Figure S21).

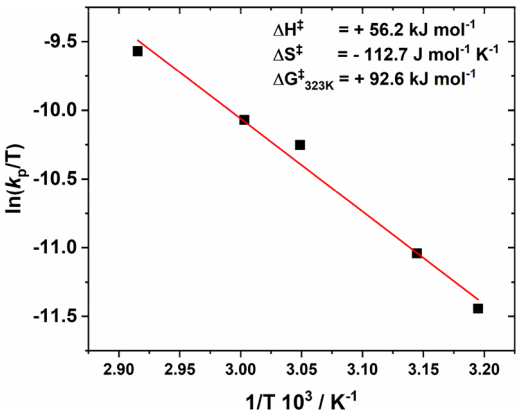


Figure 5. Eyring plot, $\ln(k_p/T)$ versus $1/T$, for complex **2** over the temperature range 40−70 °C, 3.57 mM catalyst, neat PO (6 mL), 1,2-cyclohexene diol (71 mmol), under 20 bar CO_2 (Table S3).

For example, ROCOP using 2-vinyl oxirane (vPO) is important for postfunctionalization and cross-linking of the resulting polycarbonate.[72−75] Using catalyst **2**, vPO/CO_2 ROCOP was slightly slower than for PO, perhaps due to oxirane deactivation by the allyl substituent. There are only a few vPO/CO_2 ROCOP catalysts, and compared with these, **2** shows outstanding performances. It shows equivalent activity to the highly optimized quaternary ammonium [(salen)Co(III)(NR_3)X′)] system (TOF = 40 h^{-1}, 0.1 mol % cat, 30 bar CO_2, 40 °C).[76,77] This finding demonstrates the significant potential for future improvement to this new class of catalyst, for example, by ligand structure−activity studies. ROCOP using allyl glycidyl ether (AGE) was also successful and illustrates the importance of comparing reactions according to their polymerization rate coefficient (k_p). Although the TOF for PO ROCOP appears greater, the k_p for AGE ROCOP is in fact significantly greater (15.4 vs 11.2 mM^{-1} s^{-1}). The difference arises because the intrinsic molarity of PO is higher than that of AGE (14.3 M vs 8.4 M). Therefore, after taking into consideration the absolute epoxide concentrations, the ROCOP of CO_2/AGE is faster than CO_2/PO. This result is important since it demonstrates the potential to produce unsaturated polycarbonates with even greater activity than using PO, thereby providing an efficient future route to polycarbonate amphiphiles or functionalized materials. Co-polymerization of *tert*-butyl glycidyl ether (*t*BGE)/CO_2 was about half the activity when using AGE (219 h^{-1} vs 116 h^{-1}) with a slight reduction in polymer selectivity (cyclic carbonate = 8 vs >1%). The differences may arise from different steric profiles for the two monomers. Catalysts **2** displays comparable activity to a [(salen)Co(III)(NR_3^+)$(DNP)_2$] catalyst (119 h^{-1}, 0.05 mol %, 40 °C, 15 bar CO_2)[78] Reaction of styrene oxide SO/CO_2 formed mostly styrene carbonate (91%), presumably because the electron withdrawing phenyl substituent increases the methine carbon's electrophilicity and favors backbiting by

https://dx.doi.org/10.1021/jacs.0c07980
J. Am. Chem. Soc. 2020, 142, 19150−19160

Table 3. Monomer Scope Data for CO_2/Epoxide ROCOP Using Catalyst 2[a]

entry	epoxide		time (h)	conv. (%)[b]	CO_2 (%)[c]	polym. (%)[d]	TON[e]	TOF (h^{-1})[f]	k_p (mM^{-1} s^{-1})[g]	M_n [$Đ$] (g mol^{-1})[h]
1	Acyclic	PO	4.2	34	>99	>99	1352	340	11.2	5900 [1.10]
2		vPO	23.5	60	>99	>99	2091	89	5.9	4100 [1.30]
3		AGE	5.6	51	>99	>99	1220	219	15.4	3900 [1.28]
4		^{t}BGE	7.9	46	>99	92	908	116	7.4	5100 [1.15]
5		SO	22.3	21	>99	9	511	23	n.a.	n.a.
6	Cyclic	CHO	2.3	52	>99	>99	1430	631	31.7	5900 [1.10]
7		vCHO	3.2	60	>99	>99	1285	408	24.6	9500 [1.08]
8		CPO	6.3	32	>99	95	1062	162	5.1	4200 [1.07]

[a]Reaction conditions: Catalyst 2 (3.57 mM), neat epoxide (6 mL), 1,2-cyclohexane diol (20 equiv vs 2), 20 bar CO_2 and 50 °C. [b]Epoxide conversion determined by comparison of the relative integrals in the ^{1}H NMR spectrum of PC, CC, and PE against mesitylene (6.59 ppm, 10 equiv). [c]CO_2 selectivity determined by comparison of the relative integrals in the ^{1}H NMR spectrum for PC and CC against PE. [d]Polymer selectivity determined by comparison of the relative integrals in the ^{1}H NMR spectrum for PC against CC. [e]Turnover number (TON) = number of moles of epoxide consumed/number of moles catalyst. [f]Turnover frequency (TOF) = TON/time (h). [g]$k_p = k_{obs}/[cat]^1$; k_{obs} determined as the gradient of the plot of $\ln([Epoxide]_t/[Epoxide]_0)$ vs time, [2] = 3.57 mM. [h]GPC analysis, in THF, calibrated using narrow-M_n polystyrene standards, dispersity values in parentheses. Note that Figure S22 illustrates the leading literature catalysts for each epoxide.

the nucleophilic carbonate/alkoxide intermediates. Darensbourg and co-workers applied [(salen)Co(III)(X)]/PPNCl catalysts for CO_2/SO ROCOP and noted that only X= DNP (2,4-dinitrophenolate) performed effectively (X = DNP 90%; Cl = 58%; and Br = 5% PPC formation).[79]

In the future it may be possible to improve the selectivity of catalyst 2 for polycarbonate by changing the acetate ligand or by substituting 1,2-cyclohexene diol for 1-phenyl-1,2-ethanediol as the chain transfer agent. Cyclic epoxides generally proceeded with a higher rate constant (k_p) than acyclic epoxides (Table 2). The release of ring-strain provides an additional driving force, and 6-membered ring epoxides, e.g., cyclohexene oxide (CHO) or vinyl-cyclohexene oxide (vCHO), are usually polymerized significantly faster than 5-membered ring epoxides, such as cyclopentene oxide (CPO). Catalyst 2 was highly active for CO_2/CHO ROCOP and showed a polymerization rate constant more than double that of a previous high performance [Mg(II)Co(II)] heterodinuclear catalyst (2, k_p = 31.7 mM^{-1} s^{-1} (50 °C) versus [Co(II)Mg(II)], k_p = 15.1 mM^{-1} s^{-1}(60 °C))[43] and achieves comparable activity to the quaternary ammonium cobalt catalyst systems (TOF = 1018 h^{-1}, catalyst = 0.02 mol %, 50 °C, 20 bar CO_2).[80] Its overall performance in CHO/CO_2 ROCOP is better than the widely investigated β-diiminate di-Zn-catalyst (TOF = 2290 h^{-1}, 50 °C, 0.1 mol % cat, 69 bar CO_2, 90% PCHC formation), as it is applied at 4× lower catalyst loading.[81] It is significantly less active than the tethered β-diiminate di-Zn catalysts, reported by Rieger and co-workers, which delivers poly(cyclohexene carbonate) with ∼80% carbonate linkages only (155 000 h^{-1}, 0.0125 mol %, 100 °C, 30 bar CO_2) although 2 is tested at significantly lower temperature preventing easy comparison.[82] It is also important to note that these optimized di-Zn catalysts show negligible activity for propylene oxide/carbon dioxide copolymerization (1 h^{-1}, 0.025 mol %, 60 °C, 23% polymer).[83]

ROCOP using functionalized vinyl-cyclohexene oxide (vCHO)/CO_2 is also highly active and selective; the product polycarbonate undergoes postfunctionalization, cross-linking and network formation.[84,85] The CO_2/cyclopentene oxide (CPO) ROCOP forms a polycarbonate which under certain conditions can be depolymerized to epoxide, rather than to cyclic carbonate, thus providing a future chemical recycling route.[86,87] Using catalyst 2 for the ROCOP of CPO/CO_2 resulted in polycarbonate formation with excellent selectivity (95%) (Table 2, Entry 8). The catalytic activity is high, TOF = 162 h^{-1}, particularly given the low catalyst loading applied (0.025 mol % cat, 50 °C, 20 bar CO_2, neat CPO). Indeed the activity of 2 is four times higher than the most active cobalt-salen derivative which is applied at four times higher loading (TOF = 42 h^{-1}, 0.1 mol % cat, 50 °C, 20 bar CO_2).[88] It is also double the activity of a chromium-salen derivative, again applied at four times higher loading than 2, (TOF = 77 h^{-1}, 0.1 mol % cat, 70 °C, 20 bar CO_2).[88] Overall, the heterodinuclear Co(III)/K(I) catalyst shows outstanding performance using a range of other epoxides in alternating copolymerizations with carbon dioxide. We plan to continue to optimize the ligand and metal selection so as to further increase performances.

CONCLUSION

In conclusion, a new class of heterodinuclear Co(III)/M(I) complexes were highly active, selective, and controlled catalysts for propylene oxide/carbon dioxide ring-opening copolymerizations. The complexes demonstrate the power of asymmetrical macrocycle ligands to bias the coordination chemistry and reactivity to deliver highly effective catalysis. These complexes have significant potential for future optimization, including through modifications of the substituents, metal combinations, and coligand chemistries. Since this is the first demonstration of how to exploit Group 1 metals in this catalysis, further investigation into the power of these inexpensive, colorless, and abundant metals for carbon dioxide utilization catalysis is certainly warranted. Group 1 metals offer tremendous potential in terms of operability and scale-up, and the Co(III)/K(I) catalyst challenged the performance of the status-quo tethered catalyst systems which rely on expensive salts, like PPNCl. The best catalyst, Co(III)/K(I), delivered high polymerization conversions, excellent activity, and an impressive operating temperature window (25−70 °C). The activity reached values of TOF = 800 h^{-1}, and it was applied at useful, low loading (0.025 mol %). It was also highly active for a range of other epoxides, including those substituted with alkene groups. Kinetic analyses showed an overall second order rate law and implicate a chain shuttling dinuclear mechanism. The catalysts warrant future investigation for related polymerizations, such as lactone ring-opening polymerizations, switch polymerization catalysis, and epoxide/anhydride ROCOP. The beneficial combination of Co(III) and Group 1 metals could also accelerate other carbon dioxide, and heterocumulene,

https://dx.doi.org/10.1021/jacs.0c07980
J. Am. Chem. Soc. 2020, 142, 19150−19160

transformations, including production of heterocycles, N-containing polymers, polyesters, and even carbon dioxide reduction products.

■ ASSOCIATED CONTENT

Supporting Information

The Supporting Information is available free of charge at https://pubs.acs.org/doi/10.1021/jacs.0c07980.

Characterization data of catalysts (1D and 2D NMR spectroscopy, mass spectrometry, infrared spectroscopy, and X-ray crystallography); Polymerization kinetics and characterization (NMR spectroscopy and gel permeation chromatograms) (PDF)

Crystal data (CIF)

■ AUTHOR INFORMATION

Corresponding Author

Charlotte K. Williams − *Department of Chemistry, Chemistry Research Laboratory, University of Oxford, Oxford OX1 3TA, U.K.*; orcid.org/0000-0002-0734-1575; Email: charlotte.williams@chem.ox.ac.uk

Authors

Arron C. Deacy − *Department of Chemistry, Chemistry Research Laboratory, University of Oxford, Oxford OX1 3TA, U.K.*

Emma Moreby − *Department of Chemistry, Chemistry Research Laboratory, University of Oxford, Oxford OX1 3TA, U.K.*

Andreas Phanopoulos − *Department of Chemistry, Chemistry Research Laboratory, University of Oxford, Oxford OX1 3TA, U.K.*

Complete contact information is available at: https://pubs.acs.org/10.1021/jacs.0c07980

Notes

The authors declare the following competing financial interest(s): CKW is a director of Econic Technologies, Ltd.

■ ACKNOWLEDGMENTS

The Engineering and Physical Sciences Research Council (EP/S018603/1; EP/R027129/1) and the Oxford Martin School (Future of Plastics) are acknowledged for research funding.

■ REFERENCES

(1) Burkart, M. D.; Hazari, N.; Tway, C. L.; Zeitler, E. L. Opportunities and Challenges for Catalysis in Carbon Dioxide Utilization. *ACS Catal.* **2019**, *9* (9), 7937−7956.

(2) Artz, J.; Müller, T. E.; Thenert, K.; Kleinekorte, J.; Meys, R.; Sternberg, A.; Bardow, A.; Leitner, W. Sustainable Conversion of Carbon Dioxide: An Integrated Review of Catalysis and Life Cycle Assessment. *Chem. Rev.* **2018**, *118* (2), 434−504.

(3) Hepburn, C.; Adlen, E.; Beddington, J.; Carter, E. A.; Fuss, S.; Mac Dowell, N.; Minx, J. C.; Smith, P.; Williams, C. K. The technological and economic prospects for CO_2 utilization and removal. *Nature* **2019**, *575* (7781), 87−97.

(4) Darensbourg, D. J. Chain transfer agents utilized in epoxide and CO_2 copolymerization processes. *Green Chem.* **2019**, *21* (9), 2214−2223.

(5) Wang, Y.; Darensbourg, D. J. Carbon dioxide-based functional polycarbonates: Metal catalyzed copolymerization of CO_2 and epoxides. *Coord. Chem. Rev.* **2018**, *372*, 85−100.

(6) Alagi, P.; Ghorpade, R.; Choi, Y. J.; Patil, U.; Kim, I.; Baik, J. H.; Hong, S. C. Carbon Dioxide-Based Polyols as Sustainable Feedstock of Thermoplastic Polyurethane for Corrosion-Resistant Metal Coating. *ACS Sustainable Chem. Eng.* **2017**, *5* (5), 3871−3881.

(7) Langanke, J.; Wolf, A.; Hofmann, J.; Bohm, K.; Subhani, M. A.; Muller, T. E.; Leitner, W.; Gurtler, C. Carbon dioxide (CO_2) as sustainable feedstock for polyurethane production. *Green Chem.* **2014**, *16* (4), 1865−1870.

(8) Lee, S. H.; Cyriac, A.; Jeon, J. Y.; Lee, B. Y. Preparation of thermoplastic polyurethanes using in situ generated poly(propylene carbonate)-diols. *Polym. Chem.* **2012**, *3* (5), 1215−1220.

(9) von der Assen, N.; Bardow, A. Life cycle assessment of polyols for polyurethane production using CO_2 as feedstock: insights from an industrial case study. *Green Chem.* **2014**, *16* (6), 3272−3280.

(10) Sulley, G. S.; Gregory, G. L.; Chen, T. T. D.; Peña Carrodeguas, L.; Trott, G.; Santmarti, A.; Lee, K.-Y.; Terrill, N. J.; Williams, C. K. Switchable Catalysis Improves the Properties of CO_2-Derived Polymers: Poly(cyclohexene carbonate-b-ε-decalactone-b-cyclohexene carbonate) Adhesives, Elastomers, and Toughened Plastics. *J. Am. Chem. Soc.* **2020**, *142* (9), 4367−4378.

(11) Leow, W. R.; Lum, Y.; Ozden, A.; Wang, Y.; Nam, D.-H.; Chen, B.; Wicks, J.; Zhuang, T.-T.; Li, F.; Sinton, D.; Sargent, E. H. Chloride-mediated selective electrosynthesis of ethylene and propylene oxides at high current density. *Science* **2020**, *368* (6496), 1228−1233.

(12) Lu, X. B.; Ren, W. M.; Wu, G. P. CO_2 Copolymers from Epoxides: Catalyst Activity, Product Selectivity, and Stereochemistry Control. *Acc. Chem. Res.* **2012**, *45* (10), 1721−1735.

(13) Lu, X. B.; Shi, L.; Wang, Y. M.; Zhang, R.; Zhang, Y. J.; Peng, X. J.; Zhang, Z. C.; Li, B. Design of highly active binary catalyst systems for CO_2/epoxide copolymerization: Polymer selectivity, enantioselectivity, and stereochemistry control. *J. Am. Chem. Soc.* **2006**, *128* (5), 1664−1674.

(14) Liu, J.; Ren, W. M.; Liu, Y.; Lu, X. B. Kinetic Study on the Coupling of CO_2 and Epoxides Catalyzed by Co(III) Complex with an Inter- or Intramolecular Nucleophilic Cocatalyst. *Macromolecules* **2013**, *46* (4), 1343−1349.

(15) Noh, E. K.; Na, S. J.; Sujith, S.; Kim, S. W.; Lee, B. Y. Two components in a molecule: Highly efficient and thermally robust catalytic system for CO_2/Epoxide copolymerization. *J. Am. Chem. Soc.* **2007**, *129* (26), 8082−8083.

(16) Nakano, K.; Kobayashi, K.; Nozaki, K. Tetravalent Metal Complexes as a New Family of Catalysts for Copolymerization of Epoxides with Carbon Dioxide. *J. Am. Chem. Soc.* **2011**, *133* (28), 10720−10723.

(17) Nakano, K.; Hashimoto, S.; Nozaki, K. Bimetallic mechanism operating in the copolymerization of propylene oxide with carbon dioxide catalyzed by cobalt-salen complexes. *Chem. Sci.* **2010**, *1* (3), 369−373.

(18) Nakano, K.; Kamada, T.; Nozaki, K. Selective formation of polycarbonate over cyclic carbonate: Copolymerization of epoxides with carbon dioxide catalyzed by a cobalt(III) complex with a piperidinium end-capping arm. *Angew. Chem., Int. Ed.* **2006**, *45* (43), 7274−7277.

(19) Cohen, C. T.; Chu, T.; Coates, G. W. Cobalt catalysts for the alternating copolymerization of propylene oxide and carbon dioxide: Combining high activity and selectivity. *J. Am. Chem. Soc.* **2005**, *127* (31), 10869−10878.

(20) Qin, Z. Q.; Thomas, C. M.; Lee, S.; Coates, G. W. Cobalt-based complexes for the copolymerization of propylene oxide and CO2: Active and selective catalysts for polycarbonate synthesis. *Angew. Chem., Int. Ed.* **2003**, *42* (44), 5484−5487.

(21) Allen, S. D.; Moore, D. R.; Lobkovsky, E. B.; Coates, G. W. High-activity, single-site catalysts for the alternating copolymerization of CO2 and propylene oxide. *J. Am. Chem. Soc.* **2002**, *124* (48), 14284−14285.

(22) Vagin, S. I.; Reichardt, R.; Klaus, S.; Rieger, B. Conformationally Flexible Dimeric Salphen Complexes for Bifunctional Catalysis. *J. Am. Chem. Soc.* **2010**, *132* (41), 14367−14369.

(23) Zhang, D. Y.; Boopathi, S. K.; Hadjichristidis, N.; Gnanou, Y.; Feng, X. S. Metal-Free Alternating Copolymerization of CO2 with

Epoxides: Fulfilling "Green" Synthesis and Activity. *J. Am. Chem. Soc.* **2016**, *138* (35), 11117−11120.
(24) Jia, M. C.; Hadjichristidis, N.; Gnanou, Y.; Feng, X. S. Monomodal Ultrahigh-Molar-Mass Polycarbonate Homopolymers and Diblock Copolymers by Anionic Copolymerization of Epoxides with CO2. *ACS Macro Lett.* **2019**, *8* (12), 1594−1598.
(25) Wu, G.-P.; Darensbourg, D. J. Mechanistic Insights into Water-Mediated Tandem Catalysis of Metal-Coordination CO_2/Epoxide Copolymerization and Organocatalytic Ring-Opening Polymerization: One-Pot, Two Steps, and Three Catalysis Cycles for Triblock Copolymers Synthesis. *Macromolecules* **2016**, *49* (3), 807−814.
(26) Darensbourg, D. J.; Wu, G. P. A One-Pot Synthesis of a Triblock Copolymer from Propylene Oxide/Carbon Dioxide and Lactide: Intermediacy of Polyol Initiators. *Angew. Chem., Int. Ed.* **2013**, *52* (40), 10602−10606.
(27) Cyriac, A.; Lee, S. H.; Varghese, J. K.; Park, E. S.; Park, J. H.; Lee, B. Y. Immortal CO2/Propylene Oxide Copolymerization: Precise Control of Molecular Weight and Architecture of Various Block Copolymers. *Macromolecules* **2010**, *43* (18), 7398−7401.
(28) Yoo, J.; Na, S. J.; Park, H. C.; Cyriac, A.; Lee, B. Y. Anion variation on a cobalt(iii) complex of salen-type ligand tethered by four quaternary ammonium salts for CO2/epoxide copolymerization. *Dalton Trans.* **2010**, *39* (10), 2622−2630.
(29) Na, S. J.; Sujith, S.; Cyriac, A.; Kim, B. E.; Yoo, J.; Kang, Y. K.; Han, S. J.; Lee, C.; Lee, B. Y. Elucidation of the Structure of a Highly Active Catalytic System for CO2/Epoxide Copolymerization: A salen-Cobaltate Complex of an Unusual Binding Mode. *Inorg. Chem.* **2009**, *48* (21), 10455−10465.
(30) Deng, J.; Ratanasak, M.; Sako, Y.; Tokuda, H.; Maeda, C.; Hasegawa, J.-y.; Nozaki, K.; Ema, T. Aluminum porphyrins with quaternary ammonium halides as catalysts for copolymerization of cyclohexene oxide and CO2: metal−ligand cooperative catalysis. *Chem. Sci.* **2020**, *11* (22), 5669−5675.
(31) Patil, N. G.; Boopathi, S. K.; Alagi, P.; Hadjichristidis, N.; Gnanou, Y.; Feng, X. Carboxylate Salts as Ideal Initiators for the Metal-Free Copolymerization of CO2 with Epoxides: Synthesis of Well-Defined Polycarbonates Diols and Polyols. *Macromolecules* **2019**, *52* (6), 2431−2438.
(32) Patil, N.; Bhoopathi, S.; Chidara, V.; Hadjichristidis, N.; Gnanou, Y.; Feng, X. Recycling a Borate Complex for Synthesis of Polycarbonate Polyols: Towards an Environmentally Friendly and Cost-Effective Process. *ChemSusChem* **2020**, *13* (18), 5080−5087.
(33) Yang, G.-W.; Zhang, Y.-Y.; Xie, R.; Wu, G.-P. Scalable Bifunctional Organoboron Catalysts for Copolymerization of CO2 and Epoxides with Unprecedented Efficiency. *J. Am. Chem. Soc.* **2020**, *142*, 12245.
(34) Trott, G.; Garden, J. A.; Williams, C. K. Heterodinuclear zinc and magnesium catalysts for epoxide/CO2 ring opening copolymerizations. *Chem. Sci.* **2019**, *10* (17), 4618−4627.
(35) Deacy, A. C.; Durr, C. B.; Garden, J. A.; White, A. J. P.; Williams, C. K. Groups 1, 2 and Zn(II) Heterodinuclear Catalysts for Epoxide/CO2 Ring-Opening Copolymerization. *Inorg. Chem.* **2018**, *57* (24), 15575−15583.
(36) Garden, J. A.; Saini, P. K.; Williams, C. K. Greater than the Sum of Its Parts: A Heterodinuclear Polymerization Catalyst. *J. Am. Chem. Soc.* **2015**, *137* (48), 15078−15081.
(37) Chapman, A. M.; Keyworth, C.; Kember, M. R.; Lennox, A. J. J.; Williams, C. K. Adding Value to Power Station Captured CO2: Tolerant Zn and Mg Homogeneous Catalysts for Polycarbonate Polyol Production. *ACS Catal.* **2015**, *5* (3), 1581−1588.
(38) Saini, P. K.; Romain, C.; Williams, C. K. Dinuclear metal catalysts: improved performance of heterodinuclear mixed catalysts for CO_2-epoxide copolymerization. *Chem. Commun.* **2014**, *50* (32), 4164−4167.
(39) Kember, M. R.; Williams, C. K. Efficient Magnesium Catalysts for the Copolymerization of Epoxides and CO_2; Using Water to Synthesize Polycarbonate Polyols. *J. Am. Chem. Soc.* **2012**, *134* (38), 15676−15679.
(40) Jutz, F.; Buchard, A.; Kember, M. R.; Fredriksen, S. B.; Williams, C. K. Mechanistic Investigation and Reaction Kinetics of the Low-Pressure Copolymerization of Cyclohexene Oxide and Carbon Dioxide Catalyzed by a Dizinc Complex. *J. Am. Chem. Soc.* **2011**, *133* (43), 17395−17405.
(41) Buchard, A.; Kember, M. R.; Sandeman, K. G.; Williams, C. K. A bimetallic iron(III) catalyst for CO_2/epoxide coupling. *Chem. Commun.* **2011**, *47* (1), 212−214.
(42) Kember, M. R.; Knight, P. D.; Reung, P. T. R.; Williams, C. K. Highly Active Dizinc Catalyst for the Copolymerization of Carbon Dioxide and Cyclohexene Oxide at One Atmosphere Pressure. *Angew. Chem., Int. Ed.* **2009**, *48* (5), 931−933.
(43) Deacy, A. C.; Kilpatrick, A. F. R.; Regoutz, A.; Williams, C. K. Understanding metal synergy in heterodinuclear catalysts for the copolymerization of CO2 and epoxides. *Nat. Chem.* **2020**, *12* (4), 372−380.
(44) Trott, G.; Saini, P. K.; Williams, C. K. Catalysts for CO_2/Epoxide Ring-Opening Copolymerization. *Philos. Trans. R. Soc., A* **2016**, *374* (2061), 20150085.
(45) Buchard, A.; Jutz, F.; Kember, M. R.; White, A. J. P.; Rzepa, H. S.; Williams, C. K. Experimental and Computational Investigation of the Mechanism of Carbon Dioxide/Cyclohexene Oxide Copolymerization Using a Dizinc Catalyst. *Macromolecules* **2012**, *45* (17), 6781−6795.
(46) Kember, M. R.; White, A. J. P.; Williams, C. K. Highly Active Di- and Trimetallic Cobalt Catalysts for the Copolymerization of CHO and CO_2 at Atmospheric Pressure. *Macromolecules* **2010**, *43* (5), 2291−2298.
(47) Asaba, H.; Iwasaki, T.; Hatazawa, M.; Deng, J.; Nagae, H.; Mashima, K.; Nozaki, K. Alternating Copolymerization of CO2 and Cyclohexene Oxide Catalyzed by Cobalt−Lanthanide Mixed Multinuclear Complexes. *Inorg. Chem.* **2020**, *59* (12), 7928−7933.
(48) Nagae, H.; Aoki, R.; Akutagawa, S.; Kleemann, J.; Tagawa, R.; Schindler, T.; Choi, G.; Spaniol, T. P.; Tsurugi, H.; Okuda, J.; Mashima, K. Lanthanide Complexes Supported by a Trizinc Crown Ether as Catalysts for Alternating Copolymerization of Epoxide and CO_2: Telomerization Controlled by Carboxylate Anions. *Angew. Chem., Int. Ed.* **2018**, *57* (9), 2492−2496.
(49) Deacy, A. C.; Durr, C. B.; Williams, C. K. Heterodinuclear complexes featuring Zn(ii) and M = Al(iii), Ga(iii) or In(iii) for cyclohexene oxide and CO2 copolymerisation. *Dalton Trans.* **2020**, *49* (1), 223−231.
(50) Klaus, S.; Lehenmeier, M. W.; Herdtweck, E.; Deglmann, P.; Ott, A. K.; Rieger, B. Mechanistic Insights into Heterogeneous Zinc Dicarboxylates and Theoretical Considerations for CO2−Epoxide Copolymerization. *J. Am. Chem. Soc.* **2011**, *133* (33), 13151−13161.
(51) Du, K.; Thorarinsdottir, A. E.; Harris, T. D. Selective Binding and Quantitation of Calcium with a Cobalt-Based Magnetic Resonance Probe. *J. Am. Chem. Soc.* **2019**, *141* (17), 7163−7172.
(52) Chantarojsiri, T.; Ziller, J. W.; Yang, J. Y. Incorporation of redox-inactive cations promotes iron catalyzed aerobic C−H oxidation at mild potentials. *Chem. Sci.* **2018**, *9* (9), 2567−2574.
(53) Martinez, A.; Hemmert, C.; Gornitzka, H.; Meunier, B. Synthesis and activity of macrocyclized chiral Mn(III)−Schiff-base epoxidation catalysts. *J. Organomet. Chem.* **2005**, *690* (9), 2163−2171.
(54) Reath, A. H.; Ziller, J. W.; Tsay, C.; Ryan, A. J.; Yang, J. Y. Redox Potential and Electronic Structure Effects of Proximal Nonredox Active Cations in Cobalt Schiff Base Complexes. *Inorg. Chem.* **2017**, *56* (6), 3713−3718.
(55) Kang, K.; Fuller, J.; Reath, A. H.; Ziller, J. W.; Alexandrova, A. N.; Yang, J. Y. Installation of internal electric fields by non-redox active cations in transition metal complexes. *Chem. Sci.* **2019**, *10* (43), 10135−10142.
(56) Chantarojsiri, T.; Reath, A. H.; Yang, J. Y. Cationic Charges Leading to an Inverse Free-Energy Relationship for N−N Bond Formation by MnVI Nitrides. *Angew. Chem., Int. Ed.* **2018**, *57* (43), 14037−14042.
(57) Rollinson, H.; Adetunji, J. Ionic Radii. In *Encyclopedia of Geochemistry: A Comprehensive Reference Source on the Chemistry of the*

https://dx.doi.org/10.1021/jacs.0c07980
J. Am. Chem. Soc. 2020, 142, 19150−19160

Earth; White, W. M., Ed.; Springer International Publishing: Cham, 2018; pp 738−743.
(58) Akine, S.; Utsuno, F.; Piao, S.; Orita, H.; Tsuzuki, S.; Nabeshima, T. Synthesis, Ion Recognition Ability, and Metal-Assisted Aggregation Behavior of Dinuclear Metallohosts Having a Bis(Saloph) Macrocyclic Ligand. *Inorg. Chem.* **2016**, *55* (2), 810−821.
(59) Gao, Y.; Gu, L.; Qin, Y.; Wang, X.; Wang, F. Dicarboxylic acid promoted immortal copolymerization for controllable synthesis of low-molecular weight oligo(carbonate-ether) diols with tunable carbonate unit content. *J. Polym. Sci., Part A: Polym. Chem.* **2012**, *50* (24), 5177−5184.
(60) Hinz, W.; Wildeson, J.; Dexheimer, E. M.; Neff, R. Formation of polymer polyols with a narrow polydispersity using double metal cyanide (DMC) catalysts. US6713599B1, 2006.
(61) Gürtler, C.; Hofmann, J.; Wolf, A.; Grasser, S. Method for producing polyether carbonate polyols. US20130123532A1, 2013.
(62) Ohkawara, T.; Suzuki, K.; Nakano, K.; Mori, S.; Nozaki, K. Facile Estimation of Catalytic Activity and Selectivities in Copolymerization of Propylene Oxide with Carbon Dioxide Mediated by Metal Complexes with Planar Tetradentate Ligand. *J. Am. Chem. Soc.* **2014**, *136* (30), 10728−10735.
(63) Darensbourg, D. J.; Fitch, S. B. Copolymerization of Epoxides and Carbon Dioxide. Evidence Supporting the Lack of Dual Catalysis at a Single Metal Site. *Inorg. Chem.* **2009**, *48* (18), 8668−8677.
(64) Darensbourg, D. J. Making Plastics from Carbon Dioxide: Salen Metal Complexes as Catalysts for the Production of Polycarbonates from Epoxides and CO_2. *Chem. Rev.* **2007**, *107* (6), 2388−2410.
(65) Liu, Y.; Ren, W.-M.; Liu, C.; Fu, S.; Wang, M.; He, K.-K.; Li, R.-R.; Zhang, R.; Lu, X.-B. Mechanistic Understanding of Dinuclear Cobalt(III) Complex Mediated Highly Enantioselective Copolymerization of meso-Epoxides with CO2. *Macromolecules* **2014**, *47* (22), 7775−7788.
(66) Romain, C.; Thevenon, A.; Saini, P. K.; Williams, C. K., Dinuclear Metal Complex-Mediated Formation of CO_2-Based Polycarbonates. In *Carbon Dioxide and Organometallics*; Lu, X. B., Ed.; Springer, 2016; Vol. *53*, pp 101−141.
(67) Mang, S.; Cooper, A. I.; Colclough, M. E.; Chauhan, N.; Holmes, A. B. Copolymerization of CO2 and 1,2-Cyclohexene Oxide Using a CO2-Soluble Chromium Porphyrin Catalyst. *Macromolecules* **2000**, *33* (2), 303−308.
(68) Darensbourg, D. J.; Yarbrough, J. C.; Ortiz, C.; Fang, C. C. Comparative Kinetic Studies of the Copolymerization of Cyclohexene Oxide and Propylene Oxide with Carbon Dioxide in the Presence of Chromium Salen Derivatives. In Situ FTIR Measurements of Copolymer vs Cyclic Carbonate Production. *J. Am. Chem. Soc.* **2003**, *125* (25), 7586−7591.
(69) Wu, G.-P.; Wei, S.-H.; Ren, W.-M.; Lu, X.-B.; Xu, T.-Q.; Darensbourg, D. J. Perfectly Alternating Copolymerization of CO2 and Epichlorohydrin Using Cobalt(III)-Based Catalyst Systems. *J. Am. Chem. Soc.* **2011**, *133* (38), 15191−15199.
(70) Liu, J.; Ren, W.-M.; Liu, Y.; Lu, X.-B. Kinetic Study on the Coupling of CO2 and Epoxides Catalyzed by Co(III) Complex with an Inter- or Intramolecular Nucleophilic Cocatalyst. *Macromolecules* **2013**, *46* (4), 1343−1349.
(71) Chukanova, O. M.; Bukhovets, E. V.; Perepelitsina, E. O.; Belov, G. P. The kinetics of carbon dioxide and propylene oxide copolymerization catalyzed by binary catalyst system. *Polym. Sci., Ser. B* **2015**, *57* (3), 224−227.
(72) Darensbourg, D. J.; Wang, Y. Terpolymerization of propylene oxide and vinyl oxides with CO2: copolymer cross-linking and surface modification via thiol−ene click chemistry. *Polym. Chem.* **2015**, *6* (10), 1768−1776.
(73) Scharfenberg, M.; Hilf, J.; Frey, H. Functional Polycarbonates from Carbon Dioxide and Tailored Epoxide Monomers: Degradable Materials and Their Application Potential. *Adv. Funct. Mater.* **2018**, *28* (10), 16.
(74) Yi, N.; Chen, T. T. D.; Unruangsri, J.; Zhu, Y.; Williams, C. K. Orthogonal functionalization of alternating polyesters: selective patterning of (AB)n sequences. *Chem. Sci.* **2019**, *10* (43), 9974−9980.
(75) Darensbourg, D. J.; Chung, W.-C.; Arp, C. J.; Tsai, F.-T.; Kyran, S. J. Copolymerization and Cycloaddition Products Derived from Coupling Reactions of 1,2-Epoxy-4-cyclohexene and Carbon Dioxide. Postpolymerization Functionalization via Thiol−Ene Click Reactions. *Macromolecules* **2014**, *47* (21), 7347−7353.
(76) Darensbourg, D. J.; Tsai, F.-T. Postpolymerization Functionalization of Copolymers Produced from Carbon Dioxide and 2-Vinyloxirane: Amphiphilic/Water-Soluble CO2-Based Polycarbonates. *Macromolecules* **2014**, *47* (12), 3806−3813.
(77) Chen, K.; Shi, G.; Li, H.; Wang, C.; Darensbourg, D. J. Design of Betaine Functional Catalyst for Efficient Copolymerization of Oxirane and CO2. *Macromolecules* **2018**, *51* (15), 6057−6062.
(78) Konieczynska, M. D.; Lin, X.; Zhang, H.; Grinstaff, M. W. Synthesis of Aliphatic Poly(ether 1,2-glycerol carbonate)s via Copolymerization of CO2 with Glycidyl Ethers Using a Cobalt Salen Catalyst and Study of a Thermally Stable Solid Polymer Electrolyte. *ACS Macro Lett.* **2015**, *4* (5), 533−537.
(79) Wu, G.-P.; Wei, S.-H.; Lu, X.-B.; Ren, W.-M.; Darensbourg, D. J. Highly Selective Synthesis of CO2 Copolymer from Styrene Oxide. *Macromolecules* **2010**, *43* (21), 9202−9204.
(80) Ren, W.-M.; Zhang, X.; Liu, Y.; Li, J.-F.; Wang, H.; Lu, X.-B. Highly Active, Bifunctional Co(III)-Salen Catalyst for Alternating Copolymerization of CO2 with Cyclohexene Oxide and Terpolymerization with Aliphatic Epoxides. *Macromolecules* **2010**, *43* (3), 1396−1402.
(81) Moore, D. R.; Cheng, M.; Lobkovsky, E. B.; Coates, G. W. Electronic and Steric Effects on Catalysts for CO2/Epoxide Polymerization: Subtle Modifications Resulting in Superior Activities. *Angew. Chem., Int. Ed.* **2002**, *41* (14), 2599−2602.
(82) Kissling, S.; Lehenmeier, M. W.; Altenbuchner, P. T.; Kronast, A.; Reiter, M.; Deglmann, P.; Seemann, U. B.; Rieger, B. Dinuclear zinc catalysts with unprecedented activities for the copolymerization of cyclohexene oxide and CO2. *Chem. Commun.* **2015**, *51* (22), 4579−4582.
(83) Kissling, S.; Altenbuchner, P. T.; Lehenmeier, M. W.; Herdtweck, E.; Deglmann, P.; Seemann, U. B.; Rieger, B. Mechanistic Aspects of a Highly Active Dinuclear Zinc Catalyst for the Copolymerization of Epoxides and CO2. *Chem. - Eur. J.* **2015**, *21* (22), 8148−8157.
(84) Wang, Y. Y.; Darensbourg, D. J. Carbon dioxide-based functional polycarbonates: Metal catalyzed copolymerization of CO2 and epoxides. *Coord. Chem. Rev.* **2018**, *372*, 85−100.
(85) Chen, T. T. D.; Zhu, Y.; Williams, C. K. Pentablock Copolymer from Tetracomponent Monomer Mixture Using a Switchable Dizinc Catalyst. *Macromolecules* **2018**, *51* (14), 5346−5351.
(86) Darensbourg, D. J.; Wei, S.-H.; Yeung, A. D.; Ellis, W. C. An Efficient Method of Depolymerization of Poly(cyclopentene carbonate) to Its Comonomers: Cyclopentene Oxide and Carbon Dioxide. *Macromolecules* **2013**, *46* (15), 5850−5855.
(87) Darensbourg, D. J.; Yeung, A. D.; Wei, S.-H. Base initiated depolymerization of polycarbonates to epoxide and carbon dioxide co-monomers: a computational study. *Green Chem.* **2013**, *15* (6), 1578−1583.
(88) Darensbourg, D. J.; Chung, W.-C.; Wilson, S. J. Catalytic Coupling of Cyclopentene Oxide and CO2 Utilizing Bifunctional (salen)Co(III) and (salen)Cr(III) Catalysts: Comparative Processes Involving Binary (salen)Cr(III) Analogs. *ACS Catal.* **2013**, *3* (12), 3050−3057.

https://dx.doi.org/10.1021/jacs.0c07980
J. Am. Chem. Soc. 2020, 142, 19150−19160

Predicting Co(III)K(I) Catalyst Performances Using Reduction Potentials in Carbon Dioxide and Propene Oxide Ring Opening Copolymerizations.

Wouter Lindeboom,[a] Arron C. Deacy,[a] Andreas Phanopoulos,[b] Antoine Buchard*[c] and Charlotte K. Williams*[a]

[a] Department of Chemistry, University of Oxford, 12 Mansfield Road, Oxford, OX1 3TA, United Kingdom.

[b] Department of Chemistry, Molecular Sciences Research Hub, Imperial College London, W12 OBZ, United Kingdom.

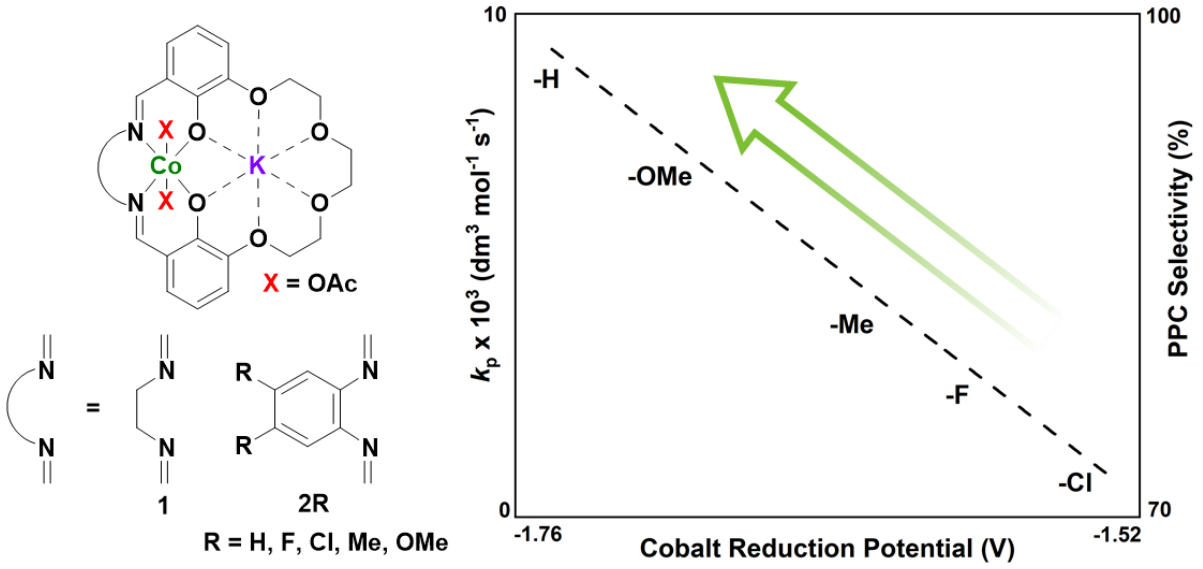
[c] Department of Chemistry, Centre for Sustainable and Circular Technologies, University of Bath, BA2 7AY, United Kingdom.

Corresponding author emails: apb46@bath.ac.uk charlotte.williams@chem.ox.ac.uk

Abstract

Carbon dioxide copolymerization is a front-runner CO_2 utilization strategy but its viability depends on improving the catalysis. This work identifies a measurable catalyst ground-state parameter, metal reduction potential, which directly correlates with both polymerization activity and selectivity. It is applied to compare a series of heterodinuclear Co(III)K(I) catalysts for propene oxide (PO)/CO_2 ring opening copolymerization (ROCOP) in terms of activity and selectivity for poly(propene carbonate) (PPC). The best catalyst shows a turnover frequency of 389 h^{-1} and PPC selectivity of >99% (50 °C, 20 bar, 0.025 mol% catalyst); performances that are field leading. Catalyst performances are rationalised by the dinuclear metallate mechanism but calculations (DFT) are too insensitive to predict performance trends which further emphasises the value of the redox potential correlation. This straightforward method to measure active site electron density and its correlation with activity and selectivity is recommended to guide future catalyst discovery for polymerizations and carbon dioxide utilizations.

Graphical Abstract



Introduction

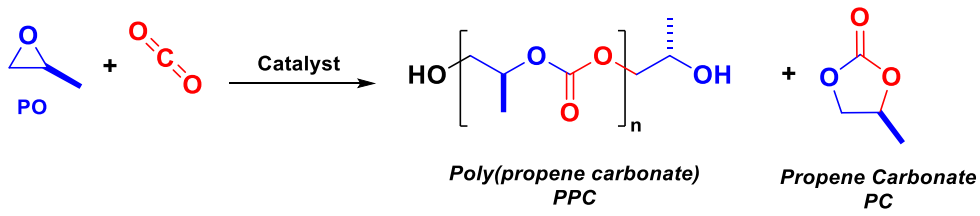


Figure 1 Propene oxide (PO)/Carbon Dioxide (CO_2) Ring-Opening Copolymerization (ROCOP) to synthesize poly(propene carbonate) (PPC) and propene carbonate (PC). The catalyst is applied with 1,2-cyclohexanediol (CHD) to deliver α,ω-hydroxyl telechelic polymer chains (catalyst: CHD, 1:20, see ESI for further details).

Utilizing CO_2 to make polymers is a front-runner technology exemplifying carbon dioxide valorization, waste recycling and reductions to greenhouse gas emissions.[1-6] Epoxide/CO_2 ring opening copolymerization (ROCOP) is truly catalytic, allows up to 48 wt% carbon dioxide uptake, yields valuable products ($1,000-10,000/tonne) and operates in conventional manufacturing plant at scale (Fig. 1).[7,8] Propene oxide (PO)/CO_2 ROCOP is particularly important since low molar mass, hydroxyl telechelic poly(propene carbonate) (PPC) reduces carbon emissions in manufacturing of home insulation, automotive and household foams, in addition to having desirable properties as a surfactant.[9-11] Life-cycle assessments show a 'triple win' where every molecule of carbon dioxide utilized saves two more by avoiding PO useage.[12] Higher molar mass PPC improves properties of bio-derived plastics, like PLA, and in block polymers furnishes toughened plastics and pressure sensitive adhesives.[13-16] PO is a commodity chemical already used at scale in polymer manufacturing, but its carbon dioxide copolymerization is challenging because PPC is the kinetic product and, in many cases, the thermodynamic product, propene carbonate (PC), shows an equivalent, or only marginally higher, barrier to formation.[17,18] The best polymerization catalysts must, therefore, combine both high rates and selectivity, under conditions suitable for scale-up. Major challenges include our inability to predict catalytic activity and selectivity and limited understanding of 'catalyst design rules'; these arise, in part, because of narrow structural diversity of known catalysts.

Understanding structure-activity relationships is a central to catalysis, from single atom heterogeneous catalysts to carbon dioxide reduction nanocatalysts to an underpinning method for machine learning to tacticity control in alkene polymerization catalysts.[19-22] It underpins polymerization catalyst design but because such catalysts are applied at very low loadings, deconvoluting effects can be demanding. Even when catalysts are studied under relevant conditions, in many cases structure-performance relationships are impossible to determine or are very complex. For example, a recent systematic investigation of heterodinuclear catalysts M(II)Mg(II) epoxide/carbon dioxide ROCOP catalysts (M= Cr(II)-Zn(II)) which revealed no correlation between activity and any physical parameters, including metal ionic radius, Lewis acidity or ligand Hammett parameters.[23] Similarly, efficient Ln_3(III)/Co(II) catalysts (Ln(III) = La-Dy), failed to show any clear trends between activity and catalyst physical properties.[24,25] One successful design target is dinuclear metal catalysts, based on pioneering work from Inoue and co-workers, and, subsequently, from Coates and co-workers using dimeric Zn(II) β-diiminate catalysts for cyclohexene oxide (CHO)/CO_2 ROCOP.[26-29] Heterogeneous catalysts also showed activity values that loosely correlated with Zn-Zn separations, although care must be taken since these catalyst surfaces and crystallinities are highly variable.[30] In 2020, we reported upon the physical basis for catalytic synergy by exploiting detailed kinetic investigations of heterodinuclear Co(II)Mg(II) catalysts: Co(II) reduces the transition state enthalpy barrier and Mg(II) reduces the transition state entropy barrier.[31] Currently, aside from targeting (hetero)dinuclear catalysts, there is very limited structure-activity correlation, rather catalyst performances tend to be (post)rationalised using DFT calculations to elucidate mechanisms.[32,33] Attempts were also made to correlate activity with computed structural parameters, for example Nozaki and co-workers showed a direct relationship between activity and computed difference between M-carbonate and M-epoxide bond dissociation energies using (planar, tetradentate ligand)M /PPNCl catalyst systems, where M = Cr(III), Co(III).[34] The discovery of boron/ammonium systems was another important advance and structure-activity investigations using tethered borane-'onium' catalysts, for CHO/CO_2 ROCOP, showed the 'C_5-tether' was the best, but there was no correlation between activity and boron Lewis acidity, or any other measurable parameter.[35-40] To develop better catalysts, this copolymerization and many other carbon dioxide utilizations need methods both to predict and understand structure-activity and selectivity relationships.

Results

Here, a series of heterodinuclear catalysts, featuring a macrocyclic ligand coordinating to Co(III)/K(I), are investigated for PO/CO_2 ROCOP (Fig. 2).[41-43] Recently, catalyst **1** showed competitive activity and selectivity with leading Co(III)/PPNCl catalyst systems and operated without additives and efficiently with alcohols (relevant to future industrialization of the process).[41] Its rate law and computed catalytic cycle (DFT) were rationalised by a dinuclear metallate mechanism, in which the rate determining step involves Co(III) coordinating and activating the propene oxide to attack by a transient K(I) carbonate nucleophile (Fig. 3).[43] This mechanism is the starting point for the current investigation which targets modifications to the Co(III) active site electron density, by varying the ligand imine substituents, and the influences upon rates and selectivity.

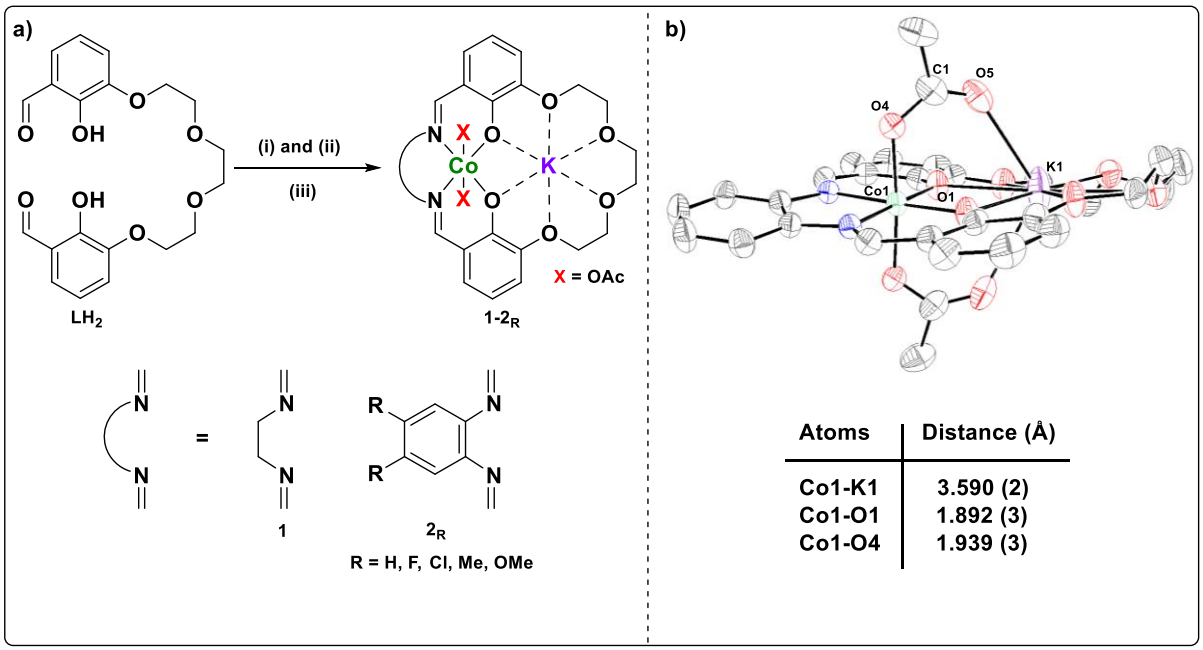


Figure 2 a) Synthesis of complexes **1**-$\mathbf{2_R}$. (i) KOAc, $Co(OAc)_2$, MeCN, 25 °C, 30 min. (ii) Diamine, MeCN, 25 °C, 16 h. (iii) AcOH, air, MeCN, 48 h. $\mathbf{2_{OMe}}$: (i) $Ba(ClO_4)_2$, MeCN, 25 °C; then Diamine, 24 h. (ii) Guanidinium sulfate, $H_2O/CHCl_3$, 25 °C, 16 h. (iii) KOAc, $Co(OAc)_2$, MeCN, 25 °C, 16 h.(iv) AcOH, air, MeCN, 48 h. b) Molecular structure for $\mathbf{2_H}$, determined by X-ray diffraction (thermal ellipsoids, 50% probability) and selected bond lengths (Table S1 and Fig. S1).

Catalysts **1**-$\mathbf{2_R}$ were synthesized by reacting the dialdehyde (LH_2) with the appropriate diamine linker, an equivalent of potassium(I) acetate and cobalt(II) acetate, followed by addition of excess acetic acid (Fig. 2a, SI for experimental details; note $\mathbf{2_{OMe}}$ was prepared differently).[41] By varying the diamines, 6 Co(III)K(I) complexes were isolated, differing only by the 'linker': ethylene (**1**), phenylene ($\mathbf{2_H}$) and substituted phenylene ($\mathbf{2_{F,\ Cl,\ Me,\ OMe}}$). The catalysts are all heterodinuclear complexes: Co(III) is always coordinated by the ligands' diphenolate diamine moieties (*O*,*N*,*N*,*O*) and K(I) by the diphenolate-tetraether moieties. All complexes were isolated pure and fully characterized using NMR (Fig. S2-S26), IR spectroscopy (Fig. S27), cyclic voltammetry (CV) (Fig. S28, Table S2), elemental analysis and, where possible, by single crystal X-ray diffraction (Table S1, Fig. 2 and S1). Typical ^{1}H NMR data show that the LH_2 aldehyde is completely consumed (9.94 ppm) and a single imine resonance forms (8.40-7.51 ppm). The phenolic protons (~10.86 ppm) disappear and new acetate and linker resonances are observed (Fig. S20-S26). All the $^{13}C\{^1H\}$ NMR spectra were assigned using COSY, HSQC and HMBC and show the expected acetate (~180 ppm), imine (162-155 ppm) and linker resonances (Fig. S2-S26). All complexes show asymmetric and symmetric acetate stretches in IR spectra (Fig. S27). Single crystals of $\mathbf{2_H}$, characterized by XRD, confirm the heterodinuclear speciation and ligand coordination modes (Fig. 2b and Table S1). The catalyst has C_2 symmetry (Co_1-K_1 axis) which renders the acetate ligands equivalent and both adopt bridging, i.e. κ_2, coordination modes. In contrast, **1** has a structure featuring both bridging and terminal acetate ligands (Fig. S1). These differences may arise from the greater 'phenylene' linker rigidity, supported by a shorter Co-K distance in $\mathbf{2_H}$ (3.5904(17) Å) than in **1** (3.6979(5) Å).

Catalysts **1**-$\mathbf{2_R}$ were each tested for PO/CO_2 copolymerization, at 50 °C, using neat PO (14 M, 6 mL), 0.025 mol % (i.e. 1:4000, catalyst:PO) catalyst loading, 20 bar CO_2 pressure and with 0.5 mol % 1,2-cyclohexanediol (CHD, 20 equiv. vs catalyst) (Fig. 1, Table 1). These conditions are demanding but relevant to production of PPC polyols where the excess diol controls molar mass; notably under these conditions other catalysts can show diminished/retarded activity.[24,41,44] Using a Parr reactor fitted with a DiComp sentinel probe, attached to an ATR-IR spectrometer, allowed for continual monitoring of absorptions, and hence concentrations, of both polymer (PPC, 1750 cm^{-1}) and cyclic carbonate by-product (PC, 1810 cm^{-1}). All catalysts showed good performances with high selectivity for PPC formation, quantitative CO_2 uptake (no ether linkages), and high selectivity

for hydroxyl telechelic PPC (Fig. 4 and S29-S39).[41] The PPC samples all showed molar mass values, consistent with theoretical values, in the target range for polyols, with monomodal, narrow dispersity distributions (Đ < 1.20).[41] Within the series of catalysts there are significant differences: the activity values, turn-over-frequency (TOF), vary from 60-390 h^{-1} and the PPC selectivity varies from 75-99%. For each catalyst, the selectivity was consistent throughout the reaction and independent of conversion, thereby suggesting that differences between catalysts relate to their structures (Fig. 4 and S29-S33).

Table 1 CO_2/PO ROCOP Productivity, Activity and Selectivity Data for Catalysts **1** and $\mathbf{2}_{H, Me, OMe, F, Cl}$.[a]

Catalyst	Productivity TON[b]	Activity TOF_{PPC} (h^{-1})[c]	Propagation Rate Coefficient k_p *10^3 (dm^3 mol^{-1} s^{-1})[d]	Selectivity PPC (%)[e]	PPC Molar Mass M_n [Đ] (g mol^{-1})[f]
1[g]	1360 ± 68	333 ± 17	11.20 ± 0.56	98	5300 [1.08]
$\mathbf{2}_H$	973 ± 49	389 ± 19	9.40 ± 0.47	>99	4000 [1.06]
$\mathbf{2}_{Me}$	1402 ± 70	101 ± 6	4.40 ± 0.22	85	5500 [1.15]
$\mathbf{2}_{OMe}$	1494 ± 75	191 ± 10	7.25 ± 0.36	96	8900 [1.11]
$\mathbf{2}_F$	1196 ± 60	73 ± 4	1.78 ± 0.09	80	4400 [1.11]
$\mathbf{2}_{Cl}$	962 ± 48	62 ± 3	1.44 ± 0.07	75	4200 [1.13]

[a]Conditions: Catalyst (0.025 mol %, 1 equiv., 3.5 mM), 1,2-cyclohexanediol (0.5 mol %, 20 equiv., 70 mM), PO (6 mL, 4000 equiv. 14 M), 20 bar CO_2, 50 °C. Note all results and errors are from experiments run in triplicate. All catalysts >99% CO_2 selectivity by ^{1}H NMR Spectroscopy (Fig. S34, Table S3). [b]Turnover number (TON) = number of moles of PO consumed / number of moles catalyst, PO conversion determined from the ^{1}H NMR spectrum from the integrals for PPC (4.92 ppm), PC (4.77 ppm) using mesitylene as an internal standard. [c]Turnover frequency of PPC (TOF_{PPC}) = (TON*PPC selectivity)/time (h). [d]$k_p = k_{obs}/[cat]^1$; k_{obs} determined from plots of $ln[PO]_t/[PO]_0$ vs time (Fig. 4 and S29-S33). [e]PPC selectivity determined from the ^{1}H NMR spectrum of the crude product by comparing integrals for PPC (4.92 ppm) vs. PC (4.77 ppm), errors ±1%. [f]Determined by GPC, in THF, calibrated with narrow-M_n polystyrene standards; dispersity values in parentheses (Fig. S35-S39). [g]Data in line with previous reports for catalyst **1**.[41]

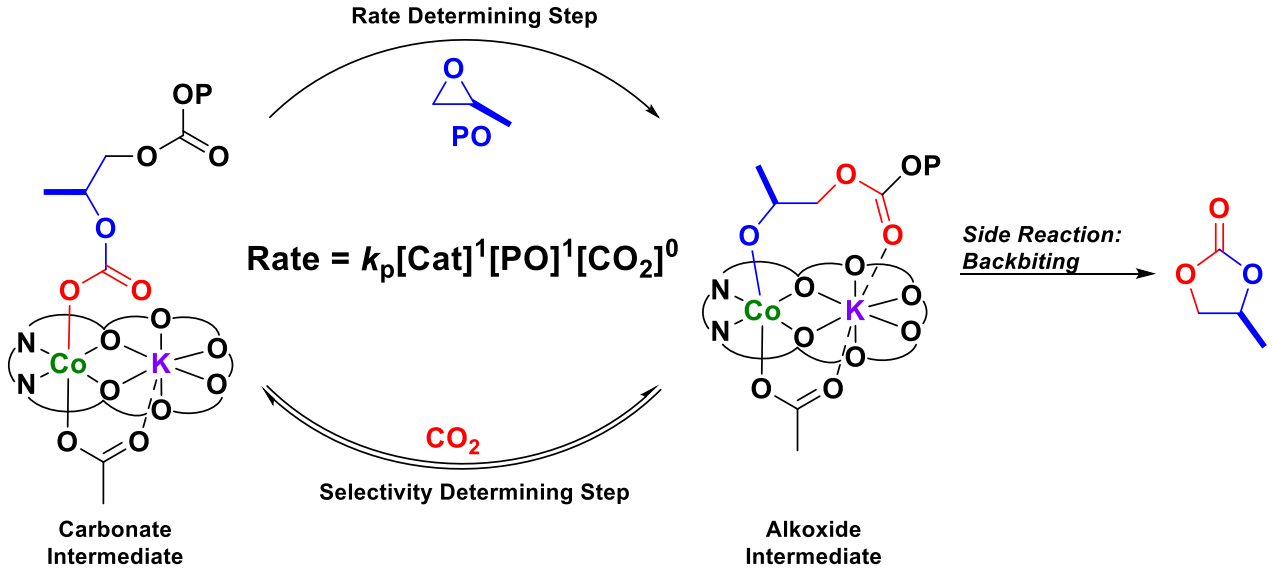


Figure 3 Cobaltate Dinuclear Mechanism for the PO/CO_2 ROCOP with rate and selectivity limiting steps identified.

The rate law for **1** is first order in both PO and catalyst concentrations but independent of carbon dioxide pressure (Fig. 3).[41] It is underpinned by the DFT calculations of the dinuclear metallate mechanism (Fig. 3).[43] From the experimental data, the rate determining step could be epoxide coordination and/or ring-opening by the carbonate intermediate but the computed mechanism suggests that ring-opening is rate limiting. The new catalysts are all assumed to operate by similiar rate laws and consistent with this all catalysts showed the expected first orders in epoxide concentrations (Fig. 4). To analyse differences in rates between the catalysts, both the catalytic turn-over frequency value (TOF) and the initial rate constants (5-20% conversion range) were determined. In other work, the initial polymerization rates, determined in a similar manner, were equivalent to integrated rates (20-80% conversion).[45] The initial rates analyses are useful since they prevent misleading point kinetic values from distorting trends and prevent any diffusion limitations which may limit performances at higher conversions and, therefore, they allow proper catalyst structure-activity comparisons.

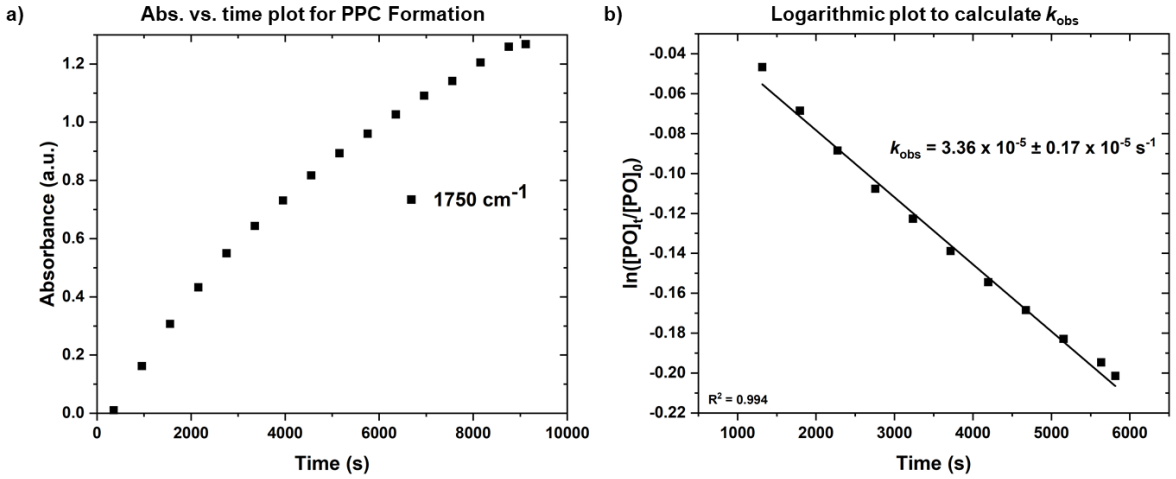


Figure 4 Exemplary Polymerization Kinetics Data for Catalyst $\mathbf{2_H}$. a) Plot showing PPC formation, analysed by changes to the absorbance at 1750 cm^{-1} (carbonyl stretch) versus time. b) Semi-logarithmic plot of PO concentration vs. time, used to determine k_{obs} (Figs. S29-S32).

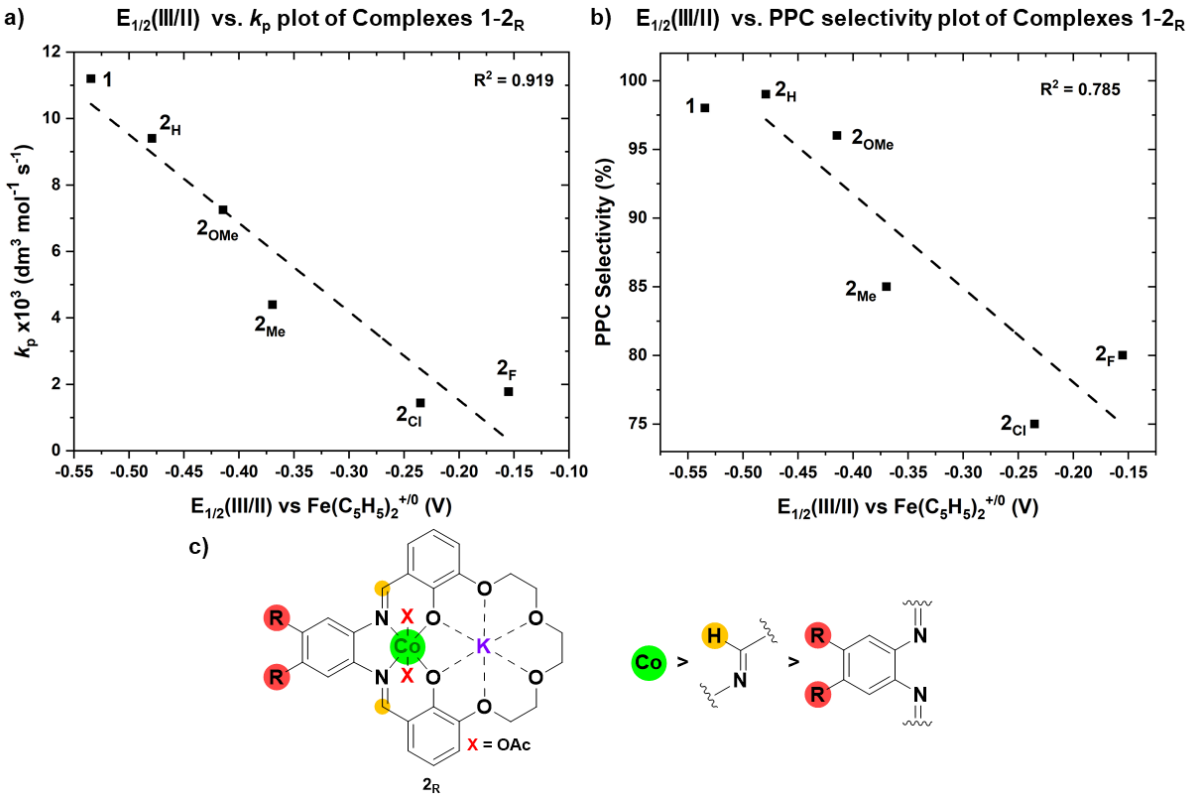
For each catalyst, the absorbance versus time data was converted into semi-logarithmic [PO] vs. time plots by independent calibration of the starting and final PO concentrations (Fig. 4). The pseudo first order rate coefficients, $k_{obs,\ PPC}$, were converted into propagation rate coefficients, $k_{p,\ PPC}$ by accounting for the catalyst concentration, using the rate law determined for **1**. The trends in propagation rate constants matched those in TOF, with values from 9.40 ± 0.47 to 1.44 ± 0.07 $mM^{-1}\ s^{-1}$ (Table 1). The catalyst featuring the rigid phenylene linker, $\mathbf{2_H}$, was the most active and selective, with a TOF of 389 h^{-1}, $k_{p,\ PPC}$ of 9.40 ± 0.47 $mM^{-1}\ s^{-1}$ and >99 % PPC selectivity. The success using the phenylene linker was particularly promising since it allowed investigation of the phenylene substituents, i.e. $\mathbf{2_{H,\ Me,\ OMe,\ F,\ Cl}}$. The substituents were all installed opposite the two N groups (imines) such that each is both para- and meta- to an imine group. All substituents are sufficiently small and at sites selected to limit any (negative) steric effects at the Co(III) active site. The methyl substituted catalyst, $\mathbf{2_{Me}}$, showed a three-fold reduction in rate, TOF = 111 h^{-1} ($k_{p,\ PPC}$ = 4.40 ± 0.22 $mM^{-1}\ s^{-1}$) and lower selectivity (85% PPC) than $\mathbf{2_H}$. The methoxy substituted catalyst, $\mathbf{2_{OMe}}$, showed TOF = 191 h^{-1} ($k_{p,\ PPC}$ = 7.25 ± 0.36 $mM^{-1}\ s^{-1}$) and selectivity of 96% but was also less effective than $\mathbf{2_H}$. Applying fluorine substituents $\mathbf{2_F}$ significantly slowed the rate, TOF = 73 h^{-1} ($k_{p,\ PPC}$ = 1.78 ± 0.09 $mM^{-1}\ s^{-1}$) and reduced selectivity, 80%, compared with $\mathbf{2_H}$. The chlorine substituted catalyst, $\mathbf{2_{Cl}}$, showed the lowest activity and selectivity, TOF = 62 h^{-1} (k_p= 1.44 ± 0.07 $mM^{-1}\ s^{-1}$) and 75% PPC selectivity**.** The best catalyst remained the phenylene variant, $\mathbf{2_H}$, but the substituent effects inform upon rate and selectivity influences.

To better understand the structure-performance relationships, it is important to characterize the active site and specifically the Co(III) since it coordinates both alkoxide and carbonate intermediates in the catalytic cycle. We reasoned that the Co(III) reduction potential values might offer information about the relative electron density at the active site. To test this notion, cyclic voltammetry experiments were conducted for all catalysts in an inert atmosphere (glove box), at ambient temperature and in acetonitrile solutions. Experiments applied a fixed catalyst concentration (1.6 mM) used an inert electrolyte (tetrabutylammonium hexafluorophosphate, 0.1 M) and fixed the scan rate (0.1 V/s) from -1.5 to 1.5 V (vs. ferrocene, see SI). All complexes showed two single electron reductions, corresponding to Co(III/II) and Co(II/I), at values consistent with those reported for other Co(III) complexes; in most cases the reductions were reversible (Fig. S28, Table S2).[46] Interestingly, a plot of the propagation rate constants (k_p) *vs*. the reduction potentials, $E_{1/2}$(Co(III/II)) or E_{red}(Co(II/I)), showed linear fits and a direct correlation (Fig. 5a, b, S40). Further, plotting the selectivity for PPC vs. the same reduction potentials (either Co(III) or Co(II)) also showed linear fits and direct correlations. Within the 'phenylene' series of catalysts, $\mathbf{2_H}$ has the most negative reduction potential, i.e. the greatest electron density at Co(III) of the $\mathbf{2_R}$ series and it performed best. Even better, the ethylene linked catalyst, **1**, showed the lowest absolute reduction potential, i.e. the highest electron density at Co(III), and the highest overall activity and selectivity. These measurements show that as the Co(III) electron density increases, and reduction potentials become more negative, so the copolymerization activity and selectivity increase. Thus, the redox measurements provide a simple predictor, based on the ground-state catalyst structure, that informs upon both of the critical polymerization performance metrics. These findings are especially surprising given the prior failures to correlate activity or selectivity to experimentally measurable catalyst parameters or properties.

With the value of Co(III) electrochemistry as 'probe' evident, other possible parameters were also examined. Plots of catalytic activity, or selectivity, against the imine protons' chemical shifts (^{1}H NMR spectra) also showed a linear relationship but with weaker correlation (Fig. S40). The greater separation of 'probe' from active site and the insensitivity of NMR spectroscopy likely cause the weaker correlation. Plots of catalyst performance metrics against the phenylene substituent Hammett parameters, σ, accounting for both meta- and para- effects, failed to show any correlation. These results highlight the limitation of using 'organic' ligand Hammett parameters to characterise metal active sites (Fig. S41). The possibility to use

Guttman Beckett, or related NMR spectroscopy experiments, to 'measure' active site Lewis acidity (by binding of epoxides or other 'model' substrates) is also not suitable. Both DFT and experimental investigations revealed that attempts to coordinate epoxides form a non-productive K(I)-epoxide intermediate. This intermediate, although the most stable adduct, shows a much higher catalytic pathway than the (higher-energy) productive Co(III)-epoxide species.[43] The same issue prevents investigations of epoxide binding by X-ray crystallography. These difficulties further highlight the benefit of using Co reduction potentials to properly measure and assess active site electronics.

Figure 5 Linear Correlations between Catalyst Activity (a) and Selectivity (b) with Co(III) Reduction Potential Values. a) Plot



of $E_{1/2}$(III/II) vs. k_p. b) Plot of $E_{1/2}$(III/II) vs. PPC selectivity. c) Schematic showing 'detectors' for rate and selectivity with accuracy of the correlation (Fig. S40-S42 for correlations with other substituents).

Discussion

The rate law is first order in both epoxide and catalyst concentrations and the proposed rate determining transition state involves a Co(III)-epoxide intermediate (**I**) being ring-opened by a transient K(I)-carbonate (**TS_{I-II}**, Fig. 6). This transition state forms a new Co(III)-alkoxide intermediate, **II**, which inserts carbon dioxide over a subsequent series of steps. The differences in rates within this series of catalysts are caused by more electron rich Co(III)/K(I) catalysts, like **1** and **2_H**, being more reactive towards epoxide ring-opening and insertion reactions. It is proposed that these electron rich catalysts have slightly destabilized epoxide coordination intermediates by having slightly less Lewis acidic Co(III) centres and may also show recuced barriers to epoxide ring-opening – i.e. catalysis is accelerated by raising the energy of the starting intermediate and lowering transition state energy. More electron rich catalysts are also expected to form destabilized Co(III)-alkoxide intermediates, which drives the subsequent carbon dioxide insertion equilibrium towards the transient Co(III)-carbonate intermediate. Even minor adjustments to the CO_2 insertion equilibria could significantly accelerate rates by increasing the concentration of 'catalyst', i.e. carbonate intermediate, available in the rate determining step.

DFT calculations examining all the different catalysts for this rate determining step were undertaken, here the experimental performance extremes are discussed, i.e. **2_H** and **2_{Cl}** (see SI for full details). These calculations do not show any significant differences between the catalysts with calculated intermediates, transition state energies and overall barriers having energies, within the error limits of DFT, that are the same. Furthermore, there was no obvious correlation between either the computed catalyst frontier energy levels, bond-lengths or ionization potentials with catalytic performance data. Overall, despite ~10x differences in experimental rates, DFT was too insensitive to provide any rationale for the measurements. The failure of computational methods to provide fine distinctions between catalysts further highlights the benefits for the use of active site reduction potentials since these measures correlate accurately with both activity and selectivity data.

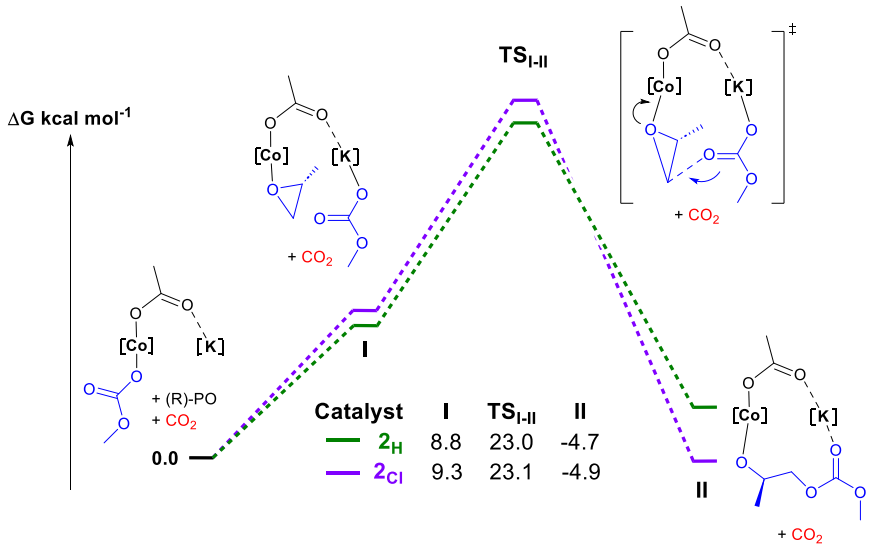


Figure 6 Illustrates the intermediates and transition states in the rate determining step of PO/CO_2 ROCOP Catalysis, with DFT calculated energies and barriers (ligand is omitted from structures for clarity, Fig. S44-S56, Table S4-S9).

The catalytic selectivity for PPC (polymer) vs. PC (by-product) is also critically important, not least because large-scale removal of high boiling cyclic carbonates is energy intensive. The mechanism also rationalizes the selectivity trends which depend upon the reactions of the alkoxide intermediate **II**. It can either react with carbon dioxide, an equilibrium process, to form the carbonate intermediate resulting in PPC propagation or 'back-bite' upon its own polycarbonate chain to form a chain-shortened alkoxide intermediate and PC.[43] The extent of the carbon dioxide equilibrium dictates which of the pathways are accessed (Fig. 7).[43] Generally, higher carbon dioxide pressures and lower temperatures should favor carbon dioxide insertion and polymer propagation. Here, the catalysts show differing PPC selectivity values under identical external conditions, which suggests their structures, and electronic properties, also influence the carbon dioxide insertion equilibrium.

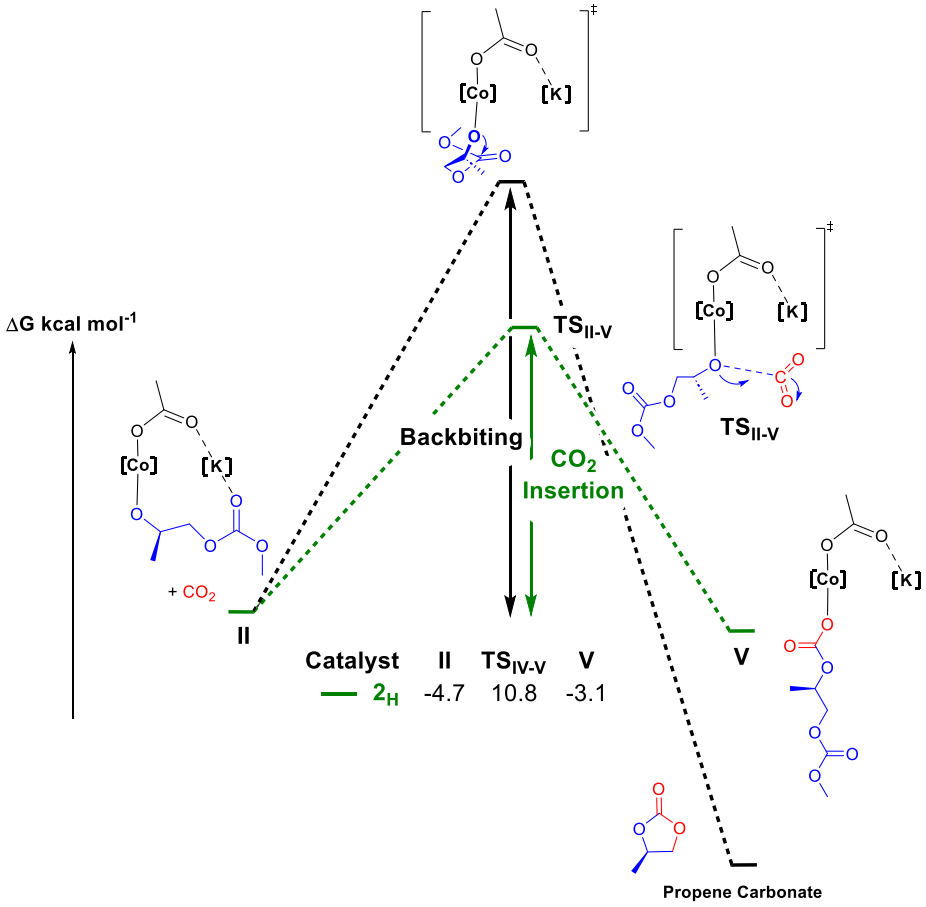


Figure 7: Schematic illustrating the selectivity determining step for $\mathbf{2_H}$ where the alkoxide intermediate forms either PPC or PC, with DFT calculated energies and barriers (ligands omitted from structures for clarity, Fig. S44-S56, Table S4-S9).

The experimental barrier to PC formation was measured by isolating the back-biting reaction.[43] This was possible by reacting the hydroxyl-telechelic polymer, PPC, with the catalysts, using variable temperatures, and measuring rates of cyclic carbonate PC formation. The experiments were undertaken using the most (**1**) and least ($\mathbf{2_{Cl}}$) selective catalysts in forward polymerization (Fig. S43). Both catalysts show equivalent, within experimental error, experimental barriers to backbiting and PC formation, i.e. **1** = 19.5 kcal mol^{-1}; $\mathbf{2_{Cl}}$ = 19.9 kcal mol^{-1}. This finding implies that by-product selectivity is not governed by different barriers to by-product formation but rather by the local concentration of the alkoxide intermediate and by the relative position of the carbon dioxide insertion equilibrium. Catalysts which show equilibria further towards the carbon dioxide insertion side have greater local carbonate intermediate concentration and show lower backbiting rates since they also show lower alkoxide intermediate concentrations; the position/extent of the carbon dioxide insertion equilibrium also influences the rate of polymerization as discussed earlier (Fig. 7). Thus, despite the by-product formation barriers being accessible under reaction conditions, faster rates and differing extents of carbon dioxide insertion control product selectivity.

The goals of catalyst design are to increase activity and selectivity and, as such, understanding structure-performance relationships is essential for rational catalyst design. Unfortunately, many homogeneous polymerization catalyses lack clear correlations between catalyst structures/physical parameters, measurable prior to catalysis, and performances. Here, a useful method to directly measure the relative electron density at the real active site, in this case Co(III), is described and its benefits are clear in terms of predicting both the activity and selectivity in the catalysis. Using electrochemical methods to characterize the catalyst, even when the catalysis does not involve any redox processes, is a useful predictor for performances. The method is attractive since cyclic voltammetry experiments are inexpensive, easy to set-up and work under inert conditions – there is no reliance on sophisticated operando spectroscopies. The 'predictor' for catalytic activity/selectivity trends should accelerate future catalyst development which is particularly desirable in this field since the copolymerization's require capital investment, including stainless-steel reactors and gas lines.

Prior unsuccessful structure activity investigations tried to correlate performances against features such as active site Lewis acidity, M-OR bond strengths, metal-ligand exchange rates or ligand Hammett parameters.[24,25,39,40,45] These failures mean that current catalyst design tends to heavily rely upon DFT calculations but their sensitivity is a major limitation.[33] This investigation highlights the importance and potential for direct measurement of active site electron density, rather than relying on parameters derived for other purposes. Electrochemical reduction potentials can be easily determined for other

metals, main group elements or even for some 'organic' active sites, thus, in future these measurements are recommended to guide other catalyst structure-performance relationships. A different application of active redox potential has been to assess catalyst lifetime, for example where thermally driven metal reduction deactivates the catalyst. Coates and co-workers applied Co(III/II) redox potential measurements, with Co(III)(salen)X/PPNX catalysts, to rationalise catalyst lifetimes in epoxide/anhydride ROCOP.[47] Other polymerization catalyses also require labile metal alkoxide/carboxylate/carbonate intermediates in the mechanisms and, thus, may also benefit from the electrochemical methods to identify more active catalysts.[48,49] For example, the industrial route to many bio-derived plastics is heterocycle (lactone/cyclic carbonate) ring-opening polymerization; coatings and surfactants are prepared using epoxide/anhydride ROCOP and switchable catalyses access recyclable plastics, thermoplastic elastomers, degradable adhesives and electrolytes.[48-54] To accelerate uptake of these sustainable polymers, which all operate by mechanisms involving Lewis acidic but labile oxygenated catalyst intermediates, use of active site reduction potential may be useful. A greater diversity of carbon dioxide utilization and storage technologies are important to deliver a net-zero emission chemical industry, yet very few are sufficiently understood for scaled operation at appropriate cost.[7,55] The methods presented here emphasise the importance of catalyst design for carbon dioxide insertion equilibria and the structure-performance trends that may inform other carbon dioxide transformations.

Conclusions

A series of homogeneous heterodinuclear Co(III)/K(I) catalysts, differing by the backbone linker group, were compared for an important carbon dioxide utilization, propene oxide/carbon dioxide ROCOP. There was a direct correlation between the active site (Co) reduction potential, and its electron density, with the catalytic activity and selectivity. The best catalysts were the most electron rich and were both faster and more selective for poly(propene carbonate). The rate and selectivity data were rationalized by the dinuclear metallate mechanism, where epoxide ring-opening was the rate determining step and carbon dioxide insertion the selectivity determining step. The ability to correlate catalyst performance data with an easy-to-measure parameter applied to the catalyst ground state is important and relevant to design better catalysts for sustainable polymer productions and carbon dioxide utilizations.

Acknowledgements

The EPSRC (EP/S018603/1; EP/R027129/1), Research England (RED, RE-P-2020-04), Econic Technologies (CASE studentship WL), the Oxford Martin School (Future of Plastics) and Royal Society (UF/160021 fellowship to AB) are acknowledged for research funding.

Data Availability Statement

The electronic supplementary information provides data to support the manuscript, all other data are available from the corresponding author.

Author contributions

WL and AD conceived and conducted all experiments; WL, AP, AB conducted all computational experiments. CW conceived the project, leads the research team and, with AB, secured the research funding.

Conflict of Interest Declaration

CW is a director of econic technologies.

References

1 Nakano, R., Ito, S. & Nozaki, K. Copolymerization of carbon dioxide and butadiene via a lactone intermediate. *Nat. Chem.* **6**, 325-331, (2014).

2 Zhu, Y., Romain, C. & Williams, C. K. Sustainable polymers from renewable resources. *Nature* **540**, 354-362, (2016).

3 Artz, J., Müller, T. E., Thenert, K., Kleinekorte, J., Meys, R., Sternberg, A., Bardow, A. & Leitner, W. Sustainable Conversion of Carbon Dioxide: An Integrated Review of Catalysis and Life Cycle Assessment. *Chem. Rev.* **118**, 434-504, (2018).

4 Scharfenberg, M., Hilf, J. & Frey, H. Functional Polycarbonates from Carbon Dioxide and Tailored Epoxide Monomers: Degradable Materials and Their Application Potential. *Adv. Funct. Mater.* **28**, 1704302, (2018).

5 Coates, G. W. & Getzler, Y. D. Y. L. Chemical recycling to monomer for an ideal, circular polymer economy. *Nat. Rev. Mater.* **5**, 501-516, (2020).

6 Yang, G.-W., Xu, C.-K., Xie, R., Zhang, Y.-Y., Lu, C., Qi, H., Yang, L., Wang, Y. & Wu, G.-P. Precision copolymerization of CO2 and epoxides enabled by organoboron catalysts. *Nat. Synth.* **1**, 892-901, (2022).

7 Hepburn, C., Adlen, E., Beddington, J., Carter, E. A., Fuss, S., Mac Dowell, N., Minx, J. C., Smith, P. & Williams, C. K. The technological and economic prospects for CO(2) utilization and removal. *Nature* **575**, 87-97, (2019).

8 Bhat, G. A. & Darensbourg, D. J. Progress in the catalytic reactions of CO2 and epoxides to selectively provide cyclic or polymeric carbonates. *Green Chem.* **24**, 5007-5034, (2022).

9 Langanke, J., Wolf, A., Hofmann, J., Böhm, K., Subhani, M. A., Müller, T. E., Leitner, W. & Gürtler, C. Carbon dioxide (CO2) as sustainable feedstock for polyurethane production. *Green Chem.* **16**, 1865-1870, (2014).

10 Darensbourg, D. J. Chain transfer agents utilized in epoxide and CO 2 copolymerization processes. *Green Chem.* **21**, 2214-2223, (2019).

11 Cao, H. & Wang, X. Carbon dioxide copolymers: Emerging sustainable materials for versatile applications. *SusMat* **1**, 88-104, (2021).

12 von der Assen, N. & Bardow, A. Life cycle assessment of polyols for polyurethane production using CO2 as feedstock: Insights from an industrial case study. *Green Chem.* **16**, 3272-3280, (2014).

13 Cyriac, A., Lee, S. H. & Lee, B. Y. Connection of polymer chains using diepoxide in CO2/propylene oxide copolymerizations. *Polym. Chem.* **2**, 950-956, (2011).

14 Beharaj, A., McCaslin, E. Z., Blessing, W. A. & Grinstaff, M. W. Sustainable polycarbonate adhesives for dry and aqueous conditions with thermoresponsive properties. *Nat. Commun.* **10**, 5478, (2019).

15 Rosetto, G., Deacy, A. C. & Williams, C. K. Mg(ii) heterodinuclear catalysts delivering carbon dioxide derived multi-block polymers. *Chem. Sci.* **12**, 12315-12325, (2021).

16 Cvek, M., Paul, U. C., Zia, J., Mancini, G., Sedlarik, V. & Athanassiou, A. Biodegradable Films of PLA/PPC and Curcumin as Packaging Materials and Smart Indicators of Food Spoilage. *ACS Appl. Mater. Interfaces* **14**, 14654-14667, (2022).

17 Diment, W. T., Lindeboom, W., Fiorentini, F., Deacy, A. C. & Williams, C. K. Synergic Heterodinuclear Catalysts for the Ring-Opening Copolymerization (ROCOP) of Epoxides, Carbon Dioxide, and Anhydrides. *Acc. Chem. Res.* **55**, 1997-2010, (2022).

18 Lidston, C. A. L., Severson, S. M., Abel, B. A. & Coates, G. W. Multifunctional Catalysts for Ring-Opening Copolymerizations. *ACS Catal.* **12**, 11037-11070, (2022).

19 Stürzel, M., Mihan, S. & Mülhaupt, R. From Multisite Polymerization Catalysis to Sustainable Materials and All-Polyolefin Composites. *Chem. Rev.* **116**, 1398-1433, (2016).

20 Mitchell, S., Vorobyeva, E. & Pérez-Ramírez, J. The Multifaceted Reactivity of Single-Atom Heterogeneous Catalysts. *Angew. Chem. Int. Ed.* **57**, 15316-15329, (2018).

21 Toyao, T., Maeno, Z., Takakusagi, S., Kamachi, T., Takigawa, I. & Shimizu, K.-i. Machine Learning for Catalysis Informatics: Recent Applications and Prospects. *ACS Catal.* **10**, 2260-2297, (2020).

22 Sun, R., Liao, Y., Bai, S.-T., Zheng, M., Zhou, C., Zhang, T. & Sels, B. F. Heterogeneous catalysts for CO2 hydrogenation to formic acid/formate: from nanoscale to single atom. *Energy Environ. Sci.* **14**, 1247-1285, (2021).

23 Reis, N. V., Deacy, A. C., Rosetto, G., Durr, C. B. & Williams, C. K. Heterodinuclear Mg(II)M(II) (M=Cr, Mn, Fe, Co, Ni, Cu and Zn) Complexes for the Ring Opening Copolymerization of Carbon Dioxide/Epoxide and Anhydride/Epoxide. *Chem. Eur. J.* **28**, e202104198, (2022).

24 Nagae, H., Aoki, R., Akutagawa, S. N., Kleemann, J., Tagawa, R., Schindler, T., Choi, G., Spaniol, T. P., Tsurugi, H., Okuda, J. & Mashima, K. Lanthanide Complexes Supported by a Trizinc Crown Ether as Catalysts for Alternating Copolymerization of Epoxide and CO2: Telomerization Controlled by Carboxylate Anions. *Angew. Chem. Int. Ed.* **57**, 2492-2496, (2018).

25 Asaba, H., Iwasaki, T., Hatazawa, M., Deng, J., Nagae, H., Mashima, K. & Nozaki, K. Alternating Copolymerization of CO 2 and Cyclohexene Oxide Catalyzed by Cobalt − Lanthanide Mixed Multinuclear Complexes. *Inorg. Chem.*, 0-5, (2020).

26 Kobayashi, M., Inoue, S. & Tsuruta, T. Diethylzinc-Dihydric Phenol System as Catalyst for the Copolymerization of Carbon Dioxide with Propylene Oxide. *Macromolecules* **4**, 658-659, (1971).

27 Moore, D. R., Cheng, M., Lobkovsky, E. B. & Coates, G. W. Mechanism of the alternating copolymerization of epoxides and CO 2 using β-diiminate zinc catalysts: Evidence for a bimetallic epoxide enchainment. *J. Am. Chem. Soc.* **125**, 11911-11924, (2003).
28 Sugimoto, H. & Inoue, S. Copolymerization of carbon dioxide and epoxide. *J. Polym. Sci., Part A: Polym. Chem.* **42**, 5561-5573, (2004).
29 Ellis, W. C., Jung, Y., Mulzer, M., Di Girolamo, R., Lobkovsky, E. B. & Coates, G. W. Copolymerization of CO2 and meso epoxides using enantioselective β-diiminate catalysts: A route to highly isotactic polycarbonates. *Chem. Sci.* **5**, 4004-4011, (2014).
30 Fieser, M. E., Sanford, M. J., Mitchell, L. A., Dunbar, C. R., Mandal, M., Van Zee, N. J., Urness, D. M., Cramer, C. J., Coates, G. W. & Tolman, W. B. Mechanistic Insights into the Alternating Copolymerization of Epoxides and Cyclic Anhydrides Using a (Salph)AlCl and Iminium Salt Catalytic System. *J. Am. Chem. Soc.* **139**, 15222-15231, (2017).
31 Deacy, A. C., Kilpatrick, A. F. R., Regoutz, A. & Williams, C. K. Understanding metal synergy in heterodinuclear catalysts for the copolymerization of CO2 and epoxides. *Nat. Chem.* **12**, 372-380, (2020).
32 Plajer, A. J. & Williams, C. K. Heterotrinuclear Ring Opening Copolymerization Catalysis: Structure–activity Relationships. *ACS Catal.* **11**, 14819-14828, (2021).
33 Darensbourg, D. J. & Yeung, A. D. A concise review of computational studies of the carbon dioxide–epoxide copolymerization reactions. *Polym. Chem.* **5**, 3949-3962, (2014).
34 Ohkawara, T., Suzuki, K., Nakano, K., Mori, S. & Nozaki, K. Facile Estimation of Catalytic Activity and Selectivities in Copolymerization of Propylene Oxide with Carbon Dioxide Mediated by Metal Complexes with Planar Tetradentate Ligand. *J. Am. Chem. Soc.* **136**, 10728-10735, (2014).
35 Zhang, D., Boopathi, S. K., Hadjichristidis, N., Gnanou, Y. & Feng, X. Metal-Free Alternating Copolymerization of CO2 with Epoxides: Fulfilling "Green" Synthesis and Activity. *J. Am. Chem. Soc.* **138**, 11117-11120, (2016).
36 Yang, G. W., Zhang, Y. Y., Xie, R. & Wu, G. P. Scalable Bifunctional Organoboron Catalysts for Copolymerization of CO2and Epoxides with Unprecedented Efficiency. *J. Am. Chem. Soc.* **142**, 12245-12255, (2020).
37 Yang, G. W., Xu, C. K., Xie, R., Zhang, Y. Y., Zhu, X. F. & Wu, G. P. Pinwheel-Shaped Tetranuclear Organoboron Catalysts for Perfectly Alternating Copolymerization of CO2 and Epichlorohydrin. *J. Am. Chem. Soc.* **143**, 3455-3465, (2021).
38 Yang, G.-W., Zhang, Y.-Y. & Wu, G.-P. Modular Organoboron Catalysts Enable Transformations with Unprecedented Reactivity. *Acc. Chem. Res.* **54**, 4434-4448, (2021).
39 Schaefer, J., Zhou, H., Lee, E., Lambic, N. S., Culcu, G., Holtcamp, M. W., Rix, F. C. & Lin, T.-P. Tertiary and Quaternary Phosphonium Borane Bifunctional Catalysts for CO2/Epoxide Copolymerization: A Mechanistic Investigation Using In Situ Raman Spectroscopy. *ACS Catal.* **12**, 11870-11885, (2022).
40 Chen, C., Gnanou, Y. & Feng, X. Borinane-based organoboron catalysts for alternating copolymerization of CO2 with cyclic ethers: improved productivity and facile recovery. *Polym. Chem.* **13**, 6312-6321, (2022).
41 Deacy, A. C., Moreby, E., Phanopoulos, A. & Williams, C. K. Co(III)/Alkali-Metal(I) Heterodinuclear Catalysts for the Ring-Opening Copolymerization of CO2and Propylene Oxide. *J. Am. Chem. Soc.* **142**, 19150-19160, (2020).
42 Lindeboom, W., Fraser, D. A. X., Durr, C. B. & Williams, C. K. Heterodinuclear Zn(II), Mg(II) or Co(III) with Na(I) Catalysts for Carbon Dioxide and Cyclohexene Oxide Ring Opening Copolymerizations. *Chem. Eur. J.* **27**, 12224, (2021).
43 Deacy, A. C., Phanopoulos, A., Lindeboom, W., Buchard, A. & Williams, C. K. Insights into the Mechanism of Carbon Dioxide and Propylene Oxide Ring-Opening Copolymerization Using a Co(III)/K(I) Heterodinuclear Catalyst. *J. Am. Chem. Soc.* **144**, 17929-17938, (2022).
44 Darensbourg, D. J. & Wu, G. P. A one-pot synthesis of a triblock copolymer from propylene oxide/carbon dioxide and lactide: intermediacy of polyol initiators. *Angew. Chem. Int. Ed.* **52**, 10602-10606, (2013).
45 Trott, G., Garden, J. A. & Williams, C. K. Heterodinuclear zinc and magnesium catalysts for epoxide/CO 2 ring opening copolymerizations. *Chem. Sci.* **10**, 4618-4627, (2019).
46 Reath, A. H., Ziller, J. W., Tsay, C., Ryan, A. J. & Yang, J. Y. Redox Potential and Electronic Structure Effects of Proximal Nonredox Active Cations in Cobalt Schiff Base Complexes. *Inorg. Chem.* **56**, 3713-3718, (2017).
47 DiCiccio, A. M., Longo, J. M., Rodríguez-Calero, G. G. & Coates, G. W. Development of Highly Active and Regioselective Catalysts for the Copolymerization of Epoxides with Cyclic Anhydrides: An Unanticipated Effect of Electronic Variation. *J. Am. Chem. Soc.* **138**, 7107-7113, (2016).
48 Longo, J. M., Sanford, M. J. & Coates, G. W. Ring-Opening Copolymerization of Epoxides and Cyclic Anhydrides with Discrete Metal Complexes: Structure–Property Relationships. *Chem. Rev.* **116**, 15167-15197, (2016).
49 Deacy, A. C., Gregory, G. L., Sulley, G. S., Chen, T. T. D. & Williams, C. K. Sequence Control from Mixtures: Switchable Polymerization Catalysis and Future Materials Applications. *J. Am. Chem. Soc.* **143**, 10021-10040, (2021).
50 Castro-Aguirre, E., Iñiguez-Franco, F., Samsudin, H., Fang, X. & Auras, R. Poly(lactic acid)—Mass production, processing, industrial applications, and end of life. *Adv. Drug Delivery Rev.* **107**, 333-366, (2016).
51 Sulley, G. S., Gregory, G. L., Chen, T. T. D., Pena Carrodeguas, L., Trott, G., Santmarti, A., Lee, K. Y., Terrill, N. J. & Williams, C. K. Switchable Catalysis Improves the Properties of CO2-Derived Polymers: Poly(cyclohexene carbonate-b-epsilon-decalactone-b-cyclohexene carbonate) Adhesives, Elastomers, and Toughened Plastics. *J. Am. Chem. Soc.* **142**, 4367-4378, (2020).

52 Chen, T. T. D., Carrodeguas, L. P., Sulley, G. S., Gregory, G. L. & Williams, C. K. Bio-based and Degradable Block Polyester Pressure-Sensitive Adhesives. *Angew. Chem. Int. Ed.* **59**, 23450-23455, (2020).

53 Gregory, G. L., Sulley, G. S., Carrodeguas, L. P., Chen, T. T. D., Santmarti, A., Terrill, N. J., Lee, K.-Y. & Williams, C. K. Triblock polyester thermoplastic elastomers with semi-aromatic polymer end blocks by ring-opening copolymerization. *Chem. Sci.* **11**, 6567-6581, (2020).

54 Gregory, G. L., Gao, H., Liu, B., Gao, X., Rees, G. J., Pasta, M., Bruce, P. G. & Williams, C. K. Buffering Volume Change in Solid-State Battery Composite Cathodes with CO2-Derived Block Polycarbonate Ethers. *J. Am. Chem. Soc.* **144**, 17477-17486, (2022).

55 Huang, R., Rintjema, J., González-Fabra, J., Martín, E., Escudero-Adán, E. C., Bo, C., Urakawa, A. & Kleij, A. W. Deciphering key intermediates in the transformation of carbon dioxide into heterocyclic products. *Nat. Catal.* **2**, 62-70, (2019).